OAK RIDGE NATIONAL LABORATORY
operated by
UNION CARBIDE CORPORATION
NUCLEAR DIVISION
for the
U.S. ATOMIC ENERGY COMMISSION

UNION CARBIDE

ORNL - TM - 2480

1

TRANSMISSION ELECTRON MICROSCOPY AND PLASTIC DEFORMATION IN NEUTRON-IRRADIATED NIOBIUM
(Thesis)

R. P. Tucker

Submitted as a thesis to the Graduate Council of The University of Tennessee in partial fulfillment of the requirements for the Degree of Doctor of Philosophy.

ORNL-TM-2480

Contract No. W-7405-eng-26

TRANSMISSION ELECTRON MICROSCOPY AND PLASTIC DEFORMATION IN NEUTRON-IRRADIATED NIOBIUM

R. P. Tucker

Submitted as a thesis to the Graduate Council of The University of Tennessee in partial fulfillment of the requirements for the degree of Doctor of Philosophy.

MARCH 1969

OAK RIDGE NATIONAL LABORATORY
Oak Ridge, Tennessee
operated by
UNION CARBIDE CORPORATION
for the
U.S. ATOMIC ENERGY COMMISSION

ACKNOWLEDGMENT

The author expresses his sincerest appreciation to his major professor, Dr. M. S. Wechsler, for his professional guidance, patience, and understanding throughout the course of this investigation and for his steadfast assistance in the long, arduous task of preparing this manuscript.

Deepest gratitude is expressed to Dr. S. M. Ohr for his many contributions to the scientific content and direction of the project and, especially, for his counsel and friendship.

This research was carried out in the Radiation Metallurgy Section of the Solid State Division at the Oak Ridge National Laboratory, operated by the Union Carbide Corporation for the U. S. Atomic Energy Commission. The author is grateful for the opportunity to perform this investigation at the Laboratory, where the necessary expertise and facilities were available. Special appreciation is expressed to Dr. D. S. Billington, Division Director, and to the many members of the Solid State Division who have made the experience a pleasant and profitable one. In particular, gratitude is expressed to Drs. J. C. Crump, III, R. E. Reed, and J. T. Stanley and to Mr. J. M. Williams for useful discussions and suggestions. The author gratefully acknowledges the assistance given in various phases of the experimental work by Mr. E. D. Bolling, Dr. R. E. Reed, and Mr. C. L. Brooks. Special thanks are due Mr. C. W. Boggs and Mr. B. F. Day for printing the photomicrographs.

The author appreciates having been permitted the use of tensile tests results obtained at Battelle Institute, Geneva, Switzerland, by Dr. M. S. Wechsler and Miss R. Bode.

The author is sincerely grateful to Mrs. Janice Sweeney for her patience and diligence in preparing the final typed manuscript and to Mrs. Lazelle Tyler for her generous assistance with the typing of numerous drafts and the proofreading of the manuscript.

For the major period of this research, the author was an Oak Ridge Graduate Fellow from the University of Tennessee under appointment from Oak Ridge Associated Universities. During the final six months of this study, the author held a National Aeronautics and Space Administration Traineeship. The financial assistance provided by the Fellowship and the Traineeship is gratefully acknowledged.

ABSTRACT

Defect clusters and plastic deformation in neutron-irradiated polycrystalline and single-crystal niobium were studied by transmission electron microscopy (TEM) and tensile testing. The following aspects of these subjects were investigated: (1) the observation and tentative determination of the nature of radiation-produced defect clusters (spot damage), (2) the crystal geometry and mechanism of dislocation channeling, i.e., the formation by slip dislocations of pathways free of defect clusters, (3) the dose dependence of the yield stress, (4) the influence of low-temperature post-irradiation annealing on the yield stress, and (5) the temperature dependence of yielding.

Niobium samples were neutron-irradiated at reactor ambient temperatures ($\sim$ 50°C for polycrystals, 90-110°C for single crystals) to doses, Φ, from 4×10^{15} to 8×10^{18} neutrons/cm^2 (E > 1 Mev). Defect clusters were observed by transmission electron microscopy in polycrystalline niobium over a range of doses from 2×10^{17} to 4.4×10^{18} neutrons/cm^2 (E > 1 Mev). The defect clusters appear as black spots under kinematical diffraction conditions and as black-white contrasts under dynamical diffraction conditions. From an analysis of the black-white contrast, the defect clusters in as-irradiated material were found to be small dislocation loops, which were identified tentatively to be predominantly interstitial. The density and size distribution of the clusters were measured as a function of neutron dose and post-irradiation annealing temperature for a dose of 2×10^{18} neutrons/cm^2.

Dislocation channels cleared of radiation-produced defect clusters were observed by TEM in polycrystalline niobium irradiated to doses

greater than about 10^{18} neutrons/cm^2 and then deformed in tension. From electron diffraction patterns and diffraction contrast ($\vec{g} \cdot \vec{b}$) analysis, the plane on which the dislocation channels form was usually the {110} type plane. The strain within the channel was deduced from the offset at channel-channel, channel-boundary, and channel-helix intersections and was found to correspond to the passage of one to three slip dislocations per slip plane. Mechanisms for the clearing of the defect clusters are: (1) chopping-up or sweeping-up by slip dislocations, (2) annihilation by anti-defects, and (3) annealing due to the heat of plastic deformation.

The yield stress in single-crystal and polycrystalline niobium was found to be proportional to the square root of the dose for $\Phi \lesssim 10^{18}$ neutrons/cm^2; at higher doses, the rate of hardening decreased markedly, i.e., a saturation effect was observed. In polycrystals, the low-dose radiation hardening was correlated with the density and size distribution of visible defect clusters on the basis of a dispersed barrier model. The observed hardening requires a cluster strength of the order of (0.5-0.8) Gb^2, where G is the shear modulus and b is the Burgers vector.

Low-temperature post-irradiation annealing at 175°C and 300-400°C gave rise to further yield stress increases ("radiation-anneal hardening"). These radiation-anneal-hardening peaks are attributed to the motion of oxygen and carbon, respectively, to the radiation-produced defect clusters. The additional increase in yield stress upon annealing at 400°C requires that the strength of the barriers be increased by as much as a factor of two in order to be consistent with the density and size distribution of visible defect clusters.

The temperature dependence of the yield stress is not substantially changed by irradiation to 2.8×10^{17} neutrons/cm^2 for test temperatures from 93°K to 298°K, which suggested that irradiation to this dose does not change the thermally-activated mechanism of deformation in single-crystal niobium.

It is concluded that radiation hardening in niobium can be explained on the basis of the short-range elastic interaction between radiation-produced defect clusters visible by TEM and slip dislocation.

TABLE OF CONTENTS

LIST OF TABLES

LIST OF FIGURES

CHAPTER I

INTRODUCTION

When a metal is subjected to bombardment by neutrons, a change occurs in its physical and mechanical properties. In recent years there has been a flourish of activity attempting to interpret property changes upon neutron irradiation in terms of the defect structure resulting from the bombardment. Many significant theoretical and experimental contributions have been made toward understanding how neutrons interact in solids to change their properties. There are two aspects as concerns radiation effects on mechanical properties, namely, radiation hardening and radiation embrittlement. In this dissertation we are primarily concerned with radiation hardening, i.e., the increase in the yield and flow stresses following neutron irradiation. The exact nature of the defects which give rise to the stress increase is not well-known, but transmission electron microscopy (TEM) provides a key toward understanding the basis of radiation hardening. However, even with the development of TEM techniques by which radiation-produced defect clusters are revealed, the literature reports relatively few attempts to directly correlate in a quantitative way the observed defect clusters with mechanical property changes.

The previously reported work attempting to correlate observed defect clusters with mechanical properties has centered on the face-centered cubic metals, especially copper. In recent years, however, increasing attention has been focused on radiation effects in body-centered cubic metals and alloys. In particular, the refractory metals

have been investigated because of high-temperature applications. Among these, niobium and vanadium are of special interest because of their low fast neutron cross sections. Within the scope of its program on the effect of radiation on body-centered cubic metals, the Radiation Metallurgy Section of the Solid State Division at the Oak Ridge National Laboratory has undertaken a fundamental study of the damage revealed by TEM in neutron-irradiated niobium and of the relationship between the observed damage and radiation hardening.

Niobium was chosen as the metal for the present study for a number of reasons. Aside from its potential importance to reactor technology, techniques for growing high purity niobium single crystals were known and the expertise and equipment for providing such crystals were available to this laboratory. At the outset of the program the ability to prepare high quality single crystals was deemed important in the overall scope of a fundamental study attempting to correlate radiation-produced damage and mechanical properties. A second important consideration was that early in the study we were able to observe direct evidence by transmission electron microscopy of radiation-produced damage in niobium[1] receiving relatively low neutron doses. Thus, niobium appeared to be much more attractive for the study than the more common body-centered cubic metal, iron, in which visible damage has been observed only after high doses, requiring long irradiation times and resulting in high induced radioactivity. On the other hand, for the doses required to produce visible damage in niobium the induced radioactivity was at a level manageable in the laboratory after a reasonable wait for decay. In fact, the long half life of 2.0×10^4 years for the decay of niobium-94 results in

niobium itself being ideally suited for irradiation studies from the standpoint of radioactivity. Tantalum and tungsten impurities are the primary sources of induced radioactivity in niobium and by selecting starting stock in which these impurities were at a very low level the radioactivity was kept within the level permitted for work in the laboratory.

In this dissertation a report is given of five interrelated aspects of the effect of fast neutron bombardment on polycrystalline and single crystal niobium and the subsequent behavior of these irradiated samples during plastic deformation: (1) the observation and preliminary determination of the nature of radiation-produced spot damage (defect clusters), (2) the crystal geometry and mechanism of dislocation channeling (defect cluster removal by slip dislocations), (3) the dose dependence of the yield stress for polycrystals and for single crystals annealed near the melting point prior to irradiation, (4) the influence of post-irradiation annealing on the yield stress, and (5) the temperature dependence of yielding in single crystals. After reviewing the pertinent literature (Chapter II) and describing the experimental details common to all aspects of the work (Chapter III), each of the five areas outlined above is treated in a separate chapter (Chapters IV-VIII). A final chapter summarizes the information presented in the preceding five chapters and presents the conclusions of this study.

CHAPTER II

LITERATURE REVIEW

An increasing interest in recent years in radiation damage, especially in body-centered cubic metals, has yielded a large accumulation of literature in this and related fields. No attempt will be made here to give a complete historical review of the literature. Rather, an attempt will be made to set the background for the present study.

This survey will be devoted to the following topics: (1) defect clusters, particularly as observed by transmission electron microscopy (TEM) in neutron-irradiated body-centered cubic (bcc) metals, (2) channeling of dislocations, i.e., formation of pathways free of defect clusters by moving dislocations, (3) radiation hardening, especially the dependence of the yield stress on neutron dose,* (4) strengthening of irradiated metals by low-temperature post-irradiation annealing ("radiation-anneal hardening"), and (5) the influence of irradiation on the temperature dependence of yielding.

---

*Dose, or equivalently fluence, is most often characterized in the literature in terms of neutron energies greater than 1 Mev. However, authors frequently use other ranges of neutron energies. Where cited by the author this information will be given below with no attempt to standardize to a common basis.

I. DIRECT OBSERVATIONS AND ANALYSIS OF DEFECT CLUSTERS

Since 1959 when direct observations by transmission electron microscopy (TEM) of neutron irradiation damage in Al,[2] Cu,[3] and Au[4] were first reported, there has appeared a copious literature describing observations of radiation damage in metals. If one were to consider also the literature in closely related areas, such as quenched-in defects, the literature becomes unwieldy for the purposes of this review. Hence, we concentrate on listing the direct observations of defect clusters in metals primarily as the result of neutron bombardment and refer the reader to recent conferences[5,6] for a discussion of quenched-in vacancy complexes. However, we consider here those papers which treat the theory of the interaction of electron beams with defect clusters regardless of origin for they present methods of determining the nature of the defect clusters by TEM.

The bombardment of a metal with neutrons creates vacancies and interstitials in the region of the displacement cascades. The defect structure is thus more complex than that introduced by quenching where only vacancies are retained. The form into which radiation-produced vacancies and interstitials agglomerate, thereby reaching a size resolvable in the electron microscope, is influenced by a number of factors. Clearly the irradiation temperature directly affects the mobility of the point defects and their agglomeration into multi-defect complexes. To compare temperature effects in various metals, a reduced or homologous temperature scale is sometimes used, in which temperatures are expressed relative to the melting point of the material. The ambient temperature in a given reactor may be widely separated on the homologous temperature

scale for different metals. Another factor influencing the agglomeration of defects is the concentration of point defects introduced. Thus, one would expect a relation between defect clusters and radiation dose. Some indication exists that the variation in neutron spectra in different reactors is capable of changing the nature of the defect clusters produced. Recently, this was suggested as a possible explanation of the conflicting results for the nature of loops observed in copper.[7,8]

Apart from irradiation dose, temperature, and spectrum, the purity of the sample and post-irradiation annealing may significantly influence the defect clusters observed by TEM. Impurity atoms are important in that they may serve as sites for heterogeneous nucleation. The most obvious influence of post-irradiation annealing on point defects is to provide increased mobility and thereby enhance the tendency for agglomeration of the defects. In some cases, it is necessary to anneal a sample after irradiation in order to observe the defect clusters, although they may well have been changed in the process of making them visible in the electron microscope.

Usually defect clusters first appear in TEM foils as spots, sometimes called "black death". These black dots or spots may be observed in some metals in the as-irradiated condition, while in others they develop only upon post-irradiation annealing. With increasing annealing temperature or time, the "black death" disappears and in its place one may observe distinct dislocation loops with the possibility that voids or stacking fault tetrahedra may develop in certain cases. Whether or not the loops are the result of growth of the black dots, new microstructural features, or a combination of these two depends

upon the irradiation and annealing conditions. Evidence for radiation-produced defects may also be inferred from the appearance of dislocations. The interaction of point defects with dislocations is indicated by the dislocation becoming helical or "joggy".

Silcox and Hirsch[3] first reported the observation by TEM of regions of strain (black spots) and dislocation loops in copper irradiated to doses in the range from 6.7×10^{17} to 1.4×10^{20} neutrons/cm^2 (E > 1 Mev) at temperatures of 35°C and 60-100°C. The loops were believed to form from the clustering of vacancies in the displacement spike and the subsequent collapse of the vacancy clusters into disks. Radiation hardening was attributed primarily to dislocations cutting the "forest" of loops. This pioneering work indicated that radiation damage was detectable by TEM and pointed the way to greater application of TEM in the study of irradiated metals. Subsequent work has revealed the presence of black spots in various metals following not only neutron irradiation but also as the result of bombardment with fission fragments, ions, and, more recently, electrons. A reference list to transmission electron microscopy in irradiated metals is presented in Table I.

In irradiated metals, the defect clusters may exist as spherically symmetrical agglomerates of vacancies or interstitials or perhaps as disks of defects which may collapse into dislocation loops. An aspect which has received considerable theoretical attention is the determination of the nature (i.e., whether vacancy or interstitial in type) of the defect clusters when they are not resolvable as loops. The basic diffraction contrast theory of the imaging of dislocations was developed by Hirsch *et al.*,[20] Howie and Whelan,[23,24] and Howie.[22] Ashby and

TABLE I

REFERENCES TO TRANSMISSION ELECTRON MICROSCOPY
IN IRRADIATED METALS

I. General Aspects, Reviews, and Theory

Amelinckx (9,10,11)
Ashby and Brown (12,13)
Bell *et al.* (14,15,16)
Edmundson and Williamson (17)
Hashimoto *et al.* (18,19)
Hirsch *et al.* (20,21)
Howie (22)
Howie and Whelan (23,24)
Littler (25)
Makin (26)
Newkirk and Wernick (27)
Rühle (28)
Rühle *et al.* (29)
Silcox and Hirsch (3)
Thomas (30)
Thomas and Bell (31)
Thomas and Washburn (32)
Von Jan (33)
Wilkens (34,35)

II. Neutron Irradiation

A. Copper

Brimhall and Mastel (36)
Brinkman *et al.* (37)
Bourret and Dautreppe (38)
Cotterill and Koppenaal (39)
Crump (40)
Essmann and Seeger (41)
Essmann and Wilkens (42)
Goland (43)
Greenfield and Wilsdorf (44,45)
Koppenaal *et al.* (46)
Makin *et al.* (47,48,49)
Makin and Manthorpe (50)
Merkle (51,52)
McIntyre (7)
McIntyre and Brown (53)
Noggle (4)
Rühle (28,54)
Rühle *et al.* (29,55)
Rühle and Wilkens (8,56)
Scheidler *et al.* (57)
Schwink and Grieshammer (58)
Sharp (59)
Silcox (60)
Silcox and Hirsch (3)
Seeger (61)
Wilkens and Rühle (62)

TABLE I (Continued)

B. Other FCC Metals

Bierlein and Mastel (63)
Brimhall *et al.* (64)
Brimhall and Mastel (65)
Brinkman *et al.* (37)
Eyre (66)
Goland (43)
Hesketh and Norris (67)
Merkle (51,52)
Piercy and Whitton (68)
Ruedl *et al.* (69,70,71)
Rühle (54)
Silcox (60)
Smallman and Westmacott (2)
Thomas and Whitton (72)
Wilsdorf (73)

C. Iron

Bryner (74,75,76)
Eyre (77)
Eyre and Bartlett (78)
Hull and Mogford (79)
Ohr (80)

D. Molybdenum

Brimhall (81)
Brimhall *et al.* (82,83)
Brimhall and Mastel (84)
Downey and Eyre (85)
Eyre and Downey (86,87)
Eyre and Roberts (88)
Kerridge *et al.* (89)
Kissinger *et al.* (90)
Laidler *et al.* (91)
Maher and Eyre (92)
Mastel *et al.* (93)
Mastel and Brimhall (94)
Meakin and Greenfield (95)
Rao and Thomas (96)

E. Other BCC Metals

Lacefield *et al.* (97)
Tucker and Ohr (1)
Rühle *et al.* (98)

F. HCP Metals

Brimhall and Mastel (99,100)

TABLE I (Continued)

III. Ion and Fission Fragment Bombardment

A. Copper

Barnes (101)
Barnes and Mazey (102)
Bowden and Brandon (103,104)
Diehl and Diepers (105)
Diepers (106,107)
Hesketh and Richards (108,109,110)
Howe *et al.* (111,112,113)
Koppenaal *et al.* (46)
Merkle (51,52)
Rühle (54)

B. Aluminum

Barnes (101,114)
Barnes and Mazey (102)
Beevers and Nelson (115,116)
Henrikson *et al.* (117)
Howe *et al.* (112,113)
Mazey and Barnes (118)
Mazey *et al.* (119)
Norris (120)
Westmacott (121)

C. Gold

Brandon and Bowden (103,104,122)
Brandon *et al.* (123)
Castaing and Jouffrey (124)
Cotterill and Jones (125,126)
Howe and McGwin (127)
Howe *et al.* (112,113)
Menter (128)
Merkle (51,52,129)
Merkle *et al.* (130)
Noggle and Oen (131)
Ogilvie *et al.* (132)
Pashley and Presland (133)
Thomas and Balluffi (134,135,136)
Venables and Balluffi (137,138)

D. Other FCC Metals

Bowden and Brandon (103,104)
Brandon *et al.* (123)
Noggle and Stiegler (139)

TABLE I (Continued)

E. BCC Metals

Beevers and Mazey (140)
Eyre and Roberts (88)
Higgins and Roberts (141)
Masters (142,143)
Noggle and Stiegler (139)

F. HCP Metals

Bernstein and Gulden (144)
Gulden and Bernstein (145)

IV. Electron Irradiation

A. Copper

Makin (146)
Scheidler and Roth (147)

B. Nickel

Bourret (148)

C. Gold

Scheidler and Roth (147)

D. Platinum

Scheidler and Roth (147)

E. Niobium

Scheidler and Roth (147)

Brown determined the strain contrast from spherically symmetrical inclusions[12] and prismatic dislocation loops.[13] The specific problem of determining the nature of small radiation-produced loops from strain contrast analysis has been treated recently both theoretically and experimentally by Rühle, Wilkens, and co-workers.[8,28,29,54-56,149] They point out that the image contrast is a function of the depth of the defect cluster in the foil and that this depth must be known to within one-quarter of the extinction distance for the metal (about 50 Å in copper) in order to determine the nature of the defect cluster. Computer calculations by McIntyre and Brown[7,53] support the conclusion of earlier calculations reported by Rühle *et al.*[29] that the contrast of defect clusters near the foil surface depends on the depth of the defect in the foil. Thomas and Bell[31] and Bell *et al.*[14-16] have proposed a method for identification of small defects using dark field images which appeals to the shape of the black-white images under dynamical diffraction conditions and to the line of no contrast between the black and white parts of the image in relation to the diffraction vector, $\vec{g}$. However, Bell *et al.*[15] indicate that it is not possible in general to determine the nature of the defect clusters unambiguously using strain contrast theory.

In using TEM to study defect clusters, there are certain experimental considerations which require attention, such as the introduction of black spots into the foil during electropolishing[29,62] or by inadvertent ion bombardment in the electron microscope.[29,62] Even with the development of a stereo technique[105] for determining the depth of clusters in the foil from TEM photographs, considerable controversy remains as to the nature of defect clusters introduced by irradiation. In copper, for

example, Essmann and Wilkens,[42] Wilkens and Rühle,[62] and Rühle[28,54] originally reported the defect clusters following neutron irradiation to be of the vacancy type, whereas McIntyre[7] and McIntyre and Brown[53] find them to be primarily interstitial. More recently Crump[40] has reported the small black spots in neutron-irradiated copper to be vacancy in character. Rühle *et al.*[55] now report that they have identified both vacancy-loops (diameters < 75 Å) and interstitial-loops (diameters > 75 Å) in the same irradiated copper foil.

There is also controversy as to the nature of the defect clusters in copper after ion bombardment. Diepers and Diehl[105] and Diepers[106,107] find the clusters are of interstitial type when copper foils are irradiated with Ar-ions (5 kev), whereas Merkle,[51,52] Hesketh and Richards,[108-110] and Howe *et al.*[111-113] report vacancy type clusters in copper following various types and energies of ion bombardment. Although the question of cluster type appears to be rather unsettled, it seems quite likely that both types of defect clusters may be present as reported by Makin *et al.*[48] and Rühle *et al.*,[55] depending on the specifics of the irradiation conditions.

The nucleation of the clusters is an important factor. The evidence from ion bombardment in the microscope at temperatures below where interstitials or vacancies are mobile (Howe *et al.*[111-113,127]) and from neutron irradiation of copper at 78°K (Makin *et al.*[48]) is that the clusters observable by TEM form heterogeneously within the displacement cascade, i.e., without requiring thermal diffusion of the point defects. Furthermore, the work of Merkle[51,52,129] on gold indicates direct correlation of the number and size of visible defect clusters with the number and

energy of primary knock-ons above a critical energy value (about 34 kev). However, for copper this direct correlation between the energy transferred in a knock-on and the size and number of defects does not appear to hold true. Merkle[51,52] and Hesketh and Richards[109,110] have suggested that this lack of correspondence results from the primary knock-ons giving rise to sub-cascades which produce defect clusters too small to be visible by TEM, i.e., less than about 20 Å.

An extensive and quantitative study of defect clusters as a function of neutron dose and post-irradiation annealing is found in the work of Makin and co-workers on copper. Makin *et al.*[49] found that the density of defect clusters in the size range up to 125 Å increases with increasing dose, and Makin and Manthorpe[50] found there was a progressive decrease in the density of defect clusters of a given size upon annealing at 275°C. The annealing occurs in two steps: first the larger loops (diameters > 50 Å) anneal in a few tens of minutes at 275°C with an activation energy of 1-1.5 ev; then the small defects (diameters < 50 Å) disappear after several thousand minutes at 275°C with an apparent activation energy of $\sim$ 2 ev. The first stage of cluster annealing is attributed by Makin and Manthorpe[50] to the dissociation of sub-microscopic vacancy clusters which subsequently annihilate interstitials present in the larger loops and contribute to the growth and stability of the larger vacancy loops. In the second stage, the larger vacancy clusters dissociate and the remaining interstitial loops are annihilated.

A question that will arise in connection with radiation hardening to be discussed in Section III is the importance of defects not visible by TEM, i.e., single point defects and multi-defect complexes smaller

than, say, 20 Å. The field ion microscope[150-153] has been successfully used to reveal the small-sized defects down to the atomic scale in a few irradiated metals. The metal most thoroughly investigated using the field ion microscope appears to be tungsten which has been examined following irradiations with neutrons,[154-156] alpha particles,[157-159] fission fragments,[155,160-162] and neutral atoms.[154,163] Other neutron-irradiated metals which have been examined in the field ion microscope include iridium,[155,164,165] molybdenum,[158,159] and platinum.[166-168] Using this technique, Ralph *et al.*[155] observed single vacancies in tungsten following fast neutron irradiation to 10^{17} neutrons/cm^2. Upon annealing at 400°C ($T/T_m = 0.18$, T_m = absolute melting temperature) for 15 hours, they observed the single vacancies to migrate to form di-vacancies and small clusters. Thus, they attribute annealing in this temperature range (known as Stage III) in tungsten to single vacancy migration. However, Attardo and Galligan[166,167] believe from their field ion microscopy of neutron-irradiated tungsten that vacancies are stable at 400°C and are removed above 700°C ($T/T_m = 0.27$, i.e., in Stage IV). Interstitial atoms have been observed by field ion microscopy in neutron-irradiated platinum by Attardo and Galligan[166,167] and in tungsten following bombardment with 20-kev helium atoms by Sinha and Müller.[163]

For body-centered cubic metals, Table II describes the radiation-produced defect clusters seen by TEM, states the conditions under which the defect clusters were observed, and cites the source of the observation. Defect clusters in molybdenum following neutron irradiation and annealing have been investigated extensively. Numerous investigations[83,85,92,94,96] have identified large loops present after annealing

TABLE II

DIRECT OBSERVATIONS BY TEM OF RADIATION-PRODUCED DEFECT CLUSTERS IN BCC METALS

Metal	Type Irradiation	Irradiation Temperature (°C)	Dose (particles/cm^2)	Description of Damage	Reference
Fe	Neutron	60-100	2.7-7.8 x 10^{16}(a)	100-300 Å dia. loops, nuclei for C or N ppt.	79
Fe	Neutron	60	0.5,5,10 x 10^{18}(a)	50-75 Å black spots, point defect clusters, at highest dose only	77
Fe	Proton or 150-kev Fe^+	20-550 ± 50	∿ 1.7 x 10^{16}	1000-1500 Å pure edge interstitial loops on {100}	142,143
Fe	Neutron	60	8.2 x 10^{20}(b) 2.5 x 10^{20}(c)	10-100 Å black spots, grow to loops upon annealing up to 400°C, disappear above 500°C, interstitial and vacancy loops	78
Fe	Neutron	30-90	0.2,1,20 x 10^{19}(d)	Black spots in Fe-0.001 wt. % C at highest dose, in Fe-0.003 wt. % C only after 300°C anneal, spots in both irons grow into loops upon heating above 350°C	74-76
Fe	Neutron	95	2.5 x 10^{18}(a)	Spot damage not observed except in vicinity of tangles	80
Mo	38-Mev He^{++} 85-kev H^+	400-500 80	1.5 x 10^{17} 6 x 10^{18}	He^{++} bombardment produced loops of radii up to 250 Å, H^+ bombardment produced small spots which anneal out in 1 hr. at 900°C without forming gas bubbles	140
Mo	Neutron	30-40	1 x 10^{18}(a)	Neither irradiation nor subsequent annealing produced loops or any other observable structure change	89
Mo	Neutron	40	1 x 10^{19}(a)	75-100 Å black spots in all irr. foils, loops only in foils with > 150 ppm C	93
Mo	Fission fragment	80	6 x 10^{13} to 1 x 10^{15}	25-125 Å black spots at lower dose increasing to interstitial loops with increased dose and upon annealing	141
Mo	Neutron	60	8.24 x 10^{20}(b) 2.5 x 10^{20}(c)	Defect clusters (up to 200 Å) become resolvable as interstitial loops upon annealing above 600°C	85
Mo	Neutron	600 ± 20	8 x 10^{17}(e)	1100 Å prismatic interstitial loops near pure edge in character	95
Mo	Neutron	40	1 x 10^{20}(a)	10^{16} black spots/cm^3, after annealing 2 hrs. at 750°C large interstitial loops on {321} planes	82
Mo	Neutron	40	0.4,0.7,1,10 x 10^{19}(a)	Spots obs. above 10^{18} n/cm^2, C promotes loop formation which saturates in density above 10^{19} n/cm^2	94
Mo	Neutron	Reactor ambient	∿ 1 x 10^{19}(a)	100 Å black spots as-irradiated become 200 Å interstitial loops after 760°C-anneal for 1 hr.	96
Mo	Neutron	60	∿ 5 x 10^{19}(f)	Mixed population of interstitial and vacancy loops after annealing at 900°C for 1 hr.	92
Mo	Neutron	60 200	2 x 10^{20}(e) 5 x 10^{19}(f)	Damage clusters more coarsely distributed in purer material and for 200°C-irradiation in which vacancy loops develop upon annealing	87
Mo	Neutron	600	3.5 x 10^{19}(a)	1000 Å interstitial loops showing depletion near grain boundary where vacancy clusters are present	83
Nb	Neutron	50	2 x 10^{18}(a)	5 x 10^{15}/cm^3 black spots identified as loops	1
W	Neutron	∿ 70	0.46,2.4,4.0, 7.3 x 10^{19}(a)	Defect clusters after 2.4 x 10^{19} increasing in size and number with dose, appearing as loops after 1090°C-anneal for 1 hr.	97

(a) (E > 1 Mev)
(b) thermal neutrons
(c) fission neutrons
(d) (E > 1.45 Mev)
(e) fast neutrons using nickel dosimeter
(f) fast neutrons

in the range 600-800°C (T/T_m = 0.30-0.37) as interstitial in character. More recently Maher and Eyre[92] have applied the method of Mazey *et al.*[119] to analyze loops in molybdenum formed by irradiation at about 60°C and subsequently annealed in the range from 750° to 1000°C or by irradiation at 600°C. They find a mixed population of both vacancy and interstitial loops. Large interstitial loops depleted near grain boundaries and vacancy clusters extending up to the grain boundaries have also been observed by Brimhall *et al.*[83] in molybdenum irradiated at 600°C.

For iron, there have been conflicting observations as to whether defect clusters are seen in the as-irradiated metal. Eyre[77] observed defect clusters in as-irradiated iron irradiated to 1 x 10^{19} (E > 1 Mev) and Eyre and Bartlett[78] observed them after 2 x 10^{20} fission neutrons/cm^2. On the other hand, Bryner[74-76] failed to see defect clusters in Ferrovac-E iron irradiated to 1 x 10^{19} neutrons/cm^2 (E > 1.45 Mev), and only a few dark spots appeared after 2 x 10^{20} neutrons/cm^2 (E > 1.45 Mev). However, the defect clusters developed upon post-irradiation annealing at 300°C (T/T_m = 0.32) or higher. It is generally felt that interstitial impurities (and whether they are in solid solution or not) are a critical factor, but a determination of their specific influence will require studies on more carefully characterized materials.

As things now stand, the method proposed by Rühle *et al.*[29] appears to permit the identification of the nature of the small defect clusters in as-irradiated metals. The method has been applied to irradiated copper with the view emerging that both vacancy and interstitial clusters are observed in the as-irradiated structure.[55] For the body-centered cubic metals, no clear determination of the nature of the small defect clusters

exists; however, upon annealing or following high temperature irradiation, where the defects are resolvable as loops, both vacancy and interstitial type clusters are found in neutron-irradiated molybdenum.[83,92] At the time the research for this dissertation was begun, the literature reported no information on the radiation damage revealed by TEM in niobium.

II. DISLOCATION CHANNELING -- DEFECT CLUSTER REMOVAL BY SLIP DISLOCATIONS

With the observation of radiation-produced defect clusters by transmission electron microscopy has arisen an important question pursuant to understanding radiation hardening, namely, the interaction of mobile dislocations during plastic deformation with the defect clusters. A number of years ago before defect clusters had actually been seen in the microscope, Cottrell[169] proposed that plastic deformation of irradiated metals would occur by the initial slip dislocations sweeping away some of the radiation-produced obstacles, making the passage of subsequent dislocations on the swept plane easier and resulting in localized "run-away" slip. The first direct experimental confirmation that the defect clusters were removed from the pathways of mobile dislocations was made by Greenfield and Wilsdorf[44,45] in neutron-irradiated-and-deformed copper. Confirming evidence of dislocation channeling in irradiated copper was reported by Seeger[61] and Essmann and Seeger[41] who suggested a correspondence between dislocation channels and the coarse slip-markings observed on polished surfaces after deformation.

Recently, Sharp[59] has investigated in some detail the width of defect-free channels in neutron-irradiated copper single crystals as a function of deformation temperature, neutron dose, and strain and has

compared these results with observations of surface slip bands. On the basis of the agreement between the width and spacing of channels observed by TEM and the width and spacing of slip bands determined from surface replicas, Sharp found strong indication that surface slip-markings and dislocation channels are consequences of the same circumstance, the passage of slip dislocations. With decreasing deformation temperature, the channel width and step height decreased; with increasing neutron dose, the channel width decreased but the step height increased. The channel width was independent of strain rate at room temperature and was rather insensitive to the amount of strain into Stage II of the stress-strain curve. However, the channel spacing did decrease with strain by new channels forming in the undeformed regions between the initial channels.

Furthermore, Sharp[59] found that the surface replicas indicated that the shear within a channel was rather uniformly distributed across its width. This result was supported by the observation that the intersections of channels were straight and not curved as would be expected if the center of the channel experienced greater shear. Under the assumption that the shear is distributed homogeneously within a channel, Sharp reported about two to three dislocations per slip plane.

From Sharp's work[59] a number of factors have emerged in regard to the mechanism of dislocation channeling. The very large shear, corresponding to the passage of several thousand dislocations per channel, holds the potential for high stress concentration, say through dislocation pile-ups, and thus may promote processes impossible at the lower stress levels in unirradiated crystals. Mechanisms of defect removal which have

enhanced probability in regions of stress concentration include: (1) glide of perfect prismatic dislocation loops on their glide cylinders,[170] (2) unfaulting of Frank loops[171] and (3) loop annihilation through coalescence of vacancy and interstitial loops. The measurements of Makin and Sharp,[172] Schwink and Neuhauser,[173,174] and Neuhauser,[175,176] which indicate that surface slip lines in irradiated copper are fully formed in times down to milliseconds, are consistent with high stresses resulting in high dislocation velocities.

Sharp[59] believes that localized cross slip is important in the formation of a channel and cites as evidence the narrowing of channels with decreasing deformation temperature and increasing dose. This contention is further supported by the observation of Brimhall and Mastel[36] that channels do not exist in irradiated-and-deformed Cu-8% Al alloy crystals, which because of relatively low stacking fault energy do not readily experience cross slipping. Climb through incorporation of defects into the dislocation is not thought to be important in the widening of a channel because the channel width was observed to decrease with increasing dose. Higher doses would tend to favor wider channels if such a climb mechanism operated.

A phenomenon similar to dislocation channeling in irradiated metals has been observed in quenched face-centered cubic metals. In this case, small dislocation loops or tetrahedral stacking faults formed from quenched-in vacancies are removed by slip dislocations. Vandervoort and Washburn[177] found that mobile dislocations combined with loops in quenched aluminum, yielding irregular, kinked dislocation lines. Observations of dislocation channels within a matrix containing dislocation loops have

been reported in aluminum (Shin and Meshii[178] and Meshii[179]) and aluminum-magnesium (Crivelli-Visconti and Greenfield[180]). Meshii[179] found a one-to-one correspondence between the width, spacing, and crystal geometry of the loop-depleted regions and surface slip bands in aluminum. In agreement with Sharp's[59] findings in irradiated copper, Meshii[179] observed that plastic deformation proceeded by formation of new channels rather than by the widening of existing ones. Furthermore, complicated dislocation tangles formed at the intersection of dislocation channels in quenched aluminum. Bapna, Mori, and Meshii[181] plastically deformed quench-hardened gold and found localized annihilation of tetrahedral stacking faults (see also, Yoshida *et al.*[182]). They determined the density of the tetrahedral stacking faults as a function of size in the deformed area and compared it with that in the undeformed area. There was a greater density of small defects in the vicinity of the channels than in the matrix which was taken as evidence that the defects were reduced in size by moving dislocations and subsequently completely annihilated to produce the channels. The defect annihilation was thought to result from cutting by dislocations or from a dislocation reaction to incorporate the defect into the dislocation line as, say, a superjog.

In the body-centered cubic metals, dislocation channels have been observed in irradiated-and-deformed iron,[78] molybdenum,[81,82] and, from the present study, niobium.[183] The crystal geometry of dislocation channels in molybdenum was found to be consistent with slip by <111> dislocations on {110} or {112} planes, whereas in iron a $[\bar{1}00]$ channel trace was observed in (001). In the past, however, relatively little

work has been reported on dislocation channeling in the body-centered cubic metals aside from observations that it exists.

Theoretical calculations of Saada and Washburn,[184] Kroupa,[185] and Kroupa and Hirsch[186] indicate that the long-range interactions between a loop and a moving dislocation are negligibly small, and only when the dislocation is sufficiently near to the loop for short-range elastic interaction does the loop serve as an obstacle to the dislocation motion. Saada and Washburn[184] examined the conditions for contact interactions in the face-centered cubic case and found the type and orientation of the loop relative to the Burgers vector and slip plane of the dislocation determined the nature of the contact interaction. Direct incorporation of perfect prismatic loops into the dislocation occurs when the loop and moving dislocation have the same or opposite Burgers vectors and when the loop intersects the dislocation slip plane. Makin[170] considered the long-range forces between dislocation loops and straight dislocations and showed that there is sufficient interaction force for moving dislocations to sweep along loops of the same Burgers vector lying within a critical distance of the slip plane.

A model for the formation of slip lines in irradiated copper was proposed by Makin and Sharp[172] in which the sweeping up of radiation-produced defect clusters by moving dislocations is a central feature. Although no detailed mechanism for the sweeping of the defects is proposed, the model does suggest the origin of the formation of channels. Upon reaching the critical stress a source emits a dislocation loop, which is held up in a matrix of defect clusters. As the first loop expands, it destroys some fraction of the defects it encounters. Each

subsequent loop from the source experiences fewer obstacles to its passage due to removal of defects by the previous loops. In this way a pile-up of loops grows. As a result of the defect removal, the stress necessary to operate the source decreases; however, this decrease in stress is partially offset by the backstress from the pile-up. As the slipped area with reduced defect density expands, a large pile-up develops which very rapidly accelerates as a result of the high stress and thus accounts for the very short times observed for the formation of slip steps on the surface. As the pile-up moves through the lattice at a high velocity, it sweeps the radiation-produced defects, leaving behind it a defect-free channel.

III. RADIATION HARDENING -- DEPENDENCE OF THE YIELD STRESS ON NEUTRON DOSE

It is well known that neutron irradiation induces a significant hardening in metals as reflected by an increase in yield stress. In this section an attempt is made to review the dispersed barrier theory of radiation hardening with brief mention of some damage mechanisms and then to present the literature on the dose dependence of the yield stress. Finally, discussion is given of the few cases where a direct correlation is made of radiation hardening with TEM observations of radiation-produced defect clusters.

Radiation Damage Mechanisms

The mechanisms of radiation damage have been discussed by numerous authors (see, for example, references 187-194) and here we shall only

outline qualitatively some of the more important aspects of radiation damage theory as relates to radiation hardening. As an energetic particle such as, say, a neutron (E > 1 Mev) moves through a crystalline solid, it collides with lattice atoms and is capable of dislodging them from their lattice sites. A displaced atom, i.e., the primary knock-on, degrades in energy through collisions with other lattice atoms along its trajectory. Depending on the energy transferred, the primary knock-on may actually displace a second atom from its lattice position, producing a secondary knock-on. In creating the secondary knock-on, a substantial part of the energy is released into the lattice surrounding the struck atom as heat. In addition, when less than the displacement energy is transferred in a collision, the struck atom experiences an increased amplitude of vibration that may be equated to an input of heat. The atoms decay from their excited state through energy transfer to neighboring atoms, thereby giving rise to a region in the crystal where the atoms have higher than normal energy. This region is called a *thermal spike*.[187] As decay through dissipation of energy (heat) returns the region to equilibrium, the thermal spike itself results in no permanent damage of the crystal. However, due to the pressure produced in a thermal spike,[187,189] it is believed that plastic deformation at the center of the spike is sufficient to generate dislocation loops with radii of 40 to 50 Å. These loops within the *plasticity spike* will be retained as the thermal spike cools only if the cooling pattern does not reverse the loop growth process or if the loops become tangled during formation of the plasticity spike.

Brinkman[195] proposed a damage mechanism known as a *displacement spike* in which a shell of self interstitials is sprayed out leaving at their center a high concentration of vacancies. The displacement spike, shown in Figure 1, occurs toward the end of the trajectory of a primary knock-on atom when its mean free path between collisions falls below an interatomic distance, producing a large concentration of vacancies surrounded by a shell of interstitial atoms. The stability of such a configuration appears questionable. Seeger[196,197] and Seeger and Essmann[198] point out that if the interstitials come to rest close to the vacancy-rich region, the displacement spike would be unstable, and that the vacancies and interstitials would largely disappear through mutual annihilation. Instead, Seeger[196,197] proposed a mechanism for the transport of mass and energy which appeals to the crystalline nature of metals in the same way as the *focuson* described by Silsbee[199] accounts for energy and momentum transport along close-packed atomic rows. In the Seeger mechanism (see Figure 2), an atom is knocked into the position of an extra atom in a close-packed row, forming a *dynamic crowdion*. The extra interstitial atom propagates along the close-packed direction through energy and mass transfer and comes to rest distantly removed on the atomic scale from the vacant lattice site where the crowdion originated. A similar second mechanism, discussed by Seeger and Essmann,[198] for removing interstitial atoms from the displacement spike is the *replacement chain*. This mechanism involves a chain of replacement collisions in which a moving atom strikes and displaces a lattice atom but is trapped itself at the lattice site, thus replacing the struck atom at the site. The struck atom subsequently undergoes the same process with a third atom,

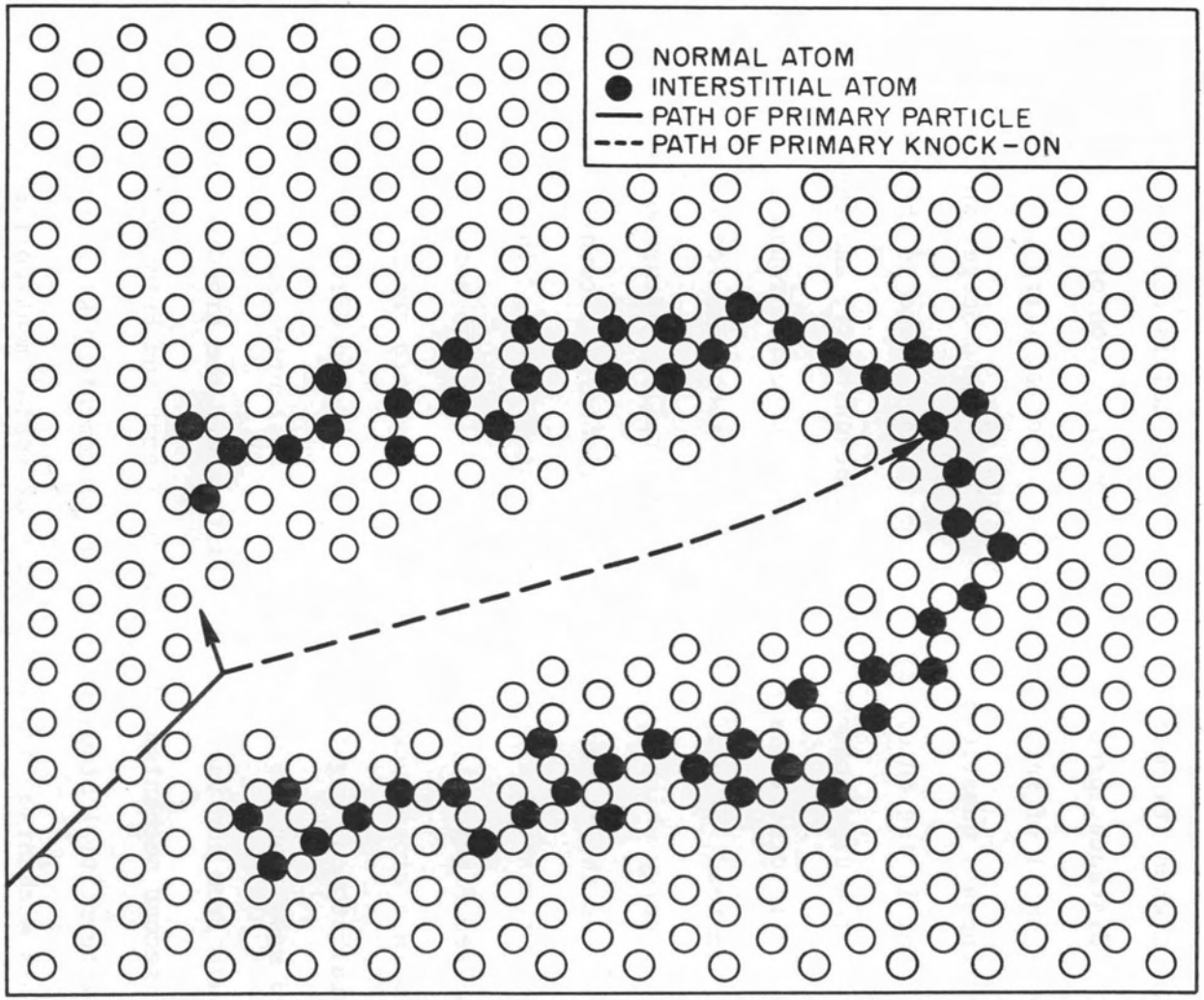

Figure 1. Schematic representation of shell of interstitial atoms created around a multiple vacancy during formation of a displacement spike (after Brinkman[195]).

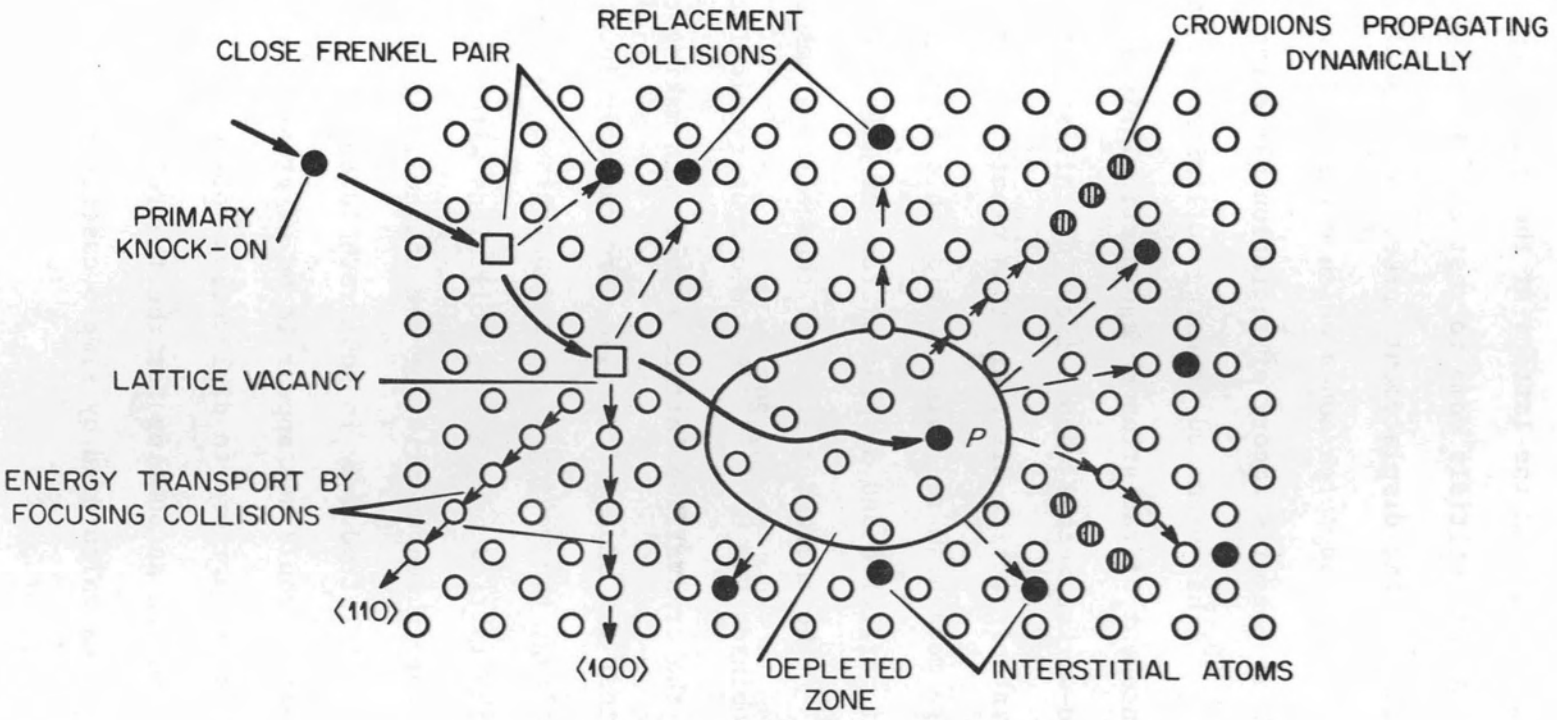

Figure 2. Schematic representation of radiation damage. P denotes the position where the primary knock-on comes to rest (after Seeger[196]).

and so on, giving rise to a sequence or chain of replacements with an interstitial coming to rest in the lattice at the end of the chain. By these two mechanisms interstitials come to rest at far distances from the vacancy-rich zone in the displacement spike. As we shall see below, it is the vacancy-rich or *depleted zones* which enter as barriers to dislocation motion in Seeger's theory of radiation hardening.

Leibfried[200,201] has examined focusing collisions in some detail and found an enhancement of radiation damage particularly at low temperatures and in cold-worked metals when a focusing collision is suddenly defocused at a point of lattice disorder, thus creating a Frenkel pair. An important damage mechanism receiving considerable attention recently is "channeling" of particles and displaced atoms of high energy through the lattice.[202-206] The characteristics of channeling atoms or particles were deduced by Robinson and Oen[202,203] from computer calculations which took into account the crystalline lattice rather than making the simplifying assumption that the atoms of a solid were randomly located in space. For channeling, the moving atom is constrained to travel down open channels in the lattice by glancing collisions with atoms in close-packed rows which form the boundaries of the channel. In this way the energy of the atom is fretted away in subthreshold collisions. Thus, the channeling of atoms would not appear to be of great importance as regards the creation of barriers to dislocation motion, but it may well be an important factor in accounting for the theoretical overestimate of damage production as calculated by simple cascade theory.[203]

Dispersed Barrier Model

The basis for models of radiation hardening is that radiation introduces clusters of defects which in some way impede the motion of slip dislocations. In the dispersed barrier model, the defect clusters are assumed to be scattered randomly on the slip plane with a density proportional to the dose, at least at low doses. During plastic deformation, the defect clusters serve as barriers to the motion of slip dislocations. The dose dependence of the yield stress is primarily the result of the decrease in the separation, ℓ, between barriers along the dislocation lines with increasing irradiation dose, Φ.

Holmes[207,208] used a rather simplified model of dispersed barriers to show that the critical shear stress is inversely proportional to ℓ. As described by Holmes (see Figure 3), a dislocation subject to an applied shear stress, τ, moves on its slip plane away from its rest position and comes up against radiation-produced barriers with a separation, ℓ, along the line as shown by the solid line in Figure 3. With increasing shear stress the dislocation pulls away from the barriers to a new (dotted) position. The applied stress gives rise to a force per unit length of dislocation with Burgers vector b equal to τb, which is directed perpendicular to the dislocation line. For an average barrier separation, ℓ, along the dislocation line, each barrier withstands a force, F_o, due to the pull of the dislocation given by

$$F_o = \tau b \ell \ , \qquad (1)$$

where F_o is the force at absolute zero temperature, i.e., the force on the barrier in the absence of an effective force due to thermal vibrations.

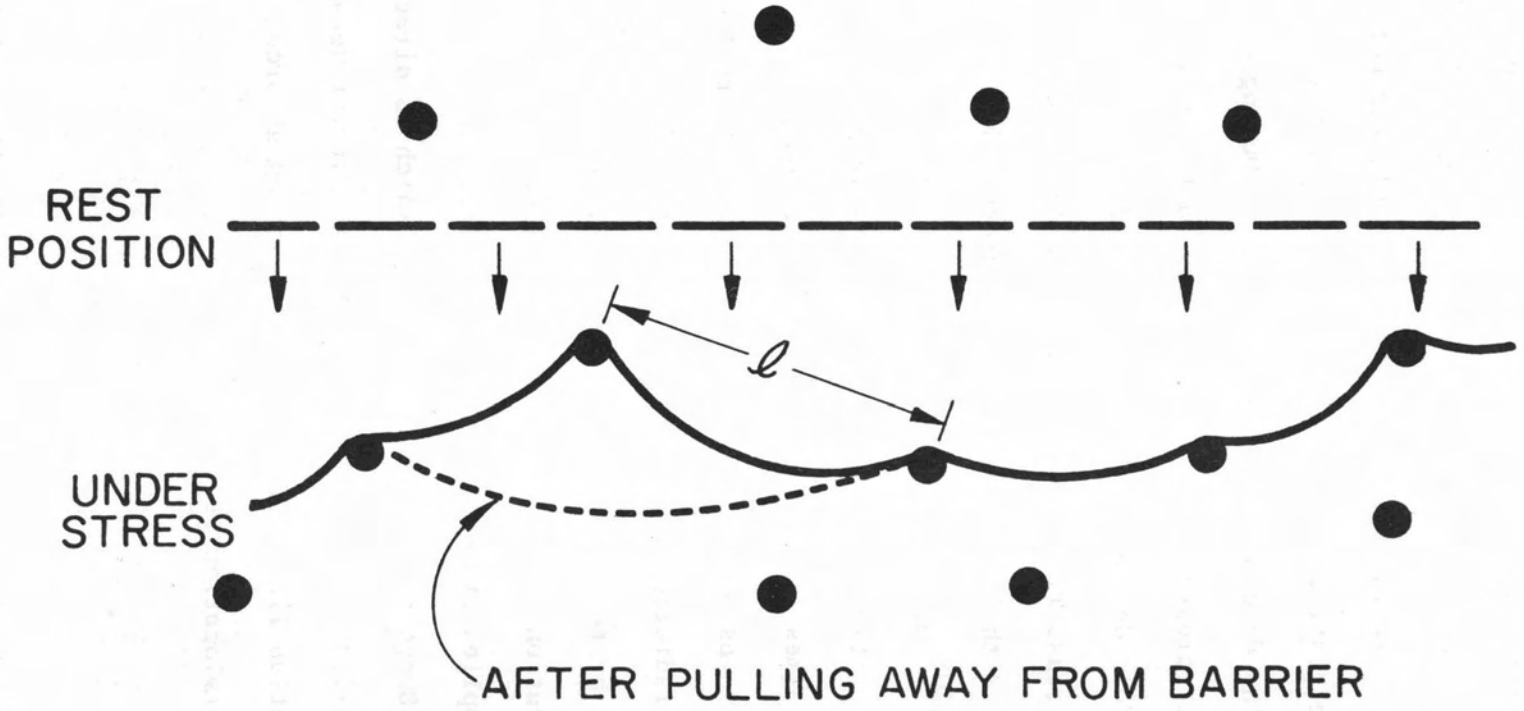

Figure 3. Segment of a dislocation line in a field of randomly dispersed barriers on a slip plane (after Holmes[208]).

If, in addition, the barrier experiences an effective thermal force, F_T, from thermal vibrations, then the total force on the barrier is given by

$$F = F_o + F_T = \tau b \ell + F_T \ . \tag{2}$$

Yielding occurs when the force on the barrier reaches a critical value, F_c. Thus the critical shear stress is given by

$$\tau_c = \frac{1}{b\ell} (F_c - F_T) \ . \tag{3}$$

Therefore, for a dislocation surmounting or breaking through the radiation-produced barriers the critical shear stress, τ_c, is found to be proportional to $1/\ell$. For the Orowan[209] approach in which the dislocations bow around rather than break through the barriers, the expression for the critical shear stress is

$$\tau_c = \alpha \frac{Gb}{\ell} \ , \tag{4}$$

where α is a constant of proportionality and G is the shear modulus. Here again τ_c is proportional to $1/\ell$. In either model the dose dependence enters through a change in the barrier spacing. The critical question then is to establish the basis for calculation of ℓ.

Holmes[208] considered the case where ℓ was assumed to be the *average* spacing of the barriers randomly distributed on the slip plane. Then for the dose range where the number of barriers per unit volume, N_v, is directly proportional to the irradiation dose the average planar

spacing is

$$\bar{\ell} = K_1 \frac{1}{\sqrt{N_v d}} , \tag{5}$$

where d is the effective size of the barrier and K_1 is a constant near one depending on the slip geometry. Replacing ℓ in equation (3) with equation (5), Holmes demonstrated a dependence of the critical shear stress on the square root of the dose.

Seeger[196,197] proposed a more detailed theory of radiation hardening based on a dispersed barrier model, where the vacancy-rich zones (i.e., depleted zones) discussed above act as barriers to the motion of slip dislocations. Although Seeger employed a somewhat more sophisticated approach than Holmes, the dose dependence of the yield stress is still basically a reflection of the decrease in barrier separation, ℓ. Seeger envisioned the radiation-produced defect clusters as potential energy "hills" which dislocations on the slip plane surmounted with the combined assistance of the applied stress and thermal vibrations. It was suggested that the strain rate in a crystal is determined by the thermally activated process by which a dislocation advances past the barriers. Using an energy criterion, Seeger[196] postulated that N dislocations per unit volume held up at N_z uniform barriers per unit volume of strength U would give a strain rate, $\dot{a}$, related in the following way to the frequency ν_o with which a dislocation of strength b attempts to overcome the barriers:

$$\dot{a} = \frac{N}{N_z} b\nu_o \exp\left(\frac{-U(\tau)}{kT}\right) . \tag{6}$$

The strength of the barrier relative to thermally activated motion of the dislocation depends upon how far up the hill the dislocation has been moved by the applied stress τ. A solution of equation (6) for τ should in principle give the dependence of the shear stress on dose, through N_z, and test temperature T. Thus, the essential problem in Seeger's approach to radiation hardening lies in determining the energy profile of the radiation-produced barriers as a function of the applied stress τ. Seeger assumed the following energy profile as a function of dislocation position x:

$$U(x) = U_o \left(\frac{1}{1 + \exp(-x/x_o)}\right) . \tag{7}$$

An applied stress τ provides an energy $b\ell_o'\tau x$, where ℓ_o' is the separation of barriers along the dislocation line. Thus, the energy required from thermal vibrations in order for a dislocation to overcome a barrier is

$$U(x) = U_o \left(\frac{1}{1 + \exp(-x/x_o)}\right) - b\ell_o'\tau x . \tag{8}$$

Using equations (6) and (8), Seeger made some simplifying assumptions to obtain the following analytical expression for the critical shear stress, τ_c:

$$\tau_c = \left(\frac{N_z}{Gb}\right)^{1/2} \cdot \left(\frac{U_o}{4x_o b}\right) \{1 - [(kT/\alpha U_o) \ln (Nb\nu_o/N_z \dot{a})]^{2/3}\}^{3/2} , \tag{9}$$

where

N_z, number of barriers per unit area of the slip plane

G, shear modulus

b, Burgers vector

k, Boltzmann constant

T, absolute temperature

N, number of active slip dislocations per unit volume

ν_o, frequency with which a dislocation attempts to surmount the barriers

$\dot{a}$, strain rate

U_o, potential energy height of the barrier

α, a factor of 2/3 which was missing in the original paper as pointed out by Schwink (see ref. 58).

The effect of neutron bombardment is reflected in equation (9) by an increase in N_z which is assumed to be directly proportional to the dose. Examination of equation (9) shows that the dose dependence of the critical shear stress enters primarily through the N_z in the first factor and is not as strongly dependent on the N_z in the logarithm. Thus, in general the Seeger theory predicts that τ is proportional to the square root of the neutron dose, Φ. In deriving equation (9) it is necessary to assume that τ is sufficiently large following irradiation in comparison to other contributions to the critical shear stress, such as the pre-irradiation value, that the effect of irradiation is the dominant factor. This condition has been shown to apply to irradiated face-centered cubic metals, copper in particular, but in general does not hold true for the

body-centered cubic metals where there is a strong temperature dependence even before irradiation. In Section V, we discuss the temperature dependence in more detail.

It is generally held that the deformation is governed by the distribution of barriers on the slip plane, and hence an expression for ℓ of the type in equation (6) is considered most frequently. However, in view of the experimental work to be described below, it is worth mentioning the dose dependence predicted by an average volumetric spacing of the form given by the following expression:

$$\overline{\ell} = K_2 \frac{1}{\sqrt[3]{N_v}} . \tag{10}$$

The substitution of equation (10) into equation (4) indicates that if the dislocations survey a volume of the crystal as may be the case when there is considerable cross slipping from one slip plane to an adjoining one, the critical shear stress would be proportional to the cube root of the dose.

A number of papers[210-215] have recently appeared in the literature which examine the motion of dislocations through a planar, random array of barriers. Foreman and Makin[213] used a digital computer to examine the movement of a dislocation with constant line tension through a random array of point obstacles of various strengths. For very weak barriers they found the average spacing ℓ of barriers along a dislocation to be approximately in agreement with the Friedel[216,217] expression

$$\ell \simeq \left(\frac{Gb}{2N_v\tau}\right)^{1/3} . \tag{11}$$

For strong barriers where the dislocation bows around the barrier, Foreman and Makin[213] found the critical shear stress to be 0.81 Gb/L where L is the average barrier spacing in the slip planes. This value for τ_c is in good agreement with that found by Kocks[212] who used a combination of statistical theory and graphical analysis in treating the case of infinitely strong barriers. Foreman[214] has treated the case where the line tension is not constant but varies logarithmically with its length and found the critical stress τ_c to be

$$\tau_c = A \frac{Gb}{2\pi} \frac{1}{L} \left[\ln \left(\frac{L}{r_o}\right) + B\right] , \qquad (12)$$

where A is nearly 1 for edge and 1.5 for screw segments and r_o is the dislocation core radius. Equation (12) has been used to explain less rapid hardening than the square root dependence on dose.

Dose Dependence of the Yield Stress

A point which has been discussed in the literature for several years is the power of the dependence of yield stress, σ, on irradiation dose, Φ, i.e., the value of n in a relation of the type

$$\sigma = A \Phi^n , \qquad (13)$$

where A is a dose-independent constant of proportionality. This question enters in the context as to whether "source hardening" or "lattice friction hardening" is the basic hardening mechanism of irradiation. Source hardening means the pinning by radiation-produced obstacles of dislocation segments which otherwise might operate as dislocation sources

say of the Frank-Read type at a lower stress. On the other hand, lattice hardening involves dislocations encountering radiation-produced barriers to their motion through the lattice after leaving the source. For source hardening the emphasis is on the increased difficulty of the initiation of dislocation motion, while lattice hardening focuses attention on the maintenance of dislocation motion through a forest of barriers that must repeatedly be surmounted in order to produce macroscopic flow.

The first extensive investigation of the dependence of the yield stress on neutron dose was on copper single crystals by Blewitt *et al.*[218] and Blewitt.[219] They observed that the yield stress varies as the cube root of the dose over the dose range of fission spectrum neutrons from 10^{16} to 10^{20} neutrons/cm^2 at test temperatures of 300, 78, and 4.2°K. Although their view was not conclusively supported by the data, Blewitt *et al.*[218] favored the source hardening mechanism. This view is inconsistent with a planar model of radiation hardening which predicts a square root dependence of the yield stress on dose as a result of lattice hardening by defect clusters.

The discrepancy between theory and experiment has spurred a number of additional experimental studies and has led to considerable controversy in regard to the interpretation of the results. Diehl[220] and Rukwied and Diehl[221] examined the dose dependence in copper single crystals, and reported agreement with a square-root dependence. They plotted their yield stress data versus both the square root and the cube root of the dose for test temperatures of 300 and 90°K. The cube-root plot required an incubation period in order to extrapolate the data to the unirradiated value. Hence Diehl[220] preferred the square-root dependence for which the

irradiated yield stress below 2 x 10^{17} neutrons/cm^2 and the unirradiated value give a straight line fit and evoked a saturation effect[222] to account for the less rapid hardening at higher doses. Makin and Minter[222] first proposed the following expression including a saturation effect, in order to fit their dose dependence data on polycrystalline copper and nickel to the lattice hardening theory:

$$\sigma_i = A\,(1 - e^{-B\Phi})^{1/2}\,, \qquad (14)$$

where σ_i is the lattice hardening stress and A and B are parameters related to the volume around an obstacle in which no new obstacle can form. Makin and Minter[222] found that their data for both copper and nickel samples in the dose range between 9.5 x 10^{17} and 1.07 x 10^{20} neutrons/cm^2 when tested at 78, 293, and 473°K showed equally good fits to $\Phi^{1/3}$ and equation (14). As regards the meaning of the saturation effect, Diehl[220] suggested that the volume necessary to account for the saturation observed is of the order of 10^7 atomic volumes. This appears to be a rather large volume from which to exclude other obstacles. Thus, Seeger[196] and Diehl[220] have proposed a saturation mechanism whereby the size of existing obstacles is reduced by the capture of dynamic crowdions.

Diehl *et al.*[223] determined the dependence of the critical resolved shear stress (lower yield stress at 4.2°K) in copper irradiated at 4.2°K. They observed a square-root dose dependence similar to that found after irradiation at about 350°K. Thus, they took this as evidence that the hardening mechanism was independent of thermally controlled migration of radiation-produced defects and therefore not primarily characterized by source hardening.

On the other hand, support for source hardening is suggested from the amplitude-dependent internal friction measurements of Thompson and Paré[224] on irradiated copper single crystals. They found that the breakaway stress was proportional to the cube root of the dose in the range from 10^{11} to 10^{14} neutrons/cm^2 (E > 0.6 Mev). Their internal friction results together with yield stress measurements of Blewitt *et al.*,[218] Diehl,[220] Fischer,[225] and Koppenaal[226] and the etch pit data of Young[227] were all reported to obey an apparent cube root relation for neutron doses from 10^{11} to 4×10^{19} neutrons/cm^2. The agreement of the yield stress data with that of Thompson and Paré on breakaway stress suggests source hardening, since the internal friction results are a measure of the stress required to unpin dislocations from the radiation-produced barriers. In rebuttal, Diehl and Schilling[228] showed that the yield stress data of Rukwied and Diehl[221] gave only a rough approximation to a straight line with a slope of one-third in a log-log plot as used by Thompson and Paré.[224] Furthermore, they reported a pronounced tendency toward saturation in the damage rate as measured by resistivity change in the same dose range where the yield stress shows saturation. Thus, they conclude that the critical shear stress is indeed proportional to the square root of the dose at low doses.

Makin and Sharp[172] have commented on the nature of radiation hardening and have suggested a lattice hardening model that possesses the deformation characteristics formerly taken as evidence of source hardening. The model holds that the critical shear stress is governed by the initial operation of the source in a matrix of radiation-produced obstacles. Since they believe that the source length is in general less

than the average spacing of obstacles, it is then very unlikely that a source can operate without the bowed-out dislocation meeting an obstacle. Thus, in a sense, both types of hardening exist from the beginning. Makin and Sharp[172] point out that the stress to expand a loop, once it is generated, decreases as its radius increases. Therefore, the yield drop usually attributed to source hardening can be equally well explained in terms of lattice hardening. Although the critical shear stress appears to be determined by the operation of a source, Makin and Sharp do not believe that radiation necessarily causes true source hardening by reducing the effective source length but that it may increase the difficulty of operating the source as the source encounters obstacles adjacent to it.

Recently, Blewitt and Arenberg[229] conducted in-reactor tensile tests at the irradiation temperature of 4.2°K on copper and found that the macro-yield stress ($\Delta\ell/\ell > 10^{-4}$) varied with the third power of the neutron dose for doses from 2.5×10^{14} neutrons/cm^2 (E > 0.5 Mev) to greater than 10^{17} neutrons/cm^2. Furthermore, for the same experimental conditions they observed the micro-yield stress increased as the third power of the dose in the range from 5×10^{15} to 5×10^{16} neutrons/cm^2. The best fit of the data to a half power dependence required a saturation effect to commence at a dose of about 5×10^{15} neutrons/cm^2 which they feel is rather unlikely. In commenting on the work of Blewitt and Arenberg, Diehl[230] indicated that the yield stress of well annealed crystals does exhibit a half power dependence on dose while the third power dependence is observed in deformed crystals.

Most recently, Blewitt *et al.*[231] have applied to their data the results of a calculation by Foreman[214] which modified the assumption that the yield stress is proportional to the reciprocal of the segment length as given in equation (12). For convenience, they rewrote the equation in the following form:

$$\sigma = D_1 (D_2 + k\Phi)^{1/2} \log \frac{(D_2 + k\Phi)^{-1/2}}{b} + B , \qquad (15)$$

where D_2 is the pre-irradiation number of pinning points and $k\Phi$ is the number of pinning points introduced by a neutron dose Φ. The segment length between pinning points is given by $(D_2 + k\Phi)^{1/2}$. Blewitt *et al.*[231] report that at high doses where D_2 becomes negligible, their data fit well to equation (15). They now believe that the yield stress in neutron-irradiated copper is governed by friction hardening.

In face-centered cubic platinum, Galligan and Attardo[168] presented some interesting results on the concentration of depleted zones as determined by field ion microscopy. They found, as is generally assumed, that in the dose range where the hardening varied as the square root of the dose the number of depleted zones per cm^3 varied linearly with the dose. For a dose of about 2×10^{18} neutrons/cm^2 the yield stress was observed to saturate. Post-irradiation annealing for 30 minutes at 300°C where the vacancies are mobile results in the yield stress varying as the third power of the dose. In the temperature range from 250 to 500°C the larger depleted zones were observed to transform to dislocation loops.

Among the body-centered cubic metals, the dose dependence of the yield stress in single crystals has been somewhat neglected in the past.

The effect of neutron irradiation on plastic deformation in iron single crystals has recently been studied in some detail by Seidel,[232-234] including an investigation of the dose dependence as described by Seidel[232] and Diehl *et al.*[235] Iron single crystals with carbon levels of 20 wt. ppm and about 8 wt. ppm or less were irradiated to neutron doses up to 2×10^{18} neutrons/cm^2 at temperatures of about 70 and 130°C. Upon testing in tension at 230, 298, and 400°K the yield stress in the higher carbon iron was found to obey a square root dependence only for low doses and was followed by complete saturation at a dose of about 3×10^{17} neutrons/cm^2. The decarburized (8 wt. ppm carbon) iron exhibited much the same behavior when tested at room temperature, but the yield stress did not appear to saturate with dose on testing at 400°K. For the room temperature test, the stress level at which the decarburized iron saturated was appreciably lower than for the 20 wt. ppm carbon iron. Applying the saturation formula of Makin and Minter[222] [see equation (14), page 38], the saturation volume was found to be approximately 10^6 atomic volumes. It was suggested that carbon had the following role in the hardening. Initially, the carbon in solution is approximately the same in the crystals with different total carbon levels. During irradiation the undissolved carbon is dispersed within the displacement cascade forming complexes with the radiation-produced defects. Thus in the crystals of higher carbon content a greater number of complexes are formed, giving rise to higher yield stresses. With increasing neutron dose, the available carbon for complex formation is exhausted causing a saturation to occur. The saturation volume is that associated with displacement

cascade including the range of dynamic crowdions, and hence the value of 10^6 atomic volumes would appear reasonable.

Recently, Ohr[236] has examined the dose dependence of polycrystalline irons of three carbon levels and two grain sizes and found that initially a square root dependence holds. As was true for the iron single crystals,[232,235] a saturation effect appears generally to set in at rather low doses and at a stress level that increases with carbon content. Hinkle *et al.*[237] have also determined the dose dependence of polycrystalline Ferrovac-E iron of two grain sizes and have reported slopes of 0.1 and 0.15 for a plot of the logarithm of the lower yield stress versus the logarithm of the dose and slopes of 0.22 and 0.35 when the increase in the lower yield stress rather than the stress itself is plotted.

For the body-centered cubic refractory metals, Wronski *et al.*[238] found that the increase in the lower yield stress upon irradiation for polycrystalline molybdenum shows a square root dependence over the dose range 0-80.0 x 10^{17} epithermal* neutrons/cm^2. Previous work from the present study has shown that the power dependence of the yield stress on neutron dose in single crystal niobium is 0.07 while the increase above the pre-irradiation level varies as the fourth root of the dose.[239,240] In Chapter VI, we present some additional experimental results on the dose dependence of niobium.

---

*"Epithermal neutrons" are neutrons with energies from thermal energy (0.025 ev) to about 0.1 Mev.

In the literature there are only a few papers which describe the effects of neutron irradiation on plastic deformation in niobium. Although these papers do not specifically treat the dose dependence, they do have some bearing on radiation hardening mechanisms. Makin and Minter[241] investigated the effects of irradiation on annealed niobium wire prepared by a powder metallurgy technique. By comparison with Tottle's[242] tensile data, they estimated their unirradiated samples contained 1600 wt. ppm oxygen. Tensile tests after neutron irradiation to 10^{20} neutrons/cm^2 indicated: (1) an increase in the yield stress from about 42 to about 53 kg/mm^2, (2) disappearance of the yield drop, (3) localized deformation, (4) uniform elongations of only one to two percent, and (5) 50 percent reduction in area at fracture as compared to 80 percent in unirradiated samples. Makin and Minter interpreted the observation of a decrease or even disappearance of the yield drop upon irradiation to mean that radiation-produced defects are not effective in locking dislocations in their pre-existing positions or in locking dislocation sources. This factor together with the significant increase in the yield and flow stresses upon irradiation suggested to Makin and Minter that lattice hardening is the dominant mechanism.

Evans, Weinberg and Van Thyne[243] used the Petch analysis to investigate radiation hardening in polycrystalline niobium irradiated over the temperature range 77-330°C. They concluded that the hardening was due primarily to an increase in the lattice frictional stress which increased with increased irradiation temperature over the range considered. In fine grained samples, the yield point was present following irradiation at 77°C but was absent after the 330°C irradiation. The rate of work

hardening was observed to decrease for samples irradiated at 77°C. In general, irradiation was observed to reduce the ductility.

Radiation Hardening and Defect Clusters

Shortly after Silcox and Hirsch[3] observed dislocation loops in irradiated copper, Makin *et al.*[48] investigated the density of defect clusters (believed to be loops) as a function of cluster size following irradiation at about 27°C and found the average diameter of the clusters increased with dose. This loop growth was taken as evidence that point defects introduced during irradiation were migrating to the loops. In order to determine whether the loops were vacancy or interstitial in character, samples were irradiated and examined in the electron microscope at temperatures of -195°C and about -120°C, respectively, where vacancies are essentially immobile in copper. Under these conditions, Makin *et al.*[48] observed defect clusters and inferred that they were composed of interstitial atoms.

Following irradiation to 2×10^{18} fast neutrons/cm^2 and post-irradiation annealing at 306°C, Makin *et al.*[48] observed a high density (1.3×10^{16} cm^{-3}) of small defects (diameter < 25 Å) not visible before annealing. They determined the defect density and the corresponding yield stress as a function of annealing time at temperature and found that the yield stress varied as the square root of the small defect density but no such dependence was found for the large defects. Thus, they concluded (as has been born out by subsequent studies by Makin *et al.*[244,245]) that the hardening was primarily due to the small defects which appeared only upon mild annealing. Another interesting observation

was the depletion of the large defects adjacent to grain boundaries whereas the small defects extended up to the boundaries.

In later work Makin *et al.*[49] determined the size distribution of defect clusters for doses in the range between 0.6×10^{18} and 3.8×10^{18} fast neutrons/cm^2. These results were compared to various theoretical models and both Makin *et al.*[49] and Varley[246] conclude that the data do not fit the theory for homogeneous nucleation by chance aggregation of randomly distributed point defects. Makin *et al.* suggested that the nuclei for the loops formed heterogeneously within the displacement spikes of the primary knock-on atoms.

The annealing of dislocation loops[50] as well as the annealing behavior of radiation hardening[247] in copper have been investigated by Makin and Manthorpe. The loop annealing has already been described in Section I; here we mention only some of the characteristics of the recovery of the radiation hardening. Annealing at 275°, 306°, and 336°C, which had little effect on the recovery of the critical shear stress, significantly reduced the Lüders extension. The critical shear stress at -195°C and the onset of Stage III at 20°C were also observed to recover more rapidly than the 20°C critical shear stress while the work hardening in Stage II recovered more slowly. The results were interpreted in terms of a size spectrum of radiation-produced defects.

Recently, Rühle[248] has presented defect density and critical shear stress measurements for neutron-irradiated copper where the volume density of defects with radii between $r - \Delta r/2$ and $r + \Delta r/2$ was described by an equation derived by Scheidler *et al.*[249]:

$$V(r)\,\Delta r = V(o)\,\exp\,(-r/r_o)\,\Delta r\ . \qquad (16)$$

The interpretation of the critical shear stress was complicated by the rather wide size distribution of the observable defects. The spectrum theory of Frank[250,251] was used to analyze the data. The critical shear stress in neutron-irradiated copper was quantitatively explained by the thermally activated motion of dislocations through a random array of vacancy type Frank dislocation loops lying on {111} planes.

The question of a defect spectrum and the strengthening mechanism in neutron-irradiated copper has been widely discussed and debated in the literature (see references 58, 173-176, 252-265). A rather detailed theory, which appears to be promising, is the recent "multiple spectrum theory" of Frank[250] which takes into account the spectrum of obstacle sizes, orientations, and distances with respect to the slip plane. Furthermore, this theory considers both dependent and independent activation processes (see Seeger[266]) for the movement of dislocations through the obstacles and provides for the possibility that the plastic deformation perhaps is preferentially controlled by the larger obstacles. This approach[251] has been used to explain the findings of Rühle[248] on neutron-irradiated copper.

For as-irradiated body-centered cubic iron, the defect clusters appear to be below the resolution of the electron microscope at doses where the hardening commences. Bryner[74-76] and Ohr[80] were unable to detect defect clusters in vacuum-melted iron irradiated to 2×10^{18} neutrons/cm^2 ($E > 1$ Mev), although the yield stress showed a significant increase in this dose range (Chow *et al.*[267], Ohr *et al.*[240]). However, after higher doses (about 10^{20} neutrons/cm^2) defect clusters have been observed in iron.[74,78] In such a case, Eyre and Bartlett[78] found that

the defect clusters and the micro-hardness anneal in about the same temperature range (300-500°C; T/T_m = 0.32-0.43) although it is conceivable that sub-microscopic defect annealing in this range may actually account for the recovery of the hardness. The work of Downey and Eyre[85] on irradiated molybdenum would support this latter view in that the micro-hardness recovers significantly below 600°C (T/T_m = 0.30), while the observable defects do not appear to change below 600°C.

Much the same sort of situation existed for neutron-irradiated nickel where Wilsdorf[73] was not able to detect visible defect clusters, while Makin and Minter[222] and Diehl[220] reported radiation hardening. Ast and Diehl[268,269] found the radiation-produced increase in the critical shear stress of nickel annealed out at about 400°C with an activation energy of 2.28 ev and attributed their results to the decomposition of vacancy defect clusters. Recently, defect clusters have actually been seen in neutron-irradiated nickel.[54,64]

The question of observable defect clusters following electron irradiations has been rather neglected in the past. Makin and Blewitt[270] did attempt to observe by TEM defect clusters in copper after irradiation with 4 Mev electrons. Although they found a substantial increase in the yield stress, they were unable to see the defect clusters. However, recent experiments in a high-voltage electron microscope by Makin[146] on copper and aluminum revealed clusters which are believed to be the result of electron bombardment. Furthermore, striking observations of defect clusters in metals irradiated with 3 Mev electrons were very recently reported in nickel by Bourret[148] and in copper, gold, platinum, and niobium by Scheidler and Roth.[147]

In regard to the size of the actual hardening agents, the current literature tends to support the view that the small defects, which may be sub-microscopic in as-irradiated metals, are primarily responsible for radiation hardening in the face-centered cubic metals. The actual size of these nonvisible defects remains in question, but it appears that 25-30 Å is the upper limit of their size. The size of the hardening agents in irradiated body-centered cubic metals has been less thoroughly studied and remains a point for discussion. However, in the following it is shown that the radiation hardening in niobium can be accounted for on the basis of the observable defect clusters.

IV. INFLUENCE OF POST-IRRADIATION ANNEALING ON THE YIELD STRESS

As pointed out in the previous section, neutron irradiation significantly increases the yield and flow stresses of metals. Moreover, there is a striking further increase in these stresses in some irradiated metals upon post-irradiation annealing, which we designate as "radiation-anneal hardening". This hardening takes place upon post-irradiation annealing at lower temperatures, before the major recovery toward the pre-irradiation value occurs. In the past, radiation-anneal hardening has been found primarily in the body-centered cubic refractory metals (e.g., niobium,[241] molybdenum,[85,271-273] and tungsten[273]); however, there is some evidence in recent work by Hinkle[274] that iron also exhibits this effect.

Radiation-anneal hardening was first reported in niobium by Makin and Minter[241] who examined polycrystalline niobium bearing about 1600 wt. ppm oxygen after irradiation with 10^{20} neutrons/cm^2 (see page 44). They

observed an increase in yield stress from an as-irradiated value of 53 kg/mm^2 to a maximum of 64 kg/mm^2 upon annealing at 100-200°C (T/T_m = 0.14-0.17). Furthermore, in the same temperature range, they found a decrease in the elongation to fracture and a return of the yield drop which had essentially disappeared in the as-irradiated samples. Makin and Minter concluded that the radiation-anneal hardening in their niobium resulted from the migration of vacancies produced during irradiation and that the yield drop return was the result of the locking of dislocation lines by vacancies condensing along them. The yield stress recovered to its pre-irradiation value between 350 and 600°C (T/T_m = 0.23-0.32).

Radiation-anneal hardening was also reported for the yield stress and micro-hardness in post-irradiation-annealed molybdenum. Makin and Gillies[271] observed an increase in the yield stress after annealing for one hour at 200°C (T/T_m = 0.16) in molybdenum irradiated to 5 x 10^{19} slow neutrons/cm^2. Subsequent work of Wronski and Johnson[272] showed a total increase of approximately 5 kg/mm^2 above the as-irradiated value of the yield stress in molybdenum, beginning for one-hour anneals at about 150°C (T/T_m = 0.15) and reaching the higher stress plateau at about 260°C (T/T_m = 0.18). In both these studies, radiation-anneal hardening was attributed to vacancy migration to dislocations. Supporting evidence for the radiation-anneal hardening in molybdenum was also reported by Downey and Eyre[85] and Moteff[273] for micro-hardness measurements. The hardening occurred upon annealing in the temperature range 150-200°C. Moteff[273] also reported similar results in irradiated tungsten.

The present understanding of the origin of radiation-anneal hardening in the refractory metals is based primarily on electrical

resistivity and internal friction measurements in irradiated or cold-worked material with some supporting evidence from strain-aging experiments. The electrical resistivity in cold-worked and irradiated body-centered cubic metals shows a pronounced annealing stage at (0.16 ± 0.04) T_m. In the post-irradiation annealing of electrical resistivity in copper, Stage III annealing occurs at about $T/T_m = 0.2$. By analogy, the stage at $T/T_m = 0.16 \pm 0.04$ in bcc metals is designated as "Stage III". Its origin in the body-centered cubic metals has been attributed to migration of intrinsic defects[85,275-282] (interstitials, di-interstitials, vacancies, or di-vacancies) or to interstitial impurity migration.[283-292] Peacock and Johnson[277] studied the recovery of the increase in the electrical resistivity in molybdenum and niobium following neutron irradiation and interpreted the Stage III recovery as the result of vacancy migration to either interstitial impurity atoms or radiation-produced defect clusters. However, Nihoul[280] analyzed the data of Peacock and Johnson[277] and found the recovery to obey second-order reaction kinetics, which led to the suggestion that the recovery was due to the migration of free interstitials to vacancies. This latter view was subsequently taken by Stals and Nihoul[281] for Stage III recovery in cold-worked niobium in agreement with their theoretical analysis[293,294] of the reaction order.

On the other hand, Rosenfield[292] pointed out that the activation energies determined for Stage III recovery in body-centered cubic metals are quite similar to energies for interstitial impurity migration and suggested that the recovery was controlled by the impurities. Indeed, Cuddy,[289,290] Dinter,[288] and Köthe and Schlät[286,287] all showed the absence of Stage III in cold-worked metals with very low interstitial

impurity levels. Recent studies at the Oak Ridge National Laboratory by Williams *et al.*[283] indicate that Stage III annealing in neutron-irradiated niobium is caused by the migration of oxygen to radiation-produced defects. This work will be described in greater detail in Chapter VII in discussing the interpretation of the present radiation-anneal hardening results.

V. EFFECT OF NEUTRON IRRADIATION ON THE TEMPERATURE DEPENDENCE OF YIELDING

Neutron irradiation imparts a marked temperature sensitivity to the yield stress of face-centered cubic metals, which is absent in the unirradiated condition. Among this group of metals, copper has been particularly well studied (e.g., references 218, 220, 222, 255-262). It is believed that irradiation introduces into copper defects surmountable by thermally activated process, whereas few such defects existed before irradiation. This behavior is in contrast to that observed for the body-centered cubic metals -- namely, the yield stress shows a large temperature sensitivity even in the unirradiated metal and exhibits a much less marked change following irradiation. In this section, we describe the various theories for the effect of radiation on the temperature dependence of the yield stress and briefly review the experimental results for irradiated body-centered cubic metals. For a more thorough treatment of the influence of test temperature on body-centered cubic metals, the reader is referred to rather recent reviews by Christian and Masters[295,296] and Conrad[297] and to several papers in the recent colloquium, "Dislocation Dynamics."[298]

In Section III, the theory of Seeger[196,197] was described which employs the equation (9), page 33, relating yield stress and test temperature. This equation may be rearranged to give

$$\left[\frac{\tau}{\tau_o}\right]^{2/3} = 1 - \left[\frac{T}{T_o}\right]^{2/3}, \qquad (17)$$

where $\tau_o = \left(\frac{N_z}{Gb}\right)^{1/2} \cdot \left(\frac{U_o}{4x_o b}\right)^{3/2}$

and $T_o = \alpha U_o / k \ln (Nb \nu_o / N_z \dot{a})$.

Equation (17) is expected to predict the temperature dependence of the critical shear stress for cases where the temperature sensitivity is due chiefly to the radiation-produced defects.

Seeger[196] showed the agreement with equation (17) for the data of Blewitt *et al.*[218] on irradiated copper single crystals and similar agreement was also found for data of Makin and Minter[222] on polycrystalline copper. However, subsequent measurements on copper by Fischer[225] and Rukwied and Diehl[221] exhibited deviations from equation (17). Diehl[220] suggested as possible causes for the deviation: (1) the presence of a spectrum of barrier sizes and hence barriers of various potential energies or (2) an over simplification of the expression for the stress-dependence of the activation energy as the result of approximations used in obtaining the analytical form in equation (17). Considering the second suggestion, Diehl found satisfactory agreement could be achieved with Seeger's theory when a more complete expression for the stress-dependence of the activation energy was used. Nevertheless, the question of a spectrum of barrier sizes

was investigated by Diehl *et al.*[255,256]; for it seemed likely that such a spectrum should exist at higher doses due to the reduction in size of the older depleted zones as they were struck by crowdions from later formed zones. The approach of Diehl and co-workers not only considered a variation in the size of radiation-produced barriers but also dealt with the inhomogeneous nature of the deformation in irradiation crystals. It was found that the barriers exhibit a rather sharply peaked distribution with an average size of, say, 20-30 vacancies per defect cluster or loop. The idea of a spectrum of barrier sizes is in disagreement with the work of Koppenaal and Arsenault[261] and the point has been debated in the literature (Koppenaal and Arsenault,[262] Diehl and Seidel[257]).

Blewitt *et al.*[218] analyzed the temperature dependence of the yield stress in irradiated copper to show a fit to the relation

$$\Delta\tau = A - BT^{1/2} , \qquad (18)$$

where $\Delta\tau$ is the increase in shear stress upon irradiation and A and B are constants. Holmes[207,208] predicted such a temperature dependence by introducing for the thermal force F_T in equation (3), page 31, the functional form obtained from an analysis of the thermal activation of a dislocation line over a barrier as suggested by Leibfried.[299] Holmes indicated that the thermal force F_T is proportional to the square root of the absolute temperature at high temperatures and constant at temperatures low relative to the Debye temperature. Thus, the critical shear stress for irradiated metals was described by

$$\tau_c = C_1 (\Phi)^{1/2} \cdot \left(1 - C_2 T^{1/2}\right) . \qquad (19)$$

Another theory of hardening is that proposed by Fleischer[300,301] for solution hardening by tetragonal distortions in the lattice. The model is again a dispersed barrier type, where the barriers are now centers of tetragonal distortion which exert on dislocations a maximum force varying inversely as the square of the separation of the defect from the slip plane. To determine the maximum force, F_{max}, Fleischer first found the interaction energy between a dislocation and a center of tetragonal distortion using the method of Cochardt *et al.*[302] and then maximized its derivative (i.e., the force) with respect to motion on the slip plane. Fleischer found that in general the maximum force depends on the relative orientation of the dislocation and the defect and is of the form

$$F_m = G \, \Delta\varepsilon \, b^4/\alpha \, y^2_{min} \, , \tag{20}$$

where G is the shear modulus, $\Delta\varepsilon$ a measure of the defect tetragonality, α a numerical value related to the interaction geometry of the order of ten for a face-centered cubic lattice, and y_{min} the minimum distance for a defect from the slip plane taken as the Burgers vector, b. From the interaction energy Fleischer also obtained an expression for the force exerted by a defect on a dislocation as a function of their separation *along* the slip plane. Using the concept of thermally activated motion of dislocations, as did Seeger,[196] Fleischer employed an approximation for the force along the slip plane to obtain the following expression for the activation energy:

$$\overline{U} = F_m \, b \, [1 - (\tau/\tau_o)^{1/2}]^2 \, , \tag{21}$$

where τ_o is the flow stress at T = 0°K. For dislocations moving at a constant velocity, the strain rate equation,

$$\dot{a} = \dot{a}_o \exp [-U(\tau)/kT] , \tag{22}$$

predicts that the energy $\overline{U}$ is proportional to kT. Thus, from equation (20) it follows that

$$\alpha kT = F_m b [1 - (\tau/\tau_o)^{1/2}]^2 , \tag{23}$$

which may be written as

$$(\tau/\tau_o)^{1/2} = 1 - (T/T_o)^{1/2} , \tag{24}$$

where $T_o = F_m b/\alpha k$, k being the Boltzmann constant.

Koppenaal[259] and Koppenaal and Arsenault[261,262] analyzed their data for irradiated copper using equation (24) and were able to show good agreement to the Fleischer theory. Makin[303] also found for copper that the Fleischer theory predicted a reasonable size for the radiation-produced obstacles but that it overestimated their number. Recently, Ono[304] examined the interaction potentials used by Seeger and Fleischer, as well as other potentials, and discussed their shortcomings and merits with regard to the prediction of the temperature dependence of the yield stress. Ono believes that equation (24) has no physical basis in the centers of tetragonal distortion because of modifications which Fleischer made in the potential in order to arrive at this analytical expression. While it is true that the modified Fleischer potential does not accurately approximate that resulting more directly from the tetragonal interactions,

Ohr[305] recently showed that the Fleischer relation, equation (24), is a general consequence of an inverse-square force law such as that pertaining to the interaction between straight dislocations and dislocation loops, and equation (24) may therefore be obtained without recourse to Fleischer's modified force-distance relation.

Frank[306-309] recently studied in some detail the strong interactions between dislocations and defects with strain fields exhibiting tetragonal symmetry. In addition to the short range forces[306] of the type treated by Fleischer, Frank also determined the contribution to the critical shear stress due to long-range elastic interactions between dislocations and elastic dipoles as reflected in the induced Snoek effect.[307] The temperature dependence of the yield stress in iron with various amounts of carbon[309] and radiation hardening in electron- and neutron-irradiated aluminum and electron-irradiated copper[308] can be explained by the tetragonal defects in accord with Frank's analysis. Furthermore, Frank[250] developed a theory for thermally activated dislocation motion through a multiple spectrum of dislocation barriers. This theory quantitatively explains the critical shear stress in neutron-irradiated copper as reported by Rühle[248] and Frank *et al.*[251]

For the body-centered cubic metals, the large temperature dependence of the yield stress has been variously attributed to (1) the intrinsic lattice properties,[295-297,310-312] i.e., the Peierls-Nabarro force or (2) impurity effects,[313-316] particularly from interstitial impurities or precipitates (see also Fleischer[317]). Although there is considerable discussion on this point in the literature (see, for example, Stein[314] and Conrad[318]), the intrinsic lattice properties appear to receive wider

acceptance (see, for example, several papers in reference 298). Nevertheless, except for those body-centered cubic metals of ultrahigh purity, Frank and Seeger[319] believe that impurity effects are dominant as the rate-controlling mechanism for plastic deformation. In fact, recently the temperature dependence of both unirradiated[309] and irradiated[232] iron was attributed to the interaction of dislocations with centers of tetragonal symmetry, such as interstitial impurities.

Among the body-centered cubic metals, the temperature dependence of the yield stress in unirradiated single crystal niobium has been especially well studied. The large rise in yield stress with decreasing test temperature has been demonstrated by Mitchell *et al.*,[320] Christian and Masters,[295] Kim and Pratt,[321] and Sherwood *et al.*[322] To our knowledge the temperature sensitivity of irradiated niobium has not been previously investigated. However, relatively little change in the temperature dependence of body-centered cubic metals after neutron irradiation was found by Arsenault[323] for polycrystalline vanadium, and Ohr *et al.*,[240] Chow *et al.*[267] and Smidt[324] for polycrystalline iron. On the other hand, irradiation caused a somewhat larger increase in the temperature dependence for compression tests on single-crystal niobium[325] and tensile tests on single-crystal iron.[232] Since these single crystals were of rather high purity, it is not unreasonable to expect irradiation to have an increased effect on their temperature dependence of yielding.

CHAPTER III

MATERIAL, EQUIPMENT, AND EXPERIMENTAL PROCEDURE

I. MATERIAL

In this investigation, niobium from different sources was used as the starting stock for the single-crystal and polycrystalline samples. The single-crystal samples were grown from an electron-beam-melted, polycrystalline bar which was swaged by stages to 3/16-inch diameter from a 3-inch-diameter ingot (Heat No. 31831) supplied by the Wah Chang Corporation, Albany, Oregon. Hereafter, samples originating from this stock will be referred to as Wah Chang niobium. The chemical analyses for two positions in the ingot prepared by the supplier are shown in Table III, along with analyses obtained at the Oak Ridge National Laboratory by the methods indicated. The major metallic impurities are tantalum and tungsten as determined by neutron activation. These two substitutional impurities are the major sources of induced radioactivity in the Wah Chang samples. The activity arises primarily from the following two reactions:

$$\underset{(99.99\%)}{{}_{73}Ta^{181}} + {}_{0}n^{1} \longrightarrow {}_{73}Ta^{182} \xrightarrow[115\ \text{days}]{} \underset{\text{Stable}}{{}_{74}W^{182}} + {}_{-1}\beta^{0} + \gamma\ , \qquad (25)$$

$$\underset{(28.4\%)}{{}_{74}W^{186}} + {}_{0}n^{1} \longrightarrow {}_{74}W^{187} \xrightarrow[24.0\ \text{hours}]{} \underset{\text{Stable}}{{}_{75}Re^{187}} + {}_{-1}\beta^{0} + \gamma\ . \qquad (26)$$

The niobium for the polycrystalline samples was obtained as dendritic powder from CIBA Limited, Basle, Switzerland. Niobium from this

TABLE III

COMPOSITION OF WAH CHANG NIOBIUM STARTING MATERIAL[a]

Element	Wah Chang Ingot Analysis, ppm		ORNL Analysis of 0.190-inch diameter Cold-Swaged Rod, Vacuum Annealed, wt. ppm			
	Top	Bottom	Leco Combustion	Vacuum Fusion	Mass Spectrometer	Neutron Activity
Carbon	30	50	20			
Oxygen	110	60		48		
Nitrogen	35	55		42		
Hydrogen	4.4	4.1		3		
Aluminum	<20	<20			15	
Boron	<1	<1			0.1	
Cadmium	<5	<5			<2	
Cobalt	<10	<10			1	
Chromium	<20	<20			3	
Copper	<40	<40			30	
Iron	<50	<50			10	
Hafnium	<80	<80			15	
Magnesium	<20	<20			5	
Manganese	<20	<20			<1	
Molybdenum	<20	<20			3	
Nickel	<20	<20			5	
Lead	<20	<20			<10	
Silicon	<50	<50			30	
Tin	<10	<10			<5	
Tantalum	<500	<500				395
Titanium	<40	<40			30	
Vanadium	<20	<20			<1	
Tungsten	245	280				282
Zirconium	<100	<100			140	

[a]Wah Chang Niobium Ingot No. 31831.

stock will be designated hereafter as CIBA niobium. Chemical analyses were not determined for the dendritic powder because of the effect of the large surface to volume ratio but were established for the compacted rod as described in the following section.

II. PREPARATION OF SINGLE-CRYSTAL RODS

Wah Chang Niobium

Wah Chang single crystals were grown from the 3/16-inch swaged rod in a Material Research Corporation electron beam floating zone refiner, Model V4-EBZ-6000. The unit consisted of a scanner assembly enclosed in a gasket-fitted glass bell jar which rested on an aluminum base. The bell jar was evacuated through a Granville-Phillips Company Cryosorb liquid nitrogen cold trap and a water-cooled baffle using a National Research Corporation 4-inch diffusion pump backed by a Hyvac 45 mechanical pump. The pumping speed of this system at the entrance to the specimen chamber was about 150 liters per second. The blank-off pressure in the bell jar before zoning was 2-5 x 10^{-7} torr. The swaged rod was mounted on the scanner assembly in V-groove mounts and passed through an aperture of 14.5 millimeters diameter in the cylindrically shaped electron beam gun assembly. The electron gun, attached to a stage that moved vertically and parallel to the specimen axis, was composed of a 23-millimeter-diameter annular filament of 0.51-millimeter-diameter tungsten wire enclosed in a beam-focusing pillbox. Focusing of the electron beam was accomplished by two grounded tantalum annular plates 8 millimeters apart equally spaced to either side of the filament. The electron beam power supply, MRC Model V4-3000, was capable of variable voltages to 5 kilovolts and a beam current to 400 milliamperes.

The swaged rods were prepared for zoning by removing several mils from the surface, using a chemical polish that was 4 parts hydrofluoric acid (48 percent) and 6 parts nitric acid (70 percent). The rod to be zoned (10 1/2 inches long) and a seed crystal (about 3 inches long) with the desired orientation were mounted vertically in the scanner assembly with a separation of approximately 1/8 inch between them. The rod was mounted in the V-groove of the upper fixture and the seed in the lower fixture by 1/2-inch wide metal strips screwed to the fixtures. The rod and the seed crystal were concentrically aligned with the aperture in the electron gun and were parallel to its direction of travel. After aligning the rod, the bell jar was lowered over the scanner assembly and evacuated.

The power supply was operated so as to maintain a potential difference between the tungsten filament and the rod of 4 kilovolts which accelerated the electrons toward the rod, yielding a 70-milliampere beam current. Care was taken to always operate the tungsten filament at a lower temperature than that of the molten zone of the rod in order to minimize contamination from tungsten. Evidence, aside from the color of the sample, that the filament was cooler than the molten zone comes from the niobium deposited on the filament. This niobium deposit completely coated the filament, thereby providing a protective coating against tungsten contamination but causing the filament to sag, reducing its lifetime. Initially, the electron gun was positioned at the gap between the rod and seed so as to melt the lower end of the rod onto the seed crystal. Then the gun position was adjusted from outside the vacuum chamber to melt the upper end of the seed crystal. The length

of the molten zone, which is determined by the surface tension of the metal, beam current, beam voltage, and beam-focusing pillbox design, was trimmed to approximately the diameter of the rod, 3/16 inch, by adjusting the beam current. After these adjustments the electron gun was set to travel automatically in an upward direction at a speed of approximately 4 inches per hour. As the rod solidified at the trailing edge of the molten zone, it had the orientation of the seed crystal. The length of the resulting single crystals was approximately 8 inches.

During melting, the pressure in the specimen chamber rose to 3-5 x 10^{-6} torr. In this investigation all rods used for single-crystal specimens were given a single upward pass of the molten zone. The rod was then allowed to cool to room temperature in the vacuum. Finely spaced concentric lines were observed on the generally smooth surface of the zoned rod. Table IV gives a comparison of typical chemical analyses of single pass, zoned rod and the starting material. It should be noted from Table IV that the zoning did not reduce the tantalum and tungsten impurity levels. Reed,[326] working with the same niobium stock, found that the metallic impurities are removed by evaporation rather than by a zoning effect. Since the boiling points of tantalum and tungsten are substantially higher than that of niobium, it is unlikely that these impurities can be reduced by zoning. Because these two impurities are the major sources of induced activity in niobium, it is desirable from the standpoint of work in the laboratory to begin with stock in which their contents are low.

TABLE IV

COMPARISON OF IMPURITIES IN WAH CHANG NIOBIUM
INITIALLY AND AFTER ONE ZONE PASS

Element	Starting Material (Weight ppm)	One-Pass Zone Refined Niobium (Weight ppm)
Carbon	-	11
Nitrogen	-	24
Oxygen	-	30
Aluminum	15	0.3
Boron	0.1	0.1
Cadmium	<2	
Calcium	<1	0.4
Chromium	3	0.7
Cobalt	1	0.06
Copper	30	0.1
Gold	<0.1	
Hafnium	15	5
Iron	10	1
Lead	<10	
Magnesium	5	
Manganese	1	0.2
Molybdenum	3	6
Nickel	5	0.3
Tantalum	400	400
Tin	<5	
Titanium	30	
Vanadium	<1	
Tungsten	300	300
Zirconium	140	20

CIBA Niobium

A stock of niobium containing low levels of tantalum and tungsten impurities was obtained in powder form from CIBA Limited. This dendritic powder was prepared by electrodeposition from a molten salt.[327] Neutron activation analysis indicated that the powder contained 1-3 wt. ppm tungsten and 16-22 wt. ppm tantalum, which is a significant improvement over their levels of about 280 wt. ppm and 400 wt. ppm, respectively, in the Wah Chang niobium (Table III, page 60).

Two procedures were used to consolidate the dendritic niobium powder: (1) electron-beam drop casting and (2) compaction by swaging and then consolidation by zoning. The method employed initially was electron-beam drop casting. The electron-beam furnace used was originally of NRC Equipment Corporation design but had been considerably modified at the Oak Ridge National Laboratory as described by Dean and McDonald.[328] The procedure, as outlined in detail in the report, is to place a charge of niobium powder on the hearth of a copper chill mold and then to play an electron beam over the charge to gradually melt it. As the molten region penetrates deeper into the charge, only a thin layer of unmelted metal supports the charge. With a rapid increase in furnace power the entire charge becomes molten and is drop-cast into a vertical chill mold below the hearth. The small drop-cast ingot was then swaged to a 3/16-inch-diameter rod. Neutron activation analysis indicated that on occasion there was a significant increase in the tungsten and tantalum contents after drop casting. At first it was felt that the pick-up of these impurities was from the T-111 alloy (Ta base - 8 wt. % W, 2 wt. % Hf) emitter. Consequently, a different consolidation technique was devised

after electron-beam drop casting only two ingots. Upon further investigation of this matter, Reed *et al.*[329] have reported that the contamination arose from volatilization from the furnace walls by the radiant heat from the beam. Fortunately, the chamber walls were relatively clean when the first ingot was cast, resulting in relatively little contamination. Typical chemical analyses of this material as drop-cast and after zoning are shown, respectively, in Columns 1 and 2 of Table V. Samples from this material were used for most of the electron microscopy and in the determination of the polycrystalline dose dependence and for one of the radiation-anneal hardening curves. Hereafter, the drop-cast CIBA niobium will be designated as CIBA-A.

Before actually determining the source of contamination from tantalum and tungsten in the drop-cast rods, a second compaction technique was designed which subsequently has become the standard preparation method. In this method, 5/8-inch O.D. copper tubing with 0.040-inch walls was first cleaned in nitric acid or a commercially prepared copper or brass dip. The tube was sealed with an end plug and then tapped full of niobium powder. A second end plug was silver soldered to close the tube which then was evacuated for approximately 12 hours through a liquid nitrogen cold trap by a mechanical pump to about 5×10^{-3} torr. The evacuated tube was sealed off and then swaged down to about 5/16-inch diameter in order to compact the powder. The copper tubing was removed by etching in concentrated nitric acid which does not attack niobium, yielding a compacted niobium rod with a diameter of about 1/4 inch.

The compacted rod was sufficiently rigid to be placed in an electron-beam zoner for consolidation. The zoner used for the consolidation was of similar design to that used for growing Wah Chang single

TABLE V

CHEMICAL ANALYSES OF CIBA NIOBIUM AT VARIOUS STAGES OF PREPARATION

Element	As Drop-Cast (Weight ppm)	Drop-Cast and Zoned (Weight ppm)	Swaged Powder (Weight ppm)	Zoned Powder Compact (Weight ppm)
Carbon	40	40	270	50
Oxygen	13	8	510	21-47
Nitrogen	22	<5	61	25
Hydrogen	2	2	5	3
Aluminum		0.1	1	0.3
Boron		∿1	3	0.3
Beryllium			0.3	0.1
Bismuth			<0.7	<0.7
Calcium		∿0.1	1	0.03
Cobalt		<0.01	2	0.06
Chromium		2	2	2
Copper		<0.02	30	0.1
Iron		0.5	20	2
Hafnium		10		
Magnesium		0.1	0.5	0.02
Manganese		0.5	0.06	0.02
Molybdenum		<0.05	<0.1	<0.1
Nickel		<0.02	30	1
Silicon		0.1	10	1
Sulfur			20	<0.2
Tin		<1		<0.1
Tantalum	45-56	46-56	16-20	20
Titanium		0.2	0.2	0.02
Tungsten		14	1	2
Vanadium		<0.01	0.6	0.02
Zinc		∿0.02	4	0.04
Zirconium		5	0.06	0.06

crystals but was capable of achieving a vacuum of 1×10^{-10} torr. The electron beam scanner and power supply were of Material Research Corporation design from the EBZ 94 unit. The scanner assembly was enclosed in a stainless steel bell jar directly above a Davis-Wilder liquid nitrogen vacuum trap which was optically isolated from a 10-inch NRC diffusion pump by a water baffle. The large diffusion pump was backed by a 4-inch NRC diffusion pump and a 425 liter per minute mechanical pump. Further details on the design and operation of this unit are reported by Reed.[326]

No attempt was made to obtain a high vacuum for the two consolidation passes on the compacted powder. Typical blank-off vacuum for the first pass was 2×10^{-7} torr with an increase to 1×10^{-5} torr during operation of the electron beam. The zone speed was about 20 centimeters per hour. During the second pass the pressure was typically 3×10^{-6} torr. Following the two passes to consolidate the powder, the zoned rod was swaged to 3/16-inch diameter. Subsequently, the swaged rod was seeded and grown as a single crystal at a zone speed of 10 centimeters per hour and a base pressure of 5×10^{-8} torr. The chemical analyses of the compacted powder and the zoned rod are given in Columns 3 and 4, respectively, of Table V.

It was found that bleeding oxygen into the specimen chamber during the first zone pass on the swaged rod reduced the carbon level without significantly changing the oxygen level. The leak rate was adjusted to maintain an oxygen pressure of 1×10^{-5} torr on the ion gage. Second and third passes were made in a vacuum of 1×10^{-7} and 5×10^{-8} torr, respectively. This technique was used to produce the low-carbon niobium for one of the radiation-anneal hardening curves

discussed in Chapter VII. Hereafter, this low-carbon CIBA niobium will be referred to as CIBA-B.

III. TENSILE SAMPLE PREPARATION

Wah Chang Niobium

All of the Wah Chang samples discussed in this dissertation were single crystals. Thus, the rod axis orientation was seeded to coincide with the desired tensile axis. In this study a single tensile axis orientation was considered, namely, that orientation for maximum resolved shear stress on the $(\bar{1}01)$ [111] slip system, the primary slip system. Thus, the desired rod axis made an angle of 45 degrees with both the normal to the $(\bar{1}01)$ plane and the [111] direction and lay in the plane determined by these two directions. The rod axis orientation was determined by the standard Laue back-reflection technique[330] before the rods were cut for tensile sample preparation. Samples from two groups of Wah Chang rods will be discussed. The rod axis orientations are shown in the [001] - [011] - $[\bar{1}11]$ standard stereographic triangle for the dose dependence samples in Figure 4 and for the temperature dependence samples in Figure 5. The samples used in this study had Schmid factors of not less than 0.496 and thus had orientations within the areas enclosed by dashed lines in Figures 4 and 5.

After determining the rod axis orientation, the rod was cut into 1.5-inch segments using a high speed, 120 grit abrasive, 0.015-inch-thick, cut-off wheel with water coolant. Tensile samples were centerless ground from the zoned-rod segments which had a 0.75-inch-long gage section and a nominal diameter of 0.085 inch. The centerless grinding operation

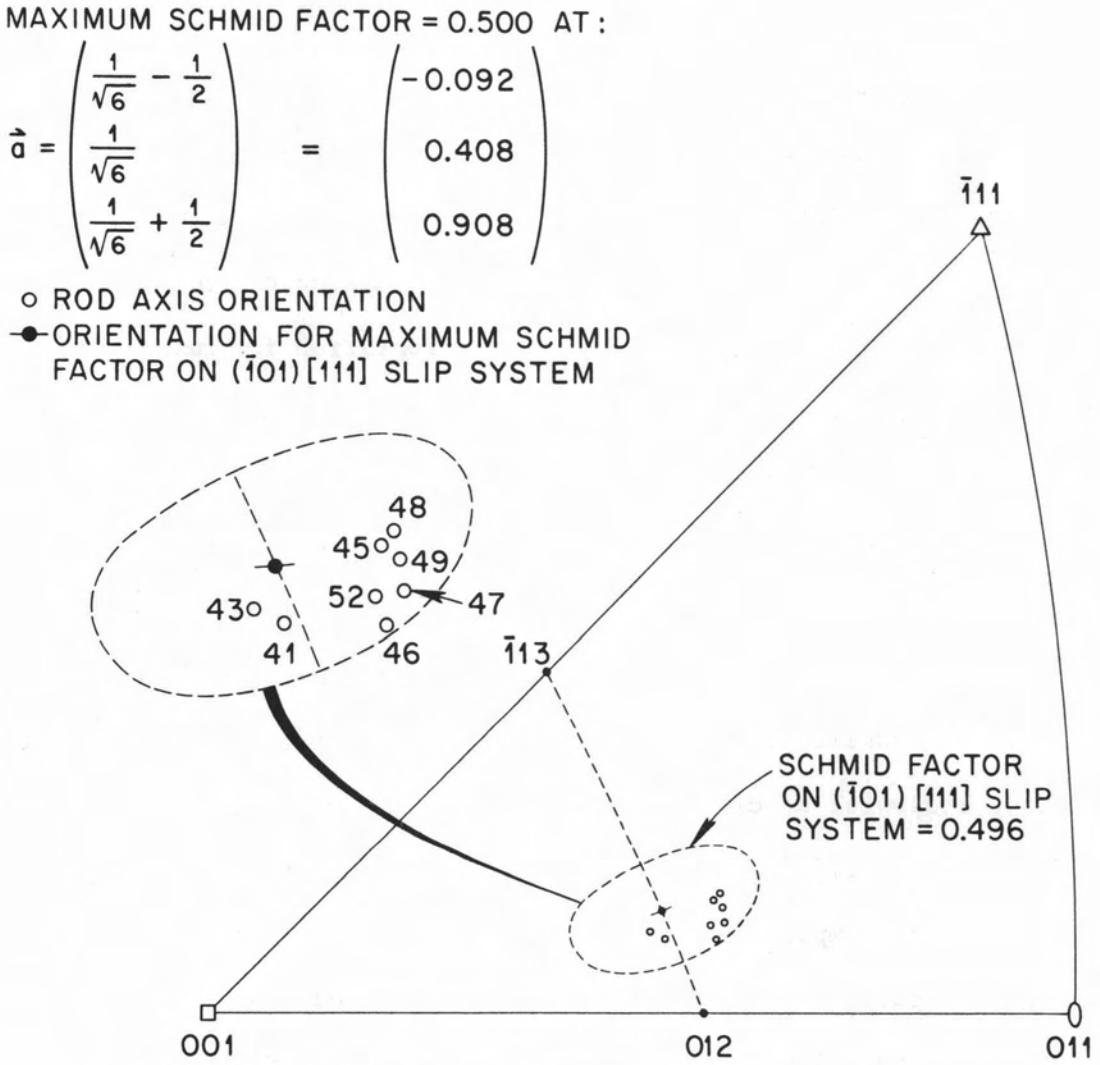

Figure 4. Standard stereographic triangle showing rod axis orientations of Wah Chang niobium single crystals used in dose dependence study.

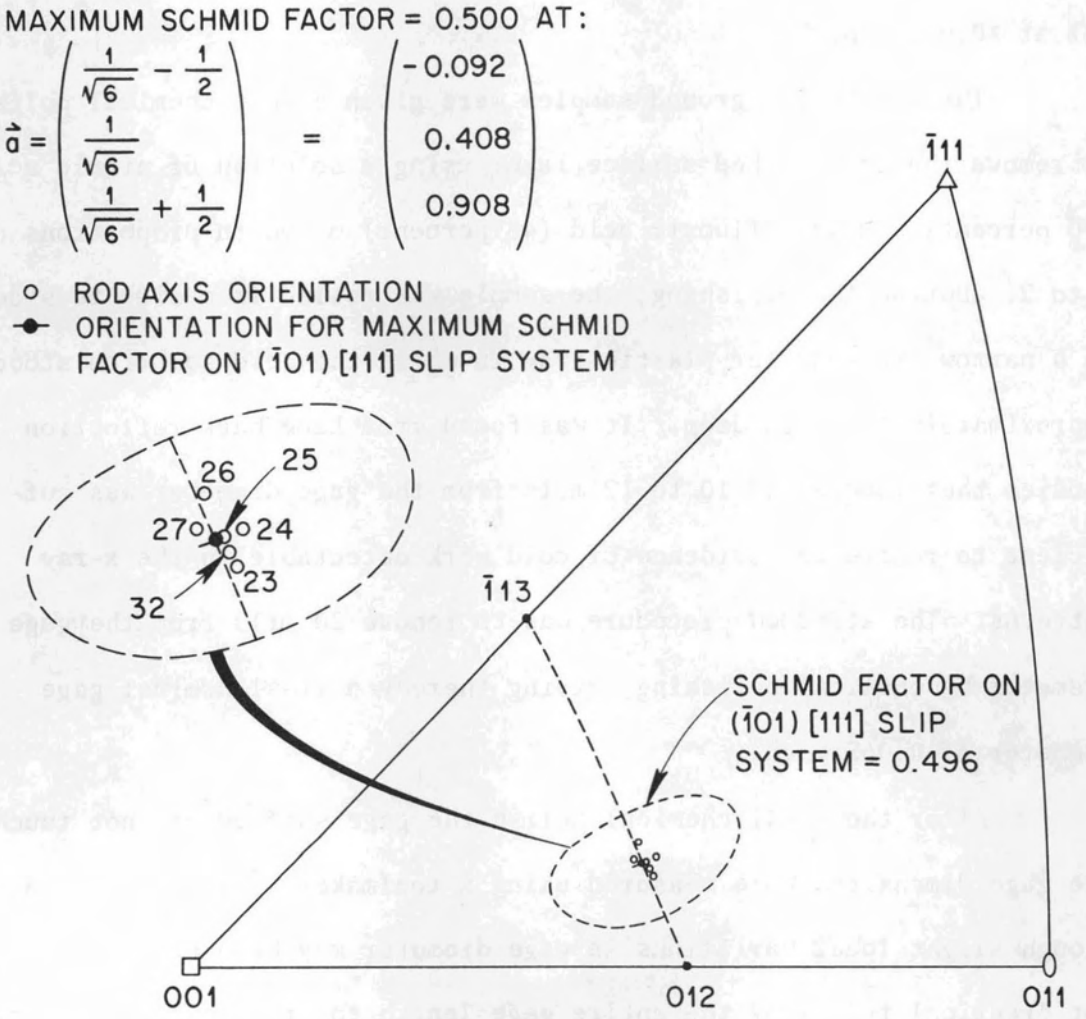

Figure 5. Standard stereographic triangle showing rod axis orientations of Wah Chang niobium single crystals used in temperature dependence study.

employed a water cooled, 120 grit wheel dressed to give a 1/8-inch radius on each edge, thus resulting in a 1/8-inch radius at the shoulders of the sample. Care was taken to minimize the gage taper to within the tolerance set at ±0.0002 inch.

The centerless ground samples were given a deep chemical polish to remove the cold-worked surface layer using a solution of nitric acid (70 percent) and hydrofluoric acid (48 percent) mixed in proportions of 3 to 2. During the polishing, the sample was rolled from side to side in a narrow, rectangular plastic tray in which the acid solution stood approximately 1/2-inch deep. It was found from Laue back-reflection studies that removal of 10 to 12 mils from the gage diameter was sufficient to remove the evidence of cold work detectable in the x-ray patterns. The standard procedure was to remove 20 mils from the gage diameter by chemical polishing, giving thereby a final nominal gage diameter of 0.065 inch.

After the final chemical polish the gage surface was not touched. The gage dimensions were measured using a toolmaker's microscope. Although slight local variations in gage diameter may have existed, it was not practical to survey the entire gage length for the absolute minimum diameter. Instead, diameters were determined at three positions along the gage for three azimuthal positions approximately 120 degrees apart. The gage positions measured were near each shoulder where experience showed a slight local minimum usually existed and close to the gage center. A typical sample diameter with the variation from the average of the nine readings is 1.6561 ± 0.0076 millimeters (0.0652 ± 0.0003 inch). For this sample the total variation in area was 0.0395 square

millimeters. For a 10 kilogram load the resulting stress variation is 0.0852 kilograms per square millimeter which is about ±1 percent variation from the average stress.

One group of Wah Chang tensile samples were annealed near the melting point in a high-vacuum annealing furnace. The setup consisted of a bakeable stainless steel chamber which enclosed a water-cooled, copper induction coil at its center. A bakeable radio frequency 20 kilowatt power feedthrough provided taps outside the chamber for connection to a Westinghouse 10 kilowatt radio frequency generator (Model 20K64). The specimens were hung by niobium wires spot-welded to the shoulder in the center of the induction coil with a split tantalum radiation shield between them and the coil. The specimen chamber was evacuated using a 6-inch NRC diffusion pump through a liquid nitrogen trap which was optically isolated from the pump by a water baffle. A 2-inch NRC diffusion pump with a water baffle served as a booster pump and was backed by a 425 liter per minute mechanical pump.

In a typical annealing sequence the five samples were placed in the chamber which was then evacuated to about 5×10^{-8} torr. The stainless steel chamber was baked overnight (approximately 16-18 hours) at 250°C. After slowly cooling the chamber to room temperature to prevent thermal shock to the ceramic feedthrough, the blank-off pressure was typically 5×10^{-9} torr or better. The samples were induction heated to 2350°C and annealed at this temperature for 5 hours. The temperature was measured using an optical micropyrometer. The apparent temperature as measured was corrected for spectral emissivity and for the effect of the glass in the chamber viewing port. The vacuum upon reaching the

annealing temperature was about 1-2 x 10^{-7} torr and decreased during the anneal to about 1-2 x 10^{-9} torr. The induction coil power was shut off quickly at the conclusion of the anneal. After the samples and water-cooled chamber walls reached room temperature, the vacuum was 2-3 x 10^{-10} torr. Reed *et al.*[331] have compared the chemical analyses of zoned and zoned-and-annealed samples as shown in Table VI. High temperature annealing has been found to improve the crystalline perfection of niobium[332,333] and to lower its yield stress.[334]

CIBA Niobium

All of the CIBA niobium tensile samples described in this dissertation were in the form of thin sheet. The tensile samples were stamped from 0.005-inch thick sheet, which had been cold rolled from single crystal rods, using a specially made die. The gage section was 4.2 millimeters wide and 12.7 millimeters long. Sheet samples of CIBA-A were given a recrystallization anneal at 1050°C for one hour in a dynamic vacuum of approximately 3 x 10^{-8} torr. The resulting grain size was about 44 microns as shown in the photomicrograph of Figure 6. Tensile samples from CIBA-B, which was somewhat purer, were recrystallized in a dynamic vacuum at 950°C for one hour, developing a grain size of about 50 microns. Following a recrystallization anneal, a partial chemical analysis for samples from rods which had been consolidated by drop casting, i.e., CIBA-A, revealed the impurity levels shown in Table VII. The interstitial impurity levels for recrystallized material from an oxygen-treated compacted and zoned rod, i.e., CIBA-B, are also given in Table VII.

TABLE VI

CHEMICAL ANALYSES OF WAH CHANG NIOBIUM BEFORE AND AFTER ANNEALING NEAR MELTING POINT

Treatment	Concentration (wt. ppm)										
	C	O	N	H	Ta	W	Fe	Cr	Ni	Zr	Cu
Zoned	42	22	4	2	356	268	6	6	<1	20	1
Zoned and Annealed	32	25	3	1	309	233	<1	<1	<1	6	<1

TABLE VII

CHEMICAL ANALYSES OF CIBA NIOBIUM AFTER RECRYSTALLIZATION ANNEAL

Material Source	Concentration (wt. ppm)								
	C	O	N	H	Ta	W	Zr	Hf	Fe
CIBA-A	60	38	5	<1	∿50	14	10	5	1
CIBA-B	35	41	5	<1	20	2	0.06		<1

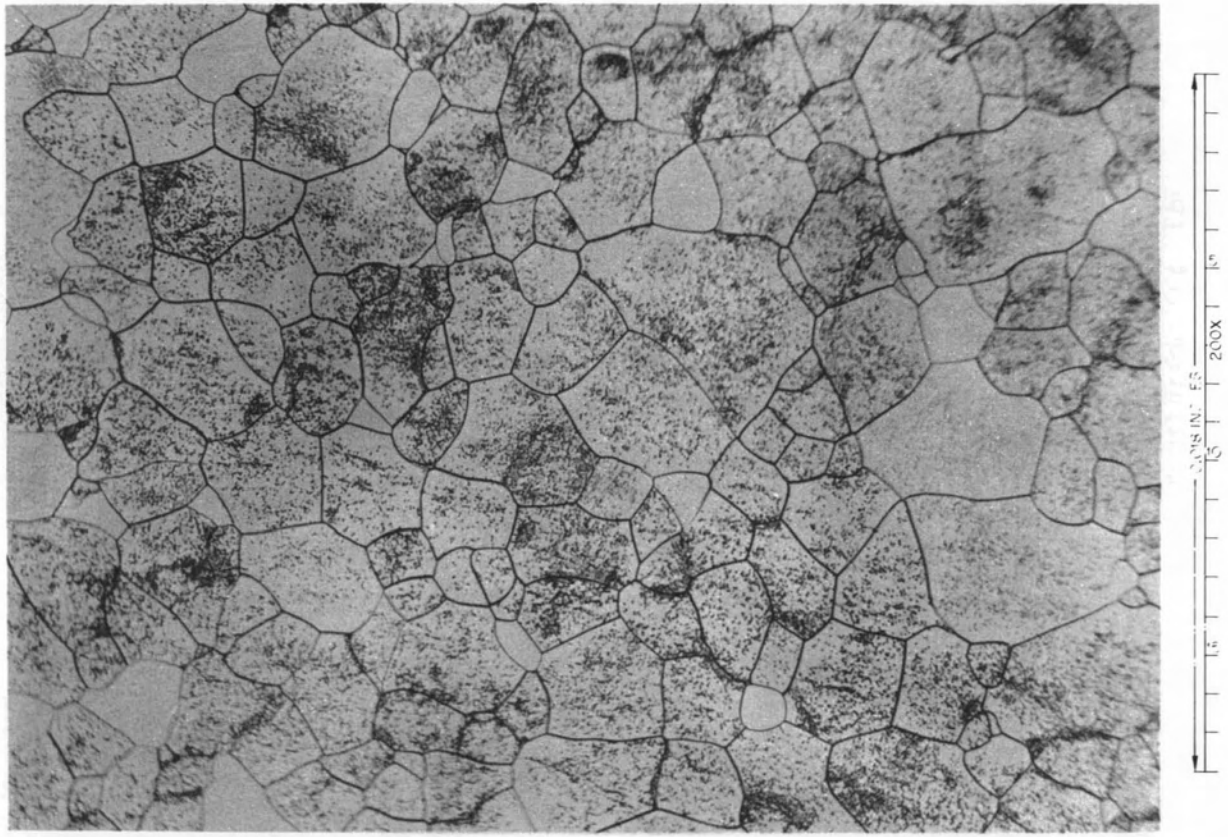

Figure 6. Grain structure in niobium after recrystallization at 1050°C for one hour. Etch pits are observable in most grains.

Etchant: 10 parts HF, 10 parts H_2SO_4, 10 parts H_2O, 1 part H_2O_2.

IV. IRRADIATION PROCEDURES

The tensile samples and pieces of niobium sheet for transmission electron microscopy were irradiated in two facilities -- the Position Five Facility (PFF) in the Bulk Shielding Reactor (BSR) and the Hydraulic Facility in the Oak Ridge Research Reactor (ORR). Since these irradiation facilities were described in some detail in a previous thesis,[239] only a brief description of the irradiation procedures will be presented here.

Ten Wah Chang single crystal tensile samples used in the temperature dependence study were irradiated at the same time in the PFF of the BSR for an effective irradiation time of 48.98 hours in periods of approximately eight hours a day. The sample holder for the PFF consisted of two circular, aluminum plates with 7/32-inch-diameter recesses into which machined cadmium sleeves of about 0.020-inch thickness and 2-inch length were placed in a bird-cage-like manner. A dummy sample with a thermocouple soldered to the bottom shoulder was placed in the rack inside a cadmium sleeve similar to that used for the experimental samples. During the irradiation time, the peak temperature was between 100 and 110°C as measured by the chromel-alumel thermocouple attached to the bottom shoulder of the dummy sample.

The fast neutron flux in the PFF was measured with the BSR at 1 megawatt power using neptunium-237, uranium-238, nickel-58, and iron-54 threshold dosimeters. These dosimeters were removed from the experiment following the first continuous irradiation period of seven hours. The flux, ϕ, of neutrons with energies greater than 1 Mev was determined as $(1.6 \pm 0.2) \times 10^{12}$ neutrons/cm^2 sec. Thus, the dose which these samples received was 2.8×10^{17} neutrons/cm^2 ($E > 1$ Mev).

All other irradiations for samples discussed in this dissertation were carried out in Tube 12 of the Hydraulic Facility of Position F-8 in the ORR. The ORR is a light-water-moderated and cooled, beryllium-reflected reactor operating at a power level of 30 megawatts. During irradiation in the Hydraulic Facility, pool water flows past the sample capsule to provide cooling. The bulk pool water temperature is generally greater than 90°F (32.2°C) and must be kept below 100°F (37.8°C) for the reactor to operate. The sample capsule insertion and removal in the Hydraulic Facility is accomplished by controlling the direction of water flow in the facility.

Two capsule designs were used for irradiations in the Hydraulic Facility. For the Wah Chang single crystals used in the dose dependence work a cadmium tube two inches long with a 2/32-inch outside diameter and 3/16-inch inside diameter served as an inner capsule. The tube was closed at each end by cadmium plugs which extended 7/32 inch into the tube such that the 1.5-inch-long sample was restricted to little freedom of movement. The design of the end plugs allowed water to enter the cadmium tube and to flow past the sample but isolated the sample from the neutrons. The cadmium tube was positioned inside an Isotopes Division standard perforated aluminum rabbit tube by two aluminum spacing rings fitted on the ends of the cadmium tube. The cadmium tube was enclosed in the aluminum rabbit by aluminum end caps which could be tapped into place.

Since cadmium has a high cross section for thermal neutrons, its primary purpose was to shield out the thermal neutrons which induce residual radioactivity by interaction with impurities in the niobium.

Because of the rather high levels of tantalum and tungsten in the Wah Chang stock, this shielding was necessary to permit handling of the irradiated samples in the laboratory after a reasonable decay time. On the other hand, the presence of cadmium provides a source of heat when it is bombarded by neutrons. Thus, the use of cadmium generates concern regarding irradiation temperature; for it is not possible under the normal operating procedures of the Hydraulic Facility to monitor the temperature of a sample with a thermocouple when in the reactor core. Attempts have been made to determine the temperature inside the cadmium tube by using low melting alloys and temperature-sensitive lacquers as previously reported.[239] The best estimate of the irradiation temperature using the cadmium capsules open to water flow is 90°C.

For the CIBA niobium sheet tensile samples and electron microscope pieces the perforated aluminum rabbit tube was used without any cadmium shielding. Because of the lower impurity levels in CIBA niobium, the induced radioactivity due to thermal neutrons was manageable without cadmium shielding. In this case where the pool water flows freely over the sample, the irradiation temperature is thought to be essentially the pool water temperature, i.e., about 40°C.

For each series of sample irradiations in Tube 12 of the ORR-F-8 Hydraulic Facility the fast neutron flux was determined using as threshold dosimeters neptunium-237, uranium-238, nickel-58 and iron-54. For the flux spectrum measurements these monitors were sealed in quartz ampoules. When the series of irradiations extended over several days, a flux spectrum was run at the beginning, middle, and end of the series. Also for the dose dependence study, bare nickel wire monitors were placed along the gage section of the tensile samples for the longer time irradiations.

The fast neutron flux in Tube 12 changed with refueling but was rather uniform after a few days from the beginning of a 60-day cycle. For the most part, samples for a given series were irradiated within a single cycle. The flux of neutrons in Tube 12 with energies greater than 1 Mev as determined by nickel monitors was typically between 2-3 x 10^{13} neutrons/cm^2 (E > 1 Mev). The irradiation schedule included times from about four minutes to 120 hours, yielding doses from 4.1 x 10^{15} to 8.2 x 10^{18} neutrons/cm^2 (E > 1 Mev). The irradiated capsules emitted the blue Cerenkov glow for all irradiation times used. The Cerenkov radiation was used to check that the capsule had actually been in the reactor core and to follow the exit of the capsule from the core. The irradiated capsules were opened in one of the ORR hot cells and the samples retrieved and stored for a period of radioactive decay.

V. TENSILE TESTING EQUIPMENT AND PROCEDURE

Most of the tensile tests were performed at Oak Ridge National Laboratory on a metric, table model Instron machine with a range of slow metric crosshead speeds. However, tensile tests of the Wah Chang single crystals used to determine the temperature dependence of the yield stress were performed for the most part by M. S. Wechsler and R. Bode at Battelle Institute, Geneva, with the analysis of the data described in this dissertation carried out at the Oak Ridge National Laboratory. In this investigation, all the single crystals were deformed at a crosshead speed of 0.02 cm/min using a decade speed reducer. For the 1.905 cm (0.75 inch) gage length, the 0.02 cm/min crosshead speed corresponds to a strain rate of 1.75 x 10^{-4} per second. The CIBA sheet samples were tested at a

crosshead speed of 0.1 cm/min which corresponds to a strain rate of 1.3×10^{-4} per second. Except for the temperature dependence study, all tests were performed at room temperature. The chart recording the load was operated at 2 cm/min. A standard electric timer was used to check the chart speed and to establish the correction in the chart motion.

The test temperatures from room temperature down to 93°C in the temperature dependence study were obtained by spraying pre-cooled nitrogen gas over the sample, grips, and pull rod which were placed within a copper-lined, styrofoam-insulated enclosure. The temperature during testing was monitored by a thermocouple mounted near the center of the gage length of the sample. The apparatus for the low-temperature tests has been described in detail in a report by Spreadborough *et al.*[335]

Grips of two designs were used in this study. For the single crystals a set of hinged split grips positioned between the load cell and the crosshead was used. The lower pull rod fitted into a cup atop the crosshead while the upper pull rod was attached to the load cell through a flexible bayonet-type coupling. The hinged clamshell-like split grips were held on the pull rods by cylindrical sleeves. The load cell was an Instron CTM tension cell with nominal full scale load ranges of 2, 5, 10, 20, 50 and 100 kilograms with a 0.4 kilogram ultra-sensitive range. The sheet samples were tested using a gripping rig which consisted of a cage attached below the crosshead and an upper pull rod extending through the crosshead. The upper grip which was attached by pull rod to the CTM load cell moved in guides on the cage. The sample was gripped by knurled surfaces screwed against the moveable upper grip and the stationary lower grip.

In an effort to maintain closer temperature control, the entire test section including the crosshead screws was enclosed in a lucite box. The test temperature was between 22 and 26°C. Prior to testing each sample the Instron was calibrated using a 3-kilogram load. A preload of about 0.2 kilogram was manually applied in most cases in order to seat the sample in the grips and to obtain good alignment. The crosshead was set in motion immediately after applying the preload. The sample was strained the desired amount (at which time the load was removed) or in some cases pulled to fracture.

VI. POST-IRRADIATION ANNEALING PROCEDURE

Anneals following irradiation of the CIBA sheet tensile samples were performed in the same dynamic vacuum system as the high temperature anneals on the single crystals, described above, or in a system of similar design. Samples of CIBA-A and CIBA-B were given anneals in the range from 100 to 800°C. Unirradiated control samples and irradiated electron microscopy (EM) pieces were also annealed at the same time as the irradiated tensile samples. The samples from CIBA-A for the anneal hardening study were annealed using a Marshall tube furnace in a quartz side-arm tube attached to the stainless steel chamber of the system used for induction heating. The blank-off pressure was typically 2×10^{-8} torr prior to heating. The temperature was controlled and recorded by a Leeds and Northrup Company Speedomax H using a chromel-alumel thermocouple. The heat-up time was approximately 7-10 minutes. Following two hours at temperature the samples were allowed to furnace cool in a dynamic vacuum.

For the annealing kinetics study and for the anneal hardening curve for CIBA-B, greater care was taken to determine the sample temperature. In these cases, a platinum-platinum 10 percent rhodium thermocouple was spot welded to a niobium boat of the same material as that to be annealed. The tensile samples and EM pieces were placed in the boat and then into a quartz side-arm tube. Upon achieving an acceptable vacuum of 2×10^{-8} torr, a preheated furnace was placed around the quartz tube to raise the specimen to the desired temperature quickly. On reaching the prescribed temperature as measured by the thermocouple the preheating furnace was removed and quickly replaced by a Marshall tube furnace preheated to the desired annealing temperature. The temperature leveled out at the set valve within 10 minutes and the anneal was carried out for the desired time at temperature. For all anneals except those described in the previous paragraph, the furnace was removed immediately after the anneal and the sample allowed to cool in the dynamic vacuum.

VII. ELECTRON MICROSCOPY

Specimen Preparation

All electron microscope specimens were prepared from the 0.005-inch-thick CIBA sheet material. The irradiated but undeformed specimens originated from special electron microscope (EM) pieces recrystallized and irradiated at the same time as the corresponding tensile samples. The EM pieces were from regions left adjacent to the gage section when the tensile samples were stamped out. Specimens were also prepared from irradiated and deformed sheet tensile samples receiving various amounts of strain.

Pieces about 4-6 millimeters square cut from the sheet material were gripped firmly but lightly in platinum tipped forceps held closed by a small rubber O-ring. The "window" technique was used. Microstop* was applied to the end of the forceps and to form a frame at the edge of the specimen. It was especially important that no cracks in the Microstop exist where the forceps tips gripped the specimen; otherwise, the specimen would be attacked preferentially there. The Microstop was allowed to dry thoroughly before commencing the electropolishing.

The electrolyte used was a solution of 15 percent hydrofluoric acid (48 percent) and 85 percent nitric acid (70 percent). The solution was placed in a 400-milliliter plastic beaker fitted with a metal ring which held two square carbon cathodes about two inches apart. The plastic beaker was placed in a 9-inch-diameter flat cylindrical dish and ice packed around it. The solution was stirred using a plastic coated stirring rod and a magnetic stirrer. The solution was stirred while cooling for approximately 15 minutes before thinning was begun. New solution was prepared after every second specimen or after a delay of about an hour from the time it was prepared. Acid fumes rose from the solution to an extent that the operation must be conducted in a well ventilated room in a chemical hood. Rubber gloves were worn as protection against the acid solution.

A Kepco direct current power supply capable of 75 volts and 2 amperes was set at 5 volts before connecting the leads to the electrodes

---

*Microstop is a nonconducting lacquer manufactured by Michigan Chrome and Chemical Company, 8615 Grinnell Avenue, Detroit, Michigan.

of the polishing bath. The metal forceps gripping the specimen formed the anode of the cell. At the time the specimen was inserted into the electrolyte the power supply was switched on. Provided the Microstop coating was continuous at the point of contact of the platinum tips and the specimen, the ammeter on the power supply registered near 0.1 amperes with a slight fluctuation of the needle detectable and no bubbles were formed. The thinning time was usually about 8-10 minutes. A light was played on the surface of the sample to aid in the detection of the first hole visible to the naked eye. Near the end of the polishing time the anode was held by hand to facilitate rapid removal upon breakthrough of the first hole.

When a hole was observed, the specimen was quickly transferred to a beaker of absolute ethanol and was washed by a cutting-like motion in the ethanol. Two additional absolute ethanol washes were employed before storing the foil in a carefully cleaned, closed container filled with absolute ethanol. The foil had its own supporting frame so it was unnecessary to use grids when placing the foil in the microscope specimen holder. When the foil was transferred to the specimen holder, the excess ethanol adhering to the surface was dried using filter paper. It was found that provided the electrolyte was thoroughly rinsed from the specimen, the foils could be kept for several days. However, there appeared to be some deterioration of the image quality if the specimen were not examined within about 48 hours.

Microscope Operation

All the foils were examined in a Hitachi 11A electron microscope operated at 100 kilovolts and equipped with a stage that could be tilted

and rotated. Liquid nitrogen traps were in use at the specimen chamber and at the electron diffraction chamber and on occasion, between the diffusion pumps and the main column to minimize contamination of the specimen. The alignment of the microscope was trimmed before each period of operation. One of the larger objective apertures (about 150 microns) was used for scanning the specimen and the smallest aperture (10-20 microns) was reserved for taking photographs. The smallest of the selected area apertures (20 microns) was used when recording a diffraction pattern.

The microscope was calibrated for the rotation of the diffraction pattern with respect to the micrograph caused by the change in the strength of the intermediate lens by using molybdenum trioxide crystals as described by Thomas.[30] The magnification was determined using a standard grating replica. In correlating the micrographs and diffraction patterns, allowance was made for both the intermediate lens rotation and the extra inversion of the image by the objective lens for the micrograph. The micrographs were printed to give normal positive prints, i.e., with the emulsion side of the plate facing the emulsion side of the printing paper.

Spot Counting Procedure

As will be discussed in the next chapter, radiation damage was observed in the electron micrographs as defect clusters or spots. The size distribution of the clusters was determined for samples receiving various treatments with the aid of a Zeiss Particle Size Analyzer TGZ 3. In order to use the analyzer the electron microscope plates were enlarged five times and printed on single weight contrast photographic paper. The particle size analyzer is a semi-automatic instrument in which an iris

diaphragm is imaged by a lens and light source onto the plane of a plexiglass plate. The enlargement of the micrograph to be measured is placed on the plate. By adjusting the iris diaphragm the diameter of a circular light spot penetrating through the enlargement can be changed and its area adjusted to correspond with the individual clusters. Each aperture interval of the iris diaphragm is correlated with a counter which records when a footswitch is depressed. At the same time the cluster is counted in a given size interval, a puncher marks the cluster as counted on the micrograph.

CHAPTER IV

OBSERVATION AND DETERMINATION OF THE NATURE OF RADIATION-PRODUCED DEFECT CLUSTERS

I. INTRODUCTION

As emphasized in Chapter II (see Table I, pages 8-11), there have been numerous observations by transmission electron microscopy (TEM) of radiation-produced defect clusters or spot damage in various metals. Nevertheless, to our knowledge defect clusters had not been observed directly by TEM in irradiated niobium prior to this work, although changes in physical and mechanical properties upon irradiation were reported. In an attempt to observe the damage, a number of pieces of the polycrystalline CIBA-A niobium sheet (see Chapter III, page 59) were irradiated to 2×10^{18} neutrons/cm^2 ($E > 1$ Mev) at about 50°C in the Hydraulic Facility at the Oak Ridge Research Reactor. Thin foils suitable for TEM were prepared by electropolishing in a solution of 85 percent nitric acid and 15 percent hydrofluoric acid by volume and examined in the Hitachi 11A electron microscope operated at 100 kilovolts.

II. OBSERVATION OF DEFECT CLUSTERS

Figure 7 shows defect clusters in the form of black spots or "black death" for a niobium foil examined under kinematical diffraction conditions, i.e., when the foil was not oriented for Bragg diffraction. The black spots ranged in size from about 30 to 170 Å. As shown in Chapter VII, the size distribution for this dose is rather sharply peaked at about 80 Å. In order to determine the spot density, it was necessary

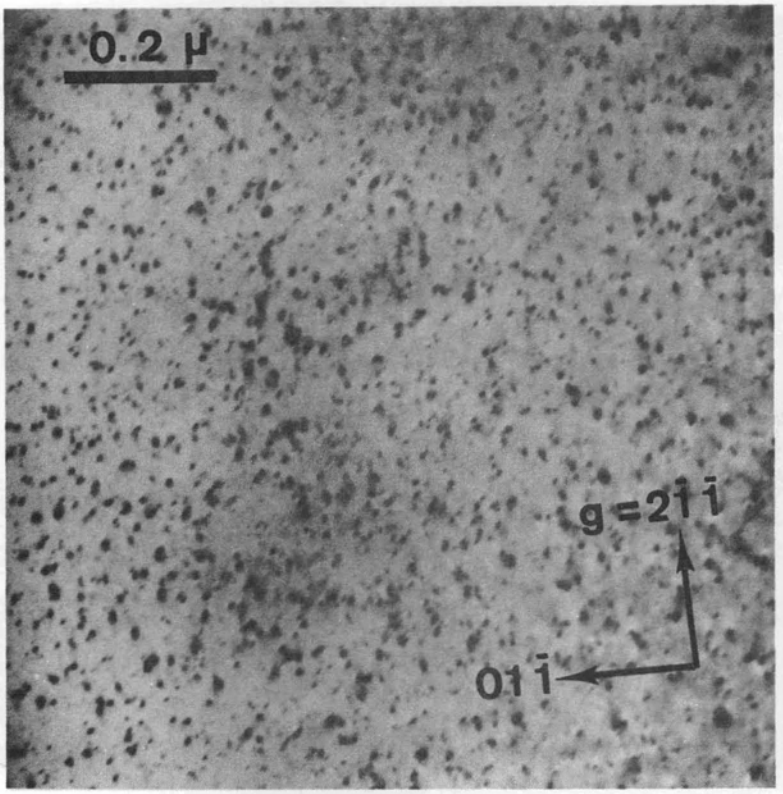

Figure 7. Defect clusters in neutron-irradiated niobium, 2 x 10^{18} neutrons/cm^2 (E > 1 Mev), revealed under kinematical diffraction conditions (s > 0).

to estimate the thickness of the foil. Although it was rarely possible to accurately establish the thickness in the exact region where a spot count was made, the thickness of the foil in regions of good transmission was estimated to be approximately 2500 Å on the basis of the projected width of slip traces created in the microscope. For this value of thickness, the overall density of spots was approximately 6×10^{15} cm^{-3}.

The question of foil thickness arises in subsequent chapters wherever a spot density is quoted. Thus, it seems appropriate to describe here some important limitations to the determination. The slip traces were produced by dislocations caused to slip by localized heating of the foil in the electron beam. As these dislocations, which extended through the foil from surface to surface, moved, they left behind a trace visible on each surface as shown in a micrograph in Chapter VII.* The contrast effect temporarily remaining after the passage of such a slip dislocation is believed to be due to a surface layer of oxide or perhaps carbon contamination (see, for example, Whelan[336] or Hirsch *et al.*[337]). The plane of the foil was determined from the electron diffraction pattern of the area and was assumed to be perpendicular to the electron beam. The projected width of the slip trace was measured on a micrograph of known magnification, and the trace direction was established from the diffraction pattern. The angle of the slip plane normal with respect to a known crystallographic direction was measured and plotted in an appropriate stereographic projection, and the slip plane was chosen to be the {110}

---

*See page 205.

consistent with this geometry. Support for assuming the {110} type plane is found from an analysis of the channeling geometry as described in Chapter V.

The foil thickness t was found using the relation

$$t = w \tan \theta \ , \tag{27}$$

where w is the projected width and θ is the angle between the foil surface and the slip plane. Hirsch *et al.*[338] point out that when the foil is tilted with respect to the electron beam it is necessary to replace θ with an angle θ' given by:

$$\theta' = \theta + \cos^{-1} \left[\frac{\cos \Psi}{(1 - \cos^2 \omega \sin^2 \Psi)^{1/2}} \right] , \tag{28}$$

where Ψ is the angle the foil is tilted relative to its position perpendicular to the beam and ω is the angle between the tilt axis and the projected width of the trace. If the tilt angle Ψ is less than 5 degrees, Hirsch *et al.*[338] indicate the error in thickness is of the order of 5-10 percent; however, for Ψ equal to 15 degrees or greater the error can be typically of the order of 50 percent. For the specific slip trace shown in Chapter VII* the foil thickness was calculated to be 2440 Å, using the method outlined above.

Perhaps the most serious source of error in foil thickness determinations by the slip trace method is introduced by the tilt due to the

---

*See page 205.

buckling or curling of the foil. Even when the tilt of the goniometer stage is taken into account, the observer may be unaware of buckling in the foil and usually is unable to compensate for it. An error also can arise in the crystallographic orientation as determined by the spot diffraction pattern. Although a foil gives rise to a spot pattern characteristic of a particular (uvw) reciprocal lattice plane, the [uvw] crystal direction in the foil may not be accurately aligned in the direction of the electron beam. A spot pattern with strongly asymmetrical intensity distribution may correspond to a tilt of about 5 degrees from the (uvw) orientation.[338] In cases where Kikuchi lines are observed the orientation may be determined with greater accuracy. Moreover, errors may creep in as a result of inaccurate calibration of the image rotation and magnification in the microscope.

In all calculations of spot density in this work the foil thickness was taken to be 2500 Å. The thickness estimated from slip trace analysis was consistent with that predicted by thickness extinction contours in regions similar in transmission quality to the regions where spots were counted. Care was taken to make the spot counts on micrographs in regions of good transmission well away from the edge of the foil. The numerous possible sources of error and the fact that the slip trace analysis was not always possible in the same region as the spot count must be kept in mind in assessing the absolute values of the spot density cited in this work. However, the densities presented here are certainly as accurate as values quoted in the literature where no determination of foil thickness was attempted but rather a thickness was more or less arbitrarily assumed. Greater accuracy is expected for the relative

values of spot density as a function of size for a given distribution curve (see Chapters VI and VII), since these values depend primarily on the care with which the spot diameters were measured from a given micrograph.

Unirradiated foils were prepared and examined in a manner identical to that for the irradiated samples. As Figure 8 shows, no defect clusters are visible. The area shown in Figure 8 contains grown-in dislocations which are in contrast; this emphasizes that the diffraction conditions were such that spot damage would have been visible if it were present. Furthermore, as will be presented in Chapter VI the density of spots increases with increasing neutron dose. Therefore, it is concluded that the spots are indeed defect clusters that are the result of fast neutron bombardment. This is believed to be the first report of direct observation by TEM of defect clusters in irradiated niobium.[1]

III. DETERMINATION OF THE NATURE OF THE DEFECT CLUSTERS

When the defect clusters are examined under dynamical diffraction conditions, i.e., when the foil is oriented for Bragg diffraction, a fraction of the clusters exhibit black-white contrast (Ashby and Brown,[13] Rühle *et al.*[29]). This is shown for neutron-irradiated niobium in Figure 9. We applied the diffraction contrast theory of Rühle *et al.*[29] and Rühle[28] to determine the nature of the defect clusters from the behavior of the black-white contrasts with changing diffraction conditions. Only preliminary results will be presented here with a more complete determination to be given elsewhere.[339]

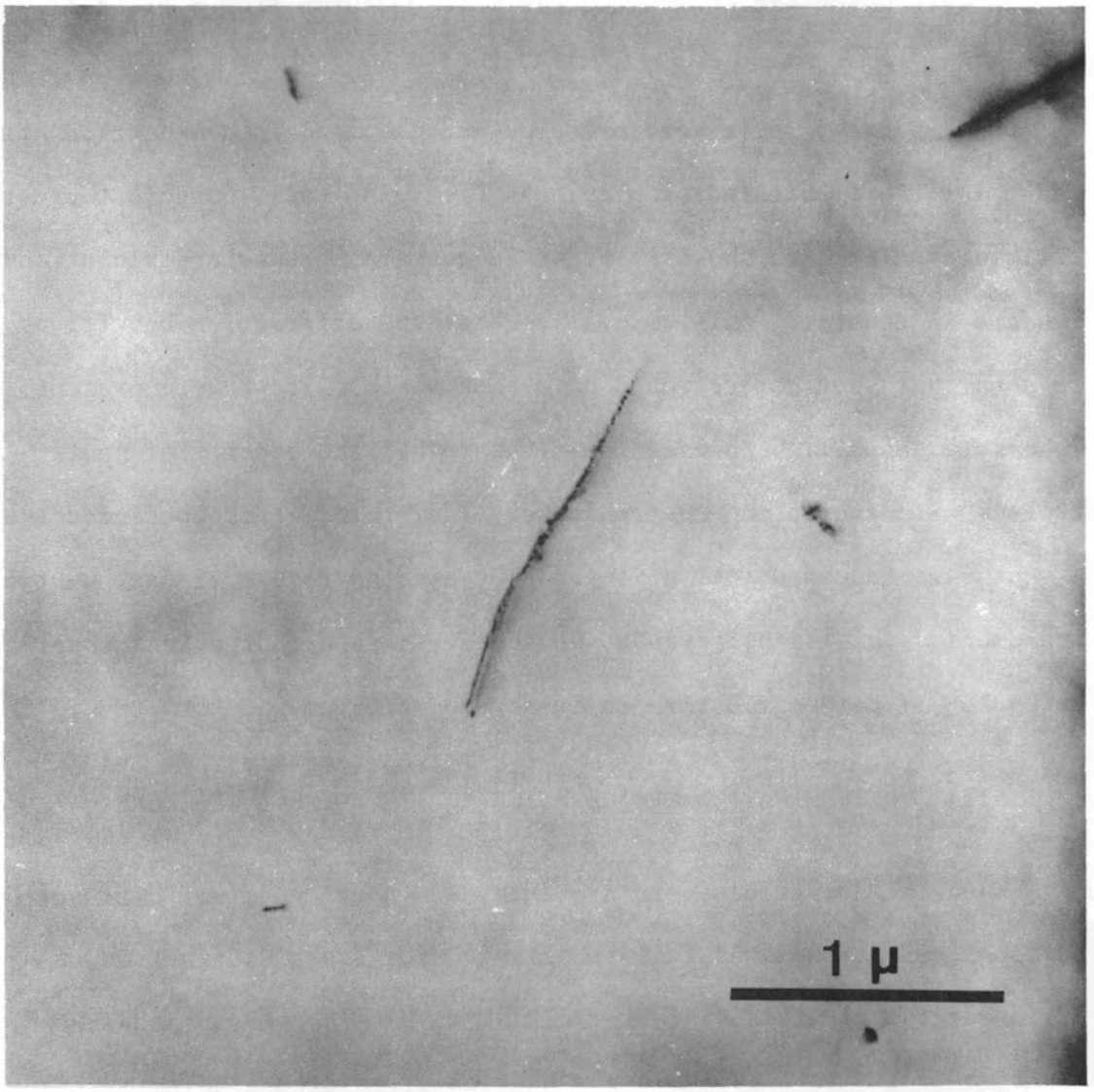

Figure 8. Transmission electron micrograph of unirradiated niobium showing the absence of black spots for diffraction conditions where grown-in dislocations are in contrast.

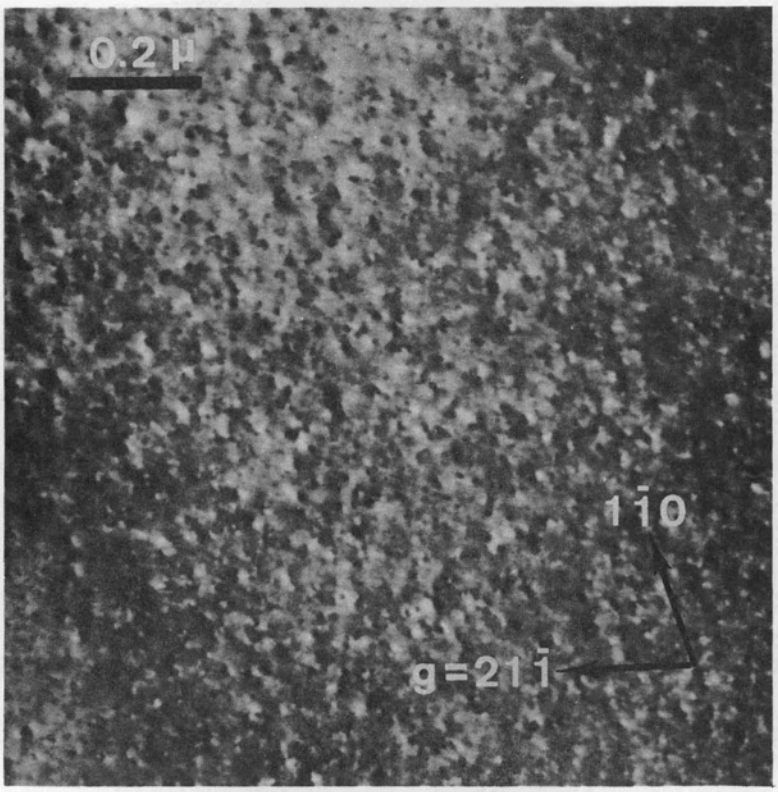

Figure 9. Black-white contrast images of neutron-irradiation-produced defect clusters in niobium shown under bright field, dynamical diffraction conditions ($s \approx 0$).

For spherically symmetrical defect clusters Phillips and Livingston[340] and Ashby and Brown[13] defined a "line of no contrast" which was observed to symmetrically separate the contrast into black and white lobes. They found the line of no contrast to lie perpendicular to the reciprocal lattice vector or equivalently the diffraction vector, $\vec{g}$, when only one strong reflection operated such as occurs under dynamical diffraction conditions. In cases where the defect cluster is not spherically symmetric, the line of demarcation between black and white lobes is not always straight or clearly delineated. Thus, Rühle *et al.*[29] chose to define a unit vector $\vec{l}$ directed from the black lobe to the white lobe of the contrast on positive prints. The vector $\vec{l}$, known as the "symmetry line," is thus parallel or antiparallel to $\vec{g}$ for spherically symmetric defect clusters.[28]

For the neutron-irradiated niobium it was generally found that the symmetry line, $\vec{l}$, of the black-white contrasts did not rotate when the foil was tilted so as to vary the diffraction vector. We take this as evidence that the defect clusters are not spherically symmetric and conclude that the majority of them are dislocation loops. For prismatic dislocation loops (Burgers vector perpendicular to plane of loop), $\vec{l}$ is perpendicular to the electron beam direction and in the plane determined by the beam direction and the Burgers vector. From the directions observed for the symmetry lines, the most probable Burgers vectors of the loops are (a/2)<110>, (a)<100>, and (a/2)<111>.

In addition, the theory and technique developed by Rühle and coworkers[28,29,54,62] permit the determination of the sign of the Burgers vector, i.e., whether the loops are vacancy or interstitial type. The

calculations of Rühle *et al.*[29] show that the sign of $(\vec{g} \cdot \vec{I})$ is opposite for loops of vacancy and interstitial type. Furthermore, the sign of $(\vec{g} \cdot \vec{I})$ exhibits an oscillation with the depth of the defect cluster in the foil, thereby separating the foil into layers near each surface. For dynamical diffraction conditions, only those defect clusters near the surfaces display black-white contrast, whereas the clusters deeper in the foil appear as black spots showing weaker contrast with depth. Then, adjacent to each surface of the foil there are three layers, L, at a depth d from the surface as follows:

$$\text{L 1:} \quad 0 \leq d \leq 0.3\xi_g' ,$$
$$\text{L 2:} \quad 0.4\xi_g' \leq d \leq 0.7\xi_g' ,$$
$$\text{L 3:} \quad 0.8\xi_g' \leq d \leq 1.2\xi_g' ,$$

where $\xi_g' = \xi_g/\sqrt{1 + w^2}$, ξ_g being the extinction distance for a given diffraction vector $\vec{g}$ and w being the normalized excitation error. The number of layers from which black-white contrasts are observed depends on the thickness of the foil, but usually the strongest contrasts are in the first two layers below each surface. The calculations show that loops of a given type lying near the beam-entrance surface exhibit a black-white contrast in bright field complementary to the contrast for loops near the exit surface. In dark field, however, the same contrast is observed near both surfaces for loops of the same type. The results of Rühle *et al.*[29] on the oscillation of black-white contrasts with depth are shown schematically in Figure 10 for a vacancy-type loop (specifically, a Frank sessile dislocation loop).

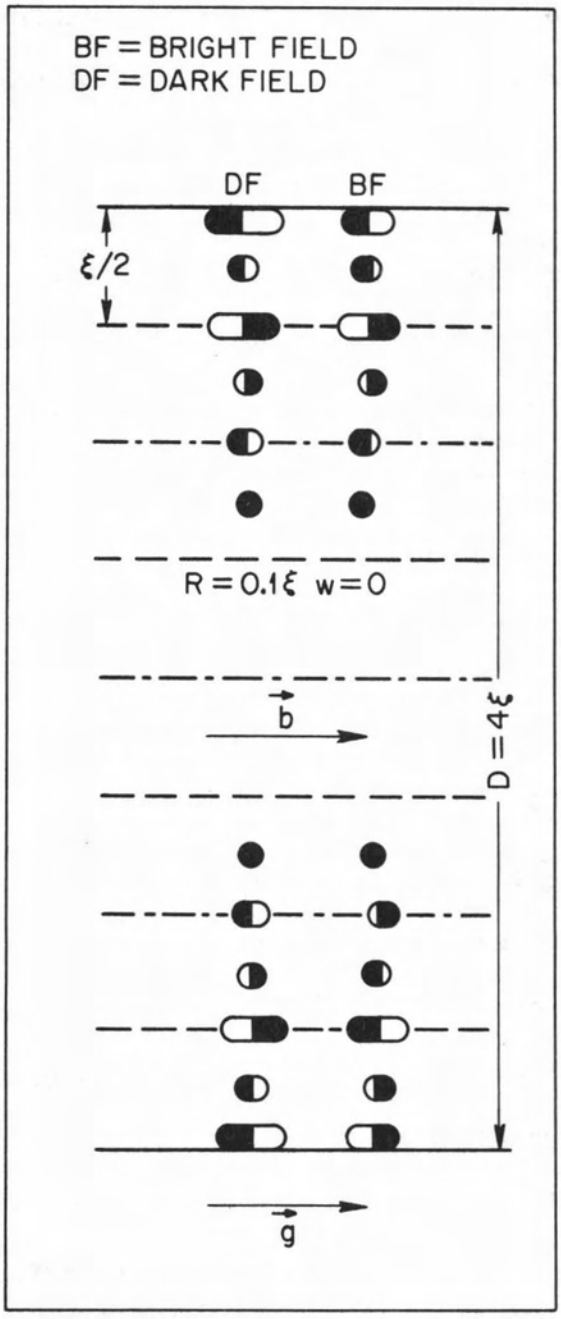

Figure 10. Schematic representation of the depth oscillation for calculated diffraction contrast from a Frank sessile dislocation loop of vacancy type and radius R (after Rühle *et al.*[29]).

Thus, in order to determine the loop type by applying the technique of Rühle *et al.*,[29] it is necessary to establish the loop depth in the foil to within one-quarter of an extinction distance, which in niobium corresponds to about 65 Å for the [110] reflection and about 114 Å for the [112] reflection.[341] Since at the time this preliminary study was made a stereo microscope for determining the depth of the loop in the foil was unavailable, we used a method mentioned by Rühle[28] that involved changing the extinction distance. The depth oscillation of the black-white contrast depends on the extinction distance, which in turn depends on the diffraction vector, $\vec{g}$, when w and the accelerating voltage for the electrons are constant. Consequently, we examined the same area of a sample in bright field under two diffraction vectors. In Figures 11a and 11b, micrographs using the $[\bar{1}10]$ and the $[\bar{1}2\bar{1}]$ reflections are shown; these reflections have extinction distances of 261 and 457 Å, respectively. The same area was observed in dark field by tilting the electron gun. The dark field micrograph of the area in Figure 11c was taken with $\vec{g} = [1\bar{1}0]$. Bell *et al.*[14] have pointed out that as a result of tilting the gun to achieve dark field conditions the sign of $\vec{g}$ is changed to the negative of what it is in bright field. Rühle *et al.*[29] have shown that a comparison of the black-white contrast of a given defect in bright and dark field micrographs establishes whether the defect lies near the upper or lower surface. This is true since defects of a given type lying near the two surfaces show complementary black-white contrast in bright field, but the same contrast behavior in dark field, i.e., the same sign of $(\vec{g} \cdot \vec{l})$ for bright and dark field, indicates the loop is near the upper surface, while opposite signs for $(\vec{g} \cdot \vec{l})$ in the two micrographs mean the loop is

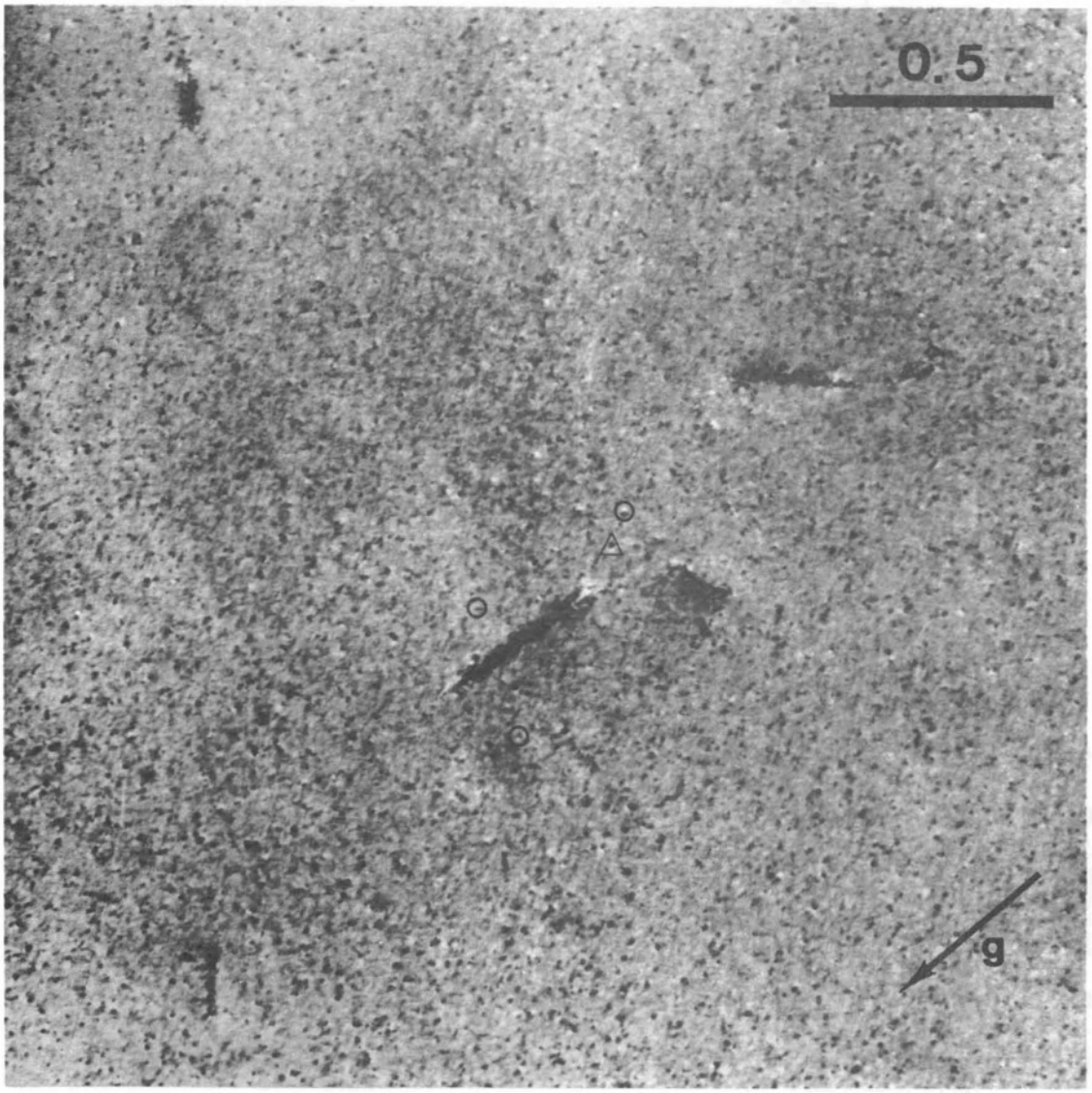

(a) Bright Field, $\vec{g} = [\bar{1}10]$.

Figure 11. Example of determination of nature of defect clusters from black-white contrast.

The same area of view is shown in each micrograph; O, interstitial loops and Δ, vacancy loops.

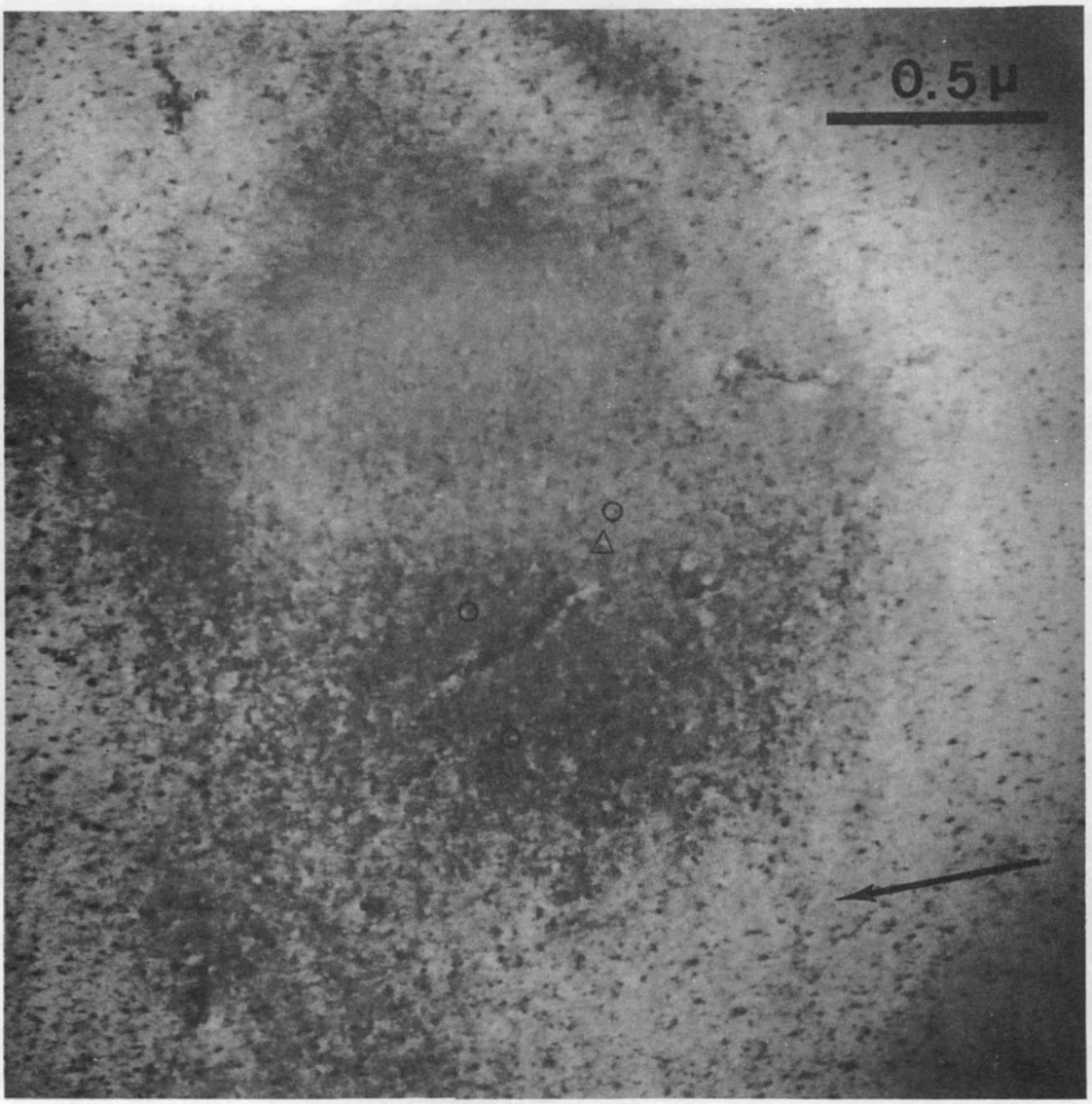

(b) Bright Field, $\vec{g} = [\bar{1}2\bar{1}]$.

Figure 11. (continued).

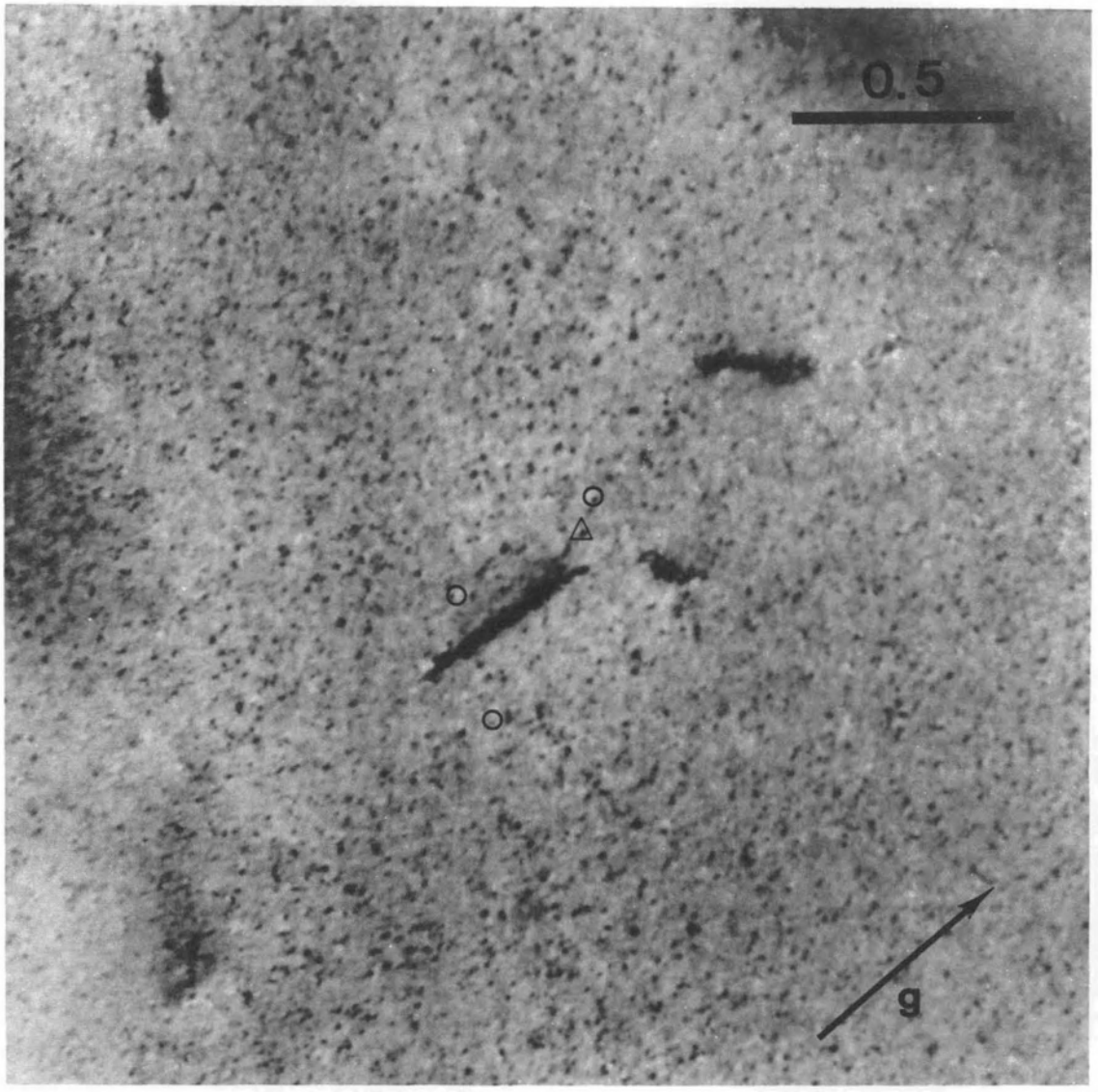

(c) Dark Field, $\vec{g} = [1\bar{1}0]$.

Figure 11. (continued).

near the lower surface. After deciding which surface the loop is near, a comparison of its black-white contrast in the $[\bar{1}10]$ and $[\bar{1}2\bar{1}]$ bright field micrographs, Figures 11a and 11b, respectively, permitted the loop type to be determined on the assumption that only defects in the two outer layers give rise to black-white contrast. This assumption seems justified in cases where the contrast is strong. Figure 12 shows schematically the sign of $(\vec{g} \cdot \vec{l})$ expected for vacancy and interstitial loops lying in the various layers for Figure 11. This method was used in an attempt to determine the nature of about 130 loops in Figure 11. Because the black-white contrast for a given loop was not clearly defined in all three micrographs, approximately one-third of the attempts were totally unsuccessful. Some uncertainty exists in approximately another one-third of the determinations because we cannot be sure that black-white contrasts were observed only from the two outer layers near each surface. For the clear cut determinations in Figure 11 and in other areas, interstitial-type loops seem to predominate, although vacancy loops are also found. The establishment of the answer to the question of loop type requires a more detailed study, perhaps using a stereo technique such as that of Diepers and Diehl.[105]

As an aside, it may be worthwhile to briefly mention two features that were observed but not investigated carefully. Figure 13 shows a dislocation in a foil from an as-irradiated sample. The dislocation near the center of the figure probably was present in the sample following the recrystallization anneal. There appears to be a high concentration of defect clusters along the dislocation as well as some depletion of clusters in the region below the dislocation, suggesting that it is a sink for the

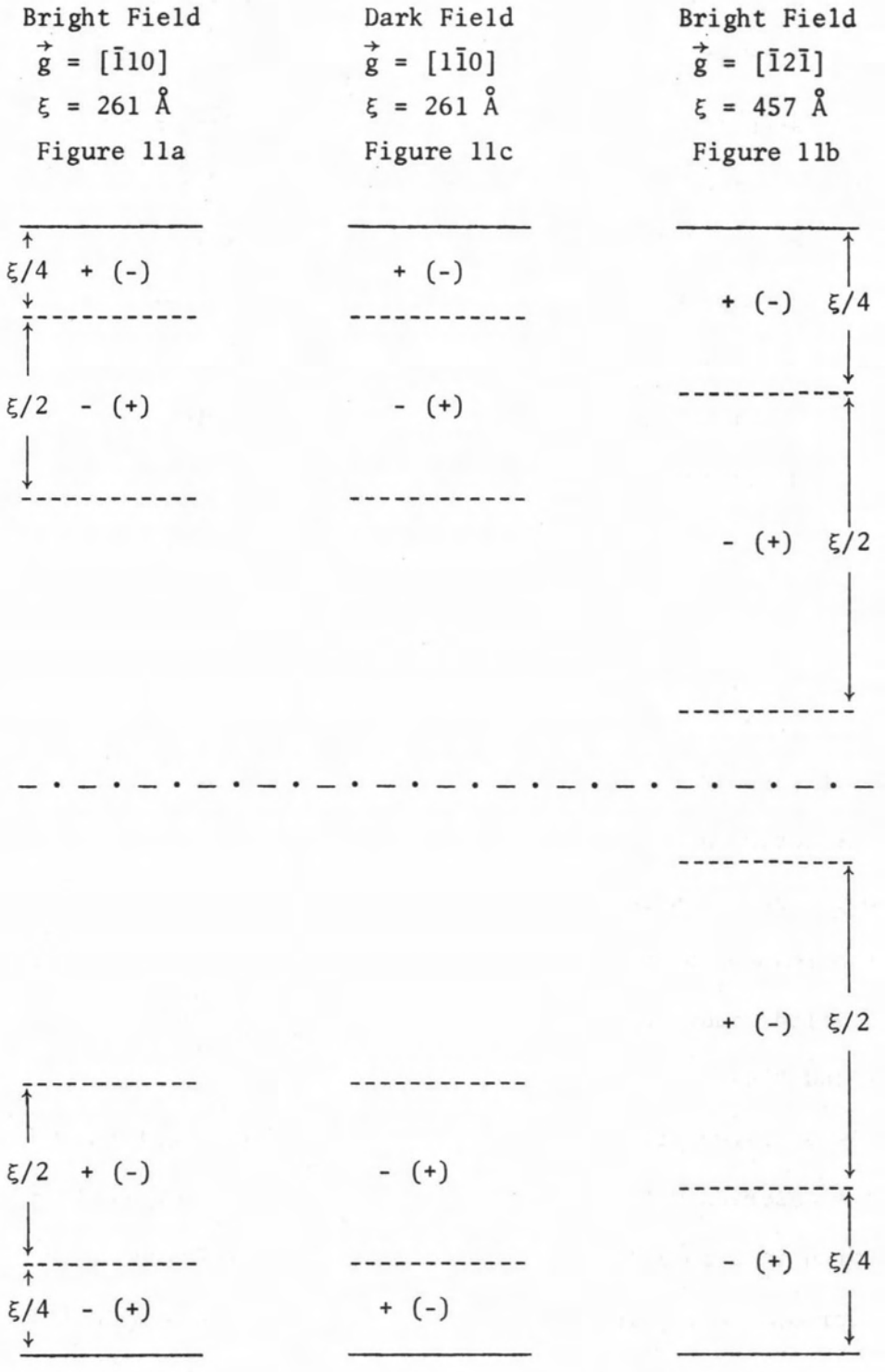

Figure 12. Predicted sign of ($\vec{g} \cdot \vec{I}$) for vacancy (interstitial) loops lying at various depths for the micrographs in Figure 11.

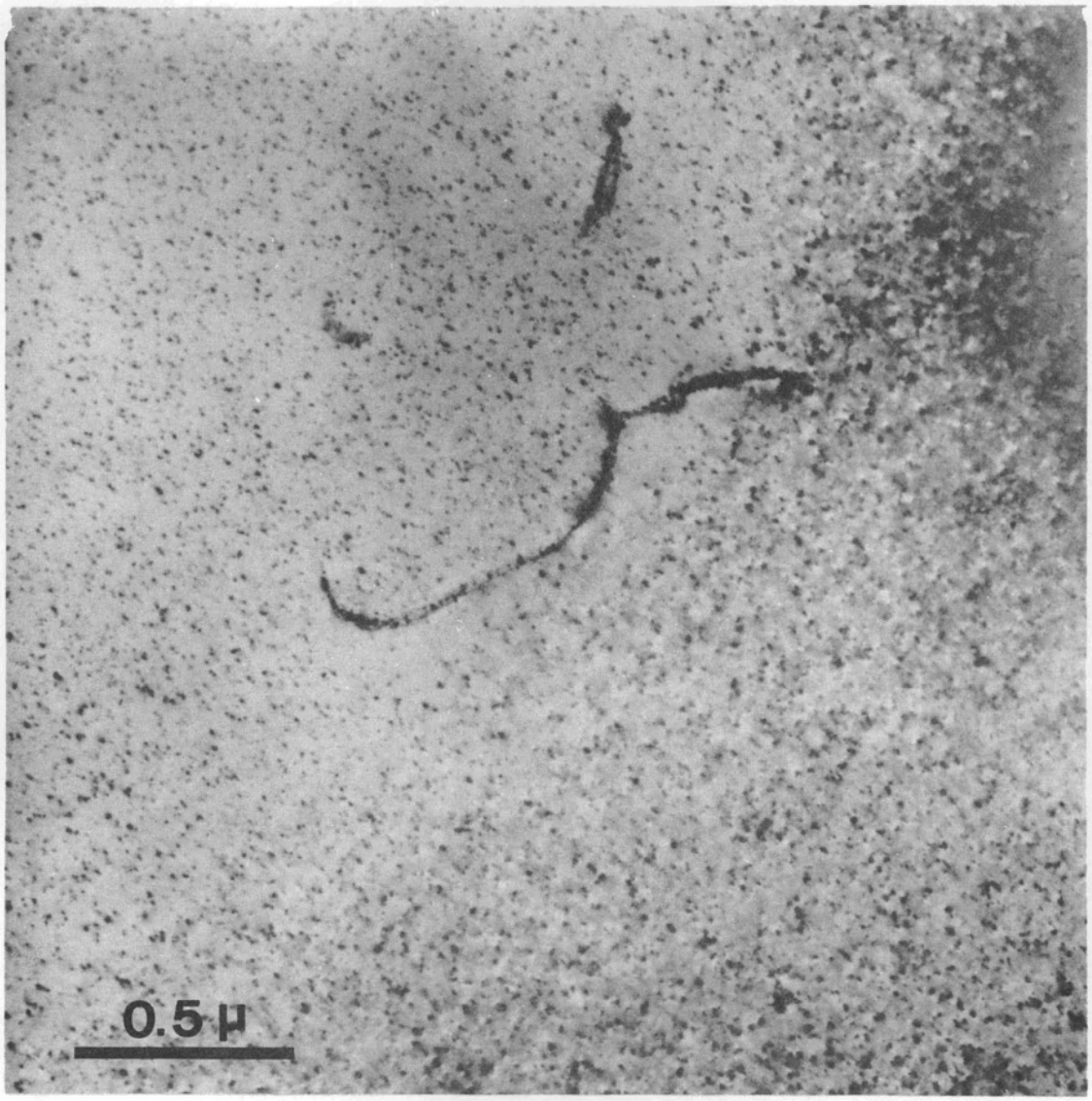

Figure 13. Depletion of radiation-produced defect clusters in region of grown-in dislocation.

clusters. Figure 14 demonstrates the rather regular dislocation structure observed in some grain boundaries.

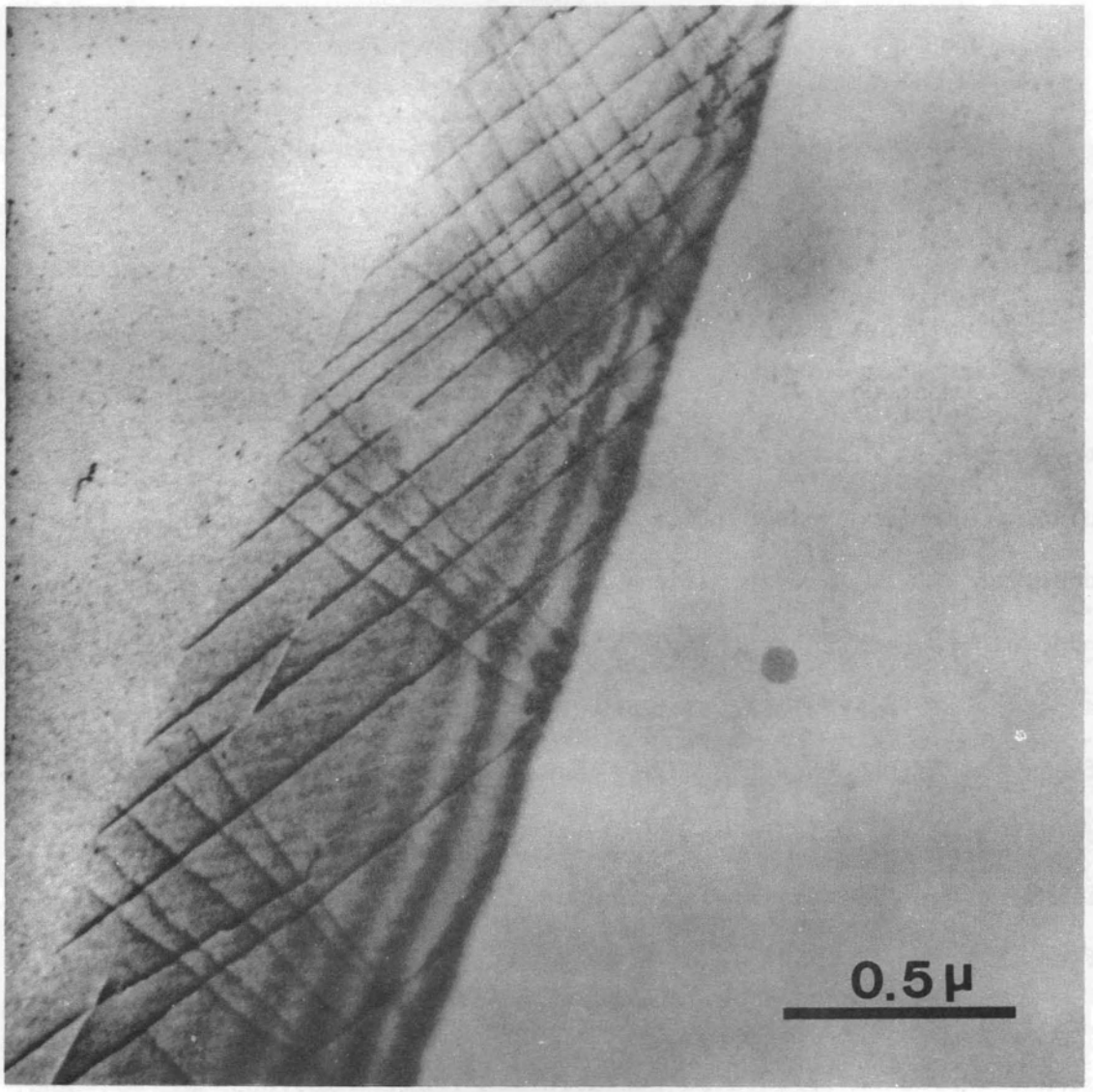

Figure 14. Dislocation array in grain boundary.

CHAPTER V

CRYSTAL GEOMETRY AND MECHANISM OF DISLOCATION CHANNELING

I. INTRODUCTION

Transmission electron microscopy (TEM) of neutron-irradiated samples after plastic deformation reveals pathways cleared of defect clusters in a matrix that retains its as-irradiated appearance. The cleared pathways generally coincide with traces of planes upon which slip is expected. It is, then, reasonable to consider the pathways to be cleared as a result of the motion of slip dislocations on the slip plane. The term "dislocation channel" describes the cleared pathway observed by TEM, and the term "dislocation channeling" describes the process by which the pathway or channel forms. The dislocation channel as observed in TEM foils is bounded by the surfaces of the foil and by the walls of the channel. The "channel plane" is one of a set of planes parallel to the wall of the channel, and the "channel trace direction" is along the line of intersection of the channel wall and the foil surface.

In body-centered cubic (bcc) metals, dislocation channels have been observed in irradiated-and-deformed iron,[78] molybdenum,[81,93] and, from the present study, niobium.[183] In the past, however, relatively little work has been reported on dislocation channeling in the bcc metals aside from the observation that it exists. The present study was conducted to investigate in greater detail the crystal geometry of channeling in neutron-irradiated niobium. Particular configurations of dislocation

channels were observed using several diffraction vectors, which permitted the Burgers vectors of prominent dislocations snagged along the walls of the channel to be deduced. The Burgers vector for these slip dislocations and the channel trace direction uniquely determined the channel plane. Some conclusions are drawn concerning the number of dislocations sweeping along the channel from observations of the offset of such markers as low-angle boundaries and dislocation helices when they are intersected by dislocation channels. Finally, some discussion is given of the mechanism of dislocation channeling.

II. CHARACTERISTICS AND CRYSTAL GEOMETRY OF DISLOCATION CHANNELING

In this section we present a series of transmission electron micrographs illustrating various features of dislocation channeling in irradiated-and-plastically-deformed CIBA-A niobium polycrystalline sheet samples. Unless stated otherwise, the TEM foils were taken from a sample irradiated to 4.4×10^{18} neutrons/cm^2 ($E > 1$ Mev) and subsequently strained 6.6 percent (to the lower yield stress) in tension at room temperature at a crosshead speed of 0.01 cm/minute (nominal strain rate of 1.3×10^{-4} sec^{-1}). The stress-strain curve for the sample showed a well-defined, sharp yield drop of 3.81 kg/mm^2. The upper and lower yield stresses were 14.16 kg/mm^2 and 10.35 kg/mm^2, respectively. The curve was generally smooth in appearance with only the slightest evidence of "jerky flow." Table VIII lists the principal features illustrated in each case discussed in this section and in Appendix A.

TABLE VIII

SUMMARY OF FEATURES ILLUSTRATED IN CASES OF DISLOCATION CHANNELING

Case Number	Special Features
1	a. Regular channel array composed of two sets of channels, one set perpendicular to foil surface and one set inclined. b. Dislocations snagged primarily on only one side of channels. c. Tangles at channel intersections. d. Dislocation array in channel. e. Splitting-off of channels due to cross slip. f. Channel not perpendicular to foil surface. g. Edge-screw character analyzed. h. $\vec{g} \cdot \vec{b}$ criterion applied. i. Some tangle dislocations identified.
2	a. Regular channel array. b. Paired dislocation channels. c. Channel-channel offset. d. Channels in early stage. e. Tangles at channel intersections.
3	a. Dislocation helix with depleted zone. b. Channel-boundary offset. c. Channel-helix offset.
4	a. Channel-boundary offset. b. Channel created at channel-boundary intersection. c. Channel extending across boundary. d. Depleted zone near boundary.
5	a. Dislocation cell structure within channel. b. Dislocations not rigidly confined to channel.
A-1*	a. Triangular pattern of channels. b. $\vec{g} \cdot \vec{b}$ criterion applied. c. Channel-channel offset. d. Conclude {110} type channel planes.
A-2*	a. Triangular pattern of channels. b. $\vec{g} \cdot \vec{b}$ criterion applied. c. No channel-channel offset. d. Stereo technique applied. e. Conclude {110} type channel planes.

TABLE VIII (continued)

Case Number	Special Features
A-3*	a. Dislocation tangle. b. Helix in channel. c. Channels not perpendicular to foil surface. d. $\vec{g} \cdot \vec{b}$ criterion applied. e. Some tangle dislocations identified.
A-4*	a. Boundary composed of regular array of parallel dislocations. b. Channel crossing boundary.

*Cases discussed in Appendix A.

Case 1 (Figures 15 and 16)

The transmission electron micrograph in Figure 15 shows a typical configuration of dislocation channels cleared of radiation-produced defects, which are believed to be predominately interstitial in nature. The two sets of intersecting channels (labeled with 1's and 2's) are fairly regularly spaced. The plane of the micrograph is (111) and the operating reflection is $[\bar{1}01]$. As shown in the figure, the approximate trace directions for Channels 1 and 2 are $[\bar{1}\bar{1}2]$ and $[\bar{1}01]$, respectively. It is interesting that the dislocations in Channels 2 appear to be associated preferentially with one wall of the channel. We note also that Channels 1 are generally straight and of uniform width over rather long distances (see especially, Channel 1b).

The defect density near the channel walls is the same as it is well within the matrix. An increased defect density would be expected if channeling dislocations repelled defect loops, causing them to move to the channel wall, say by prismatic slip. On the other hand, if many errant channeling dislocations penetrated the channel walls (say by cross slipping from the channel into the matrix), they would presumably annihilate defect clusters, lowering the density of clusters near the channel wall. Since the density of clusters changes abruptly at the channel wall, neither of these processes is likely to be important. For Channels 2, there is some suggestion of variation in defect density near the channel wall. This can, however, be accounted for on the basis of the wedge-shaped matrix region formed because the walls of Channels 2 are inclined, as demonstrated below.

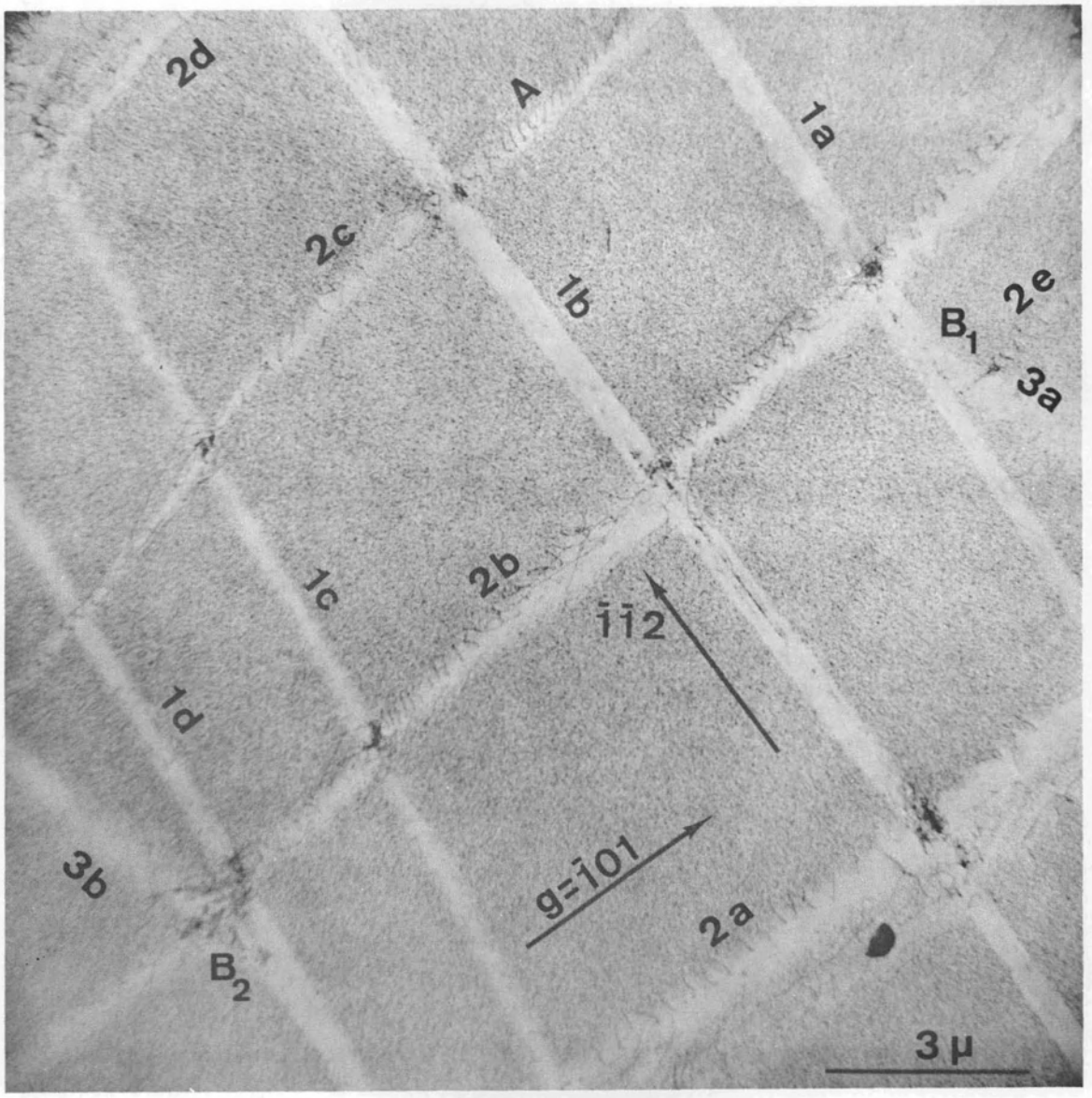

Figure 15. Nearly rectangular pattern of dislocation channels in neutron-irradiated niobium (Case 1).

Note veering off of Channels 3a and 3b at B_1 and B_2.

A characteristic feature at channel intersections is dislocation tangling. It shows clearly that dislocation tangling is a consequence of intersections of two distinct slip dislocations. Another feature at channel intersections is the splitting and veering off of a new channel. This is seen in Figure 15 at B_1 and B_2, where the new Channels 3a and 3b are formed, possibly as a result of the cross slipping of channel dislocations when they encounter the stress field of the tangled dislocations. Another possibility is that the tangle itself acts as a dislocation source, which spins out dislocations along the cross slip plane (see Case A-1, Appendix A).

A field of view adjacent to the right-hand edge of Figure 15 is shown under reflections $[01\bar{1}]$ and $[\bar{1}10]$ in Figures 16a and 16b, respectively. This area is of particular interest, for in it is displayed an array of channeling dislocations which have been retained in the channel. The number designation of channels in this (111)-foil and the channel-trace directions as determined from the electron diffraction pattern are shown in Figure 16a. The channel traces 2e and 3a are along $[\bar{1}10]$ and $[01\bar{1}]$, respectively, and traces 1 and 4 along $[11\bar{2}]$ and $[2\bar{1}\bar{1}]$, respectively.

We shall consider the contrast of the dislocations for various operating reflections, two of which are shown in Figures 16a and 16b. In bcc metals, the <111> close-packed direction is the normal slip direction and hence the Burgers vector direction for slip dislocations. Diffraction contrast theory predicts[342] that $\vec{g} \cdot \vec{b} = 0$ means invisibility or weak contrast for dislocations, where $\vec{g}$ is the diffraction vector and $\vec{b}$ is the Burgers vector. In Tables IX and X the contrast for dislocations

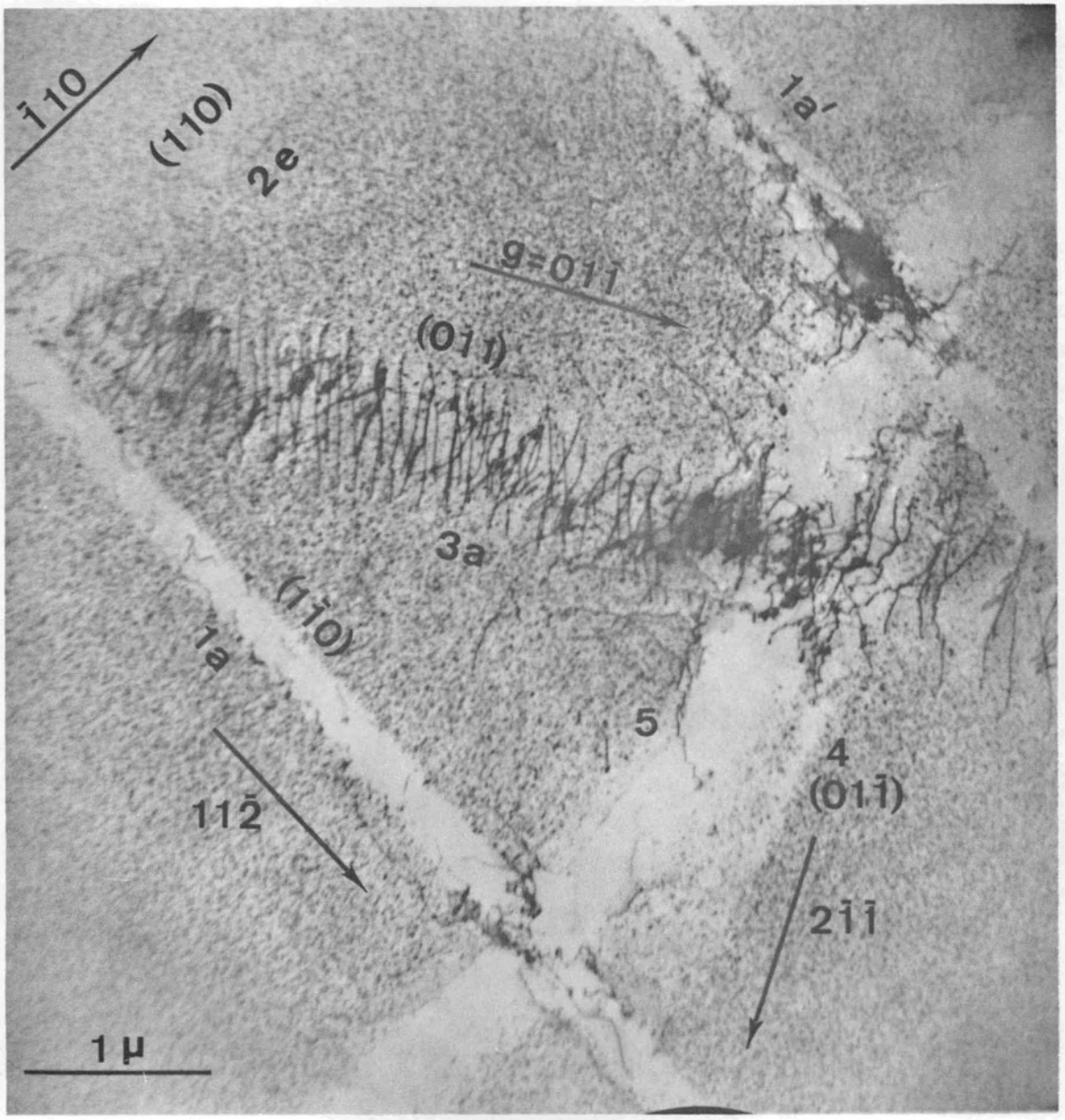

(a) Visible with $\vec{g} = [01\bar{1}]$.

Figure 16. Dislocation array within channel (Case 1).

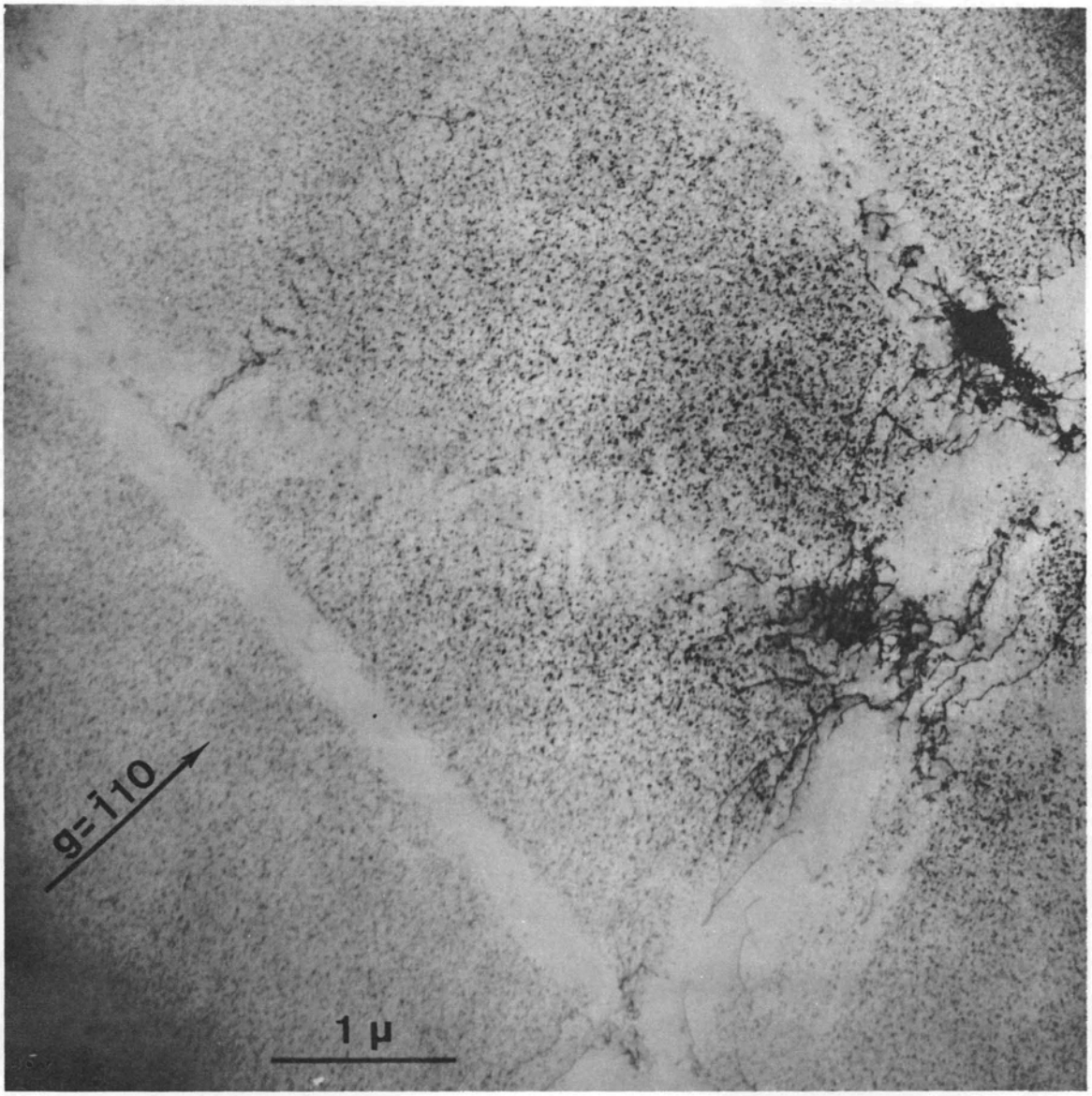

(b) Invisible with $\vec{g} = [\bar{1}10]$.

Figure 16. (continued).

TABLE IX

CONTRAST FOR DISLOCATIONS IN CASE 1

Channel Number	Contrast for Dislocations Parallel to Channel		
	$\vec{g} = [01\bar{1}]$ Fig. 16a	$\vec{g} = [\bar{1}10]$ Fig. 16b	$\vec{g} = [1\bar{2}1]$ Not Shown
1a,1b	S	W	S
2e	W	S	S
3a	S	W	S
4,5	W	S	S

S = Strong contrast, i.e., the dislocation is visible ($\vec{g} \cdot \vec{b} \neq 0$).

W = Weak contrast, i.e., the dislocation is invisible ($\vec{g} \cdot \vec{b} = 0$).

TABLE X

VALUES OF $\vec{g} \cdot \vec{b}$ FOR DISLOCATIONS IN CASE 1

$\vec{b}$	$\vec{g} \cdot \vec{b}$		
	$\vec{g} = [01\bar{1}]$	$\vec{g} = [\bar{1}10]$	$\vec{g} = [1\bar{2}1]$
(a/2)[111]	0	0	0
(a/2)[$\bar{1}$11]	0	1	-1
(a/2)[1$\bar{1}$1]	-1	-1	2
(a/2)[11$\bar{1}$]	1	0	-1

under three operating reflections is compared to $\vec{g} \cdot \vec{b}$ for <111> Burgers vectors. From these tables we conclude that the Burgers vectors for dislocations lying in the channels are as shown in Table XI. Since the Burgers vector for a slip dislocation must lie in the channel plane, the Burgers vector and the channel trace direction uniquely determine the channel plane. The channel planes thus determined are tabulated in Table XI.

It should be noted, as indicated in Table X, that the [111] dislocations are always invisible for reflections from the planes of the [111] zone. However, since the tensile axis lies in (111) to within a few degrees, [111] dislocations are expected to be subjected to little or no shear stress and thus to be of relatively little importance in the deformation under consideration.

It is interesting to note from Table XI that dislocations channeling along Channels 1 and 3a have the same Burgers vector, $(a/2)[11\bar{1}]$. Thus, dislocations moving in Channel 1a can transfer to Channel 3a by cross slipping from $(1\bar{1}0)$ to (011). The fact that no tangle is observed at the intersection of Channels 1a and 3a (Figure 16b) would lend support to this idea. Note, however, tangling is observed at the intersections of Channel 3a with Channels 2e and 5, for which the channeling dislocations have Burgers vectors different from those in Channel 3a. If the dislocations observed in Channel 3a were pure screw with an $(a/2)[11\bar{1}]$ Burgers vector, then their projection on the (111) plane would lie in the $[11\bar{2}]$ direction. If they were pure edge, then their projection would lie in the $[\bar{1}10]$ direction. The projection of the dislocations in Channel 3a actually makes an angle of about 45 degrees with the $[11\bar{2}]$ direction.

TABLE XI

CRYSTAL GEOMETRY OF CHANNELS IN CASE 1

Channel Number	Channeled Plane	$\vec{b}$ for Channeling Dislocations	Channel Trace Direction	Angle Between [111] and Plane Normal
1a,1b	$(1\bar{1}0)$	$(a/2)[11\bar{1}]$	$[11\bar{2}]$	90°
2e	(110)	$(a/2)[\bar{1}11]$	$[\bar{1}10]$	35° 16'
3a	(011)	$(a/2)[11\bar{1}]$	$[01\bar{1}]$	35° 16'
4	$(01\bar{1})$	$(a/2)[\bar{1}11]$	$[2\bar{1}\bar{1}]$	90°

Thus, the dislocations appear to lie almost exactly halfway between the pure edge and pure screw orientation. However, the edge character may have been introduced during thinning. There is some suggestion that many of the dislocations seen in Channel 3a are paired, with the two dislocations comprising the pair lying in opposite walls of the channel. These paired dislocations appear to have approximately the same length but are displaced with respect to one another. This is the type of displacement expected for the projection of dislocation lines lying on opposite walls of a channel, such as Channel 3a, inclined to the foil surface.

In general, the tangles observed at the intersections of channels are rather complex three-dimensional dislocation arrays. However, as regards the tangle at the intersection of Channels 3a and 5, comparison of Figure 16a and Figure 16b indicates that $[11\bar{1}]$ dislocations, which are the channeling dislocations for Channel 3a, comprise part of the tangle.

Examination of a number of other cases under several diffraction vectors in a manner similar to Case 1 has provided supporting evidence that the channel planes are for the most part {110}, although a few cases of {112} channel planes were observed. An equilateral-triangular configuration of channels was observed rather frequently. An analysis of such configurations by diffraction contrast and by stereo techniques, described in Appendix A, showed in these cases that the channel planes were the three {110} planes intersecting (111) at right angles.

Case 2 (Figure 17)

Figure 17 shows a cross grid composed primarily of two sets of channel traces, denoted by A's and V's. The plane of the micrographs

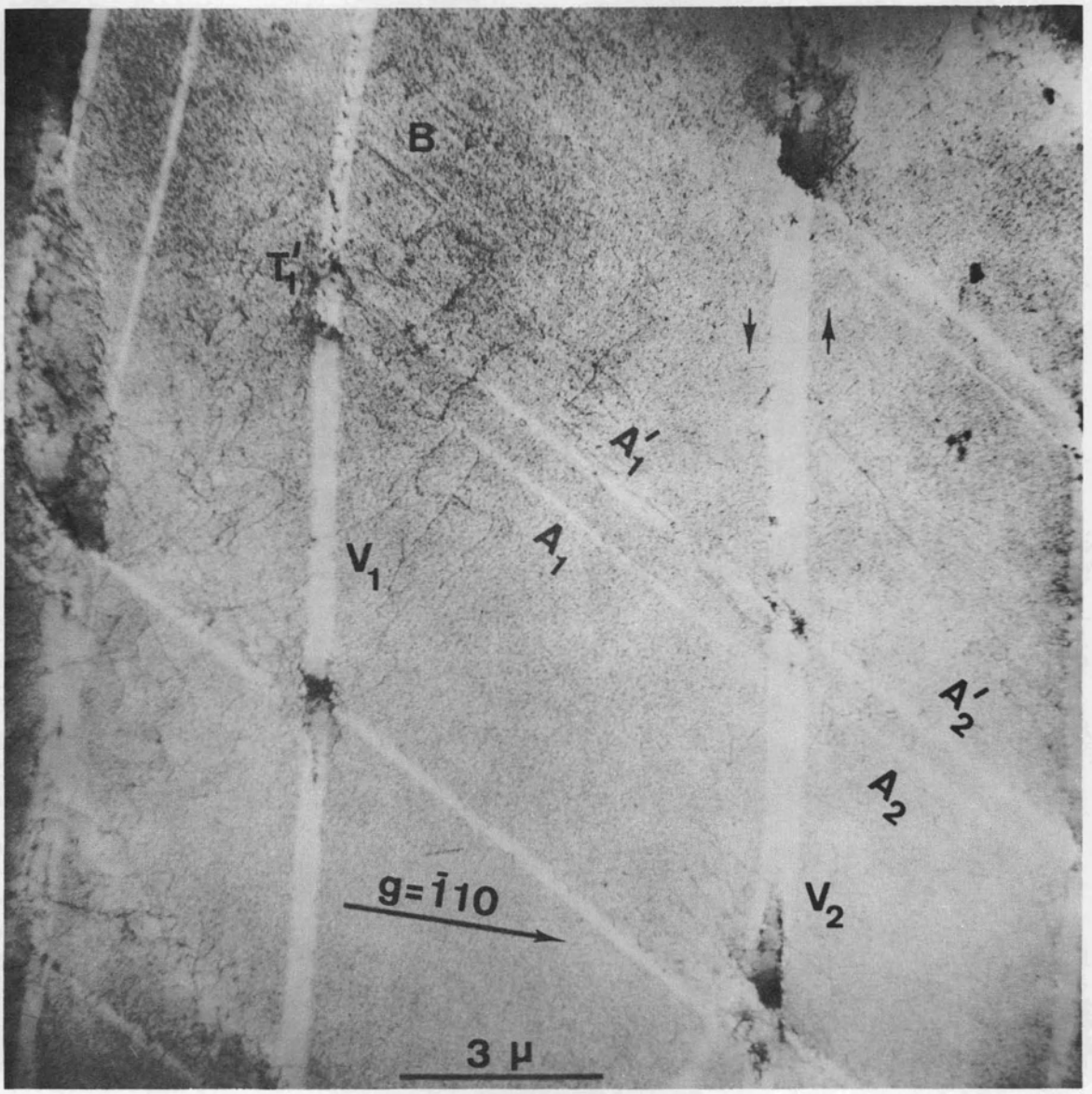

(a) Left Field of View.

Figure 17. Cross grid of dislocation channels showing dislocation tangles at intersections and channel-channel offset (Case 2).

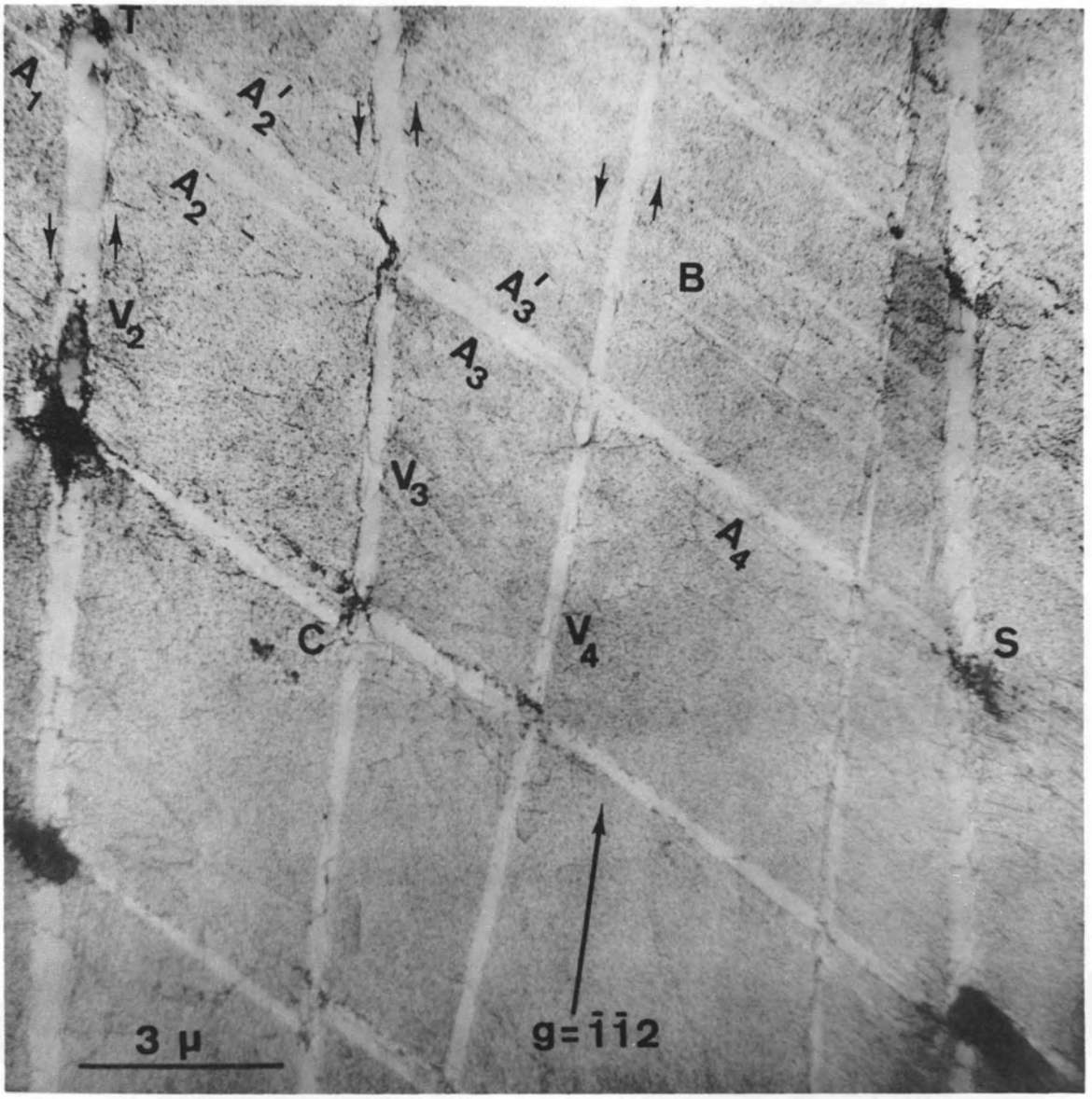

(b) Right Field of View.

Figure 17. (continued).

is again (111) and the operating reflections are $[\bar{1}10]$ and $[\bar{1}\bar{1}2]$ in Figures 17a and 17b, respectively. The channels which lie diagonally in the micrographs, e.g., A and A', are most likely $(\bar{1}01)$ planes channeled by $[1\bar{1}1]$ dislocations, based on the observed trace direction, $[1\bar{2}1]$. The indices of the generally vertical channels (Channels V) are less certain because of their lack of parallelism and changes of direction. The {110} plane that has a trace nearest the direction of these channels is $(\bar{1}10)$.

We have mentioned previously that dislocation tangling and channel splitting occur at channel intersections. A third feature often observed is channel offset, as seen in Figure 17 where the vertical and diagonal channels intersect. A clear example is located at C in Figure 17b, where the diagonal segment to the right of the vertical Channel V_3 is displaced upward with respect to the segment to the left (also see Case A-1, Appendix A).

Another interesting feature is the pair of Channels A and A', whose entire length was observed in the two micrographs of Figure 17. Tangles are again seen at the ends of the channels and at most intersections along their lengths. The upper channel segments, A_1', A_2', and A_3', are essentially straight and in line while the lower channel segments, A_1, A_2, A_3, and A_4, are offset from one another at intersections with V channels. It seems reasonable to postulate the following sequence of events. Initially, a diagonal channel extended from S to T_1', possibly due to the operation of a source at S. Then, the Channels V_2, V_3, and V_4 operated, causing the shear displacements indicated by the short arrows in Figure 17. This caused the channel previously extending from S to T_1' to consist of the

offset segments A_4, A_3, A_2, and A_1. Finally, the source at S operated again, which produced the in-line channel segments A_3', A_2', and A_1'.

Most of the channels seen in the micrographs appear to be fully formed like channels A and V. However, at B in Figure 17, we do see several ill-formed narrow channels which are along the trace direction $[1\bar{2}1]$ for $(\bar{1}01)$ planes.

Case 3 (Figure 18)

A striking feature observed in another (111)-foil is the dislocation helix shown in Figure 18. Aside from the fact that helices are rather infrequently observed in high-purity metals, its occurrence here is of particular interest since the offset produced where a channel crosses it provides a measure of the number of dislocations moving along the channel. The channel is observed to cross a boundary at the upper right in Figure 18a.

The helical character of the feature in Figure 18a is seen more clearly at A' in the higher magnification micrograph in Figure 18b. Discrete, closed prismatic loops exist at A with the same axis as the helix. The helical feature lies along $[01\bar{1}]$, and lower magnification micrographs indicate that it extends over a distance of at least 9.5 microns. Its axis is generally straight, but does exhibit some twisting as seen at B, Figure 18a. Notice, also, that the spot damage is depleted on either side of this array. The spacing between turns and loops is essentially uniform over the length of the feature and is about 280 Å. The radii of the helix and loops are approximately 350 to 450 Å.

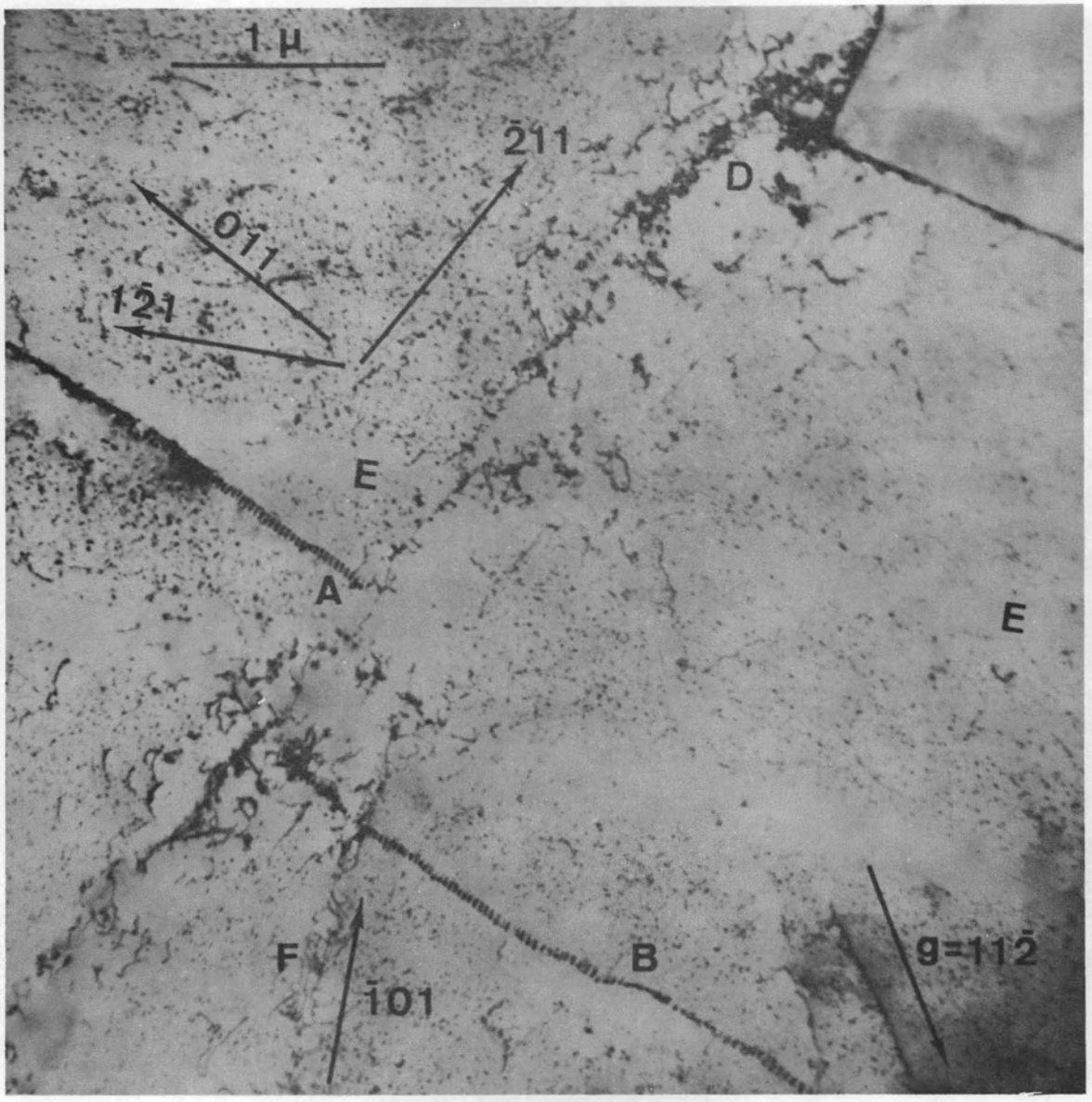

(a) Low Magnification View.

Figure 18. Channel-dislocation helix offset (Case 3).

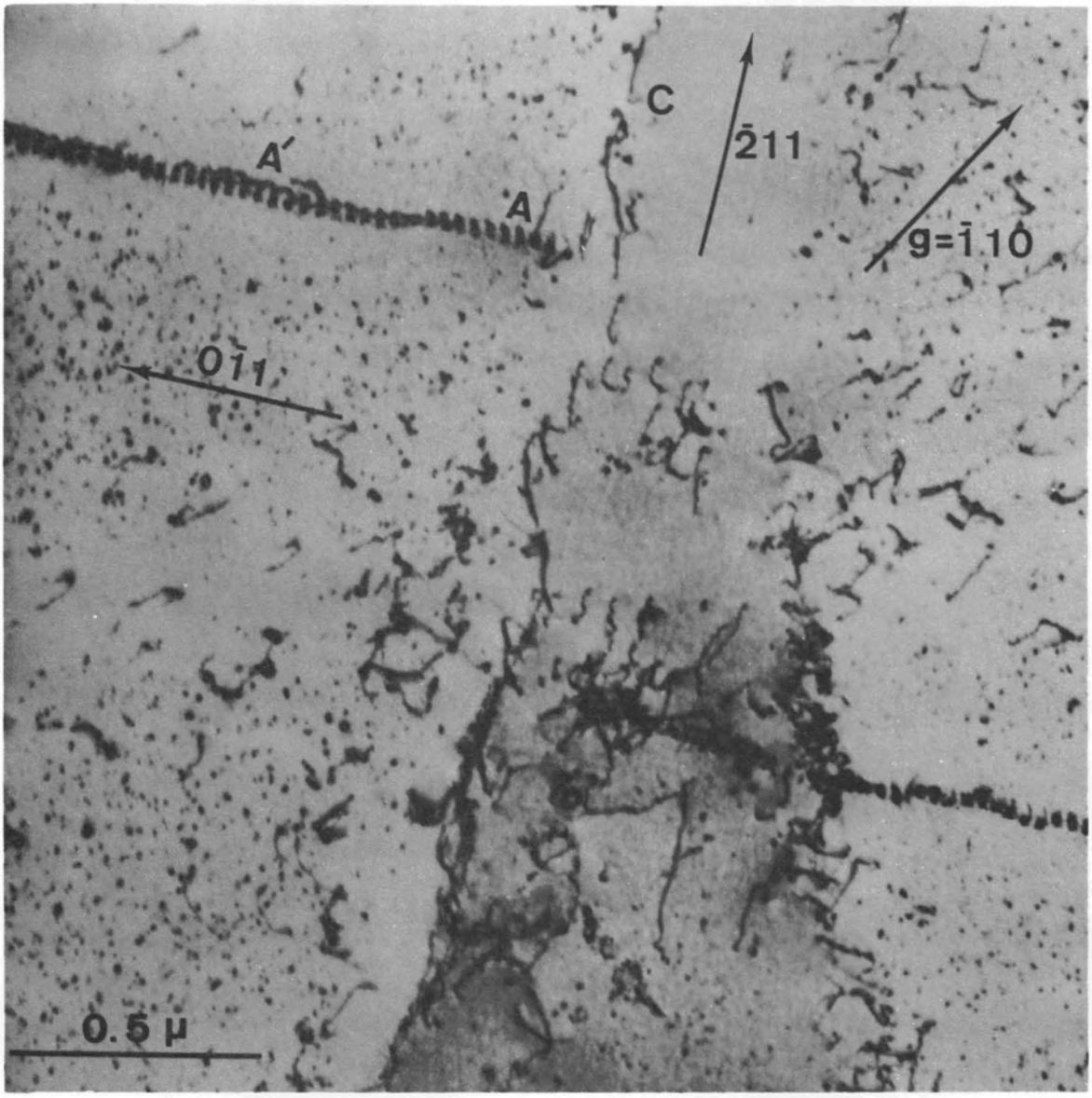

(b) High Magnification View.

Figure 18. (continued).

Helical dislocations are generally considered (e.g., by Mitchell[343]) to form from screw dislocations by climb processes, with the axis of the helix in the direction of the Burgers vector of the screw. If this be true, the long length of the helix in Figure 18 along $[01\bar{1}]$ suggests that it originated from a grown-in $[01\bar{1}]$ screw dislocation.

The trace of the channel that caused the offset in the helix is along $[\bar{2}11]$, and thus the channel plane is probably $(01\bar{1})$. The offset of the helix in the $[\bar{2}11]$ direction is 9500 Å. Dislocations with (a/2) $[\bar{1}11]$ Burgers vectors moving in $(01\bar{1})$ are believed to produce the observed offset. The magnitude of the component of an (a/2)$[\bar{1}11]$ Burgers vector in the $[\bar{2}11]$ direction is 2.70 Å. Therefore, the number of dislocations required to give the observed offset of the helix is about 3500. From Figure 18, the channel width is 4500 Å. Since the spacing between {110} planes is 2.33 Å, approximately 1900 $(01\bar{1})$ planes are needed to account for the channel width. The ratio of the number of dislocations to the number of planes within the channel is 1.8.

In Figure 18a, two channels cross the helical feature at angles not perpendicular to its axis. The channel marked E lies along $[1\bar{2}1]$ and is perpendicular to $[\bar{1}01]$. In this case, the channeled plane is most likely $(\bar{1}01)$, with (a/2)$[1\bar{1}1]$ the Burgers vector for the channeling dislocations. The trace of Channel F is in the $[\bar{1}01]$ direction with (101) as the most likely channel plane. The angle between the normal to the (101) plane and the [111] direction is 35° 16'. Considerable dislocation structure is observed in Channel F. Very little, if any, offset is to be seen where these channels cross the helix.

Case 4 (Figure 19)

In contrast to previous cases, the plane of the micrograph in Figure 19 is (112). The electron diffraction patterns taken from either side of the offset feature indicate that it is a low-angle boundary. The offset in the boundary lies at the intersection of the boundary with Channel G. Although not clearly apparent in Figure 19, the trace of Channel G continues in the same direction to the left of the boundary, as seen in other micrographs. As an aside, Channel K is another channel that apparently originated at the offset due to stress concentrations there. From the trace geometry and the contrast analysis, the slip vector and the slip plane of Channel G are deduced as $(a/2)[\bar{1}11]$ and $(0\bar{1}1)$, respectively.

The magnitude of the offset in the boundary in Figure 19 provides the basis for a calculation of the number of channeling dislocations operating in Channel G. The offset displacement on the micrograph corresponds to 12,100 Å, and the magnitude of the component of the Burgers vector $(a/2)[\bar{1}11]$ in (112), along $[\bar{4}21]$, is 2.52 Å. Therefore, about 4800 dislocations are required to produce the offset. The width of the trace of Channel G is 4000 Å, which is provided by a stack of about 1600 $(0\bar{1}1)$ planes intersecting (112). Thus, on the average, about three $[\bar{1}11]$ dislocations have been channeled down each $(0\bar{1}1)$ plane. The magnitude of the channeling shear due to Channel G in Figure 19 is also seen by the displacement of the channel trace at H to its position at H'. It is apparent that Channel H-H' must have formed before Channel G.

The almost horizontal offset segment of the boundary in Figure 19 is remarkably straight, which suggests that the channeling dislocations

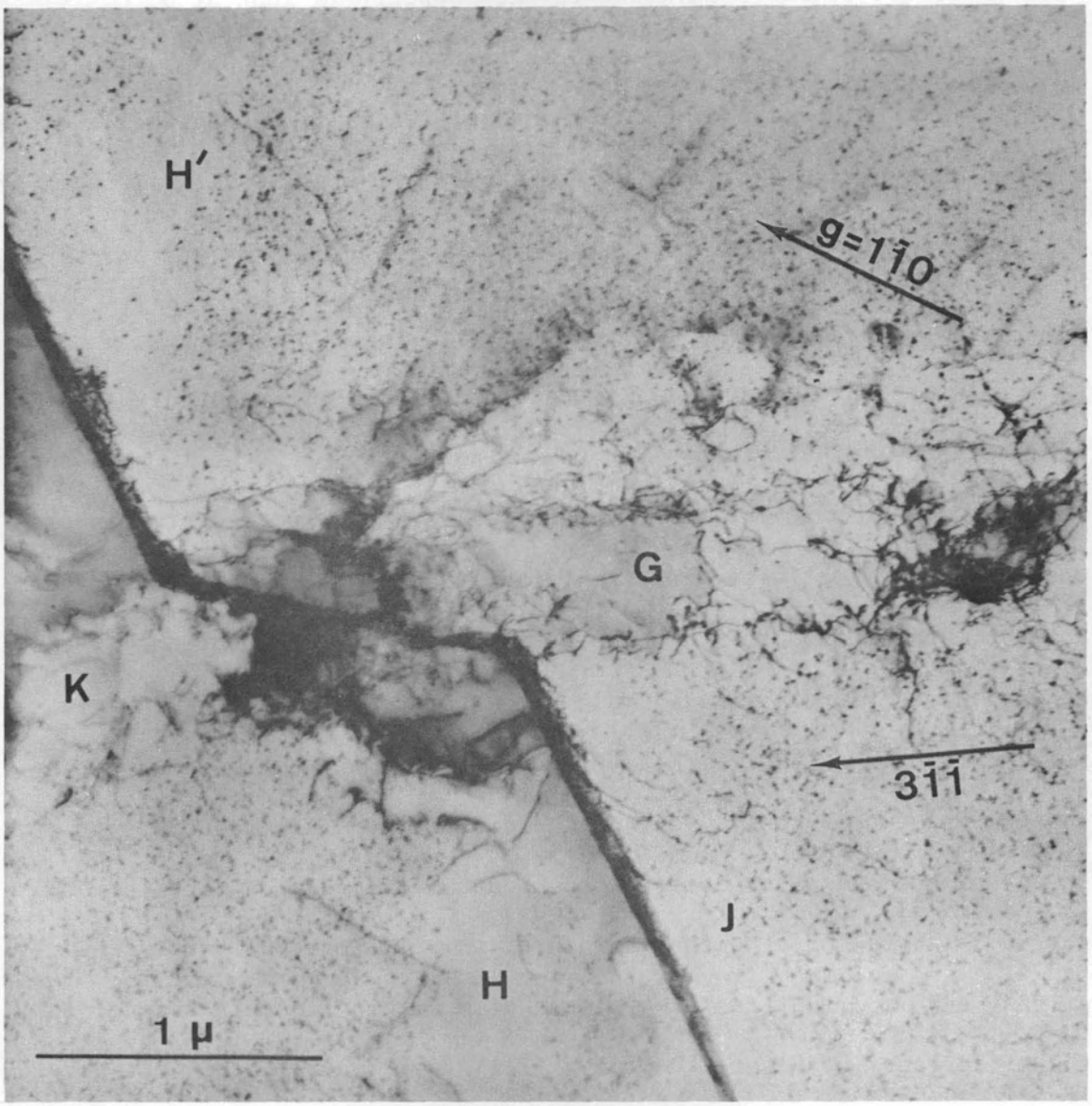

Figure 19. Large channel-boundary offset in a (112) foil (Case 4).

were distributed uniformly across Channel G. It is interesting, also, that the boundary is lengthened in the region of the offset. The depletion of defect clusters adjacent to the boundary is seen at J.

The offset feature was seen in numerous micrographs. Three types of offsets were observed: channel-channel (Case 1), channel-helix (Case 3), and channel-low angle boundary (Case 4) offsets. Table XII summarizes the analysis of the geometry of various cases of channel offset.

Case 5 (Figure 20)*

In Case 5, attention is focused on a sample irradiated to 1.8 x 10^{18} neutrons/cm^2 and then strained in tension 2.7 percent in an identical manner to the sample for the preceding cases. As expected, the lower dose resulted in a lower density of radiation-produced defect clusters. In fact, were it not for the high concentration of dislocations at the channel edges the relatively small number of defect clusters in the matrix would make it difficult to clearly determine the bounds of the channel in some regions. Many of the dislocations are rather "joggy" in appearance and a few deformation-produced dislocation loops are observed. In view of a nominal strain of only 2.7 percent a rather surprising and important feature is seen at M within the main channel in the micrographs of Figure 20 from a (111) foil, namely, the well-developed cell structure. The fact that a cell structure is observed after such a relatively low nominal strain emphasizes the concentration of strain within the channel. As previously pointed out from slip line observations,

---

*Speculation on the crystal geometry and on the Burgers vectors of the dislocations in Figure 20 is presented in Appendix B.

TABLE XII

ANALYSIS OF OFFSETS AT CHANNEL INTERSECTIONS

Type Offset	Channel Plane	Channel Width (Å)	No. Planes per Channel Width	Offset Magnitude[c] (Å)	Offset Direction[c]	$\vec{b}$ for Channeling Dislocations	No. Dislocations per Offset	Ratio[d]
Channel-Channel[a]	$(\bar{1}10)$	2500-3330	1070-1430	3330	$[11\bar{2}]$	$(a/2)\ [11\bar{1}]$	1230	0.9-1.2
Channel-Channel[a]	$(\bar{1}01)$	3300	1290	3000	$[1\bar{2}1]$	$(a/2)\ [1\bar{1}1]$	1110	0.9
Channel-Helix[a]	$(01\bar{1})$	4500	1930	9500	$[\bar{2}11]$	$(a/2)\ [\bar{1}11]$	3520	1.8
Channel-Boundary[a]	$(01\bar{1})$	4500	1930	6710	$[\bar{2}11]$	$(a/2)\ [\bar{1}11]$	2490	1.3
Channel-Boundary[b]	$(01\bar{1})$	3960	1600	12,100	$[\bar{4}21]$	$(a/2)\ [\bar{1}11]$	4790	3.0
Channel-Boundary[a]	$(\bar{1}10)$	5550	2380	5940	$[11\bar{2}]$	$(a/2)\ [11\bar{1}]$	2200	0.9

[a]Plane of view: (111).

[b]Plane of view: (112).

[c]As observed in plane of view.

[d]Ratio = number of dislocations per offset divided by the number of planes per channel width.

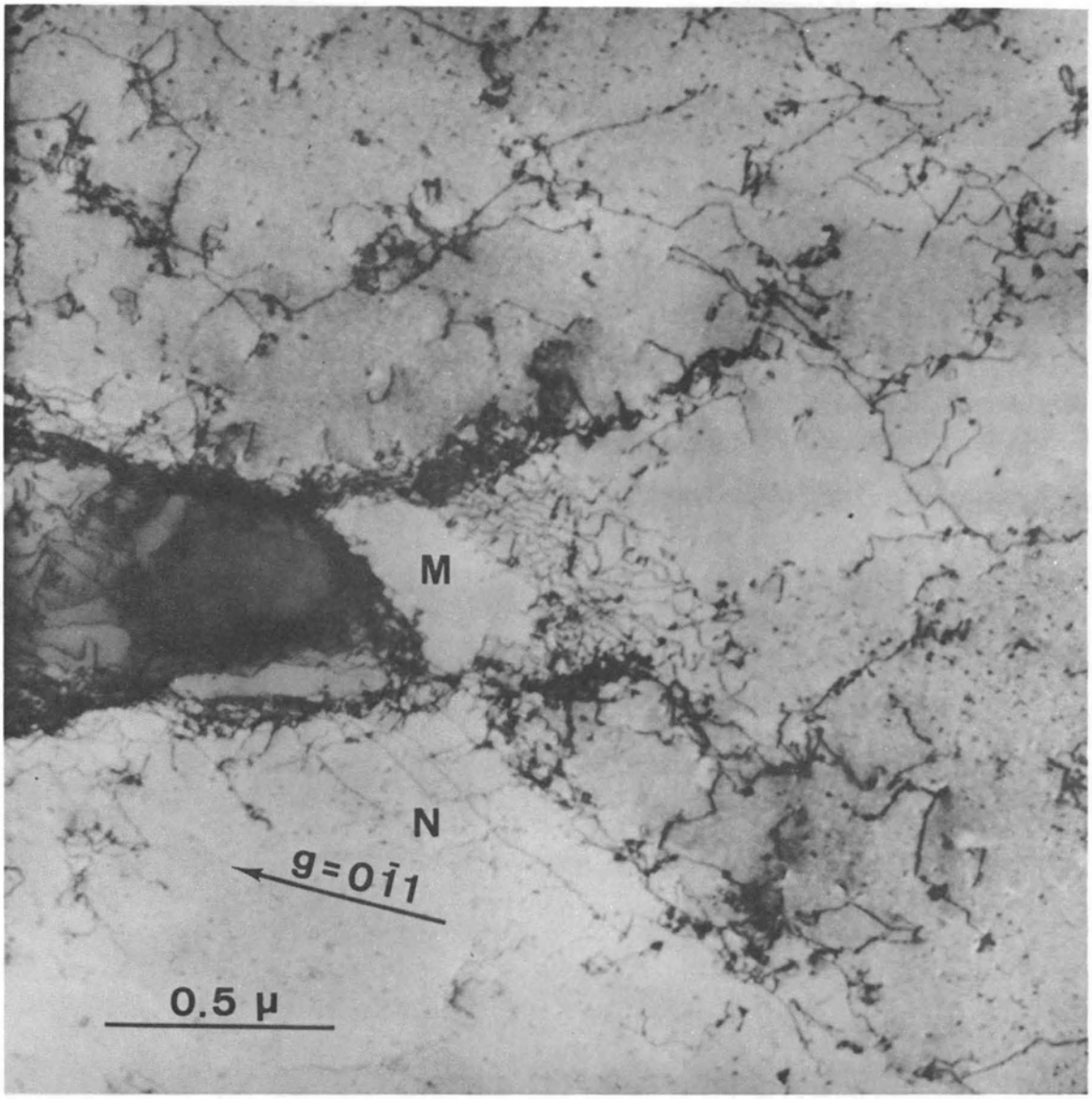

(a) $\vec{g} = [0\bar{1}1]$.

Figure 20. Dislocation cell structure within channel observed after 2.7 percent nominal tensile strain (Case 5).

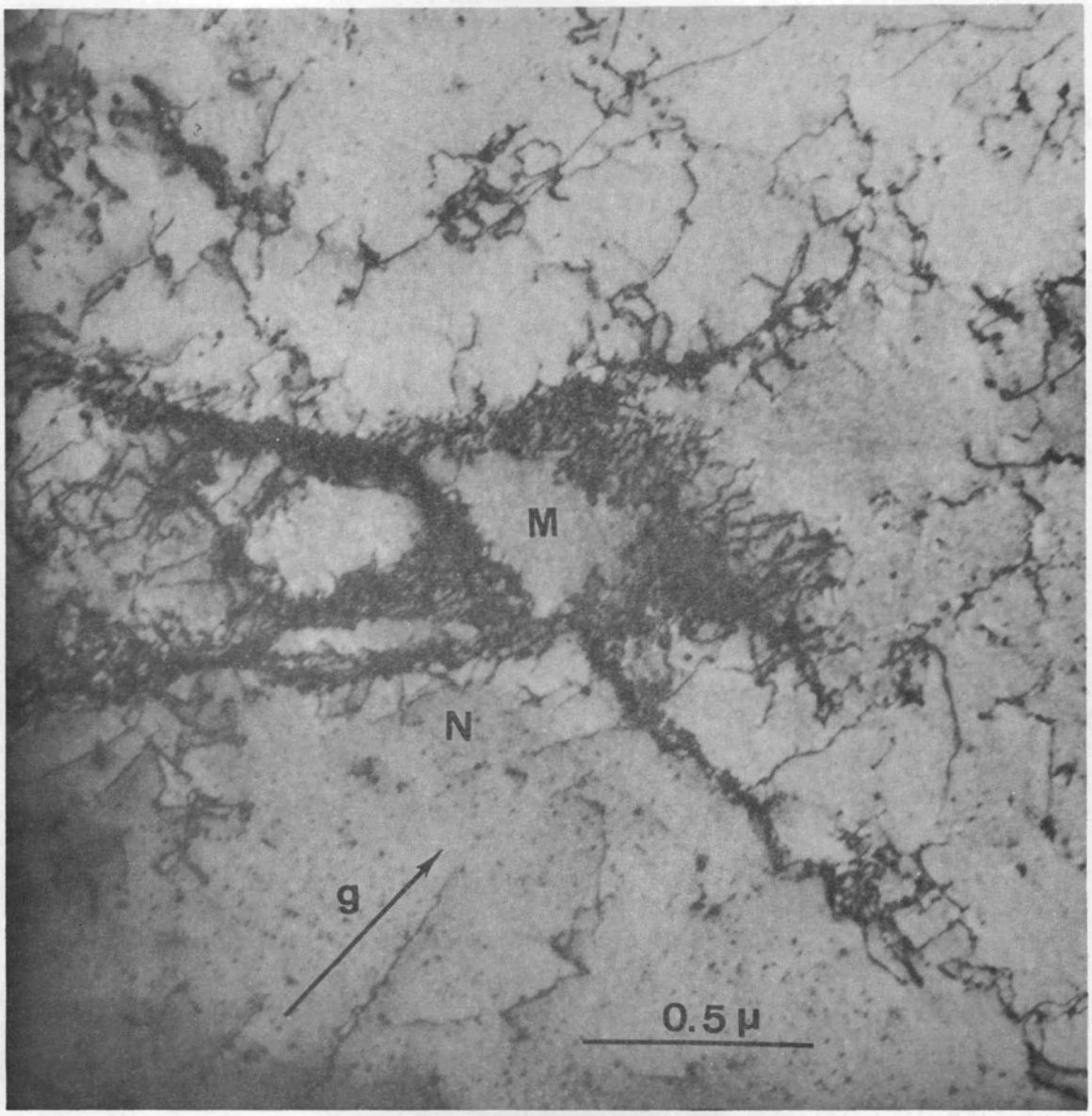

(b) $\vec{g} = [\bar{1}10]$.

Figure 20. (continued).

the inhomogeneous nature of the deformation must be taken into account when analyzing stress-strain curves from irradiated samples.

In Figure 20, the cell walls generally lie along crystallographic directions of importance in the crystal slip geometry. The dark tangle lying across the main channel to the left of M is in the $[11\bar{2}]$ direction, and the cell walls joining this tangle on the right are aligned with the channel trace direction, $[\bar{1}2\bar{1}]$. On the other hand, to the left of the dark tangle the uppermost cell wall is in the $[0\bar{1}1]$ direction. A comparison in Figure 20a and 20b of the wall across the channel to the right of M reveals that when viewed under the $[0\bar{1}1]$ and $[\bar{1}10]$ reflections, respectively, entirely different sets of more or less parallel "joggy" dislocations are brought into contrast. These sets of dislocations appear to be interlaced into a network as they form a cell wall. This high concentration of dislocations in the cell walls is in marked contrast to the cell interior (e.g., at M) which is almost entirely free of dislocations. As suggested in the micrographs in Figure 20 and seen more clearly in other micrographs not shown, a second channel intersects the main channel near M and extends toward the lower right.

A point of interest is the appreciable amount of dislocation structure outside the well-defined channel, indicating that at lower doses slip dislocations are less rigidly confined to channels. Thus, we suggest that there is a critical dose and in turn a critical density of defects required to cause deformation by the channeling mode. At lower doses the deformation, though hindered by radiation-produced defect clusters, is rather homogeneous. So long as the deformation is more or less homogeneous, the stress to move a dislocation is proportional to

the planar density of defect clusters. Following a transition region where the deformation can neither be classified as homogeneous nor strictly heterogeneous, the deformation enters the heterogeneous mode, i.e., channeling (see, for example, Cases 1-4) where all the slip dislocations no longer encounter the density of defects characteristic of the dose, since pathways free of defect clusters are available. In Chapter VI, we apply these ideas to the interpretation of the dose dependence of the yield stress.

III. DISCUSSION OF THE CHARACTERISTICS AND MECHANISM OF DISLOCATION CHANNELING

The observation of an offset where microstructural features are crossed by dislocation channels is quite significant, because it provides a measure of the direction and the magnitude of the shear displacements produced by the channeling dislocations. We conclude from Table XII that, on the average, 1-3 dislocations move along the channel per atomic plane within the channel. This agrees with Sharp's estimates of 2-3 dislocations per plane for neutron-irradiated copper.[59] Sharp estimated this quantity by dividing the shear displacement as observed from surface slip markings by the channel width observed by transmission electron microscopy. Since our determination is based on the shear displacement and channel width *for the same channel*, the contention that surface slip lines correspond to dislocation channels is strengthened.

An important aspect of dislocation channeling is the concentration of strain within the channels. This is consistent with the coarsening of slip lines seen on polished surfaces of irradiated metals. For niobium,

this has been illustrated previously.[239,344] The magnitude of the shear strain within the channels may be estimated from the offset magnitudes and channel widths (Table XII, page 131); the shear strains vary from about 1 to 3. Despite the great inhomogeneity of strain in the irradiated material as a whole, the strain within the channel appears to be distributed uniformly. This is seen quite clearly in Figure 19, page 129, since the offset segment of the low-angle boundary is straight. This, again, is a conclusion, based on surface replicas, reached by Sharp.[59] The uniformity of shear within the channel is consistent with the observation that there generally appear to be no defect clusters within the cleared channel when the channel plane is perpendicular to the plane of view. If, on the average, two dislocations per plane are considered to sweep down the channel, it is not necessary to assume that each plane receives two dislocations. Macroscopic uniformity of slip within the channel would also be achieved if packets of, say, 20 dislocations were to sweep down single planes spaced about 10 planes apart. But for complete annihilation of the damage clusters within the channel, the spacing between the dislocation packets should not exceed the diameter of the clusters, which typically corresponds to about 35 planes.[240]

The mechanism most often discussed[59,170,184,185,345,346] whereby the defect clusters are removed by the slip dislocations is the *sweeping-up or chopping-up* of the defect clusters. Regarding the defect cluster as a prismatic loop, we may make use of contact interactions between prismatic loops and slip dislocations discussed by Saada and Washburn[184] and Kroupa and Hirsch.[186] When the Burgers vectors of the prismatic loop and the slip dislocation are the same, a portion of the loop becomes

incorporated into the slip dislocation as the slip dislocation cuts through the loop. A smaller loop is then left behind. Repetition of this process could reduce the loop to the point where it becomes unstable and disappears. However, when the Burgers vectors of the prismatic loop and slip dislocation are not the same, the loop cannot be incorporated into the slip dislocation, and hence the chopping mechanism becomes inoperative. We have mentioned above that the concentration of defect clusters observed immediately adjacent to the channel appears to be the same as in the defect-clustered matrix. Therefore, in the cutting or sweeping process it is necessary that the clusters be somehow incorporated into the slip dislocations and not simply swept aside.

A second mechanism is the *annihilation by anti-defects* of defect clusters as a result of the motion of slip dislocations. Since the damage clusters in as-irradiated niobium are thought to be primarily interstitial in character, the anti-defects must be vacancies. Vacancies may be associated with dislocation motion in two ways. Vacancies may be created by the nonconservative motion of jogs on the slip dislocation, or radiation-produced vacancies may be dragged to the interstitial clusters by slip dislocations. The latter possibility derives some support from the appearance of small defect spots in the transmission electron micrographs of niobium post-irradiation-annealed at 600°C, as is mentioned below. In another experiment, we have annealed at 600°C a niobium sample that was previously irradiated and then deformed to produce dislocation channels. Upon examination in the electron microscope, the small vacancy clusters or spots were present in the matrix but absent in the dislocation channels as shown in Figure 21. Sharp[59] has also commented on the absence

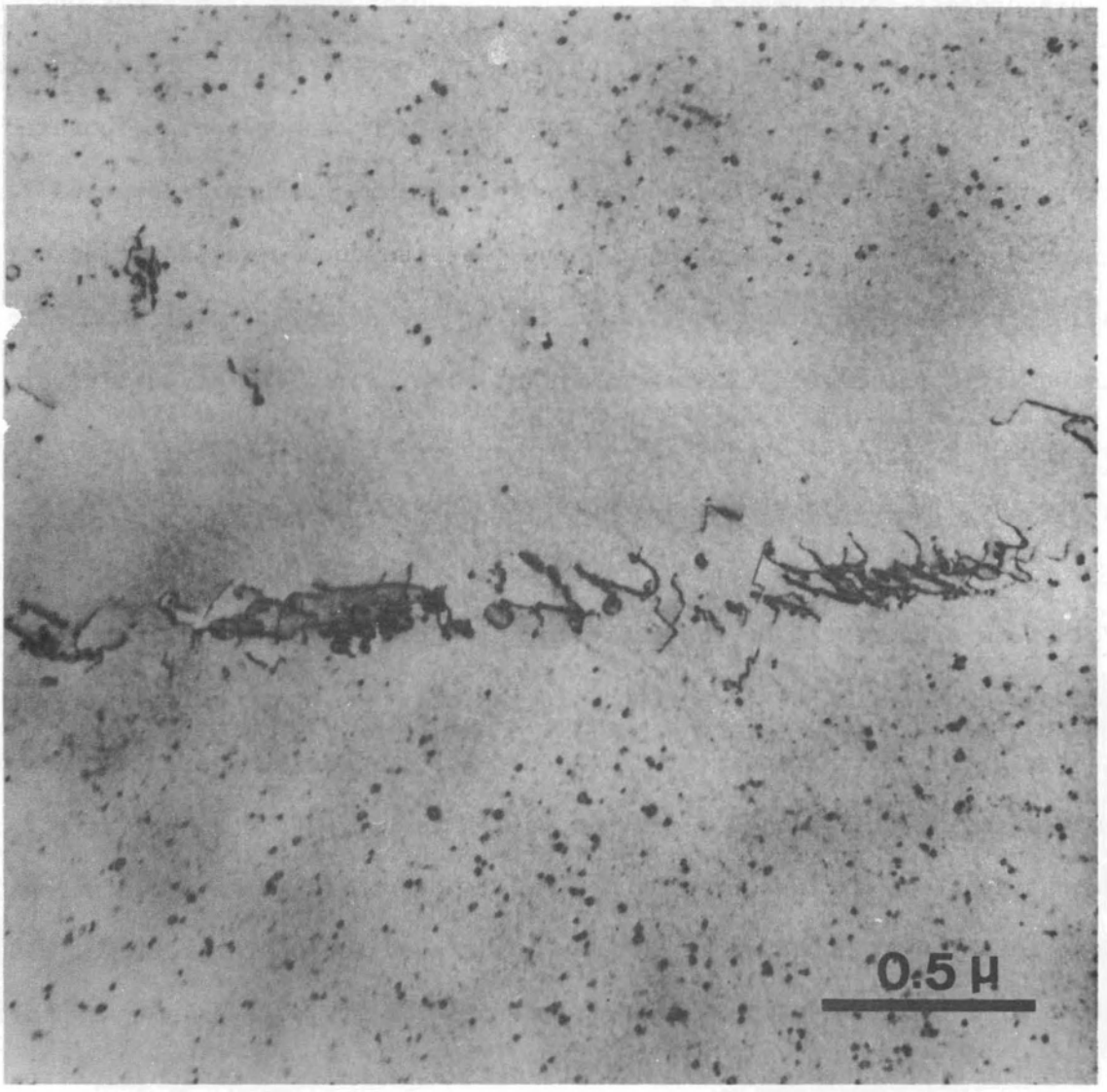

Figure 21. Channel in irradiated niobium annealed at 600°C after formation of channel.

Note the absence of defect cluster within channel and the presence of small defect clusters in matrix.

of spots within channels in post-irradiation-deformed-and-annealed copper. This suggests that the submicroscopic radiation-produced vacancies in the channels were caused to recombine with the interstitial defect clusters as a result of the motion of the channeling slip dislocations.

A third mechanism, not previously discussed in any detail to our knowledge, is that due to the *heat of plastic deformation*. In this mechanism, it is suggested that the motion of the channeling dislocations produces an input of energy that is largely converted into heat, thus causing an increase in temperature possibly capable of annealing the defect clusters. Each (a/2)<111> dislocation produces a shear displacement of $b = \sqrt{3}\ a/2$ and the {110} spacing is $\sqrt{2}\ a/2$, where a is the lattice parameter. Therefore, each dislocation gives rise to a shear strain of $\sqrt{3}/\sqrt{2}$. If, from Table XII, page 131, we consider about two dislocations per plane to operate in the channeling shear, the shear strain becomes $2\sqrt{3}/\sqrt{2} = 2.5$. This shear occurs at a shear-stress level corresponding to the yield stress, or about $\tau = 7.1\ kg/mm^2$. The energy of plastic deformation per unit volume is, therefore,

$$E_{PD} = 18\ kg/mm^2 = 42\ cal/cm^3\ . \qquad (29)$$

Niobium has a specific heat at room temperature of about 0.06 cal/gm deg = 0.54 cal/cm^3 deg.[347,348] Therefore, under adiabatic conditions, if all the energy of plastic deformation were converted into heat, the temperature rise would be about 80°C. Calorimetric measurements of the fraction of the energy of plastic deformation that is converted into heat indicate that it is quite large for most metals.[349] No values appear to be

available for niobium, but Wang and Brown[350] reported that the fraction is 92-96 percent for iron.

The effect of external heating on defect clusters in irradiated niobium is described in Chapter VII. Upon heating to 400°C, the total defect cluster density decreased slightly and the cluster size increased somewhat. These changes in the defect clusters are accompanied by a further increase in yield stress ("radiation-anneal hardening"). Above 400°C, the cluster density continued to decrease and the cluster size increased further. Also, additional small spots appear on the transmission electron micrographs after annealing to 600°C, which are attributed to vacancy clusters. Similar small vacancy clusters upon annealing have been suggested for molybdenum.[83,92] After annealing at 800°C, only a low density of large loops remains, and the yield stress returns to its pre-irradiation value. Thus, under conditions of external heating, temperatures between 400°C and 800°C are necessary to remove defect clusters.

It would seem on first examination, therefore, that the increase of about 80°C above room temperature calculated above from the heat of plastic deformation is insufficient to cause the annihilation of defect clusters within the channels. However, the calculation assumes that the energy of plastic deformation is distributed equally among all the atoms in the channel. It is quite possible that, since the defect clusters are themselves the major barriers impeding the slip dislocations, the energy of plastic deformation is expended in localized bursts at the defect clusters. Under such conditions, the process would be essentially adiabatic and quite high local temperatures could be reached. For example,

if the energy of plastic deformation were considered to be expended effectively among atoms in volumes surrounding the defect clusters comprising one-tenth of the atoms in the channel, the local increase in temperature would be about 800°C instead of 80°C as calculated above.

Dislocation channeling in irradiated metals has not been sufficiently, thoroughly studied as yet to permit a choice among the three mechanisms described. The third mechanism particularly, that of annealing as a result of high local temperatures generated by the conversion of the energy of plastic deformation into heat, seems worthy of further consideration. However, although it might well provide a basis for understanding the mechanism of the clearing of defect clusters eventually, the simple calculation above indicates that sufficiently high temperatures are not produced unless it is assumed that the heat of plastic deformation is concentrated at the defect clusters. It is possible that a combination of the second and third mechanisms operates, i.e., that the heat of plastic deformation mobilizes the submicroscopic radiation-produced vacancies, which then migrate to the interstitial clusters and annihilate them.

The above discussion has focused attention on the mechanism of the removal of defect clusters from the cleared channels. A related question is how the dislocation channeling process is initiated. Figures 15, page 113, and 17, page 121, illustrate that the channels are often widely and regularly spaced, suggesting that the presence of one channel triggers the formation of another one. As pointed out by Sharp,[59] this is evidence for a long-range internal stress in the irradiated-and-deformed material. Thus, it seems likely that a dislocation channel, initiated at a single point of stress concentration, activates the formation of other dislocation

channels in its neighborhood. The dislocation tangles at the intersection of channels or where a channel crosses another microstructural feature may well serve as concentrations of stress from which additional channels emanate.

Some insight into the motion of dislocations in irradiated niobium can be gained from the slip traces seen in Figure 22, which were observed in a foil from a sample strained 2.8 percent following a dose of 4.4 x 10^{17} neutrons/cm^2 (E > 1 Mev). Although the slip traces were created by dislocations slipping in the foil due to beam heating and thus are not necessarily representative of bulk behavior, the wavy nature of the traces, nevertheless, emphasizes the importance of cross slipping in irradiated samples. Furthermore, the dislocation at P, which extends through the foil from surface to surface, is not smooth itself but presumably reflects the influence of defect clusters in its path by the wavy appearance of the line near its lower end in the micrograph. The opposite sense of the black-white contrast for the paired traces indicates that the patterns observed are on opposite surfaces of the foil. It seems reasonable to conclude that cross slipping is one mechanism whereby dislocations by-pass radiation-produced defect clusters at lower doses. When the dose becomes sufficiently high, cross slipping becomes increasingly more difficult. It is under these conditions of higher stresses and correspondingly higher dislocation velocities that the channeling mechanism commences.

Figure 23 shows what may be a source for channeling dislocations in a foil from a sample irradiated to 1.8 x 10^{18} neutrons/cm^2 (E > 1 Mev) and nominally strained 2.7 percent. A dislocation, perhaps grown-in,

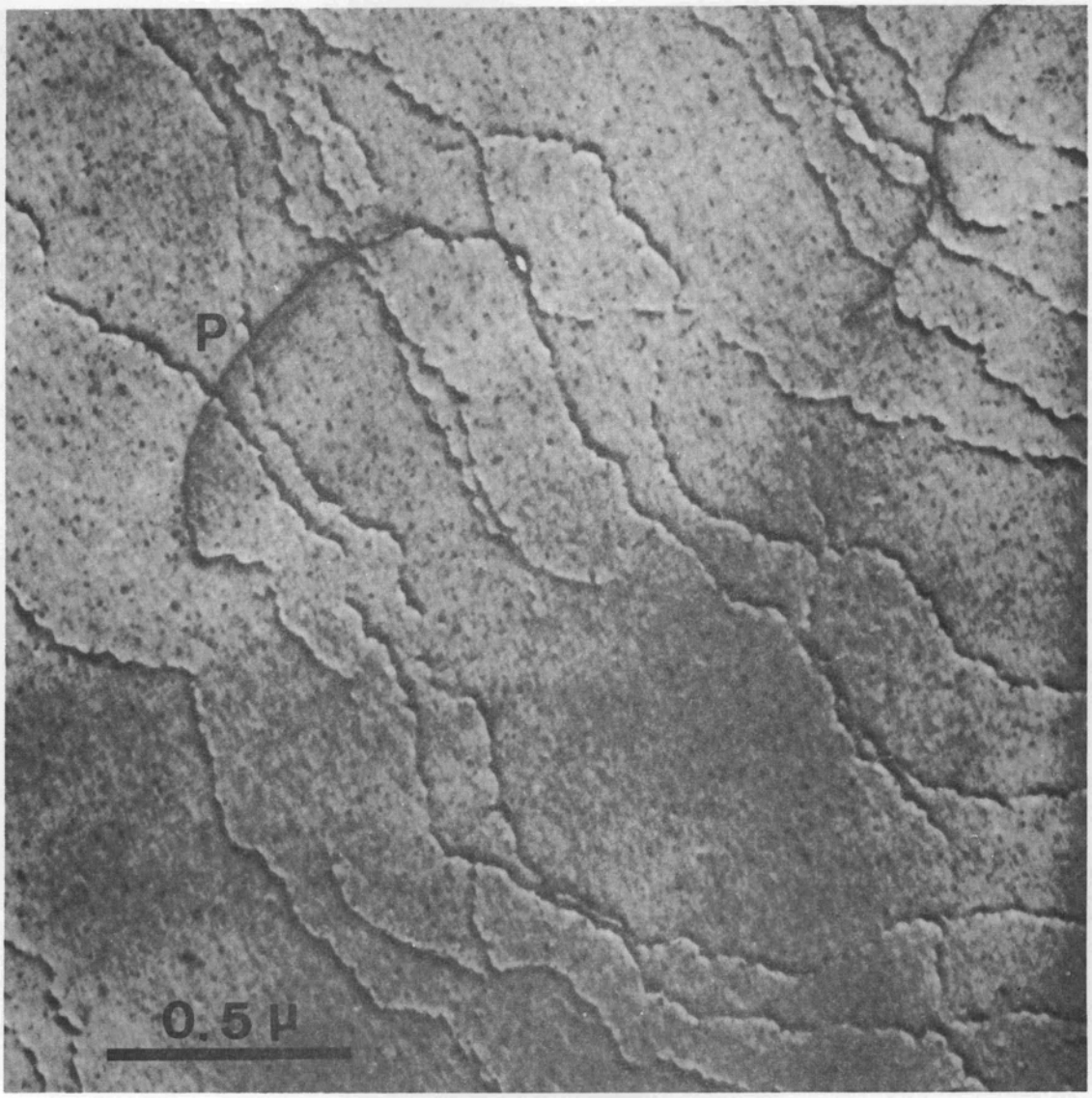

Figure 22. Slip traces on foil surfaces resulting from dislocations slipping due to beam heating.

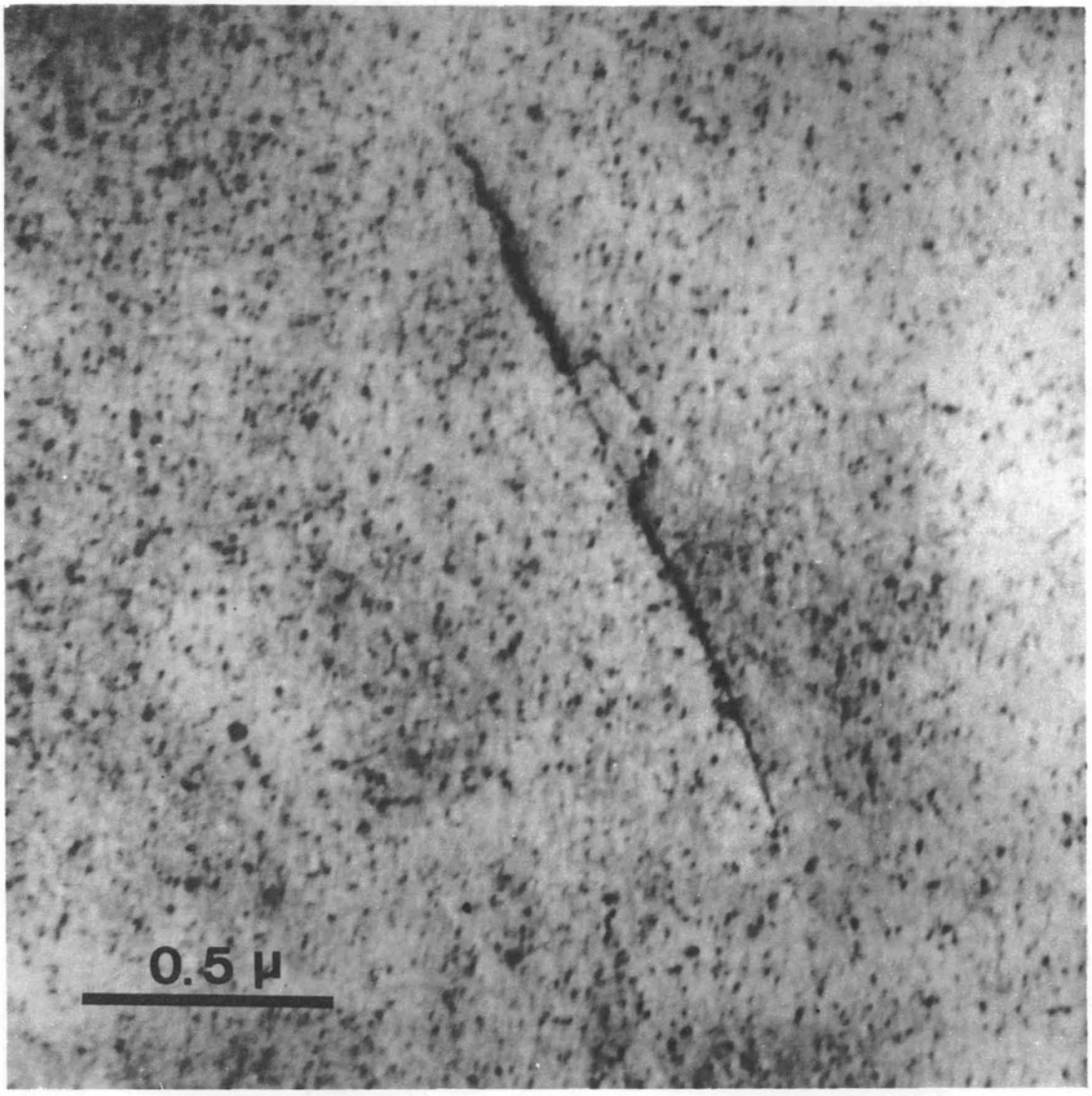

Figure 23. Possible dislocation source at grown-in dislocation.

has become strongly pinned by defect clusters. However, under the applied stress it appears to have put forth a loop which presumably can eventually expand and thereby become an active source.

In a relatively impure niobium sample, not previously mentioned, we observed an early stage in the formation of channels in a foil prepared after the sample was inadvertently bent. The sample received a dose of about 8×10^{18} neutrons/cm^2 (E > 1 Mev). In Figure 24 we observe an inclusion at Q from which numerous dislocations emanated. The dislocations farthest from the inclusion are of shorter length than those following along more or less the same pathway behind them. The dislocations appear to have piled up against a barrier at R. The shorter dislocations near R appear to be loops similar to those punched out by the inclusion at S. It then seems reasonable to suggest that the inclusion at Q punches out loops which initially find it difficult to expand due to the defect clusters. Subsequent loops, however, expand more readily since they encounter fewer clusters. In this way a pile-up of dislocations reaches a sufficient level of stress concentration to move rapidly through the crystal, removing the defect clusters as it advances.

In the stress field of an inclusion such as that in Figure 24, we may speculate that the stresses are sufficiently high to cause defect clusters to coalesce into a dislocation line. The dislocation lines could become pinned and bowed out at obstacles such as the dislocations at T and U, thus becoming potential sources.

The phenomenon of dislocation channeling plays a central role in the plastic deformation of irradiated metals. The yield stress at higher doses is likely governed by the stress to initiate the formation of

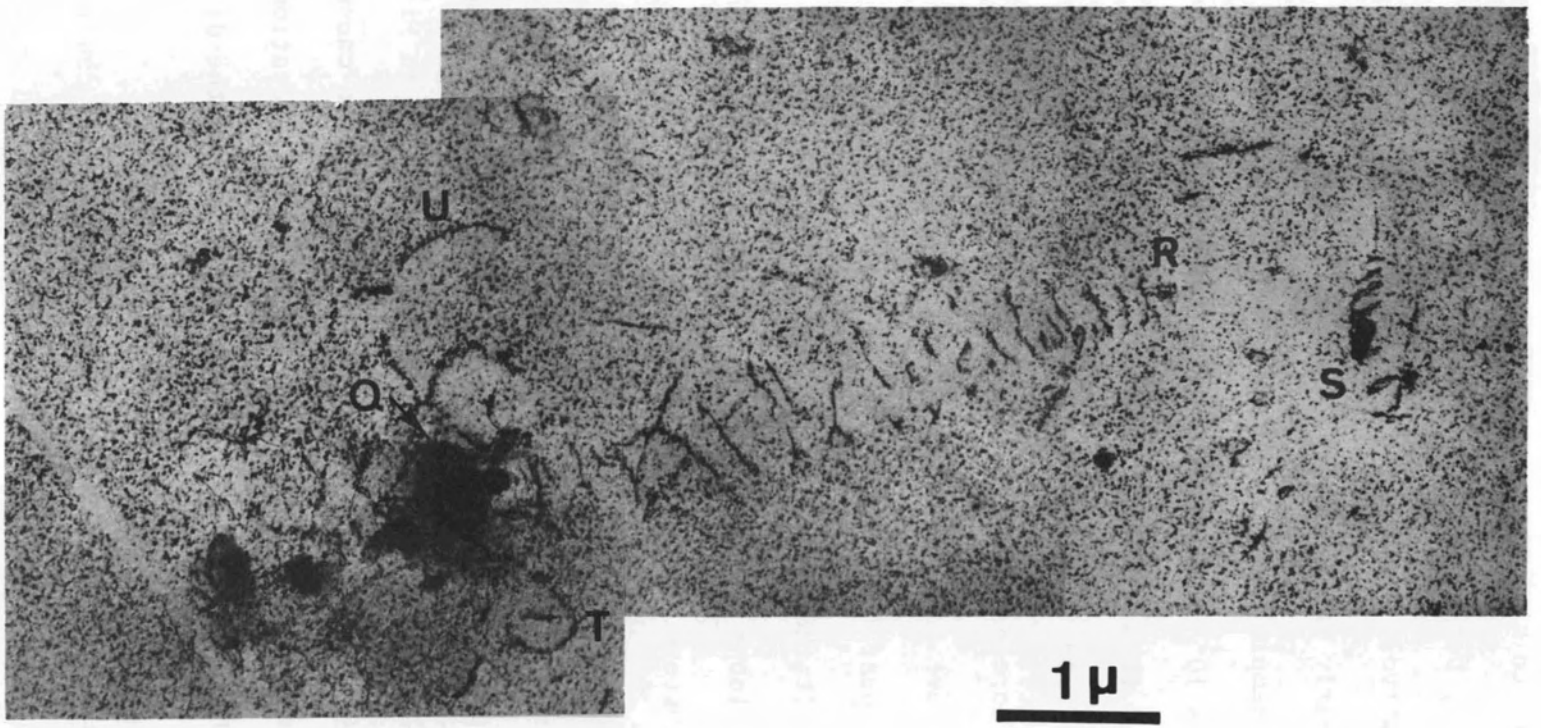

Figure 24. Dislocations emanating from inclusion and forming channel.

dislocation channels, and the work-hardening behavior depends upon the manner in which strain is concentrated in the channels and the way in which the channels propagate to encompass the entire gage section of the sample.

CHAPTER VI

DOSE DEPENDENCE OF RADIATION HARDENING

I. INTRODUCTION

The dose dependence of radiation hardening has an important bearing on the mechanism of the phenomenon. As mentioned in Chapter II, the model most frequently employed is the dispersed barrier model, in which the hardening agents or barriers to dislocation motion are considered to be randomly distributed in the solid. Under the action of a shear stress τ, the dislocation presses against the barrier with a force F given by

$$F = \tau b \bar{\ell} , \tag{30}$$

where $\bar{\ell}$ is the average interbarrier spacing, b is the Burgers vector, and the critical shear stress is reached when F achieves a critical value for either breaking through or bowing around the barrier. Thus, the yield stress (for an equiaxed polycrystal or a single crystal oriented for maximum Schmid factor) is

$$\sigma = 2\tau = \frac{2F}{b\bar{\ell}} , \tag{31}$$

and the dose dependence enters chiefly through the dependence of $\bar{\ell}$ on the dose Φ.

A key question is the way in which the barriers to dislocation motion in the unirradiated metal (U-barriers) combine with those produced upon irradiation (I-barriers) to give the observed yield stress.

It is helpful to distinguish between two cases:

A. U- and I-barriers acting independently: In this case, the net shear stress acting on the dislocation line at the I-barriers upon yielding is $\tau-\tau_u$, where τ_u is the unirradiated critical shear stress, and equation (31) becomes

$$\sigma - \sigma_u = \frac{2F_i}{b\bar{\ell}_i} , \tag{32}$$

where σ_u is the corresponding unirradiated yield stress, $\bar{\ell}_i$ is the average interbarrier distance between the I-barriers alone, and F_i is the critical force necessary to surmount them. On the assumption that all the I-barriers have the same diameter, d_i, $\bar{\ell}_i$ may be written

$$\bar{\ell}_i = \frac{1}{\sqrt{n_i d_i}} , \tag{33}$$

where n_i is the number of I-barriers per unit volume. Then

$$\sigma = \sigma_u + \frac{2F_i}{b} (n_i d_i)^{1/2} . \tag{34}$$

B. U- and I-barriers acting jointly: Now equation (31) becomes

$$\sigma = \frac{2\bar{F}}{b\bar{\ell}} , \tag{35}$$

where

$$\bar{\ell} = \frac{1}{\sqrt{n_u d_u + n_i d_i}} , \tag{36}$$

n_u and d_u being the density and size of U-barriers, and $\overline{F}$ is an effective critical force. Then equation (35) may be written

$$\sigma = \frac{2\overline{F}}{b} (n_u d_u + n_i d_i)^{1/2} . \tag{37}$$

Since $\sigma = \sigma_u$ when $n_i = 0$, equation (37) becomes

$$\sigma^2 = \sigma_u^2 + \frac{4\overline{F}^2}{b^2} (n_i d_i) . \tag{38}$$

Most of the previous work on dose dependence has been on face-centered cubic (fcc) metals over a range of doses where $\sigma_u << \sigma$, in which case the distinction between equations (34) and (38) is unimportant. However, σ_u for body-centered cubic (bcc) metals is usually much greater than for fcc metals, and it becomes necessary to attempt to distinguish between the two cases.

A further important question is the extent to which the I-barriers can be associated with the defect clusters observed by transmission microscopy. In earlier work by Makin *et al.*[48,244] on copper, it was concluded that only the defect clusters with diameters below 50 Å contribute to the radiation hardening. As will be shown, the present work on niobium indicates that hardening can be correlated with defect clusters of all sizes. In order to take the size distribution of defect clusters into account, the quantity $n_i d_i$ in the above expressions is replaced by

$$I_c = \int_0^\infty n' d_c \, dd_c , \tag{39}$$

where n' is the defect cluster density per unit size interval and the symbol d_c is used instead of d_i to connote that the I-barriers are now being specifically identified as the clusters seen in the electron microscope. Then equations (34) and (38) become

$$\sigma = \sigma_u + \frac{2F_i}{b} I_c^{1/2} \tag{40}$$

and

$$\sigma^2 = \sigma_u^2 + \frac{4\bar{F}^2}{b^2} I_c \ , \tag{41}$$

respectively.

In this chapter, experiments as a function of dose on two types of samples are described: (1) polycrystalline sheet samples of CIBA-A niobium, on which tensile tests and transmission electron microscopy (TEM) were performed, and (2) single crystal Wah Chang niobium samples, which were tensile tested only. The values of I_c were determined from the sizes and densities of the defect clusters observed by TEM, and these were compared with the measured yield stresses in the light of equations (40) and (41). The results indicate a somewhat better fit to equation (41), but in either case a strong tendency toward a saturation in yield stress for doses above about 10^{18} neutrons/cm^2 (E > 1 Mev) is seen. The origin of the saturation and the mechanism of the hardening are discussed below.

II. TENSILE TESTS AND TRANSMISSION ELECTRON MICROSCOPY IN IRRADIATED POLYCRYSTALLINE NIOBIUM

Polycrystalline sheet tensile samples and sheet TEM samples were irradiated at approximately 50°C in the Hydraulic Facility of Position F-8 in the Oak Ridge Research Reactor to doses between 7.3×10^{16} and 4.4×10^{18} neutrons/cm^2 (E > 1 Mev). Figure 25 shows typical stress-strain curves as a function of neutron dose. The irradiation causes an increase in the yield and flow stresses and a tendency toward a decrease in the rate of work hardening and the uniform and fracture strains.

Transmission electron micrographs of the defect clusters, taken under kinematical conditions, are shown in Figure 26 for samples given various doses. The diffraction vector for each micrograph is a <110> type. The plates were printed at five times their size, and the defect cluster density was determined as a function of cluster size using a Zeiss Particle Size Analyzer. The size interval was about 10 Å, but it varied slightly from sample to sample. The number of defect clusters in a given size interval was divided by the size interval and by the volume of the foil in which the clusters were counted, thus forming the defect cluster density size-distribution function n'. In Figure 27, n' is plotted versus cluster size for various doses; n' was too low for the dose of 7.3×10^{16} neutrons/cm^2 to permit an accurate count. For doses up to 1.8×10^{18} neutrons/cm^2, the total density (area under the curve) increased steadily with a shift in the distribution toward smaller sizes. However, for the dose of 4.4×10^{18} neutrons/cm^2, the cluster density decreased sharply and the cluster sizes coarsened considerably. It will

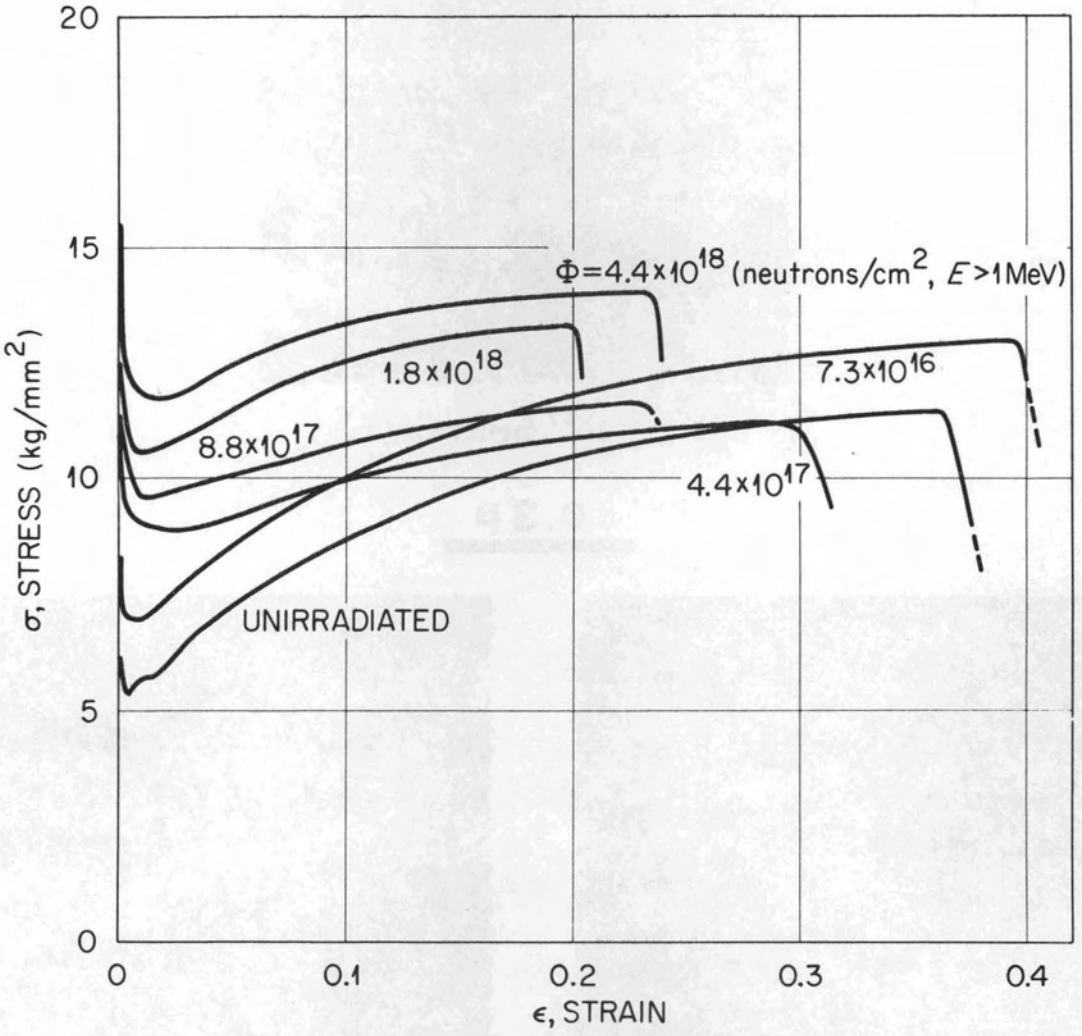

Figure 25. Stress-strain curves for polycrystalline niobium sheet samples neutron-irradiated to the indicated dose at ∿ 50°C and tested in tension at 25°C.

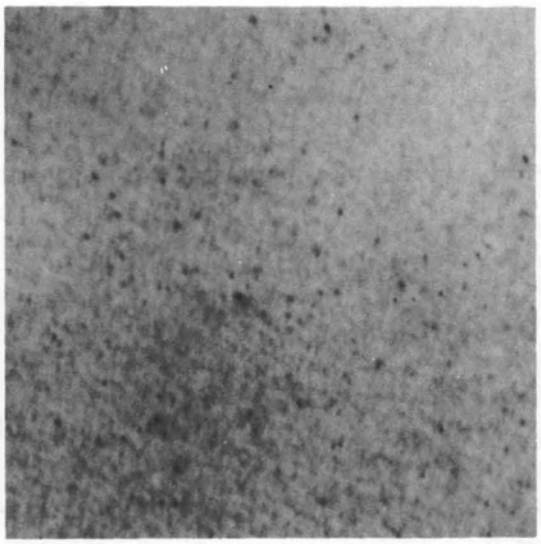

2.2×10^{17} neutrons/cm^2

0.3 μ

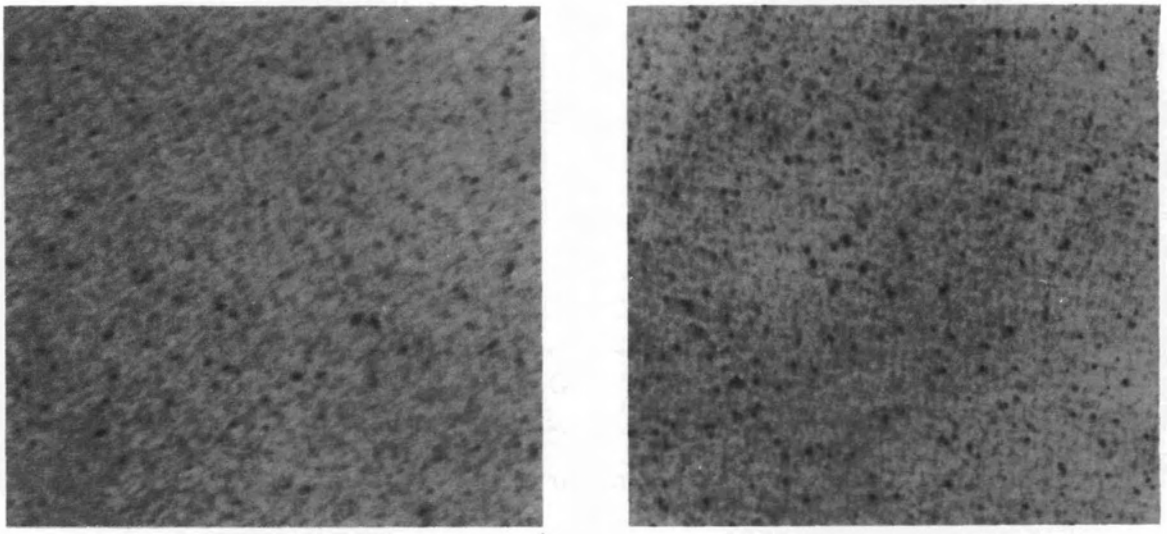

Figure 26. Defect clusters as revealed under kinematical diffraction conditions ($s > 0$) in CIBA-A niobium neutron-irradiated to the doses indicated.

The diffraction vector $\vec{g}$ for each of the micrographs is a <110> type.

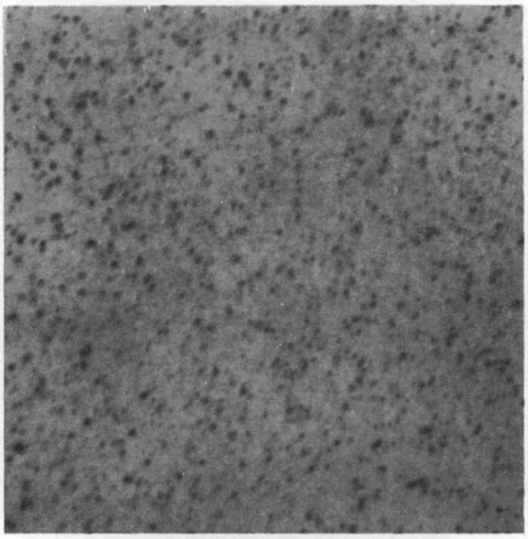

1.8×10^{18} neutrons/cm^2

0.3 μ

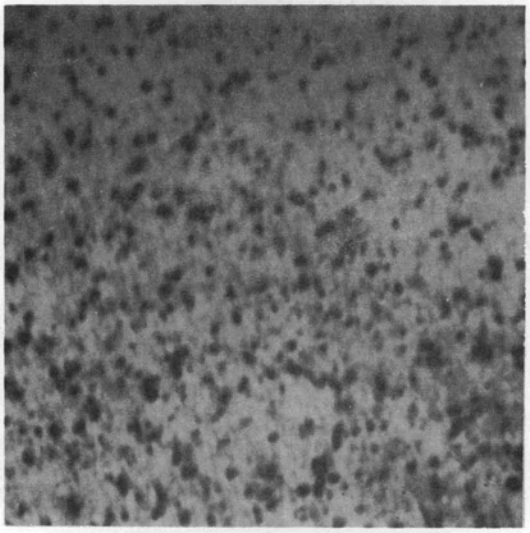

4.4×10^{18} neutrons/cm^2

Figure 26. (continued).

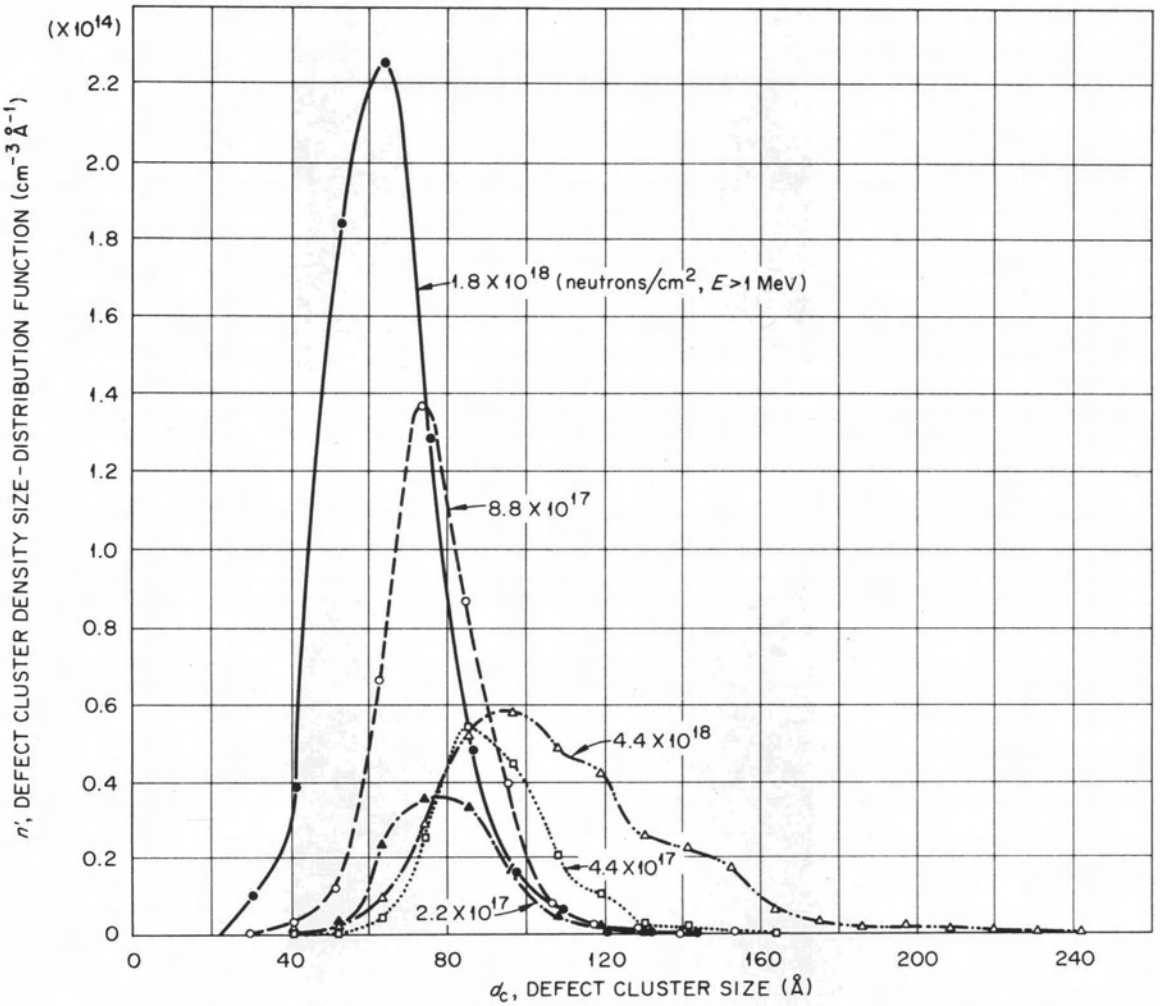

Figure 27. Defect cluster density size-distribution function versus defect cluster size for polycrystalline niobium neutron-irradiated to the doses shown.

Irradiation temperature ∿ 50°C.

be shown below that this dose lies in the range where the increase in yield stress is saturated with respect to increasing dose.

In order to test equations (40) and (41), page 151, the quantity I_c as defined in equation (39), page 150, was evaluated from each of the n'-versus-d_c curves in Figure 27. The I_c values are tabulated in Table XIII as a function of dose. Values of the total density, n, and the average cluster size, $\overline{d}_c$, are also included in Table XIII. From the definition of I_c, it may be seen that

$$I_c = n\,\overline{d}_c\ . \tag{42}$$

I_c is plotted as a function of dose in Figure 28. At low doses (say, below 1.3×10^{18} neutrons/cm^2), I_c increases linearly with Φ. I_c, however, fails to extrapolate to zero at zero dose. The failure to do so may not be outside experimental error. On the other hand, it may be that the defect cluster density increases somewhat more rapidly in the very early stages of the irradiation (below 2.2×10^{17} neutrons/cm^2) than it does in the range 2.2×10^{17} to 1.8×10^{18} neutrons/cm^2. Another important feature of Figure 28 is the saturation in I_c above about 1.3×10^{18} neutrons/cm^2, suggesting that the saturation in radiation hardening is a consequence of the density and size distribution of the defect clusters and is not due to an extraneous factor.

Figure 29 shows a plot of σ versus $(I_c)^{1/2}$ according to equation (40), and Figure 30 shows σ^2 versus I_c according to equation (41). The fits to these equations are equally good, but the extrapolation to the unirradiated yield stress at $I_c = 0$ is much better for equation (41)

TABLE XIII

DEFECT CLUSTER PARAMETERS AS A FUNCTION OF DOSE, AS MEASURED FROM TEM MICROGRAPHS

Φ cm^{-2}	n cm^{-3}	I_c cm^{-2}	$\bar{d}_c$ (Å)
(x 10^{17})	(x 10^{15})	(x 10^{8})	
2.2	1.31	10.4	80
4.4	1.82	17.9	98
8.8	3.90	29.9	77
18	7.42	47.4	64
44	3.58	39.0	109

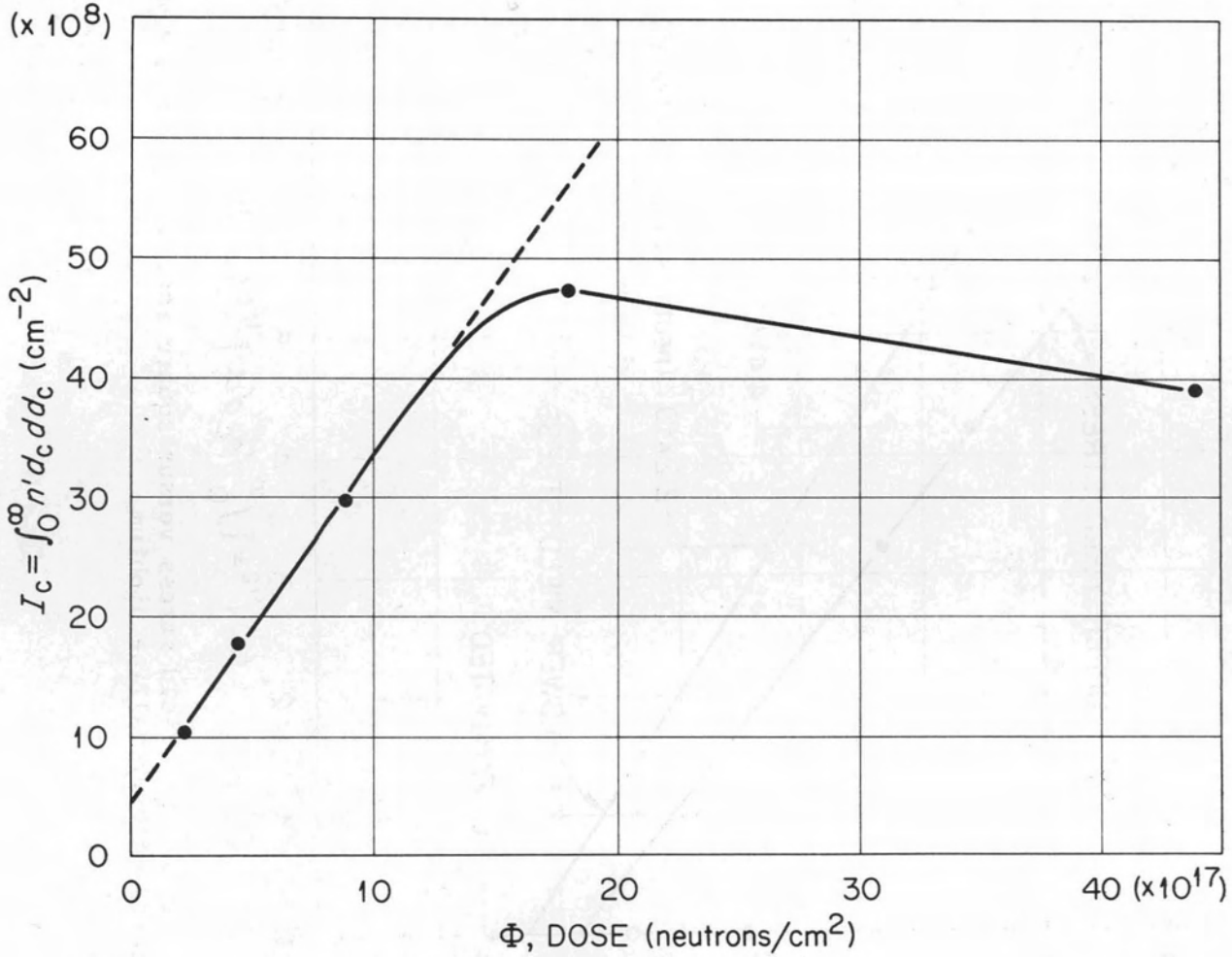

Figure 28. I_c versus neutron dose for polycrystalline niobium.

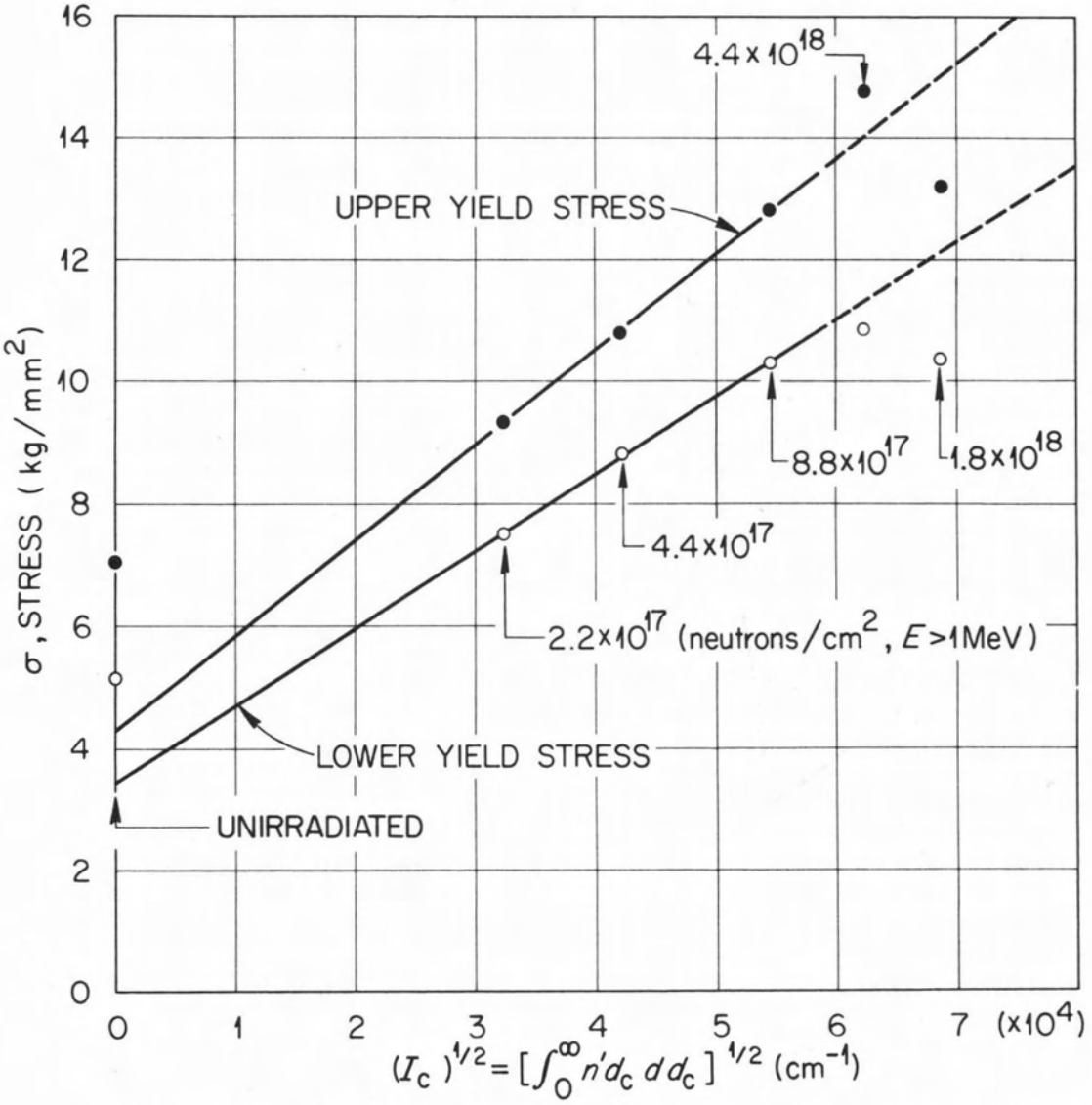

Figure 29. Yield stress versus square root of I_c for neutron-irradiated polycrystalline niobium.

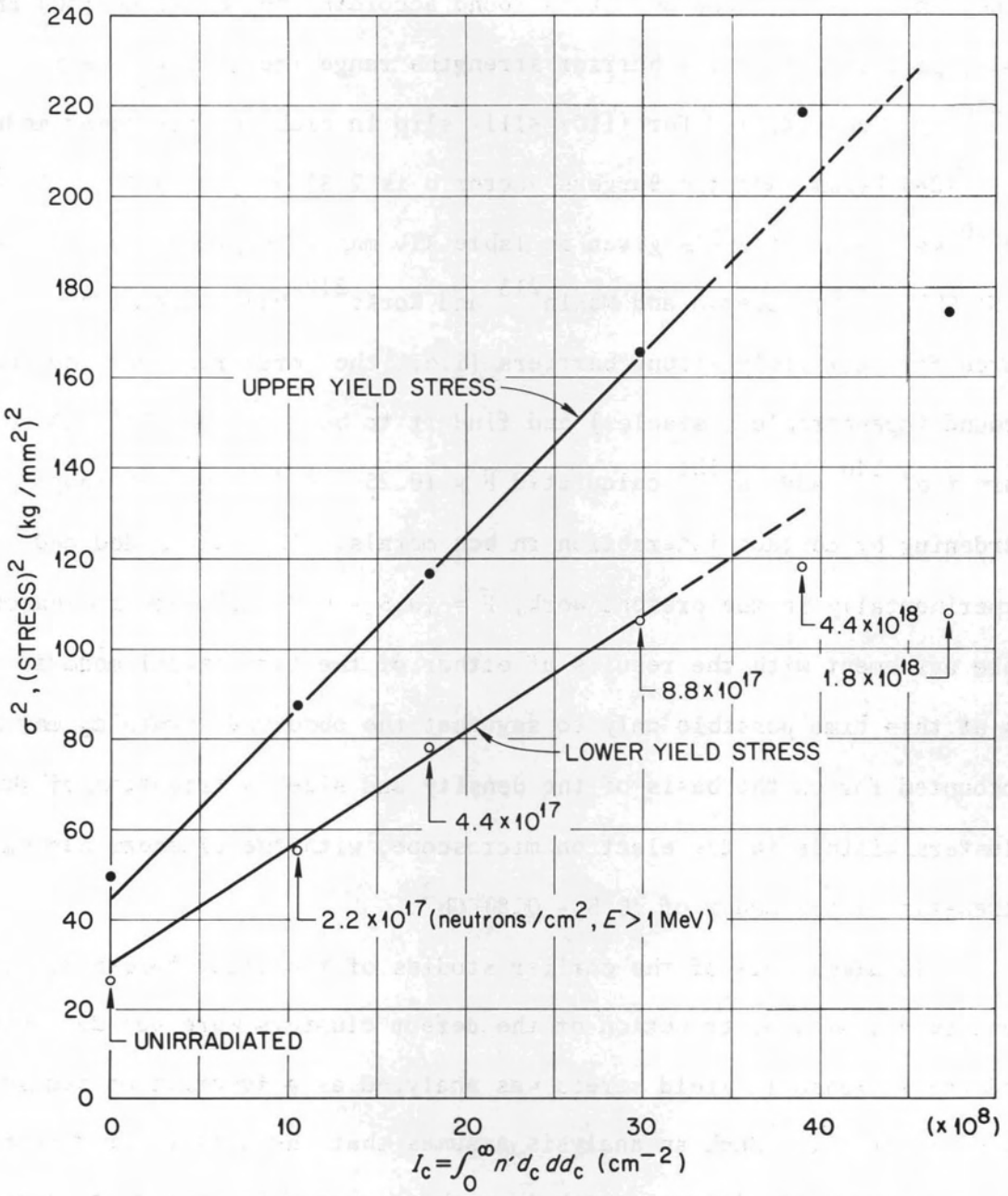

Figure 30. Square of yield stress versus I_c for neutron-irradiated polycrystalline niobium.

(Figure 30) than for equation (40) (Figure 29). From the slopes of the lines in Figures 29 and 30, it is found according to equations (40) and (41), page 151, that the barrier strengths range from 1.8 to 2.9 x 10^{-10} kg (Table XIV). For {110} <111> slip in niobium, the shear modulus G is 4280 kg/mm^2 and the Burgers vector b is 2.85 Å, giving Gb^2 = 3.48 x 10^{-10} kg. Thus, the $\overline{F}$'s given in Table XIV may be expressed as (0.5 - 0.8) Gb^2. Now, Foreman and Makin[213] and Kocks[212] have calculated the force for infinitely strong barriers (i.e., the force required for bowing around impenetrable obstacles) and find it to be about 0.8 Gb^2. Also, Ohr *et al.*[240] and Ohr[351] calculated $\overline{F}$ = (0.25 - 0.50) Gb^2 for loop hardening by contact interaction in bcc metals. The values deduced experimentally in the present work, $\overline{F}$ = (0.5 - 0.8) Gb^2, are in reasonable agreement with the results of either of the theoretical models. It is at this time possible only to say that the observed hardening may be accounted for on the basis of the density and size distribution of defect clusters visible in the electron microscope, with the clusters having strengths of the order of (0.5 - 0.8) Gb^2.

In almost all of the earlier studies of radiation hardening, the density and size distribution of the defect clusters were not determined, and the increase in yield stress was analyzed as a function of neutron dose, Φ, itself. Such an analysis assumes that the density of defect clusters increases linearly with Φ, with no change in size distribution, whereas Figure 27, page 156, shows that the size distribution changed appreciably with Φ. Nevertheless, if this assumption is made, it is possible to replace $n_i d_i$ in equations (34), page 149, and (38), page 150,

TABLE XIV

BARRIER STRENGTHS AND CROSS SECTIONS, BASED ON I_c DETERMINATION BY TRANSMISSION ELECTRON MICROSCOPY

	Case	Slope	$F^{(a)}$ (kg)	$\sigma_c^{(b)}$ (barns)	F/Gb^2
σ vs $\Phi^{1/2}$	Lower yield stress	0.58 $\frac{kg}{mm^2}$ Å	1.80×10^{-10}	0.048	0.52
(Fig. 31)	Upper yield stress	0.71	2.25	0.046	0.65
σ^2 vs Φ	Lower yield stress	0.79 $(\frac{kg}{mm^2})^2$ Å^2	2.28	0.069	0.66
(Fig. 32)	Upper yield stress	1.22	2.86	0.068	0.82

(a) From Figures 29 and 30 and equations (40) and (41), respectively.

(b) From equations (43) and (44) using $n_o = 5.56 \times 10^{22}$ cm^{-3}, b = 2.85 Å, and $\overline{d}_c$ = 80 Å [average for Φ = (2.2 - 18) x 10^{17} neutrons/cm^2, E > 1 Mev; Table XIII, page 158].

by $n\bar{d}_c$, where n is the total defect cluster density and $\bar{d}_c$ is the mean cluster size considered independent of Φ. As a representative value of $\bar{d}_c$, we shall take the average of the $\bar{d}_c$ values for $\Phi \leq 18 \times 10^{17}$ neutrons/cm^2 (Table XIII, page 158), which gives (80 ± 9) Å. The density may then be expressed as

$$n = n_o \sigma_c \Phi , \tag{43}$$

where n_o is the atomic density and σ_c is the cross section for producing a dislocation barrier. Equations (34) and (38) then become

$$\sigma = \sigma_u + \frac{2F_i}{b} (n_o \sigma_c \bar{d}_c \Phi)^{1/2} \tag{44}$$

and

$$\sigma^2 = \sigma_u^2 + \frac{4\bar{F}^2}{b^2} (n_o \sigma_c \bar{d}_c \Phi) \tag{45}$$

for the cases of U- and I-barriers acting independently and jointly, respectively. In Figures 31 and 32, the yield stresses are plotted according to equations (44) and (45), respectively. The extrapolation to the unirradiated yield stress is better for equation (44), especially for the lower yield stress. From the slopes of the fits to equations (44) and (45) in Figures 31 and 32, respectively, it is possible to evaluate σ_c using the F's determined from equations (40) and (41), page 151, and Figures 29, page 160, and 30, page 161, and the average defect cluster size, $\bar{d}_c$ = 80 Å, evaluated from the size distribution as mentioned above. The results tabulated in Table XIV indicate that σ_c = 0.06 ± 0.01 barns. Since the scattering cross section for neutrons in

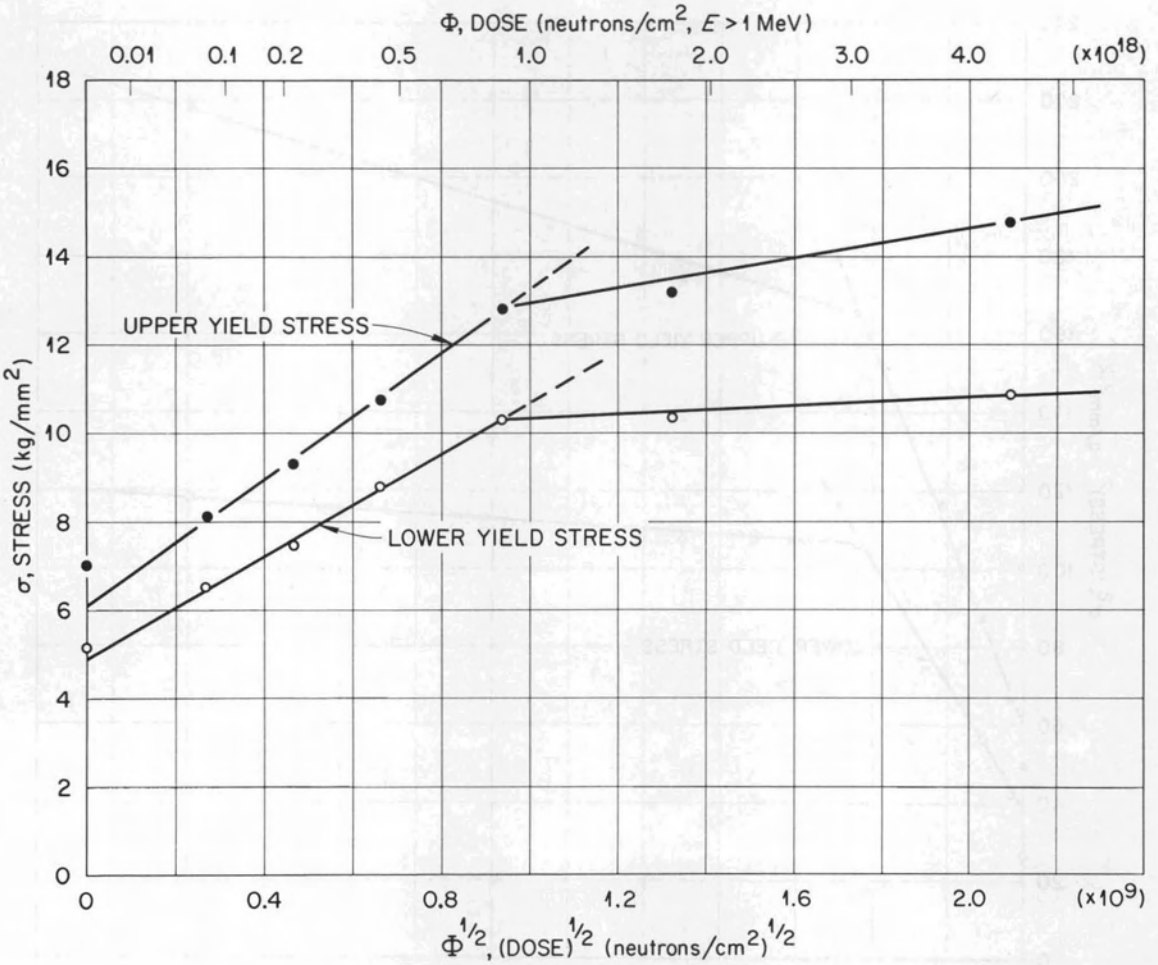

Figure 31. Yield stress versus square root of the dose for polycrystalline niobium, showing least squares straight line fit to low-dose portion.

Irradiation temperature, ∿ 50°C; test temperature, 25°C.

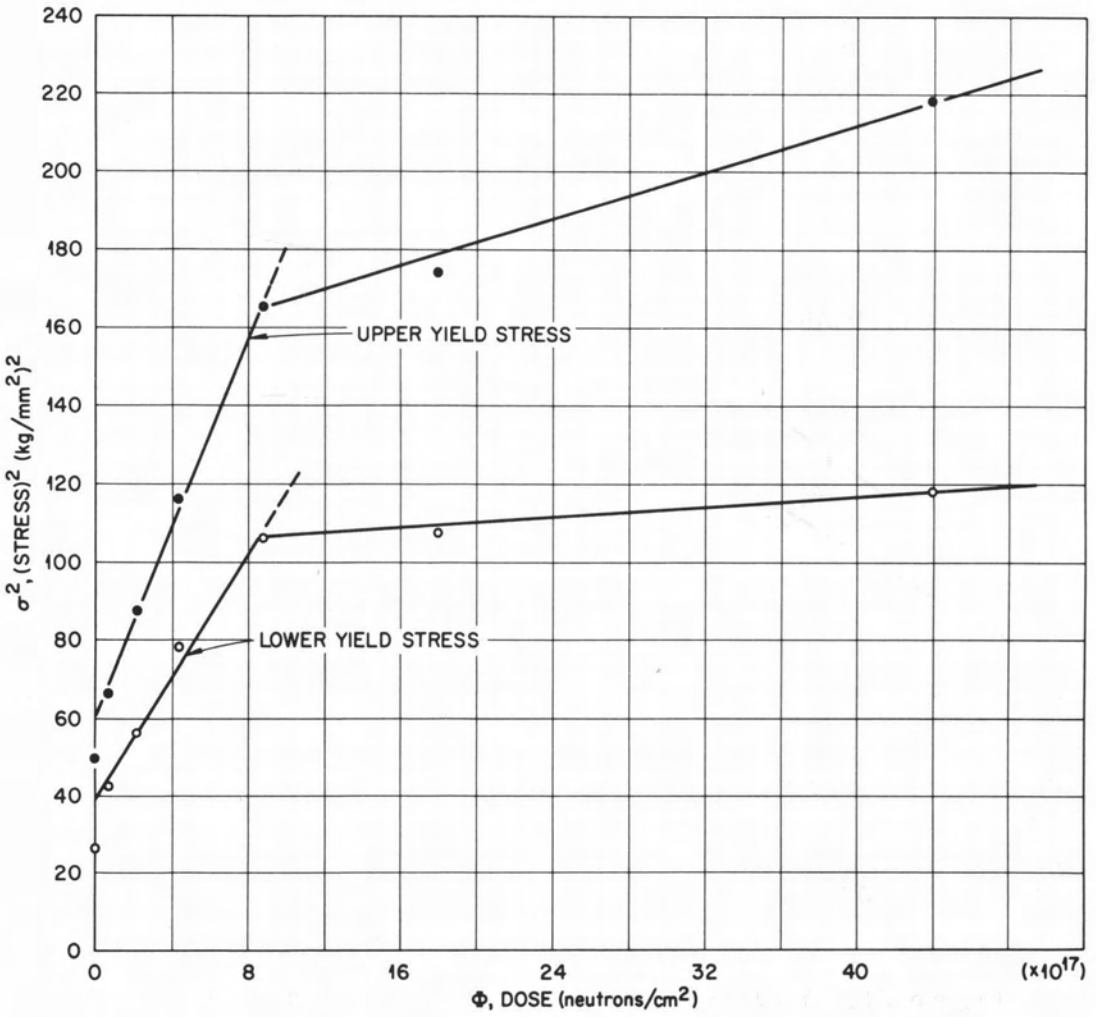

Figure 32. Square of the yield stress versus dose for polycrystalline niobium, showing least squares straight line fit to low-dose portion.

Irradiation temperature, ∿ 50°C; test temperature, 25°C.

niobium is about seven barns,[356] this result suggests that only one primary collision in about 133 yields a defect cluster that serves as a barrier to slip dislocations.

III. TENSILE TESTS IN IRRADIATED SINGLE CRYSTALS

Single-crystal tensile samples of Wah Chang niobium were annealed for five hours at 2350°C, irradiated at 90°C over a range of doses up to 8×10^{18} neutrons/cm^2 (E > 1 Mev), and subsequently tensile tested at room temperature. The upper yield stress is plotted according to equations (44) and (45) in Figures 33 and 34, respectively. The low dose region of Figure 34 is shown on an expanded scale in Figure 35. The quality of the fits in the low-dose region (below 10^{18} neutrons/cm^2) is about the same for the two cases, although the extrapolation to the unirradiated yield stress is slightly better for the $\sigma^2 - \Phi$ plot (Figure 34) than for the $\sigma - \Phi^{1/2}$ plot (Figure 33). An evaluation of σ_c was carried out from the slopes of the low-Φ portions of the curves in Figures 33 and 35 in the same manner as described above for polycrystalline samples. Based on the F values determined by TEM and the upper yield stresses for the polycrystalline samples (Table XIV), σ_c turns out to be about 0.05 barns, in good agreement with the value 0.06 barns for the polycrystalline samples.

IV. DISCUSSION OF DOSE DEPENDENCE

The observation of the density and size distribution of defect clusters as a function of dose has enabled us to analyze the radiation hardening in terms of I_c, equation (39), page 150, a quantity more

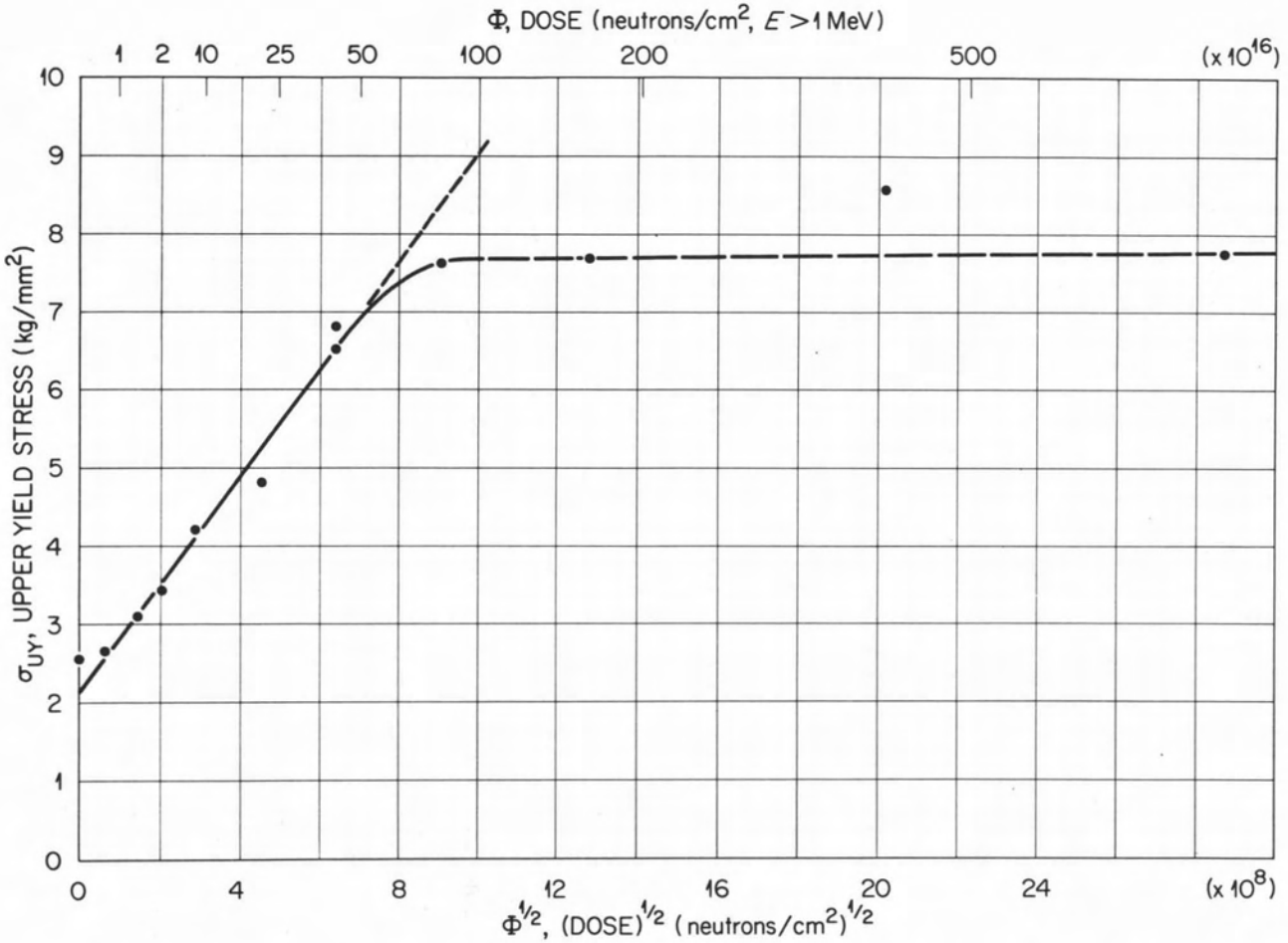

Figure 33. Upper yield stress versus square root of the dose for single crystal niobium, showing least squares straight line fit to low-dose portion.

Irradiation temperature, 90°C; test temperature, 25°C.

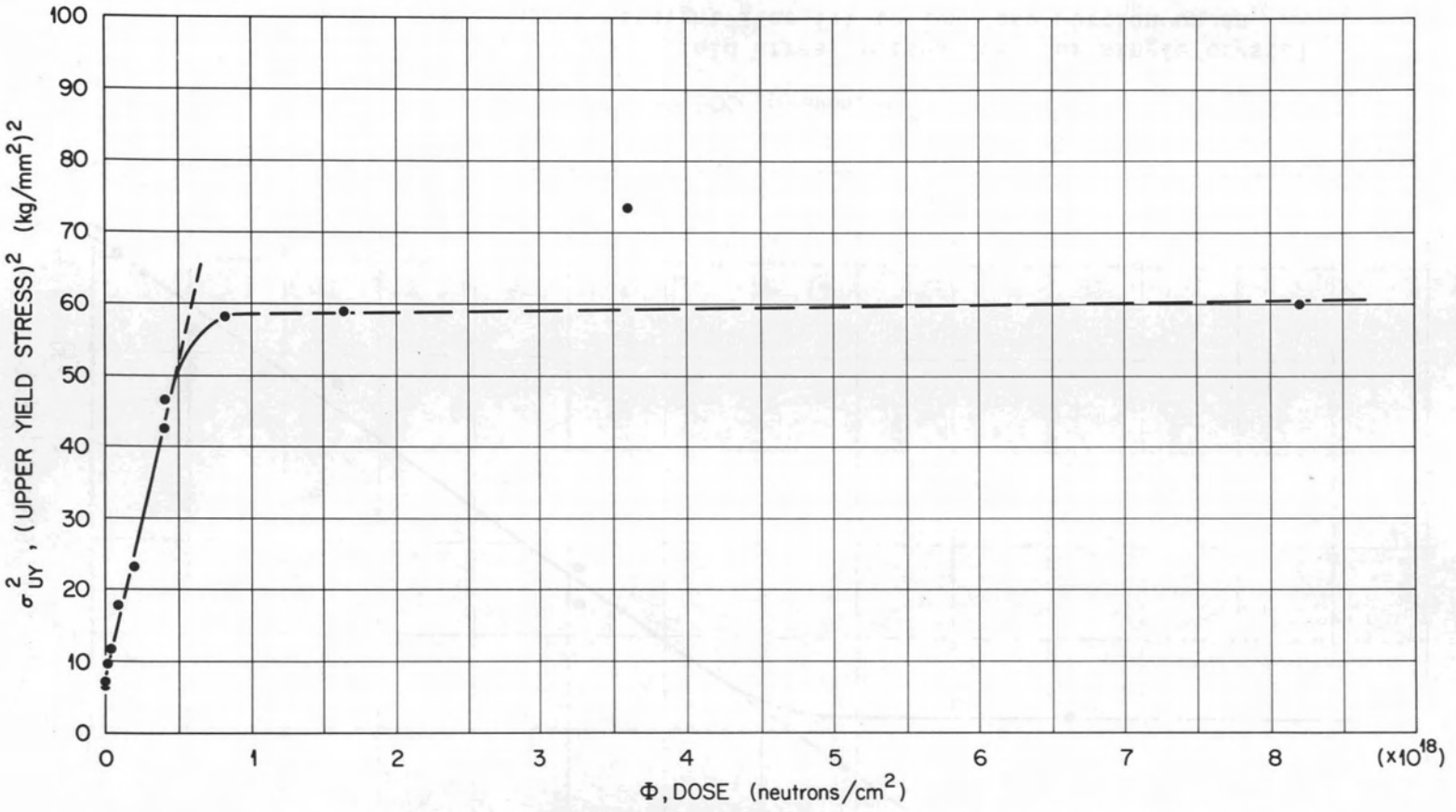

Figure 34. Square of upper yield stress versus dose for single crystal niobium, showing least squares straight line fit to low-dose portion.

Irradiation temperature, 90°C; test temperature, 25°C.

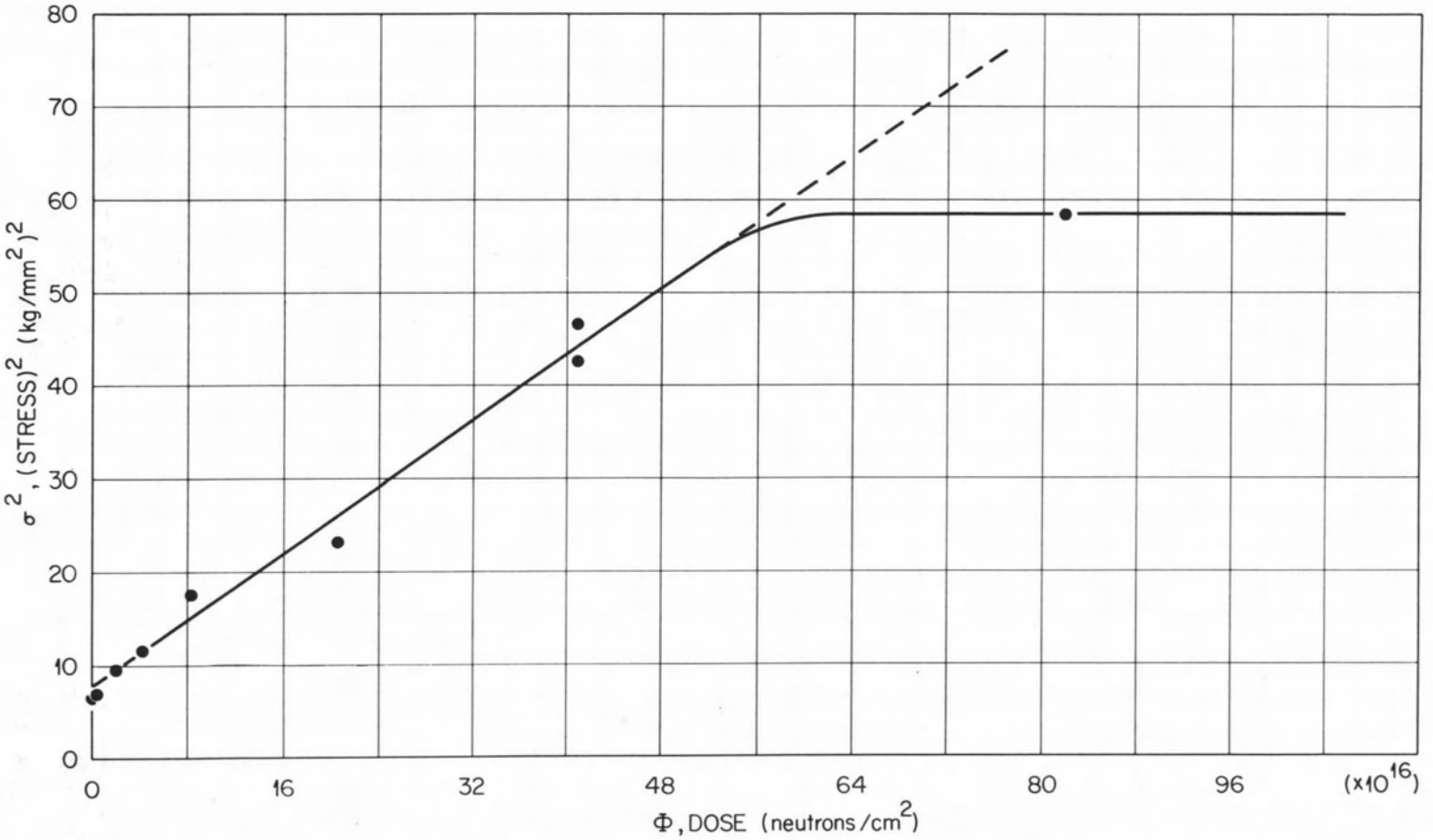

Figure 35. Square of upper yield stress versus dose for single crystal niobium, showing least squares straight line fit to low-dose portion on an expanded scale.

Irradiation temperature, 90°C; test temperature, 25°C.

fundamental than the dose itself. The fit to σ^2 versus I_c [equation (41), page 151] extrapolates better to the unirradiated yield stress than the fit to σ versus $I_c^{1/2}$ [equation (40), page 151], thus suggesting that the U- and I-barriers act jointly in resisting the forward motion of slip dislocations in response to an applied shear stress. This conclusion is not a strong one, however, because the range of I_c values over which the fits are made is short due to the early onset of saturation in the increase in yield stress with increasing dose. For either case, independent or joint action of the U- and I-barriers, the critical force F for surmounting the barrier is (0.5 - 0.8) Gb^2 (Table XIV, page 163); this corresponds to *strong* barrier hardening, i.e., to F values close to the Orowan bowing-around stress indicated by Foreman and Makin[213] and Kocks,[212] to be about 0.8 Gb^2 for a random distribution of obstacles. The cross section corresponding to the production of these strong barriers is about 0.06 barns. This assumes that the size of the barrier is 80 Å, roughly equal to the average defect cluster size observed in the TEM micrographs for the lower doses ($\Phi \leq 1.8 \times 10^{18}$ neutrons/cm^2, Table XIII, page 158) where the hardening rate is still rather high.

At higher doses, the hardening rate of niobium is observed to decrease. This reduction in hardening rate or "saturation effect" at higher doses has also been observed for the fcc metals copper[220,222] and nickel[222] and for the bcc metal iron.[232,352] Makin and Minter[222] have suggested that an exclusion volume, V, exists about a defect cluster within which no additional defect clusters can form. In this case, the number of defect clusters (or depleted zones) per unit volume

is given by

$$N_z = \frac{1}{V} [1 - \exp (-B\Phi)] , \tag{46}$$

where

$$B = n_o \sigma_z V , \tag{47}$$

n_o being the number of atoms per unit volume and σ_z the cross section for the production of a depleted zone. This cross section, σ_z, is to be distinguished from σ_c as used above [equations (43) - (45), page 164], since σ_c is the cross section *deduced* from the observed hardening rate and the defect cluster size distribution (Table XIV, page 163). As a measure of the dose at which saturation occurs, we may define Φ_s, where

$$\Phi_s = \frac{1}{B} = \frac{1}{n_o \sigma_z V} . \tag{48}$$

At the dose Φ_s, N_z is given by

$$N_z (\Phi_s) = \frac{0.632}{V} . \tag{49}$$

If the exclusion volume is assumed to be spherical with a diameter D equal to the barrier size d_i [equation (34), page 149], then equation (34) becomes

$$\sigma = \sigma_u + A [1 - \exp (-B\Phi)]^{1/2} , \tag{50}$$

where

$$A = (24/\pi)^{1/2} F/bD . \tag{51}$$

From equation (50) it may be seen that the initial hardening rate is given by

$$S = \lim_{\Phi \to 0} \frac{d\sigma}{d\Phi^{1/2}} = AB^{1/2} \quad . \tag{52}$$

Thus, S is the slope of the fit to the curve of σ versus $\Phi^{1/2}$ at low doses, as given in the upper portion of Table XIV, page 163. A similar analysis of the saturation effect may be based on the fit to the curve of σ^2 versus Φ (lower portion of Table XIV), but most of the earlier work has been described in terms of saturation to this case. The saturation parameters, A and B, for niobium based on σ^2 versus Φ are not very different from those based on σ versus $\Phi^{1/2}$, and, therefore, the conclusions are the same.

The parameters appearing in equations (46) - (51) have been evaluated (Table XV), based on data in the literature for copper,[220] nickel,[222] and iron,[232,352] and on the present work for niobium. The doses have been adjusted to correspond to a common basis, i.e., to neutrons with energies greater than 1 Mev, assuming a fission spectrum. Table XVI gives values of a_o (Ref. 353), n_o, b, G (the shear modulus, Refs. 354 and 355), Gb^2, and σ_z (Ref. 356). The σ_z values were chosen approximately equal to the neutron scattering cross sections corresponding to neutron energies near 1 Mev. The barrier strengths in Table XV lie in the range (0.01 - 0.1) Gb^2, and, therefore, they correspond to a weak barrier model. Since the barriers are weak, the density, N_z, necessary to sustain the applied stress, is large. In particular, N_z is much larger than the density of defect clusters seen by TEM. For example,

TABLE XV

BARRIER STRENGTHS, BASED ON NEUTRON SCATTERING CROSS SECTIONS (σ_z) AND BARRIER SIZE EQUAL TO SATURATION EXCLUSION DISTANCE (D)

Metal	Ref.	$\sigma_u^{\dagger}$ kg/mm^2	$S = AB^{1/2}$ (kg/mm^2) Å	A kg/mm^2	$\Phi_s = 1/B$ cm^{-2}	$N_z(\Phi_s) = \frac{0.63}{V}$ cm^{-3}	$V = \frac{1}{\Phi_s \sigma_z}$ at. vol.	$D = (6V/\pi)^{1/3}$ Å	$F_i = (\frac{\pi}{24})^{1/2} bDA$ kg	F_i/Gb^2
					(x 10^{17})	(x 10^{17})	(x 10^6)		(x 10^{-10})	
Copper single crystals	220									
LYS		0.2	0.68	5.6	6.8	1.1	0.49	220	0.11	0.056
Nickel polycrystals	222									
LYS		17	0.46	31	450	78	0.007	50	0.15	0.031
Iron single crystals	232									
Annealed										
LYS		3.4	3.0	9.0	0.87	0.14	3.8	440	0.35	0.095
UYS		3.4	3.7	10.8	0.85	0.14	3.9	440	0.43	0.12
Decarburized										
LYS		3.4	1.6	4.7	0.87	0.14	3.8	440	0.18	0.049
UYS		3.6	2.1	6.1	0.87	0.14	3.8	440	0.24	0.065
Iron polycrystals	352	18.5	0.41	17.6	190	30	0.02	74	0.12	0.032
Niobium single crystals	present									
UYS	work	2.1	0.69	5.6	6.6	1.6	2.2	195	0.11	0.033
Niobium polycrystals										
LYS	present	4.9	0.58	6.0	10.8	2.7	0.13	166	0.10	0.030
UYS	work	6.1	0.71	8.9	15.7	3.9	0.09	146	0.13	0.039

†Extrapolated value, assuming $\sigma \propto \Phi^{1/2}$ at low doses.

TABLE XVI

CONSTANTS USED IN TABLE XV

Metal	a_o (Å)	n_o (cm^{-3})	b (Å)	G (kg/mm^2)	Gb^2 (kg)	σ_z (barns)
		($\times 10^{22}$)		($\times 10^{3}$)	($\times 10^{-10}$)	
Copper	3.615	8.47	2.56	3.11	2.04	3
Nickel	3.524	9.14	2.49	6.03	3.74	3
Iron	2.866	8.50	2.48	6.02	3.70	3
Niobium	3.301	5.56	2.85	4.28	3.48	7
Reference	353			354,355		356

Bourret and Dautreppe[357] observed a density of 6 x 10^{16} defect clusters per cm^3 for nickel irradiated to 4 x 10^{18} neutrons/cm^2, whereas N_z for nickel at this dose is 1 x 10^{18} cm^{-3} from equation (46), page 172, and Table XV, page 174. Similarly, our TEM measurements on niobium indicate a density of 7 x 10^{15} defect clusters per cm^3 after a dose of 1.8 x 10^{18} neutrons/cm^2 (Table XIII, page 158), whereas N_z for niobium at this dose is 3 x 10^{17} cm^{-3} according to equation (46) and Table XV.

As concerns S, the hardening rate in the low-dose limit, Table XV shows that S is about the same for the upper yield stress of single crystals and polycrystals of niobium [0.69 (kg/mm^2) Å for single crystals as compared to 0.71 (kg/mm^2) Å for polycrystals). On the other hand, the S's for Seidel's single crystals of iron[232] lie in the range (1.6 - 3.7) (kg/mm^2) Å, as compared to McRickard's value of 0.17 (kg/mm^2) Å for iron polycrystals.[352] The near agreement in hardening rates for single crystals and polycrystals of niobium suggests that the discrepancy in the hardening rates obtained by Seidel[232] and McRickard[352] for iron is not due to the difference between single crystals and polycrystals. Another point of interest is that the hardening rates are 20-30 percent greater for the upper yield stresses than for the lower yield stresses for both niobium (present work) and iron (Seidel[232]).

McRickard[352] has pointed out that a sudden jump in yield stress occurs at very low doses (below 10^{16} neutrons/cm^2, E > 1 Mev) for polycrystalline iron, as is seen from the fact that curve of σ versus $\Phi^{1/2}$ extrapolates to a point above the unirradiated yield stress at zero dose. A similar sudden jump is seen in the present work on polycrystalline niobium when σ^2 is plotted versus Φ (Figure 32, page 166). On the other

hand, no low-dose jump in yield stress is seen for single crystals, neither for iron (Seidel,[232] Figures 3 and 4), nor for niobium (present work, Figure 34, page 169). The fact that the curve of I_c versus Φ for polycrystalline niobium extrapolates to a positive intercept at $\Phi = 0$ (Figure 28, page 159) indicates that the jump in yield stress, where it exists, is a consequence of a sudden increase in the number and/or size of the defect clusters. As a result, when σ^2 is plotted versus I_c (Figure 30, page 161) instead of Φ (Figure 32, page 166), no sudden increase in yield stress is seen at very low doses.

The plot of I_c versus Φ (Figure 30, page 161) also has a bearing on the origin of the saturation of the radiation hardening for it shows that I_c saturates rather abruptly at a dose of about $(1.5 - 2.0) \times 10^{18}$ neutrons/cm^2. A coarsening of the defect clusters accompanies the saturation in I_c, as is seen in Figure 27, page 156. A saturation and coarsening of defect clusters seen by TEM was also reported by Bourret and Dautreppe[357] for nickel. The abruptness of the saturation in I_c and also in the radiation hardening suggests that a critical dose is reached after which no new clusters are formed and the existing ones grow larger. A model for such a process has been discussed by Varley.[246] The correlation of the saturation in I_c with the saturation in hardening suggests that the yield stress need not reach a stationary value with increasing dose, as is predicted by equation (50), page 172, but it may increase or even decrease depending on how the decrease in the density and the increase in size of the defect clusters affects the value of I_c.

A complicating factor is the possibility that the mechanism of slip dislocation motion may change in such a way as to promote dislocation

channeling after the critical dose is reached and coarsening of the defect clusters occurs. Some support for this idea, though by no means conclusive, is gained from an examination of TEM micrographs for samples irradiated to various doses and then strained to approximately the lower yield point. Figures 36-39 show TEM micrographs of samples irradiated to 2.2, 8.8, 20, and 44 x 10^{17} neutrons/cm^2, respectively. No dislocation channels are seen in Figure 36 (2.2 x 10^{17} neutrons/cm^2, below the critical dose) and they are rarely seen at such a low dose; the dislocations are tangled and in an early stage of cell formation as is characteristic of unirradiated niobium at higher strains. In Figure 37 (8.8 x 10^{17} neutrons/cm^2, slightly below the critical dose), the dislocation tangles appear somewhat more aligned (upper left to lower right), but again no clear indication of a dislocation channel is seen. In Figure 38 (20 x 10^{17} neutrons/cm^2, slightly above the critical dose), a dislocation channel is delineated by the elongated tangled dislocation structure and the reduction in defect cluster density; however, wide regions exist at this dose in which dislocation channels were not observed. Finally, in Figure 39 (44 x 10^{17} neutrons/cm^2, above the critical dose), well-defined dislocation channels are seen with significantly fewer dislocation tangles in the defect-rich matrix. The dislocation channels probably start at regions of high stress concentration. Once an incipient channel is formed, dislocation motion is concentrated within the channel, where the defect cluster concentration is low. The stress level at which the channeled dislocations move should be largely independent of the defect cluster concentration in the matrix and thus independent of dose.

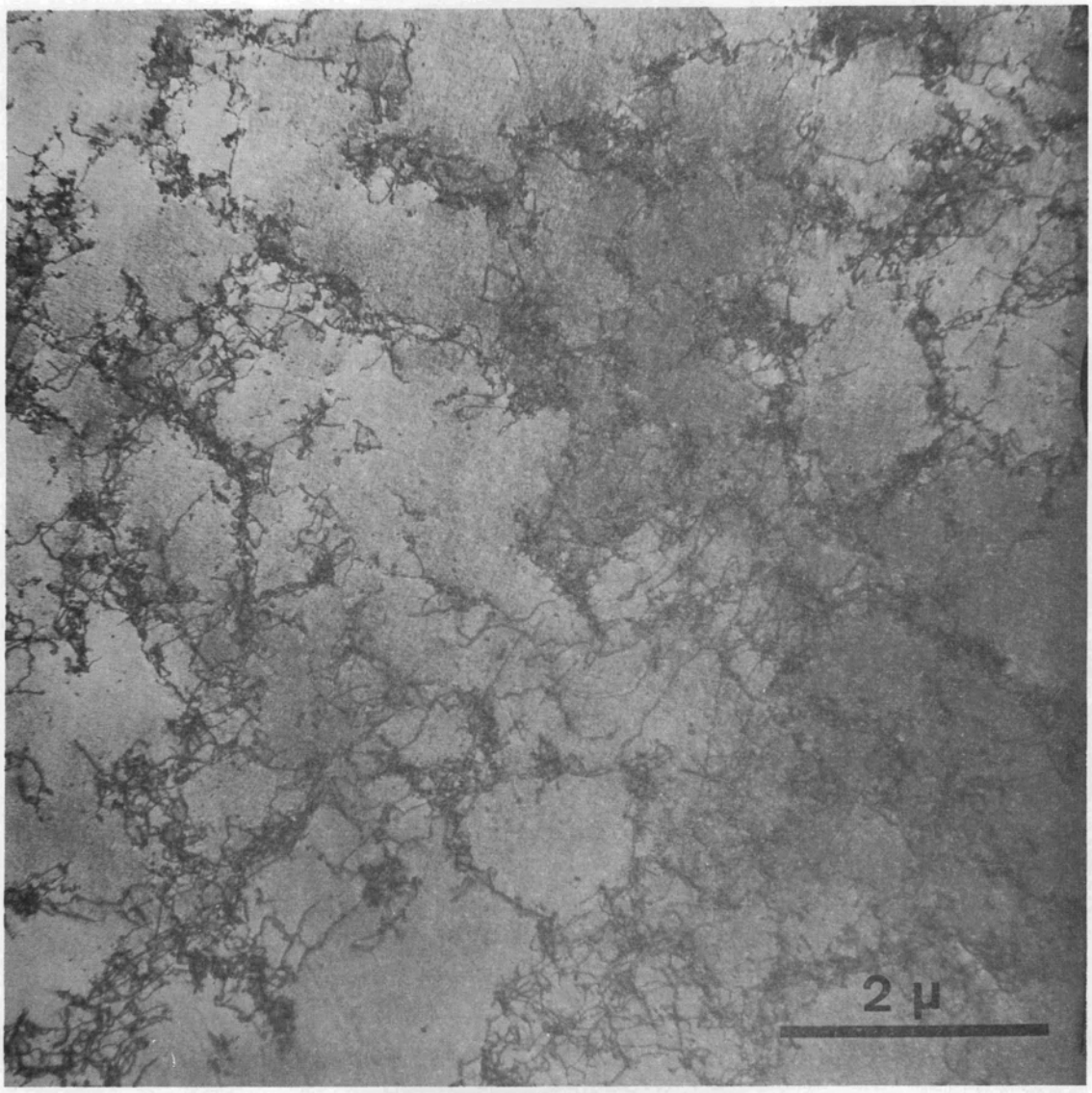

Figure 36. Dislocation tangles in CIBA-A niobium irradiated to 2.2×10^{17} neutrons/cm^2 (E > 1 Mev) and strained 2.8 percent in tension.

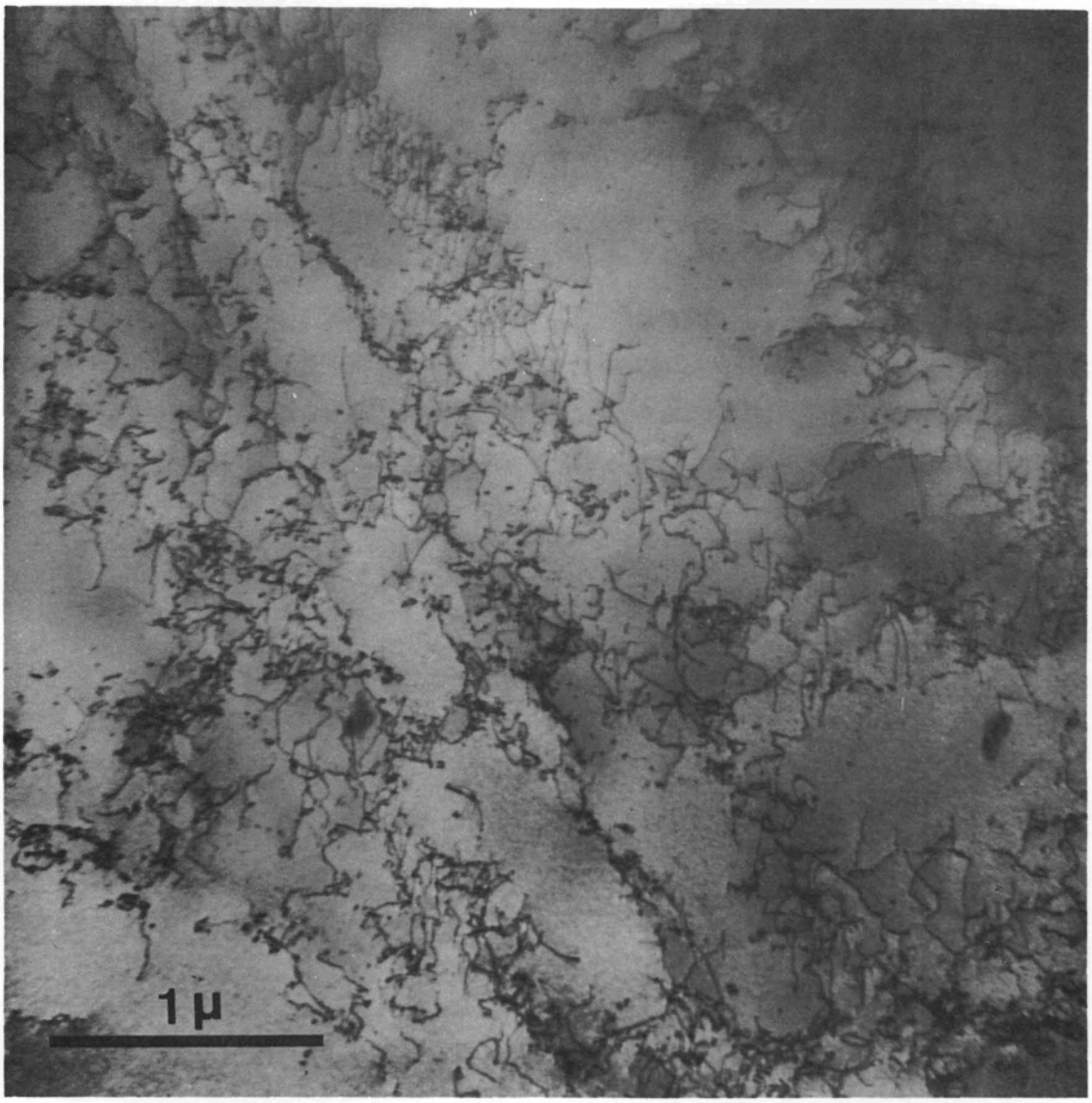

Figure 37. Dislocation structure in CIBA-A niobium irradiated to 8.8×10^{17} neutrons/cm^2 (E > 1 Mev) and strained 2.8 percent in tension.

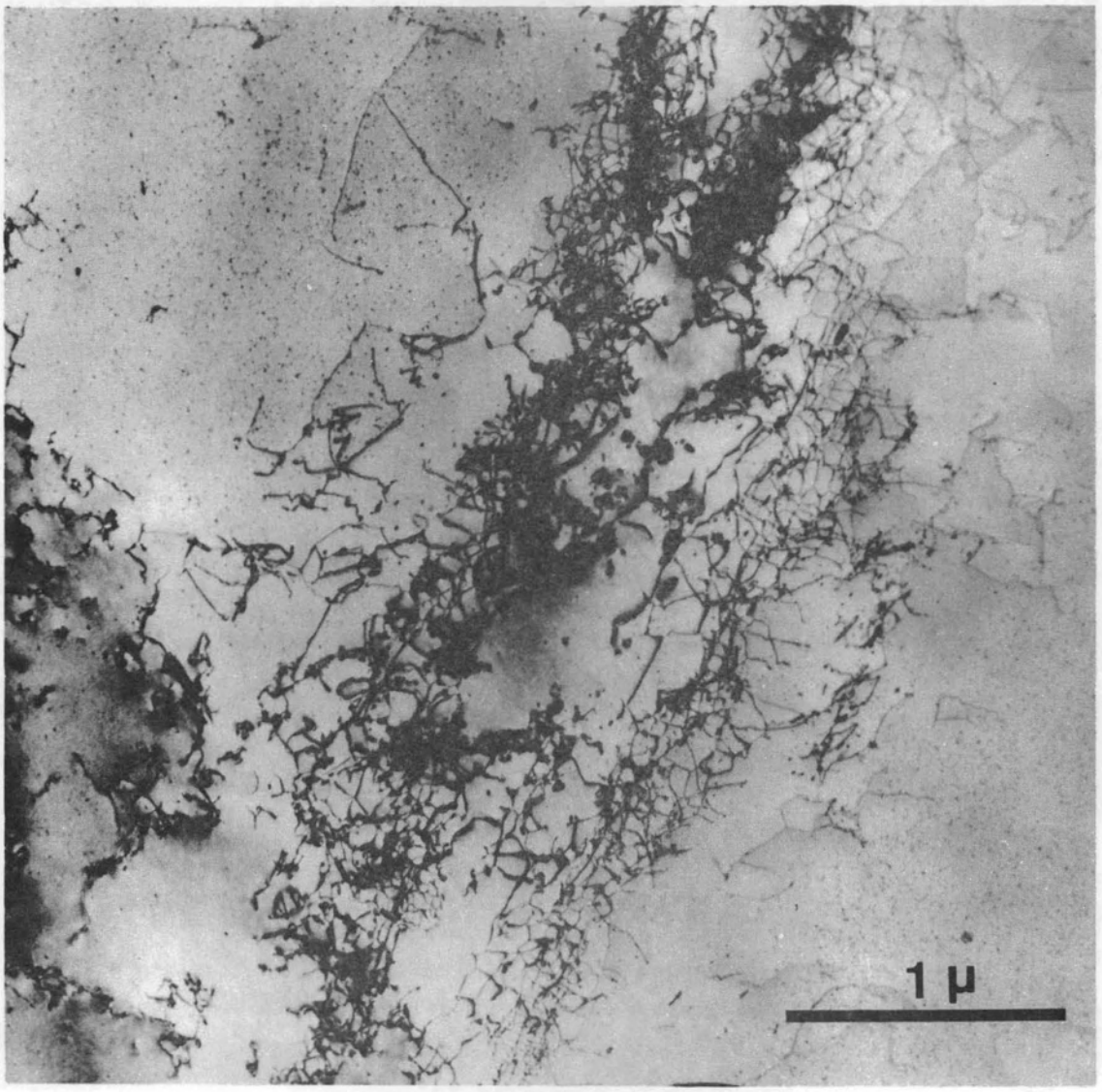

Figure 38. Dislocation channel in CIBA-A niobium irradiated to 2.0×10^{18} neutrons/cm^2 (E > 1 Mev) and strained 2.0 percent in tension.

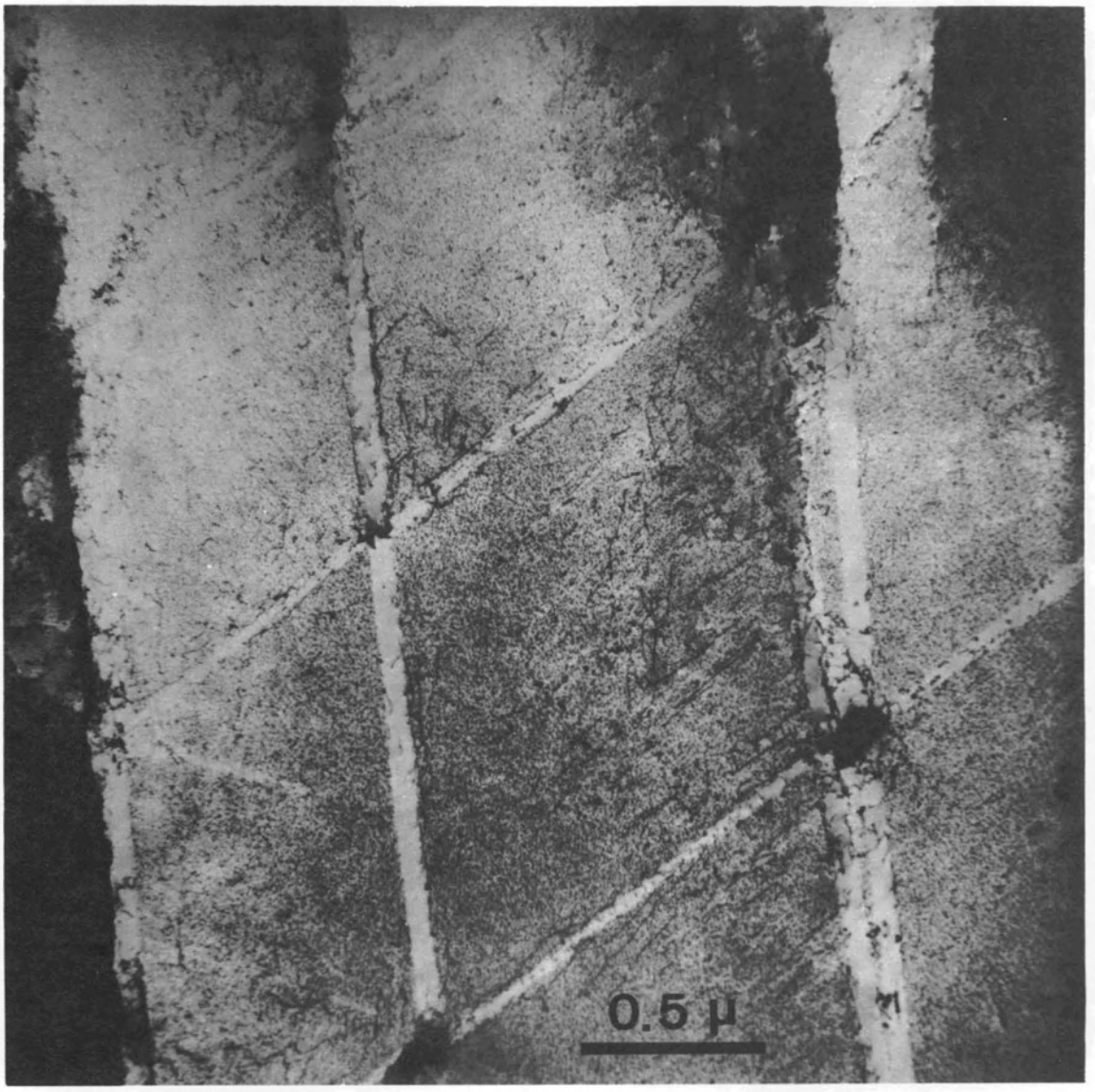

Figure 39. Dislocation channels in CIBA-A niobium irradiated to 4.4×10^{18} neutrons/cm^2 (E > 1 Mev) and strained 6.6 percent in tension.

Another basis for understanding the saturation phenomenon lies in the effect of interstitial impurities. Seidel[232] has suggested that the dislocation obstacles in iron consist of complexes of individual radiation-produced defects and impurity carbon atoms, which is consistent with a higher saturation yield stress for his annealed (20 wt. ppm carbon) than for his decarburized (< 8 wt. ppm carbon) samples. Some support for the viewpoint that radiation hardening correlates with the interstitial impurity content is found in the present study on niobium. In the next chapter, irradiation experiments are described on two niobium stocks which differed by approximately a factor of two in impurity carbon level. For samples irradiated to the same dose of 2×10^{18} neutrons/cm^2, the yield stress upon irradiation was observed to increase proportional to the square root of the carbon contents. Since a dose of 2×10^{18} neutrons/cm^2 is slightly above the dose at which saturation commences, our results are in agreement with the suggestion of Seidel that the stress at saturation is governed by the interstitial impurities. However, it is not clear from the present work that the saturation phenomenon in niobium can itself be directly correlated with the depletion of free interstitial impurities such as carbon. For niobium, electrical resistivity and internal friction measurements[283] have shown that interstitial impurities, particularly oxygen, can become trapped at radiation-produced defects. However, the trapping occurs at temperatures above about 120°C, whereas the irradiation temperature for our polycrystalline tensile samples was 50°C. Furthermore, as we shall see in the next chapter, a further hardening occurs when irradiated niobium (dose = 2×10^{18} neutrons/cm^2) is annealed above 120°C

("radiation-anneal hardening"), and it is therefore reasonable to associate this with the motion of impurities to the dislocation obstacles, thereby strengthening them. Thus, not all of the interstitial impurities appear to be associated with radiation-produced defect clusters at the onset of saturation.

CHAPTER VII

RADIATION-ANNEAL HARDENING -- AN EFFECT OF POST-IRRADIATION ANNEALING ON THE YIELD STRESS

I. INTRODUCTION

In Chapter II, "radiation-anneal hardening" was defined as the increase in yield and flow stresses produced in irradiated metals upon low temperature post-irradiation annealing. This hardening effect has been observed primarily in body-centered cubic refractory metals. Some time ago, Makin and Minter[241] first reported radiation-anneal hardening in neutron-irradiated niobium containing about 1600 wt. ppm oxygen; the hardening was observed at 100-200°C, near $T/T_m = 0.16$. They attributed the large increase in yield stress in their niobium upon post-irradiation annealing to the migration of radiation-produced vacancies to dislocation lines, pinning the dislocations, and increasing the stress necessary to move them. However, as is discussed more fully below, recent resistivity and internal friction measurements in irradiated niobium by Williams *et al.*[283] have shown that oxygen becomes trapped at radiation-produced defects upon annealing in the range 100-200°C. Therefore, the results of our experiments on radiation-anneal hardening are interpreted in terms of the motion of interstitial impurities, particularly oxygen and carbon, to radiation-produced defects.

In this chapter, the results of radiation-anneal-hardening studies on niobium of three purities are presented. Table XVII shows that the interstitial impurities levels are relatively low, particularly as

regards oxygen when compared to 1600 wt. ppm oxygen in the niobium of Makin and Minter.[241] Polycrystalline samples from CIBA-A and CIBA-B niobium were tested in tension, and foils from CIBA-A samples were examined by transmission electron microscopy following irradiation to 2×10^{18} neutrons/cm^2 (E > 1 Mev) at about 50°C and annealing for two hours in a dynamic vacuum at temperatures up to 800°C. The defect cluster size distribution was determined in an effort to correlate the radiation-anneal hardening with the number and sizes of defect clusters. In addition, some results of radiation-anneal hardening are presented for Wah Chang niobium single crystals irradiated to 2.8×10^{17} neutrons/cm^2 (E > 1 Mev) at 100-110°C.

TABLE XVII

INTERSTITIAL IMPURITIES IN NIOBIUM STOCKS USED IN RADIATION-ANNEAL-HARDENING STUDIES

	Concentration (wt. ppm)			
Material	C	O	N	H
CIBA-A	60	38	5	< 1
CIBA-B	35	41	5	< 1
Wah Chang	11	30	24	2

II. TENSILE TESTS

CIBA-A Niobium

Figure 40 shows the lower yield stress in CIBA-A niobium, determined at 24°C, for irradiated and unirradiated samples as a

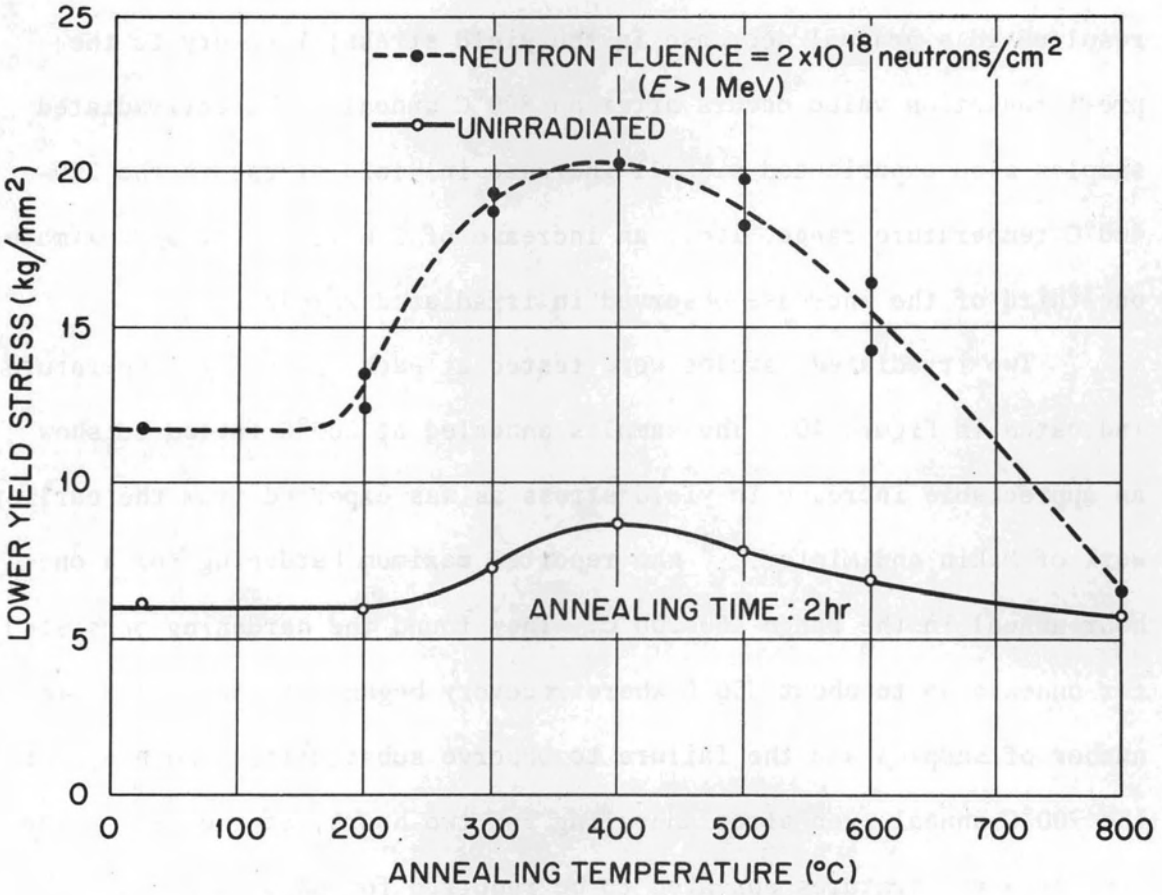

Figure 40. The lower yield stress of neutron-irradiated and unirradiated CIBA-A niobium as a function of annealing temperature for two-hour anneals.

function of annealing temperature. Neutron irradiation increased the yield stress from 6.1 to 11.7 kg/mm^2 (an increase of 5.6 kg/mm^2) and post-irradiation annealing at about 400°C brought the yield stress to 20.3 kg/mm^2 (a further increase of 8.6 kg/mm^2). Annealing above 400°C resulted in a gradual decrease in the yield stress; recovery to the pre-irradiation value occurs after an 800°C anneal. The unirradiated samples also experienced a small increase in yield stress in the 200-400°C temperature range, i.e., an increase of 2.6 kg/mm^2 or approximately one-third of the increase observed in irradiated samples.

Two irradiated samples were tested at each annealing temperature indicated in Figure 40. The samples annealed at 200°C failed to show an appreciable increase in yield stress as was expected from the earlier work of Makin and Minter,[241] who reported maximum hardening for a one-hour anneal in the range 180-200°C. They found the hardening persisted for anneals up to about 350°C where recovery began. Because of a limited number of samples and the failure to observe substantial hardening for the 200°C anneal even after annealing for two hours, at the time higher annealing temperatures appeared to be required for hardening. Consequently, the available samples of CIBA-A were annealed at temperatures above 200°C and the annealing behavior from room temperature to 200°C was not studied in this material. It is now felt, based on results for the CIBA-B material (described immediately below), that had anneals been carried out between 100°C and 200°C, a radiation-anneal-hardening peak would have been observed. As is pointed out later, the radiation-anneal hardening below 200°C is believed to be associated with the motion of oxygen and that above 200°C with the motion of carbon.

As regards the yielding characteristics of the radiation-annealed samples, it was observed that the yield drop was prominent after neutron irradiation, but after annealing at 300 and 400°C, it was quite small. However, the yield drop was observed to return and to increase with annealing temperatures above 500°C. These results lend support to the contention that interstitial impurities are removed from solid solution at temperatures where radiation-anneal hardening takes place, and furthermore, that they do not segregate at slip dislocations or their sources.

CIBA-B Niobium

A second study of radiation-anneal hardening was carried out using CIBA-B niobium. The carbon level was 35 wt. ppm for CIBA-B, as compared to 60 wt. ppm for CIBA-A niobium, whereas the other interstitial impurities levels were very nearly identical in the two materials (see Table XVII). Figure 41 shows a plot of the lower yield stress of CIBA-B niobium as a function of post-irradiation annealing. The yield stress exhibits two radiation-anneal-hardening peaks. The first lies at 120-200°C, which is the temperature range for the motion of oxygen to radiation-produced traps as revealed by internal friction and electrical resistivity measurements.[283] The second, broader, peak in Figure 41 has its maximum at 300-400°C or roughly in the same temperature range as the radiation-anneal-hardening peak seen for CIBA-A niobium (Figure 40). The temperature range of 300-400°C correlates with that for resistivity annealing attributed to carbon.[358] The lower temperature for the oxygen peak than for the carbon peak is consistent with the lower migration enthalpy for oxygen (1.18 ev) than for carbon (1.43 ev) in niobium.[359,360] The

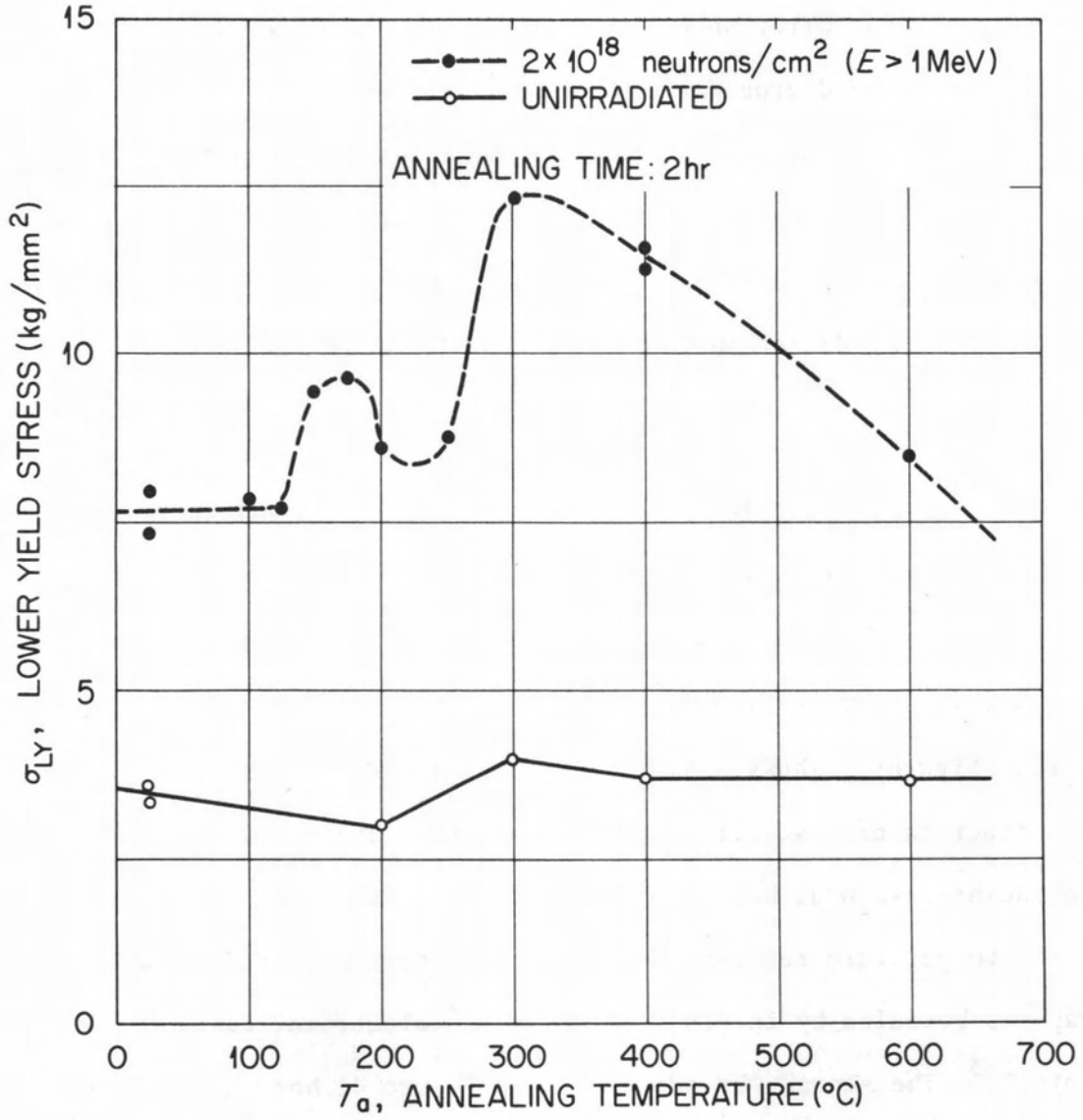

Figure 41. The lower yield stress of neutron-irradiated and unirradiated CIBA-B niobium as a function of annealing temperature for two-hour anneals.

smaller magnitude of the lower-temperature or oxygen peak (an increase of 2 kg/mm^2) in Figure 41 suggests that oxygen is a less effective hardener than carbon, since the oxygen concentration is somewhat higher than the carbon concentration in CIBA-B niobium (Table XVII, page 186). The oxygen concentrations in CIBA-A and CIBA-B niobium are about equal, but the oxygen peak was not detected in CIBA-A, as mentioned above, because anneals were not carried out at 120-200°C.

The magnitude of the carbon peak at 300-400°C is greater for CIBA-A (Figure 40) than for CIBA-B (Figure 41) niobium, which is consistent with the higher carbon content of CIBA-A niobium (Table XVII). The higher carbon content of CIBA-A niobium is also indicated by better defined anneal-hardening peak for the unirradiated material.

Wah Chang Niobium

A preliminary study on Wah Chang niobium by Wechsler and Bode[361] indicates that radiation-anneal hardening also occurs in single crystals. The experiment involved the annealing in vacuum and testing of two pairs of single crystals from rod number 32 (see Figure 5, page 71). An unirradiated crystal and a crystal irradiated to 2.8×10^{17} neutrons/cm^2 comprised each pair of samples, which were given identical annealing treatments. The crystals were subjected to a series of load-unload tensile tests at room temperature. During the unload portion of the cycle, the crystals were annealed at succesively higher temperatures. The total strain was such that little if any work-hardening would have taken place in a continuous test.[239] Figure 42 shows the load-elongation curves for one pair of samples. The flow stress at approximately the

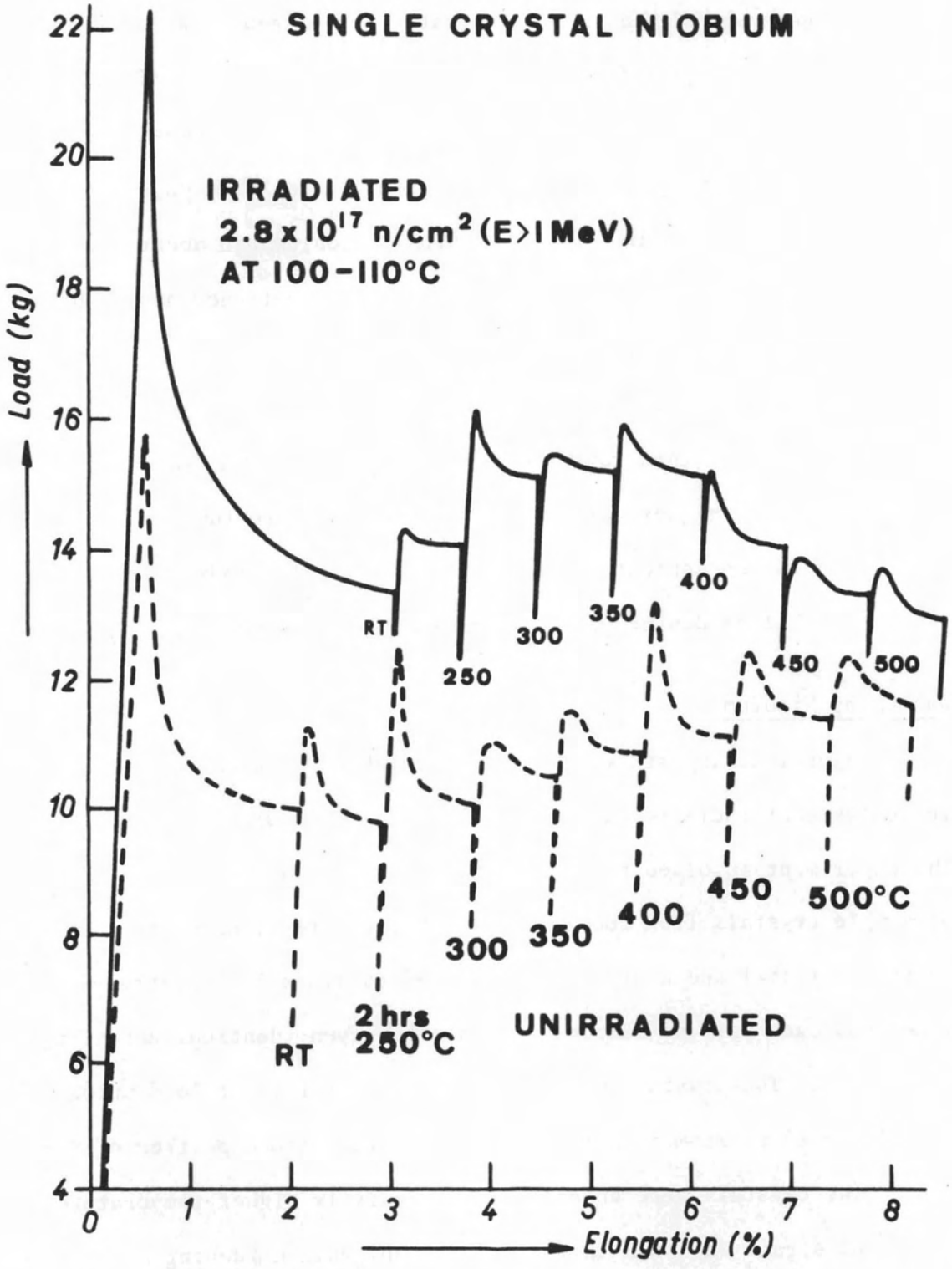

Figure 42. Load-elongation curves for unirradiated and neutron-irradiated Wah Chang single crystals, showing the effect of annealing during the unload portion of load-unload tensile tests.

same strain was determined for each sample in a given pair after two-hour anneals in 50°C increments up to 550°C. The difference in the flow stresses for the unirradiated and irradiated crystals are plotted as a function of annealing temperature in Figure 43. The curve shows a clear indication of a radiation-anneal-hardening peak at about 300°C.

III. TRANSMISSION ELECTRON MICROSCOPY

Foils for TEM were prepared from as-irradiated and post-irradiation-annealed CIBA-A niobium tensile samples. In addition, other samples were deformed in tension in order to investigate dislocation channeling in post-irradiation-annealed material.

As-Irradiated and Post-Irradiation-Annealed Samples*

Figure 44 shows radiation-produced defect clusters as black spots under the kinematical diffraction condition for undeformed samples as-irradiated and after annealing for two hours at 200-800°C. At first glance, these micrographs reveal no striking change in appearance as a result of increased annealing temperature up to 400°C, which is the temperature where maximum hardening was observed in this material (see Figure 40, page 187). However, determinations of the defect cluster density size-distribution function, n', for as-irradiated and 400°C-post-irradiation-annealed samples indicate that indeed a change in defect cluster distribution occurred upon 400°C-annealing. Figure 45 represents plots of n' versus defect cluster size for three samples as measured on

*Also see Appendix C.

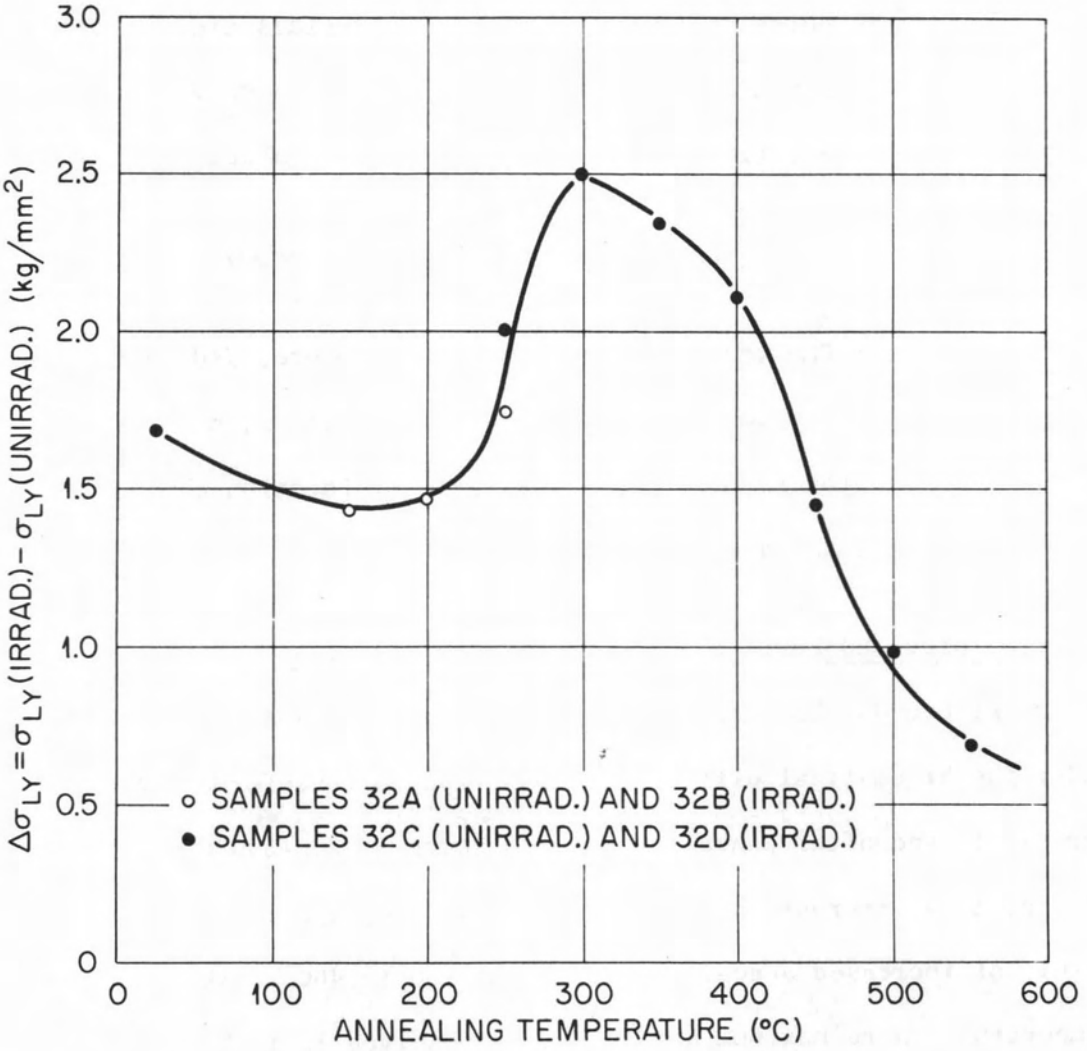

Figure 43. Radiation-anneal hardening in Wah Chang single crystal niobium.

The difference between yield stresses for irradiated (2.8×10^{17} neutrons/cm^2 at 100-110°C) and unirradiated samples as a function of isochronal (2 hours) annealing temperature.

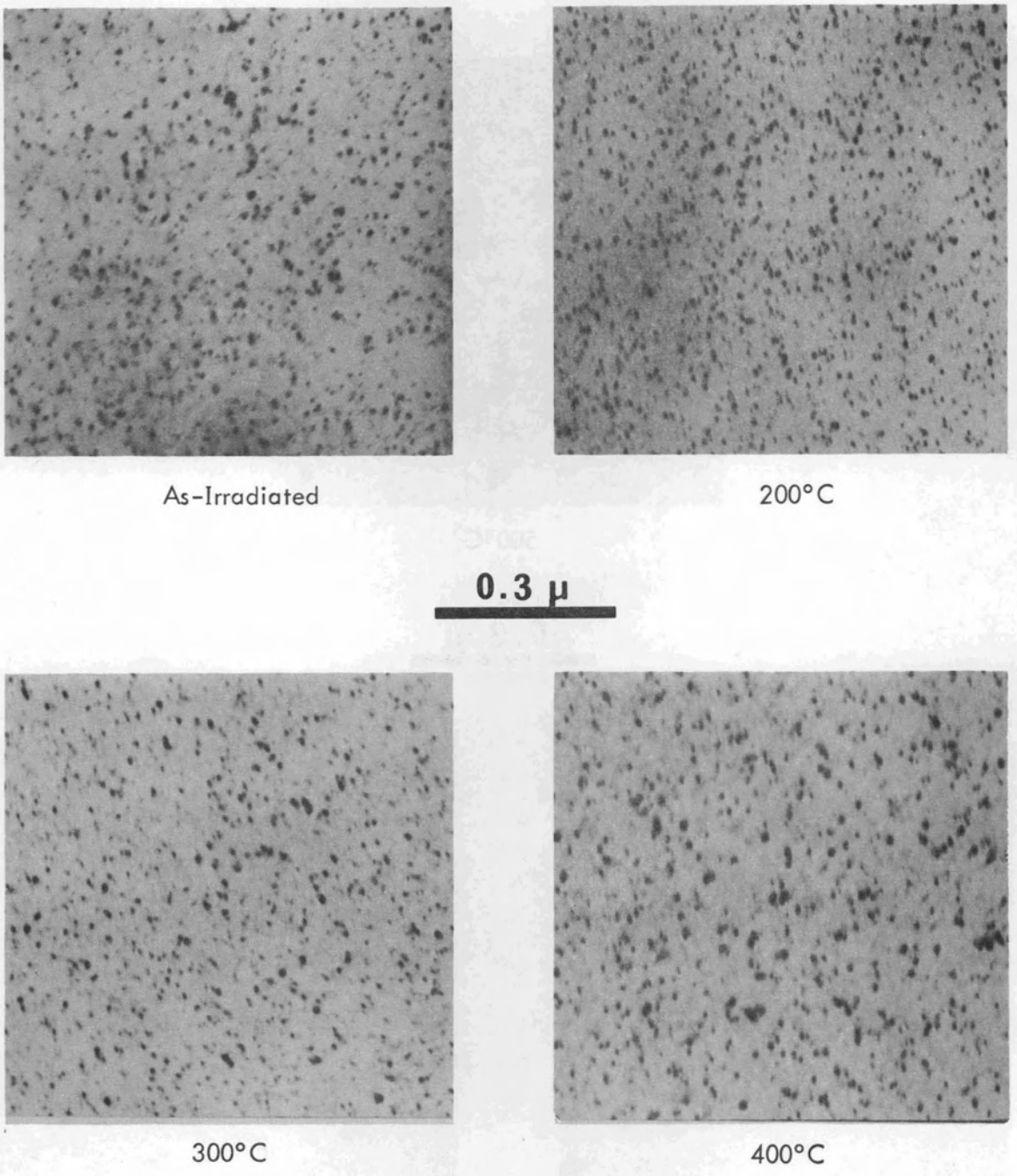

Figure 44. Defect clusters in neutron-irradiated CIBA-A niobium as a function of two-hour post-irradiation anneals at the temperatures indicated.

Dose = 2×10^{18} neutrons/cm^2 (E > 1 Mev). Irradiation temperature ~ 50°C.

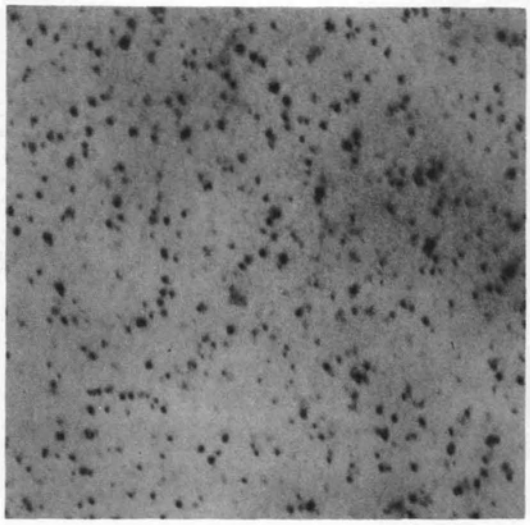

500°C

0.3 μ

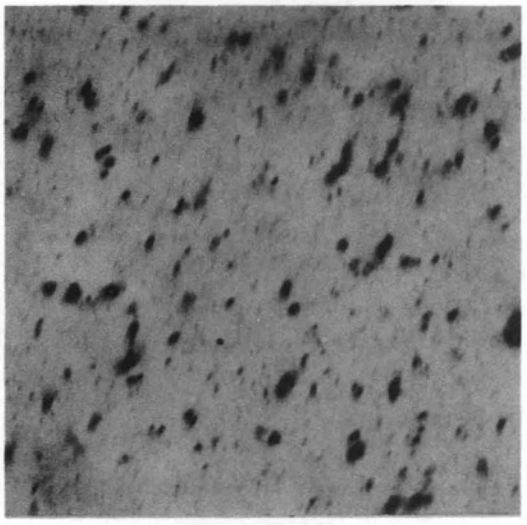

600°C

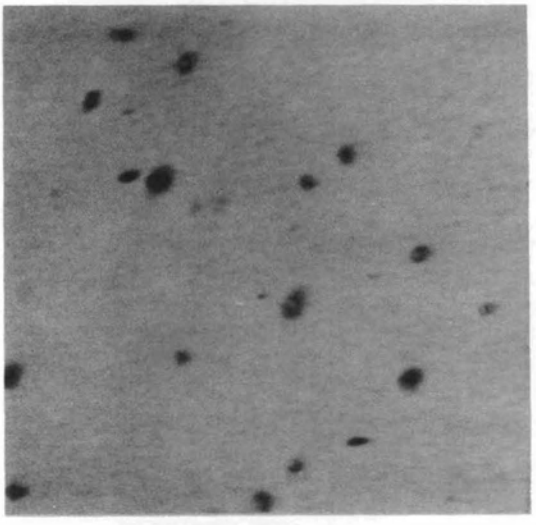

800°C

Figure 44. (continued).

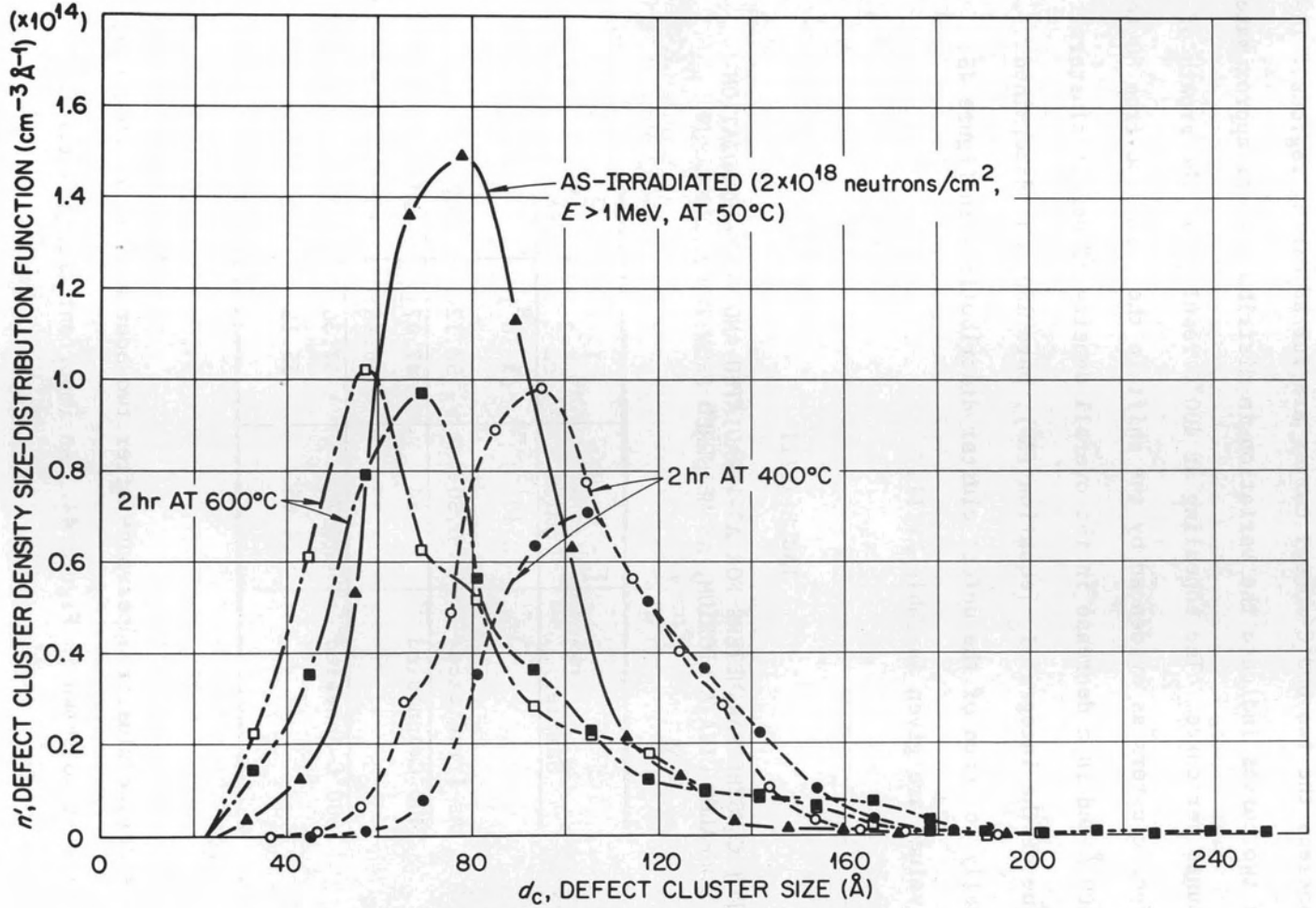

Figure 45. Defect cluster density size-distribution function versus defect cluster size in as-irradiated and post-irradiation-annealed CIBA-A niobium.

a Zeiss Particle Size Analyzer. The two curves for the 400°C-annealed niobium are for defect cluster counts from different regions in the same foil, whereas the two 600°C-anneal curves are for adjoining regions. The sets of two curves indicate the variation in distribution for approximately 1500 counts per curve. The annealing at 400°C resulted in the growth of the defect clusters as evidenced by the shift in the peak size from 80 to about 100 Å and in a decrease in the overall density of defect clusters. The value of the integral I_c [equation (39), page 150] was determined graphically for each of the defect cluster distributions in Figure 45. The I_c values are given in Table XVIII.

TABLE XVIII

DEFECT CLUSTER PARAMETERS FOR AS-IRRADIATED AND POST-IRRADIATION-ANNEALED CIBA-A NIOBIUM, AS MEASURED FROM TEM MICROGRAPHS

Sample	n cm^{-3}	I_c cm^{-2}	$\bar{d}_c$ (Å)
	($\times 10^{15}$)	($\times 10^{8}$)	
As-Irradiated	6.50	53.12	82
400°C-Annealed	4.84	47.97	99
	3.72	40.45	109
600°C-Annealed	4.75	37.36	79
	4.85	35.15	72

The defect cluster appearance after two-hour anneals at 500, 600, and 800°C are also shown in Figure 44. An important change after the

anneal at 600°C is the presence for the first time of numerous small spots throughout the sample. A striking difference between these spots appearing after a 600°C-anneal and those present after lower temperature anneals is seen in Figure 46. In the vicinity of the grain boundary the larger defect clusters, which are present in as-irradiated samples, are no longer found, whereas the new, small defects are seen near the boundary. This observation of a depletion of the larger defect clusters adjacent to a boundary and the appearance of a second group of clusters is similar to the observations of Makin *et al.*[49] in neutron-irradiated copper following a mild anneal at 300°C and of Brimhall *et al.*[83] and Maher and Eyre[92] in irradiated molybdenum. Since the larger defect clusters present in the as-irradiated sample are believed to be predominately interstitial in nature and furthermore since vacancies are generally believed to migrate at higher temperatures than interstitials, it is reasonable to infer that the small defect clusters seen in niobium after the anneal at 600°C are vacancy clusters.

The plot of n' as a function of defect cluster size for the 600°C-annealed sample in Figure 45 reveals a substantial decrease in the density of the large clusters. On the other hand as was said before, there is an increased density of small clusters compared to the 400°C-annealed sample. These curves show a peak size of about 60 Å. Establishment of the actual size of the defect clusters, particularly at small sizes, is a rather difficult experimental problem, since increasing the enlargement of micrographs to where the smallest clusters are of a size convenient for measurement simultaneously makes the demarcation between cluster and background

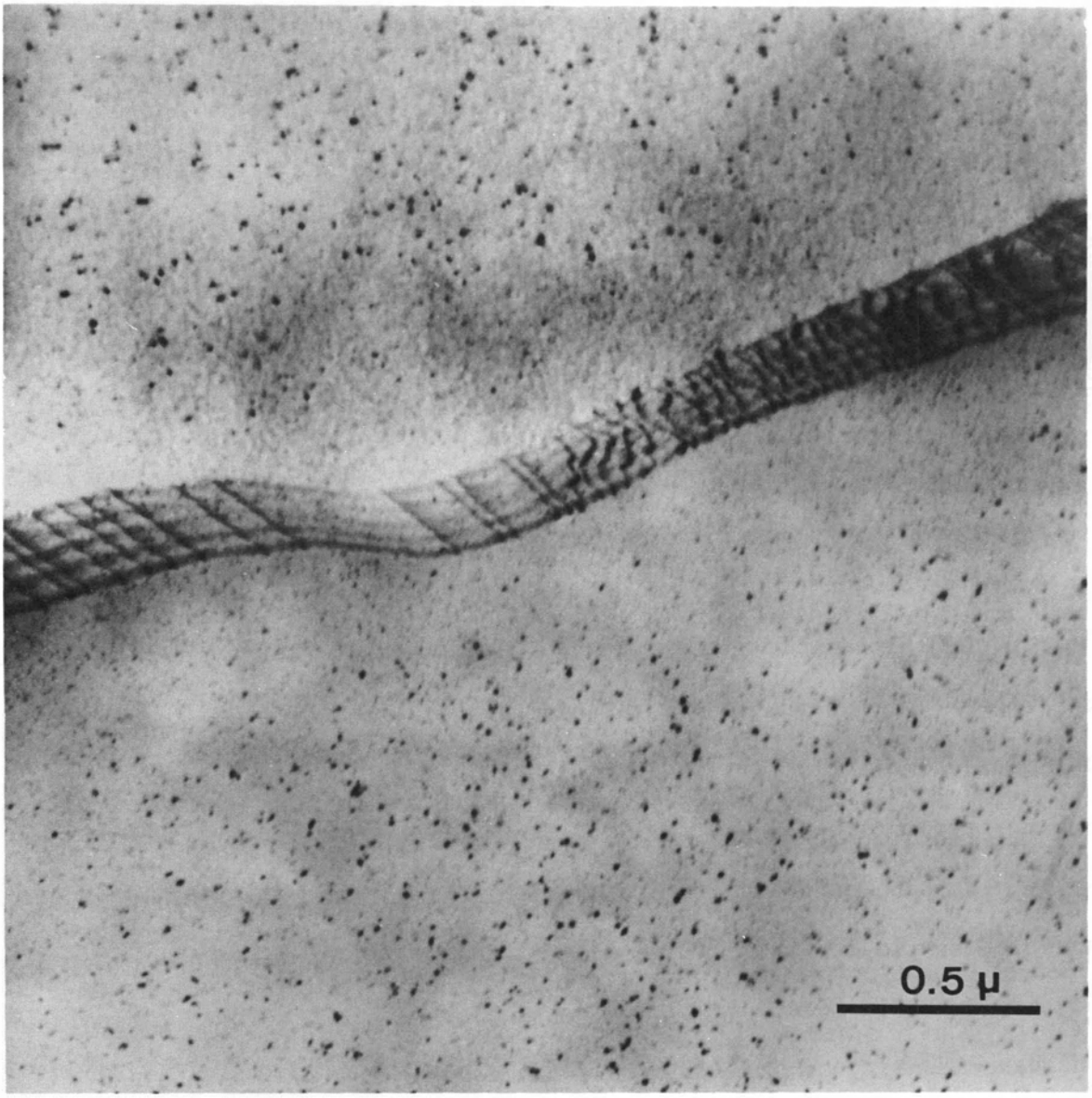

Figure 46. Defect clusters in neutron-irradiated CIBA-A niobium after a two-hour post-irradiation anneal at 600°C, showing two types of clusters.

The large defect clusters are depleted in the vicinity of the grain boundary, whereas the small clusters show no depletion.

diffuse. Thus, the decrease in density at cluster sizes below the peaks near 60 Å for the 600°C anneal in Figure 45 is not well established.

Following the anneal at 800°C for two hours, most of the defect clusters have annealed out, leaving only a relatively few large dislocation loops. These loops, which are clearly resolvable in the electron microscope, were analyzed and found to be both vacancy and interstitial in type, with the latter being somewhat more predominant.[362]

Post-Irradiation-Annealed-and-Deformed Samples*

Samples of CIBA-A niobium irradiated to 2×10^{18} neutrons/cm^2 ($E > 1$ Mev) were deformed in tension after post-irradiation anneals between 200 and 800°C and then examined in the electron microscope. As reported in Chapter VI, a dose of 2×10^{18} neutrons/cm^2 is just slightly greater than the dose at which the yield stress first exhibits saturation. In irradiated-and-deformed samples, TEM micrographs (see, for example, Figure 36, page 179) show considerable dislocation tangling in the defect-cluster-rich matrix for doses less than the transition dose, whereas at higher doses dislocation channeling predominates (Figure 39, page 182). For doses in the transition region (such as 2×10^{18} neutrons/cm^2) both types of deformation structure are observed in irradiated samples.

In samples post-irradiation annealed for two hours in the temperature range near 400°C where maximum radiation-anneal hardening is observed in CIBA-A niobium, there is little evidence of dislocation channeling and considerable dislocation structure in regions rich in defect clusters.

---

*Also see Appendix D.

The deformation structure in post-irradiation annealed samples is, however, quite inhomogeneous. For example, Figures 47 and 48 show two regions with widely different appearance from a sample annealed at 300°C and then nominally strained 2.2 percent. Figure 47 shows extensive dislocation tangling and a relatively high density of large dislocation loops (e.g., at A). Since these large loops are not observed in undeformed samples similarly annealed, they are thought to be part of the debris left behind as slip dislocations were forced through the defect clusters. On the other hand, in the vicinity of the boundary in Figure 48, one observes much less dislocation tangling and the formation of dislocation braids. The absence of dislocation channels in these regions where deformation has occurred supports the contention that channeling is less prevalent in radiation-anneal-hardened samples. The decreased tendency for dislocation channel formation is taken as evidence that the post-irradiation annealing has in some way made more difficult the removal of defect clusters by the slip dislocations. Consequently, during deformation most of the dislocations are forced to move through a matrix rich in defect clusters. It is suggested below that interstitial impurities migrate to radiation-produced defect clusters during annealing, thereby strengthening them.

Figure 49 rather strikingly illustrates that the defect clusters in annealed samples are effective barriers for slip dislocations. The micrograph is for a sample annealed for two hours at 600°C and subsequently strained 1.1 percent. Heating of the foil in the electron beam caused many of the dislocations seen in Figure 49 to move while under

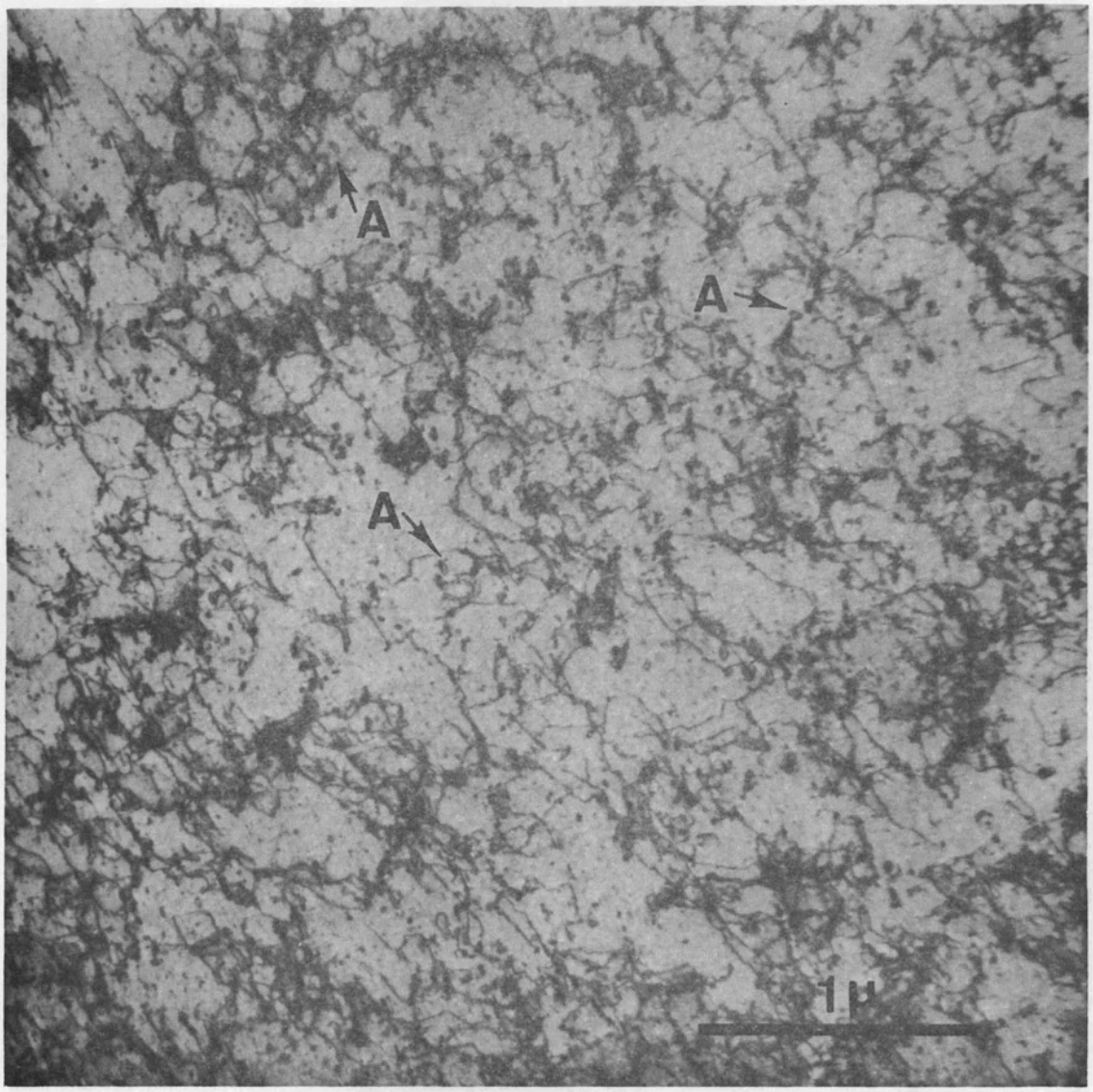

Figure 47. Dislocation and defect cluster structure in neutron-irradiated CIBA-A niobium post-irradiation annealed at 300°C and subsequently strained 2.2 percent in tension.

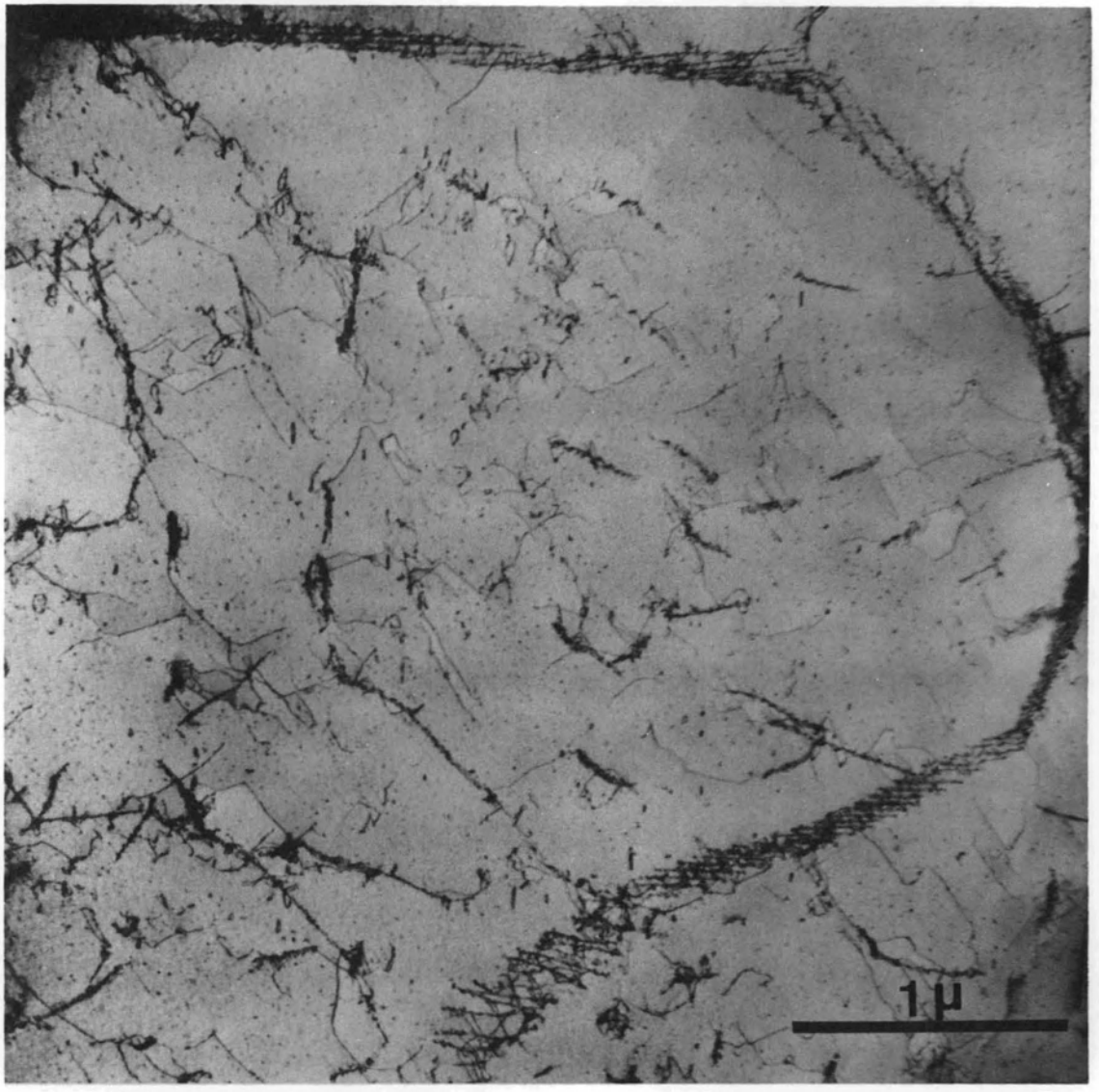

Figure 48. Boundary and dislocation braids in neutron-irradiated CIBA-A niobium post-irradiation annealed at 300°C and subsequently strained 2.2 percent in tension.

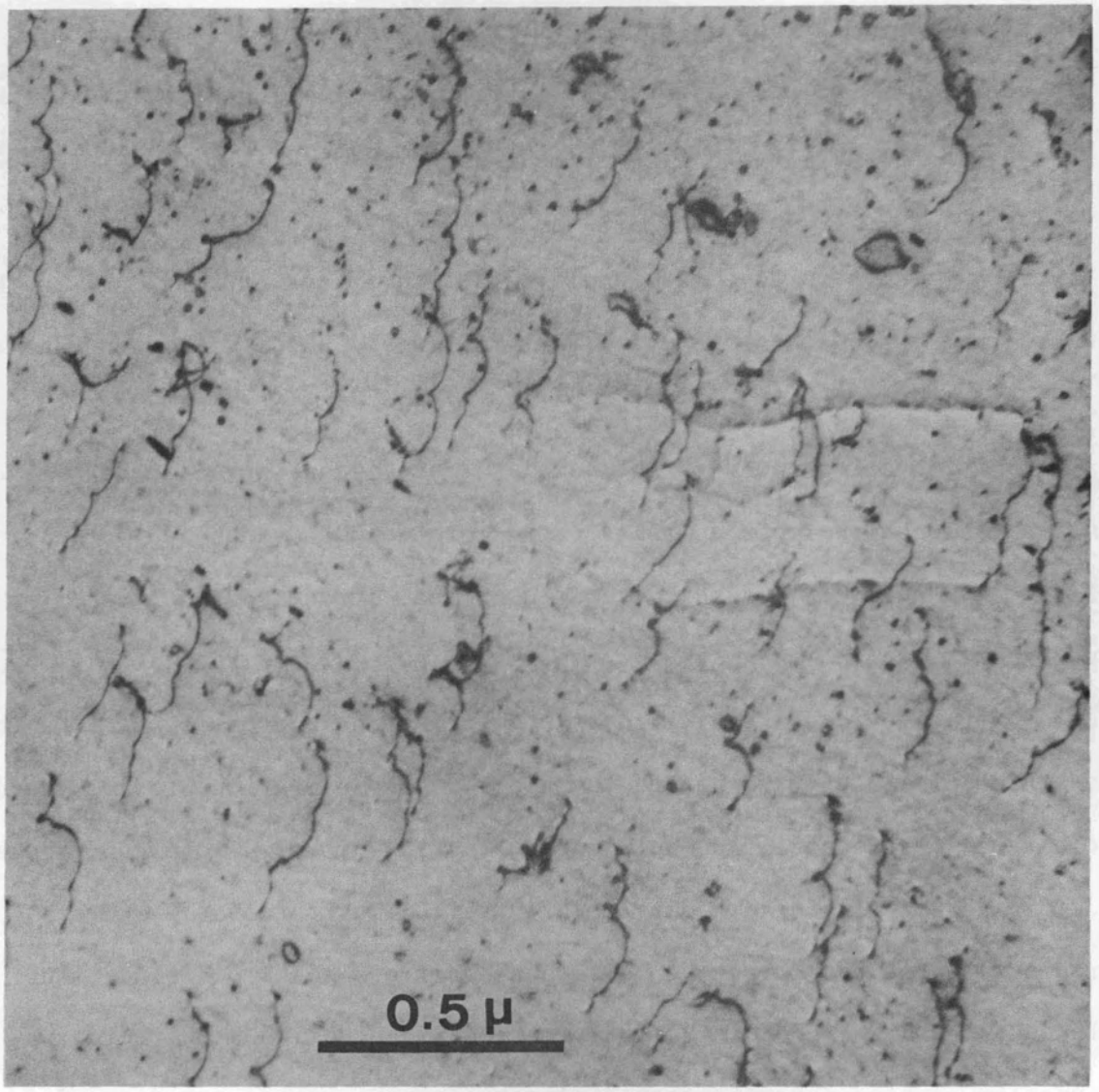

Figure 49. Slip dislocations bowed out between defect clusters in neutron-irradiated CIBA-A niobium post-irradiation annealed at 600°C and subsequently strained 1.1 percent in tension.

At the right in the micrograph is an example of a slip trace used to estimate the foil thickness, as described in Chapter IV, pages 90-92.

observation. Many of these dislocations are substantially bowed out between clearly visible defect clusters, suggesting that the clusters are strong barriers, as is borne out below. The average separation between pinning points as observed in Figure 49 is 1520 Å, which is in reasonable agreement with $\bar{\ell} = (I_c)^{-1/2}$ = 1660 Å as determined from the average of the two I_c values for the 600°C-annealed TEM samples. In Figure 49, there is also an example of a slip trace, at the right in the micrograph, used to estimate the foil thickness, as described in Chapter IV, pages 90-92.

In annealed-and-deformed samples there is an increased density of large dislocation loops as illustrated for the 600°C-annealed sample in Figures 49 and 50. Figure 50 shows a typical structure resulting from deformation in the bulk sample. In this figure, loops such as the one at A are believed to result from the deformation, whereas loops like the one at B are thought to be due to the growth of radiation-produced defect clusters. The association between deformation-produced loops and those due to defect clusters is particularly well illustrated at C where radiation-produced loops can be seen as barriers to slip dislocations. Indeed, the higher density of deformation-produced loops in radiation-annealed samples suggests that dislocations have bowed around the defect clusters, too strong to be broken through or swept up.

Following an anneal at 800°C, most of the radiation-produced defect clusters are clearly resolvable as dislocation loops. Figure 51 shows the type of dislocation structure seen after a strain of 0.8 percent. The yield stress in this sample has nearly recovered to its unirradiated level. The micrograph reveals several regular dislocation arrays. It

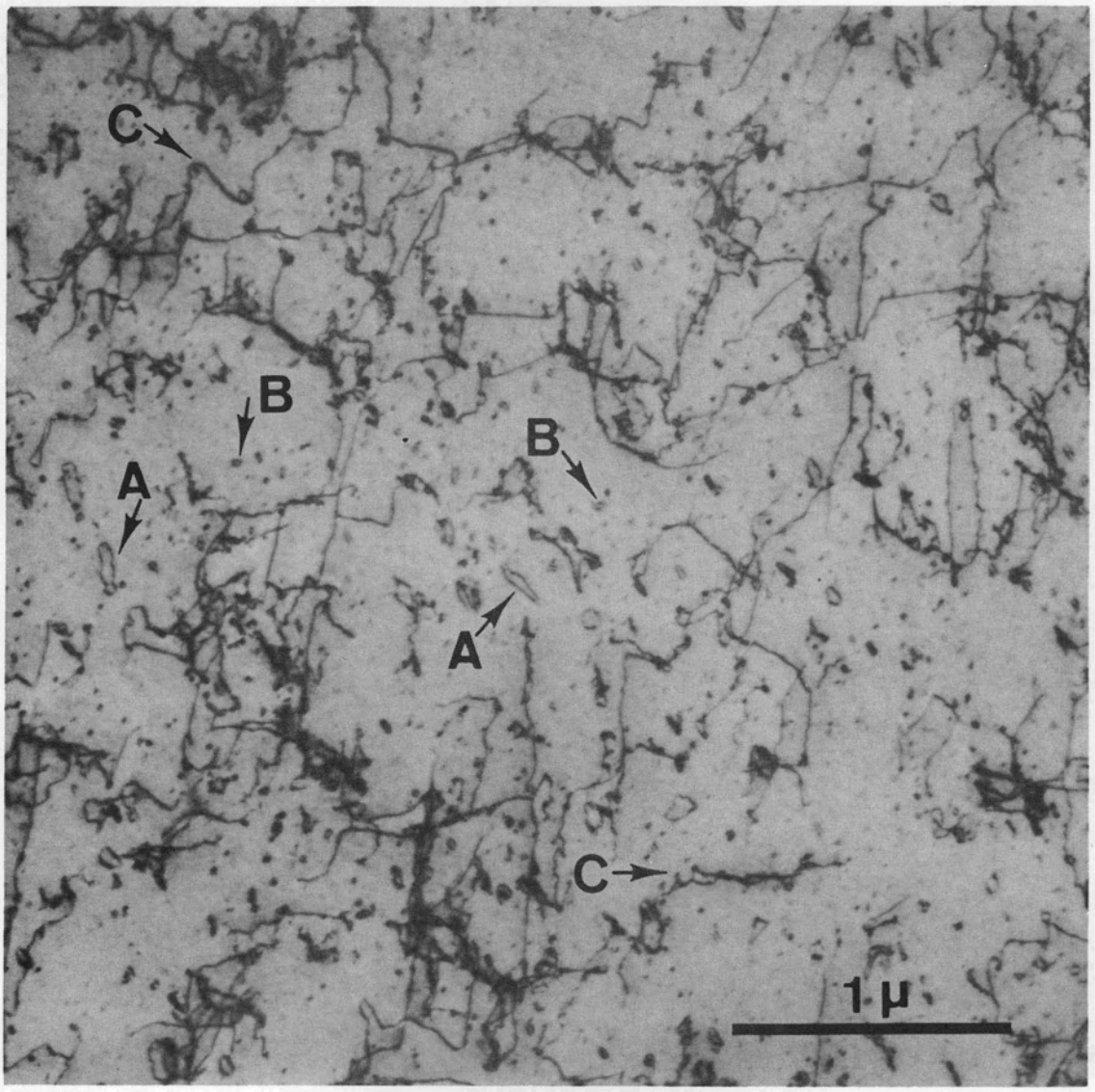

Figure 50. Dislocation and defect cluster structure in neutron-irradiated CIBA-A niobium post-irradiation annealed at 600°C and subsequently strained 1.1 percent in tension.

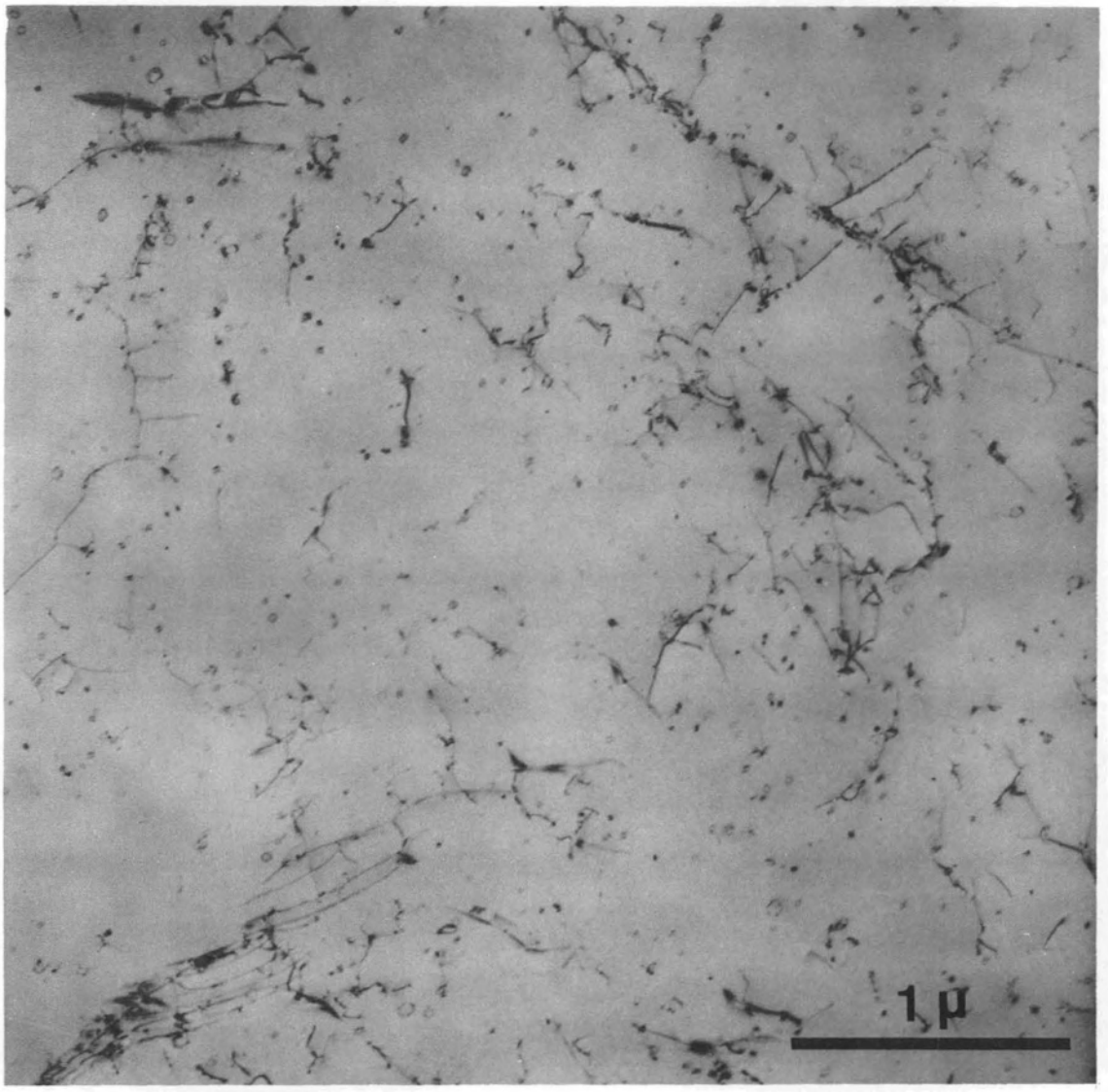

Figure 51. Dislocation arrays and loops in neutron-irradiated CIBA-A niobium post-irradiation annealed at 800°C and then strained 0.8 percent in tension.

is suggested that these structures originate from grown-in dislocations or possibly upon annealing from the coalescence of the radiation-produced defect clusters. Certainly the recovery in the yield stress is in part a reflection of the decreased density of clusters. However, as pointed out below, the recovery is also due partially to a weakening of the barriers *per se* upon annealing above, say, 500°C.

IV. DISCUSSION OF THE MECHANISM OF RADIATION-ANNEAL HARDENING

In Section II of this chapter it is shown that polycrystalline CIBA niobium, which has a relatively low interstitial impurity content, exhibits radiation-anneal hardening in two distinct temperature ranges centered at 120-200°C and 300-400°C, respectively. In addition, some evidence is presented to indicate that the Wah Chang single crystals also show an increase in yield stress upon post-irradiation annealing. The following discussion presents the evidence in support of the idea that radiation-anneal hardening is caused by the trapping of interstitial impurities at radiation-produced defect clusters.

Radiation-Anneal Hardening at 120-200°C

Figure 41 shows that a post-irradiation anneal for two hours at 175°C resulted in an increase of 2.0 kg/mm^2 in the yield stress of CIBA-B niobium irradiated to 2 x 10^{18} neutrons/cm^2. This increase is believed to be due to the strengthening of the radiation-produced defect clusters as the result of the migration of interstitial oxygen to the clusters where the oxygen becomes trapped. The basis for this interpretation is the evidence recently obtained by Williams *et al.*[283] on the annealing of

oxygen in neutron-irradiated niobium. The internal friction and electrical resistivity results of Williams *et al.* are summarized as follows:

(1) The oxygen internal-friction peak was appreciably reduced in height following irradiation upon annealing at 120-200°C.

(2) The electrical resistivity decreased with the same isothermal annealing kinetics at 150°C as the decrease in internal friction. This agreement was taken as evidence that the two property changes reflected the same process.

(3) The activation energy of the process at 150°C was 1.19 ev which agrees with the diffusion activation energy for oxygen in niobium.[359,360]

(4) A pronounced decrease in resistivity upon annealing between 120 and 200°C was observed in an irradiated sample only when oxygen was present.

Thus, Williams *et al.*[283] concluded that during post-irradiation annealing between 120 and 200°C oxygen is trapped at radiation-produced defect clusters such as those reported by Tucker and Ohr.[1] Indeed, Bullough *et al.*[284] showed that the kinetics reported by Williams *et al.*[283] for the process occurring at 150°C in neutron-irradiated niobium are consistent with the drift of oxygen to dislocation loops.

In view of the results of Williams *et al.*[283] and Bullough *et al.*,[284] we associate the radiation-anneal hardening in CIBA-B niobium at 120-200°C with the migration and trapping of oxygen at radiation-produced defect clusters. At present, the details of how oxygen trapped at defect clusters causes an increase in the yield stress are not known.

However, a possible mechanism is mentioned below in connection with the radiation-anneal hardening at 300-400°C.

Radiation-Anneal Hardening at 300-400°C

Figures 40 and 41 show radiation-anneal-hardening peaks at 300-400°C, respectively, in CIBA-A and CIBA-B niobium irradiated to 2 x 10^{18} neutrons/cm^2. The maximum increase in stress of 8.5 kg/mm^2 above the as-irradiated level was greater for CIBA-A niobium, which contained 60 wt. ppm carbon, than the stress increase of 4.6 kg/mm^2 observed in CIBA-B niobium, which contained 35 wt. ppm carbon. This increase in the magnitude of the radiation-anneal hardening with increasing carbon concentration, together with the additional evidence presented in the following paragraphs, suggests that carbon is responsible for the radiation-anneal-hardening peak at 300-400°C.

In Chapter VI, the yield stress following irradiation is observed to correlate well at low doses with the defect clusters seen by TEM, based on a dispersed barrier model. Since TEM has revealed a change in the size distribution of the defect clusters upon annealing at 400°C (Figure 45, page 197), it is important to see whether the yield stress increase can be accounted for by the change in defect cluster distribution. In answering this question, appeal is made to equation (40), page 151, which may be written as

$$\sigma(i\text{-}a) = \sigma(a) + \frac{2F(i\text{-}a)}{b} [I_c(i\text{-}a)]^{1/2} , \qquad (53)$$

where (i-a) connotes the value in the radiation-annealed condition and (a) indicates the value in the annealed condition. The stress increase

after radiation-anneal hardening relative to the increase upon irradiation, denoted by (i), is given by

$$f = \frac{\sigma(i\text{-}a) - \sigma_u(a)}{\sigma(i) - \sigma_u} = \frac{F(i\text{-}a)}{F(i)} \left[\frac{I_c(i\text{-}a)}{I_c(i)}\right]^{1/2} . \qquad (54)$$

For CIBA-A niobium (Figure 40, page 187), the value of the parameter f as determined from the yield stresses is 2.05. It follows from equation (54) and the average of the I_c values in Table XVIII, page 198, that F(i-a) after the 400°C anneal is 2.25 times the as-irradiated barrier strength F(i). Thus, radiation-anneal hardening in CIBA-A niobium cannot be explained on the basis of the change in I_c alone. A similar analysis based on equation (41), page 151, gives F(i-a) = 2.01 F(i) following the anneal at 400°C. Therefore, in order to explain radiation-anneal hardening consistent with the observed defect clusters, a maximum increase by approximately a factor of two in the strength of the defect clusters is required.

For the 600°C-anneal data analyzed according to equation (54), F(i-a) = 1.9 F(i), which is a slight decrease in barrier strength compared to the 400°C-anneal case. Thus, it is suggested that the yield stress recovery after the 600°C anneal (see Figure 40, page 187) is due to the combined effect of decreasing I_c (see Table XVIII, page 198) and the barrier strength. The decrease in barrier strength may be a reflection of the gradual breakup of the defect cluster-impurity complex by, say, carbon returning to solid solution.

Another possible source of radiation-anneal hardening is the agglomeration upon annealing of radiation-induced defects into clusters

not visible in the electron microscope. Since interstitial clusters appear to predominate in as-irradiated niobium, it is likely that the submicroscopic clusters would consist of vacancies. The assumption then would be that these clusters reach the optimum size to serve as effective barriers to dislocations upon annealing at 400°C and thus cause the increase in the yield stress. Then, during annealing at 600°C, these vacancy clusters grow to a size, which for the first time becomes visible by TEM. Williams *et al.*[358] have presented evidence which tends to discount such a mechanism. In a sample containing about 30 wt. ppm carbon and less than 3 wt. ppm oxygen, the resistivity increased after neutron irradiation, but it decreased upon annealing between 200 and 350°C to well *below* its pre-irradiation value. This implies that the species migrating in the temperature interval where radiation-anneal hardening occurs is not directly identifiable with defects, such as vacancies, produced by irradiation. Furthermore, the hardening seen in Figure 40, page 187, for the unirradiated material supports this conclusion.

Williams *et al.*[358] associate the decrease in resistivity for annealing between 200 and 350°C with the migration of carbon and its subsequent removal from the lattice by precipitation. They observed a decrease in resistivity for isochronal anneals of unirradiated as well as irradiated niobium containing carbon but essentially no decrease in resistivity for samples of low carbon content (i.e., less than about 4 wt. ppm). The resistivity showed a greater decrease for irradiated samples than for unirradiated material with the same amount of carbon in solution. Therefore, it seems reasonable to associate the rather small increase in yield stress for unirradiated CIBA-A niobium between

200 and 400°C (see Figure 40, page 187), as well as the larger increase for irradiated material with the migration of carbon. The evidence from the work of Williams *et al.*[358] for carbon trapping at radiation-produced dislocation loops, however, does not establish the case for carbon as firmly as the case for oxygen trapping at 120-200°C. A number of sources contribute to the uncertainty in the interpretation of the resistivity, internal friction, and radiation-anneal-hardening data in terms of the motion of carbon in the temperature range 200-400°C. In the first place, carbon is known to have a rather low solubility in niobium, and its precise state even in unirradiated material is not well known. Also, when oxygen is present, as it is in the radiation-anneal-hardening samples, the oxygen appears to have the initial claim to the radiation-produced loops. Thus, there may be competition between oxygen and carbon for sites at the loops on annealing between 200 and 300°C. Furthermore, Williams *et al.*[358] suggested that above 300°C oxygen dissociates from the loops and returns to solution, thereby adding to the complexity of the situation.

As mentioned in Chapter VI, radiation hardening in CIBA-A and CIBA-B niobium also seems to bear a relation to the carbon content. The yield stress increase upon irradiation, $\delta = \sigma(i) - \sigma(u)$, is 5.66 kg/mm^2 for CIBA-A niobium and 4.15 kg/mm^2 for CIBA-B niobium. The ratio $\delta(A)/\delta(B) = 1.36$, whereas the square root of the ratio of corresponding carbon concentration is 1.31. Although the point requires additional experimental verification, the yield stress increase upon irradiation appears to correlate with the square root of the carbon concentration in agreement with the results of Seidel on iron.[232]

At the present time, the hardening between 200 and 400°C in niobium is believed to be related to the motion of carbon, presumably to dislocation loops in the irradiated material. Although the firm establishment of carbon as the actual source of the 200-400°C radiation-anneal hardening is not yet possible, it seems likely that if the hardening does arise from interstitial impurities, the explanation lies in the effect of the impurities on the short-range contact interaction. This is suggested by the TEM results which indicate that post-irradiation annealing up to 400°C changes the character of the loops in such a way as to make it more difficult for slip dislocations to remove them and, consequently, more difficult to create dislocation channels.

CHAPTER VIII

TEMPERATURE DEPENDENCE OF YIELDING IN NEUTRON-IRRADIATED SINGLE CRYSTAL NIOBIUM*

I. INTRODUCTION

A distinguishing feature of plastic deformation in unirradiated body-centered cubic (bcc) metals, in comparison to face-centered cubic (fcc) metals, is the pronounced increase in their yield stress with decreasing test temperature. This behavior characteristic of bcc metals has been demonstrated for single crystal niobium by Christian and Masters,[295] Mitchell *et al.*,[320] Kim and Pratt,[321] Sherwood *et al.*,[322] and Orava *et al.*[363] However, to our knowledge, the effect of neutron irradiation on the temperature dependence of the yield stress had not previously been investigated in single crystal niobium, at the time the present study was begun.

Neutron irradiation is known to introduce a marked temperature dependence to the yield stress of fcc metals, whereas the temperature sensitivity of bcc metals does not appear to be greatly changed, at least at relatively low doses where substantial changes occur in fcc metals. The absence of appreciable change upon irradiation in the temperature dependence of the yield stress of bcc metals has been shown by Arsenault[323] for polycrystalline vanadium and by Ohr *et al.*,[240]

---

*The sample preparation and the analysis of the data were carried out at Oak Ridge National Laboratory, while most of the tensile tests were performed at Battelle Institute, Geneva.

Chow *et al.*,[267] and Smidt and Bement[324] for polycrystalline iron. However, a somewhat larger increase in the temperature dependence upon irradiation has been reported for compression tests on single crystal niobium by Guberman and Reed[325] and for tensile tests on single crystal iron by Seidel.[232]

In this chapter, the effect of neutron irradiation on the temperature dependence of the yield stress in single crystal niobium is presented in an abridged version. A more complete description of this work is given by Wechsler, Tucker, and Bode.[344]

II. TENSILE TEST RESULTS

As described more fully in Chapter III, Wah Chang niobium was the starting stock from which single crystal rods for the temperature dependence study were grown with the axis orientations shown in Figure 5, page 71. Approximately one-half of the tensile samples from these rods were irradiated to a dose of 2.8×10^{17} neutrons/cm^2 ($E > 1$ Mev). The unirradiated and irradiated samples were tensile tested at an applied strain rate of 1.75×10^{-4} sec^{-1} over a range of temperatures from room temperature to 93°K (crystals were tested at 298, 219, 171, 119, and 93°K).

Unirradiated Samples

At all test temperatures, the unirradiated single crystal niobium exhibited a yield drop with a tendency for an increased magnitude with decreasing test temperature. The crystal tested at room temperature showed three stage hardening with the onset of Stage II at approximately

40 percent strain, where previous studies indicate the beginning of secondary slip as detected by surface slip markings[239,364] and the departure of the tensile axis orientation from the great circle containing the slip plane normal [$\bar{1}$01] and the slip direction [111].[239,364,365] Furthermore, as reported by other authors,[320,334,363,366-369] there is a small stage zero, i.e., rapid hardening immediately after the yield drop and prior to Stage I.

With decreasing test temperature a corresponding decrease in fracture strain is observed, and in fact, at 119°K plastic instability occurs immediately after yielding. At 93°K, a small amount of serrated yielding was observed prior to fracture. The yield behavior and surface slip marking on {112} planes[344] suggest that at 93°K deformation is by twinning. Figure 52 shows the upper and lower shear stresses as a function of test temperature for the unirradiated niobium single crystals of the present study, together with the curves of Christian and Masters,[295] Mitchell *et al.*,[320] Kim and Pratt,[321] and Sherwood *et al.*[322] The present data lie well within the envelope of literature values, which reflects the variation in purity, orientation, and strain rate.

Irradiated Samples

Comparison of the stress-strain curves before and after neutron irradiation for a given test temperature indicates in general that irradiation increases the yield stresses and the magnitude of the yield drop but decreases the rate of work hardening and the uniform and fracture strains. Figure 53 shows the lower critical resolved shear stress as a function of test temperature for unirradiated and irradiated niobium

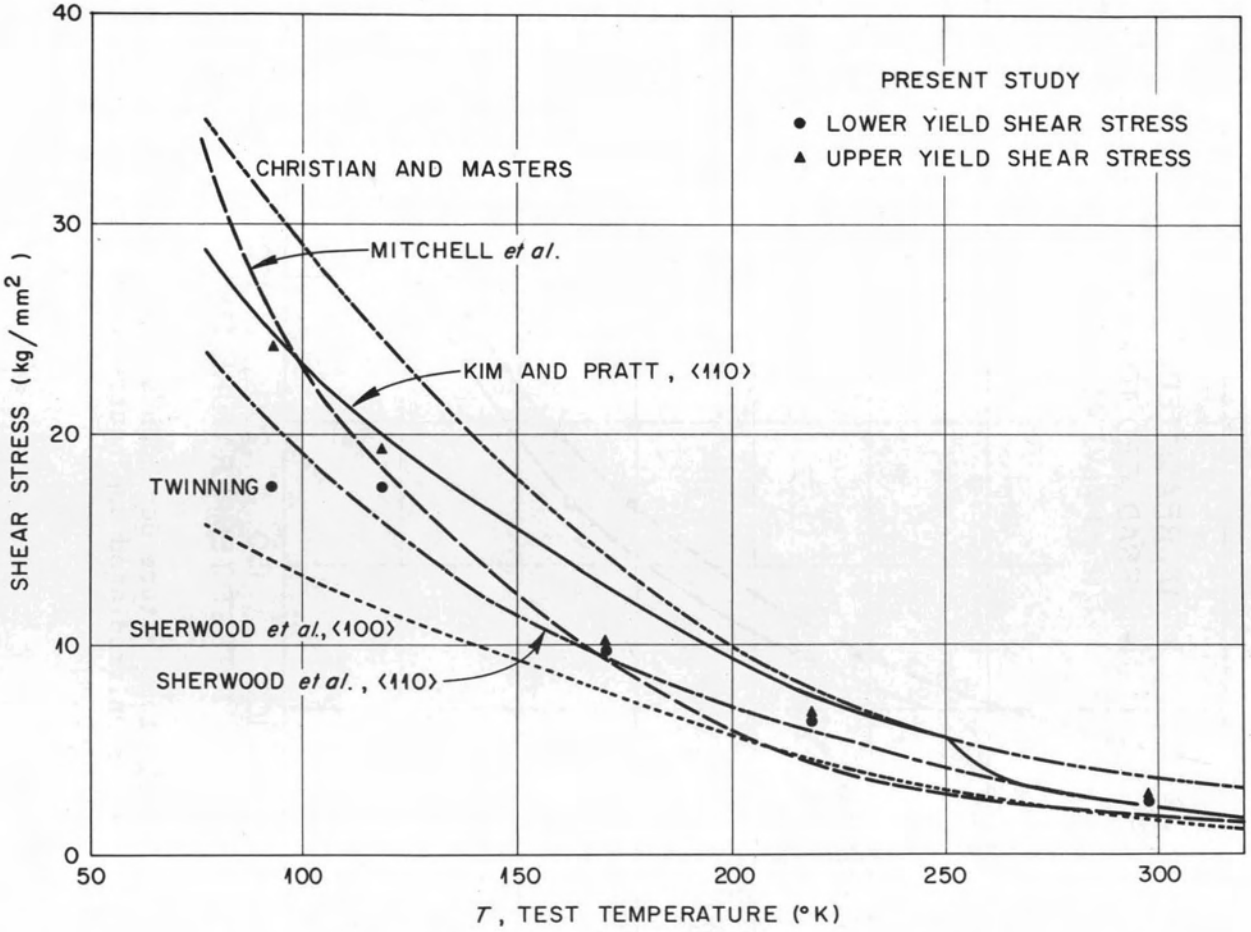

Figure 52. Upper and lower yield shear stresses versus test temperature for the present study and after Christian and Masters,[295] Mitchell *et al.*,[320] Kim and Pratt,[321] and Sherwood *et al.*[322] for unirradiated niobium single crystals.

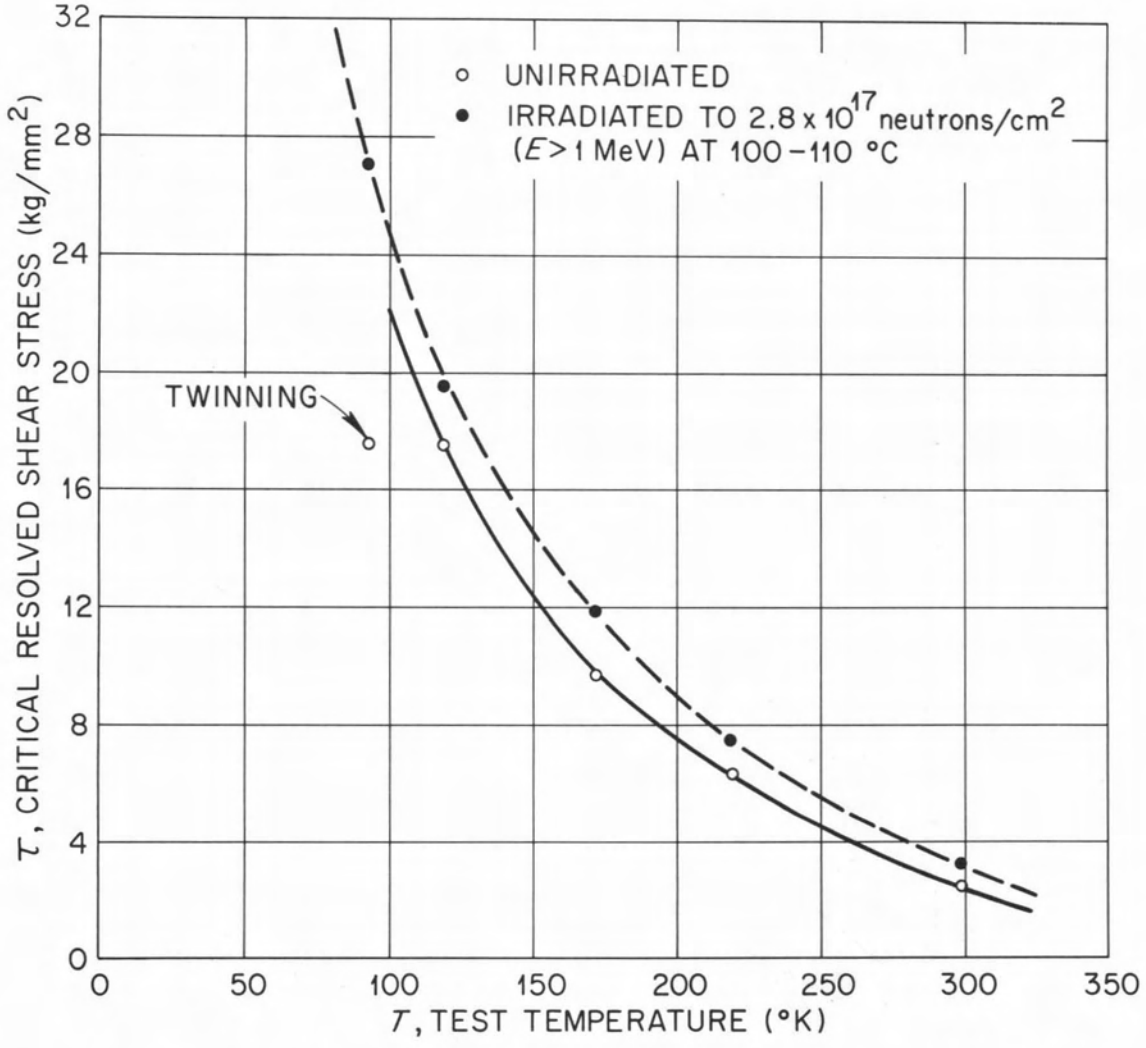

Figure 53. The temperature dependence of the critical resolved lower shear stress for unirradiated and neutron-irradiated Wah Chang niobium single crystals.

single crystals. Irradiation to 2.8 x 10^{17} neutrons/cm^2 (E > 1 Mev) increased the critical shear stress approximately the same amount at all test temperatures with a suggestion of a slightly greater increase at lower test temperatures. It should be noted that at 93°K, twinning appears to be suppressed in the irradiated sample. The decreased tendency for twinning after irradiation is consonant with the inhibition of twinning due to room temperature pre-straining[370] or the introduction of impurities.[295,371] In this regard, Ohr[372] has recently pointed out an analogy between the effects of pre-strain and irradiation on the work hardening characteristics of iron.

The decrease in the rate of work hardening and fracture strain in the irradiated niobium are probably reflections of the tendency for slip to be concentrated inhomogeneously in coarse slip bands. Figure 54 compares the surface slip line patterns of unirradiated and irradiated (4.2 x 10^{17} neutrons/cm^2) crystals strained 10 percent in tension, for the surfaces oriented with the [1$\bar{2}$1] direction horizontal and perpendicular to the direction of view (see Figure 13, Ref. 239). The unirradiated sample exhibits the typical wavy slip distributed rather homogeneously and diffusely as a function of distance along the axial direction. On the other hand, the irradiated sample displays slip markings that are sharp, deep, and distributed inhomogeneously, i.e., separated by undeformed regions. The coarsening of slip lines upon irradiation is almost surely a consequence of deformation by dislocation channeling as discussed in Chapter V. Any analysis of work hardening after irradiation obviously is complicated by the inhomogeneity of the deformation process.

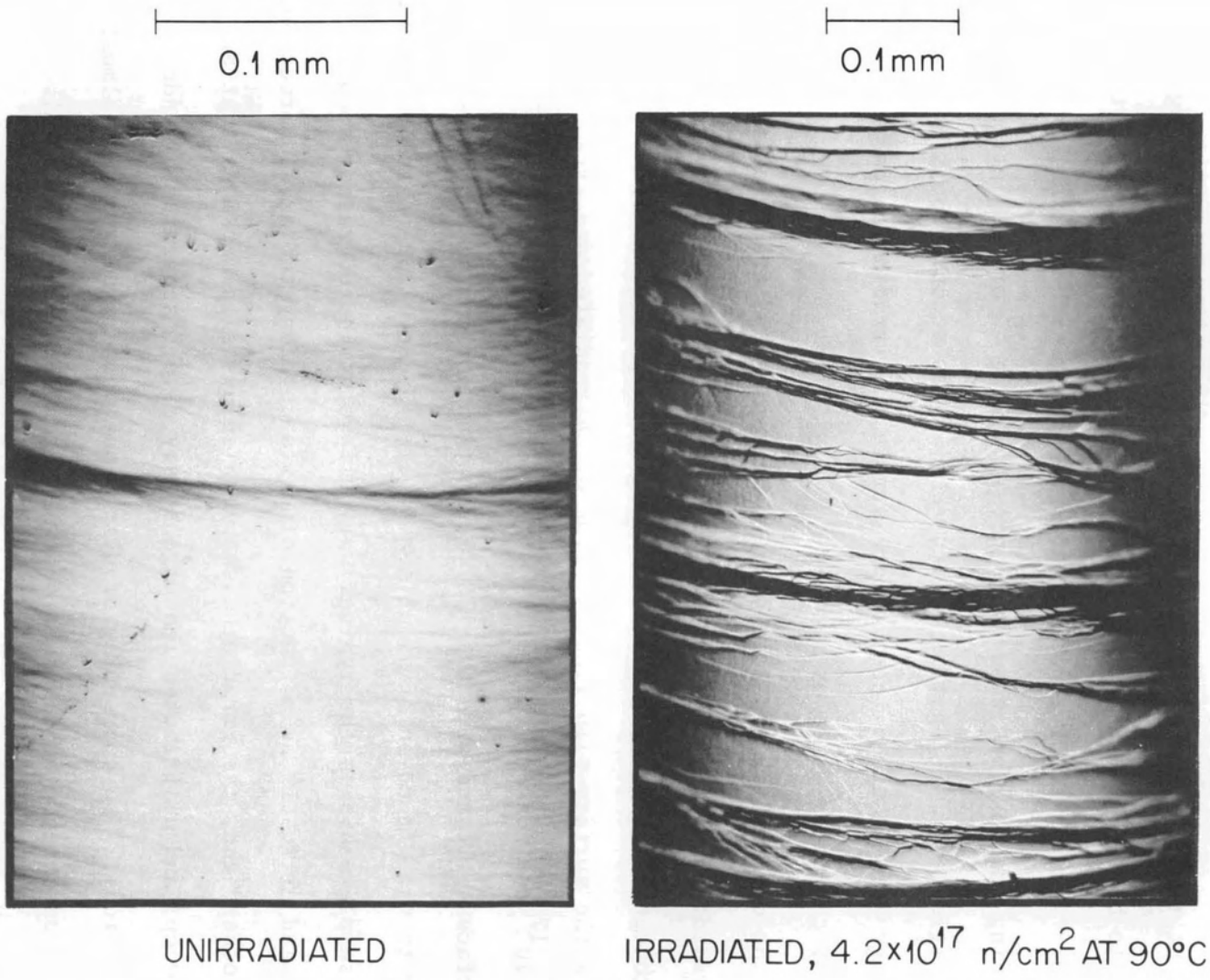

Figure 54. Slip lines in Wah Chang single crystal niobium after 10 percent strain, as viewed in direction perpendicular to the tensile axis (vertical) and to the [1$\bar{2}$1] direction (horizontal).

III. DISCUSSION OF THE TEMPERATURE DEPENDENCE OF YIELDING

As discussed previously (see Chapters II and VI), the dispersed barrier model, in which radiation-produced barriers to dislocation motion are assumed to be distributed at random on the slip plane, is generally used to explain radiation hardening. The temperature dependence of the yield stress depends then upon the overcoming of these barriers by thermal activation. A rate theory approach (see Chapter II and also Ono[304] and the references given there) has been employed by several authors to derive analytical expressions for the yield stress as a function of test temperature. Two expressions frequently cited are those due to Seeger,[196]

$$\left(\frac{\tau}{\tau_o}\right)^{2/3} = 1 - \left(\frac{T}{T_o}\right)^{2/3} , \qquad (55)$$

and to Fleischer,[301]

$$\left(\frac{\tau}{\tau_o}\right)^{1/2} = 1 - \left(\frac{T}{T_o}\right)^{1/2} . \qquad (56)$$

When the data of Figure 53 are plotted according to these relations, a distinct concave-upward curvature is observed for equation (55), Figure 55, whereas equation (56) gives good straight line fits, Figure 56. For the Fleischer relation, the intercept on the temperature axis, T_o, for the least-squares fit to the unirradiated and irradiated data is the same value, namely, 443°K = 170°C. The least-squares straight lines diverge from this common value with decreasing temperature; however, the apparent larger increase in τ for the irradiated sample at lower test

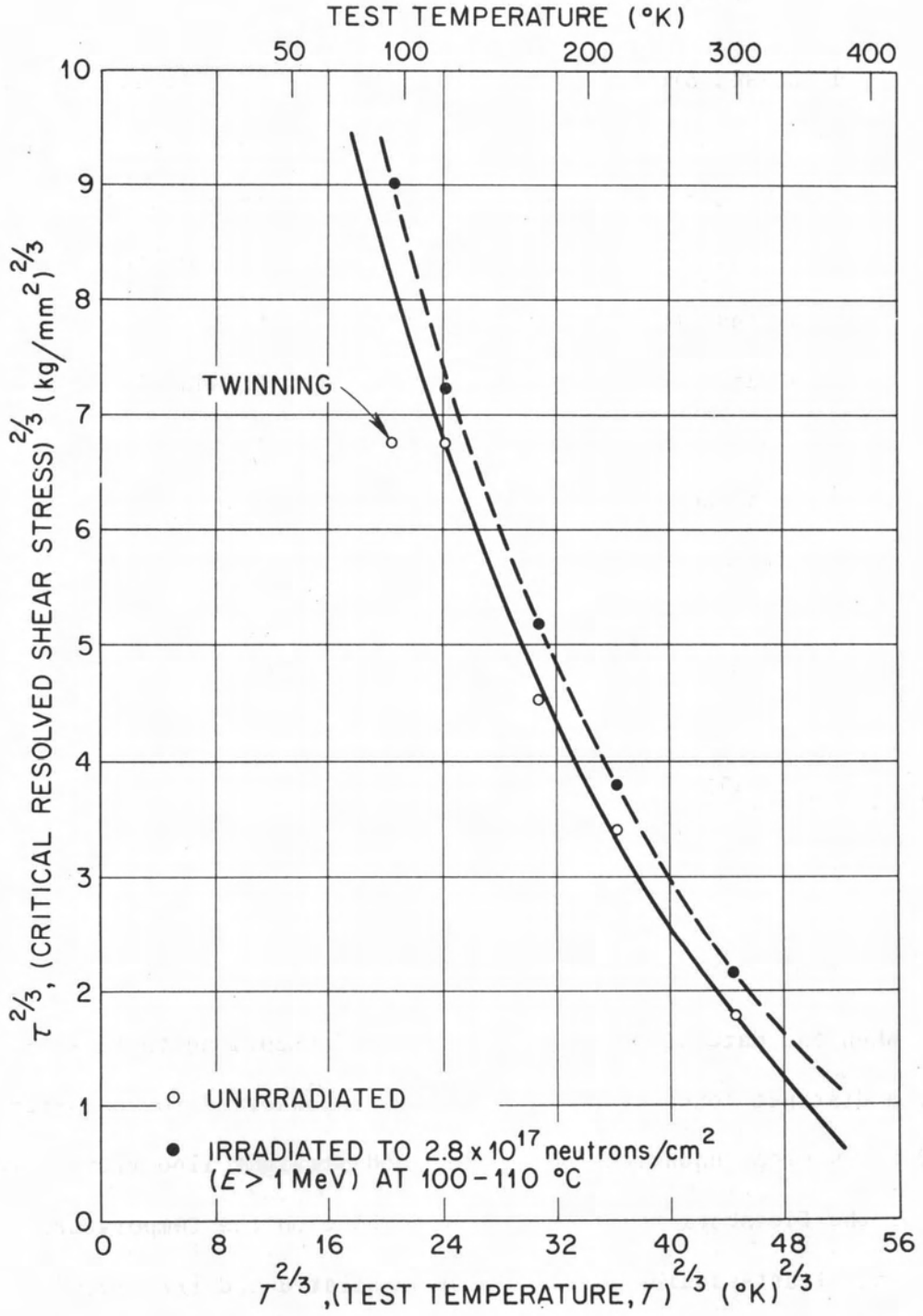

Figure 55. The temperature dependence of the critical resolved lower shear stress for unirradiated and irradiated Wah Chang niobium single crystals plotted according to equation (55).

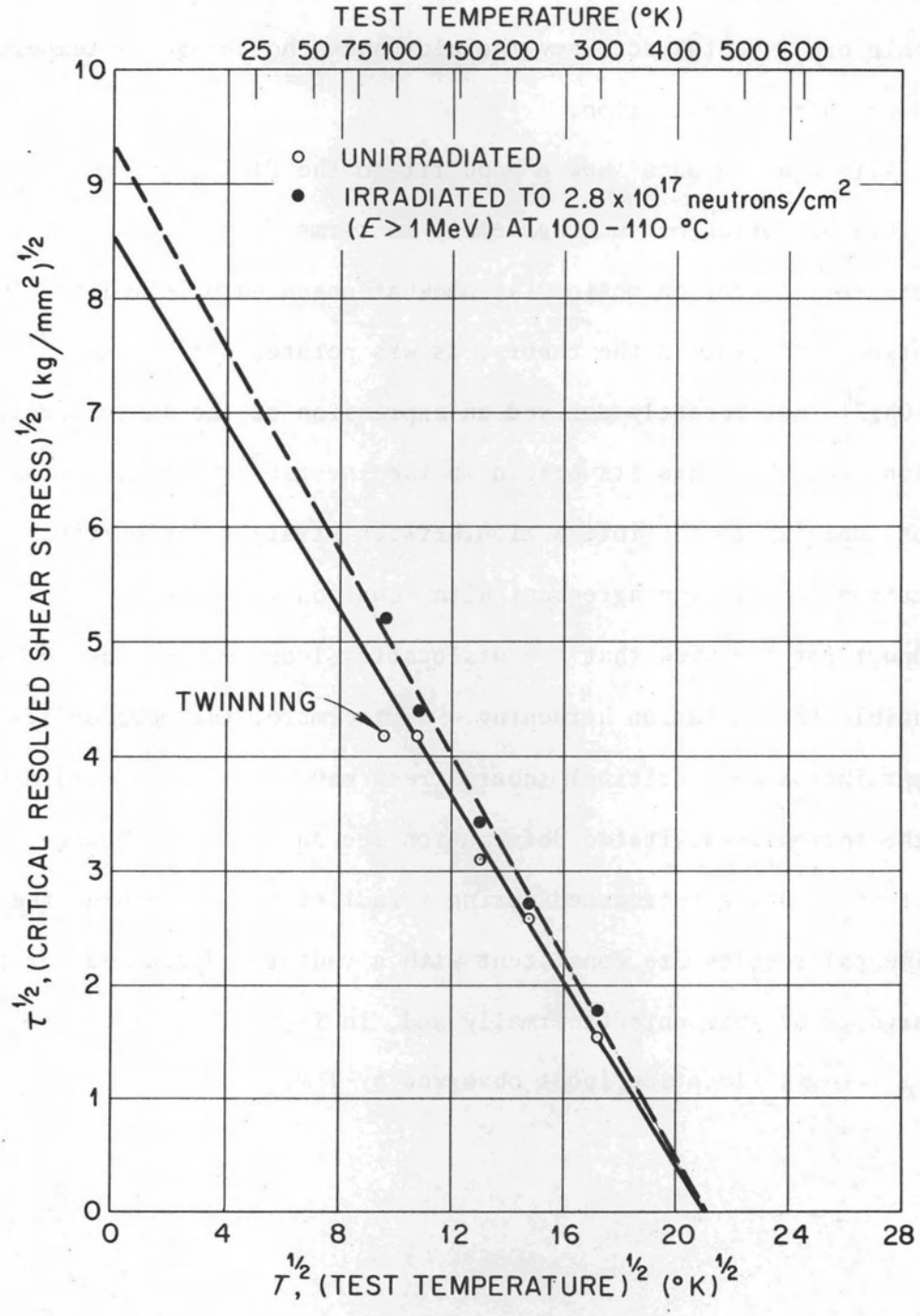

Figure 56. The temperature dependence of the critical resolved lower shear stress for unirradiated and irradiated Wah Chang niobium single crystals plotted according to equation (56).

temperatures is not outside the standard deviation for the data. Thus, to within experimental accuracy the plot shows no change in temperature dependence after irradiation.

Although the data show a good fit to the Fleischer equation, the exact interpretation of such agreement in terms of the nature of the barriers to dislocation motion is somewhat obscured by simplifying assumptions inherent in the theory, as was pointed out by Ono.[304] However, Ohr[305] has recently derived an expression of the same form as equation (56) which has its origin in the inverse-square force law such as that applying to the interaction between straight dislocations and dislocation loops. The agreement with equation (56), then, may be taken as support for the view that the dislocation loops visible by TEM are responsible for radiation hardening. Furthermore, the more or less constant increase in critical shear stress may be taken as evidence that the thermally-activated deformation mechanism is not changed by the defect clusters introduced during irradiation. Therefore, the experimental results are consistent with a radiation-produced barrier too large to be surmounted thermally and, in fact, of a size in agreement with the dislocation loops observed by TEM.

CHAPTER IX

SUMMARY AND CONCLUSIONS

This dissertation describes effects of neutron irradiation on niobium poly- and single crystals as revealed by transmission electron microscopy (TEM) and tensile tests. The principal findings of the study are:

(1) The first report in niobium that neutron irradiation produces a damage structure (defect clusters), which is visible by TEM.[1] The defect clusters are identified by black-white contrast analysis as small dislocation loops which are found tentatively to be predominantly interstitial in as-irradiated material. The density and size distributions of the defect clusters are shown as a function of neutron dose and post-irradiation annealing temperature.

(2) Tensile deformation of polycrystalline niobium irradiated to doses greater than 10^{18} neutrons/cm^2 (E > 1 Mev) results in dislocation channels cleared of radiation-produced defect clusters as seen by TEM.[183] The plane on which the dislocation channels form is usually {110}, as determined by the channel-trace direction and the Burgers vectors of slip dislocations in the channels. Offsets produced where dislocation channels intersect other microstructural features indicate that the strain in the channel corresponds to the passage of one to three slip dislocations per slip plane (a shear strain of $\sqrt{3}/\sqrt{2}$ per slip dislocation) for a nominal tensile strain of 6.6 percent, thus emphasizing the concentration of strain in the channels. Three mechanisms for the removal of defect clusters within the channels are discussed: chopping-up or

sweeping-up by slip dislocations, annihilation by anti-defects, and annealing due to the heat of plastic deformation. Establishment of the mechanism of dislocation channeling remains open for further theoretical and experimental study.

(3) For doses up to approximately 10^{18} neutrons/cm^2, the measured yield stress increase in polycrystalline niobium is predicted on the basis of a dispersed barrier model and the density and size distribution of defect clusters visible in the electron microscope. The observed radiation hardening gives a cluster strength of the order of (0.5-0.8) Gb^2, i.e., strong barrier hardening. The cross section for the production of defect clusters is 0.06 ± 0.01 barns, whereas the neutron scattering cross section for niobium is about seven barns. Thus, it appears that only one primary collision in 133 is effective in producing a defect cluster that serves as a barrier to slip dislocations. At doses above about 10^{18} neutrons/cm^2 both polycrystalline and single crystal niobium exhibited a decreased rate of hardening or "saturation effect." The exclusion volume as determined from the saturation equation of Makin and Minter[222] is of the order of 10^6 atomic volumes. At about (1.5-2.0) x 10^{18} neutrons/cm^2 the defect cluster density-size distribution shows a rather abrupt saturation, suggesting that few new clusters are being formed and that existing ones are growing. This saturation in the defect clusters is in accord with the observed saturation of the yield stress with dose. Furthermore, there is some indication that at about the dose where saturation begins, dislocation channeling becomes the prevalent mode of deformation.

(4) Low temperature post-irradiation annealing gives rise to two hardening peaks in niobium. The radiation-anneal-hardening peak at 120-200°C is believed to be associated with the motion of oxygen to radiation-produced defect clusters, whereas the 300-400°C peak is thought to be due to the motion of carbon. For a dose of 2×10^{18} neutrons/cm^2, the magnitude of the increase of the 300-400°C peak appears to be proportional to the carbon content. Moreover, the magnitude of the initial stress increase upon irradiation is proportional to the square root of the carbon content.

Post-irradiation annealing at 400°C tends to shift the defect cluster density-size distribution to a larger peak size. Annealing at 600°C results in the appearance of a new group of small-sized defect clusters believed to be vacancy in nature and in a corresponding decrease in the peak size. The radiation-anneal hardening cannot be accounted for on the basis of the changes in the distribution of clusters alone. However, the visible defect cluster distribution is consistent with radiation-anneal hardening after the 400°C anneal for a defect cluster strength 2.25 times the as-irradiated cluster strength. The decreased tendency for channel formation in niobium post-irradiation annealed at 400°C and then deformed is taken as evidence that indeed the defect clusters are more difficult for slip dislocations to remove. Annealing at 600°C decreases the density of larger-sized loops; also, the cluster strength begins to recover and is 1.9 times the as-irradiated cluster strength. The 800°C anneal results in recovery of the yield stress to nearly the unirradiated stress and in a reduction of the number of defect clusters, leaving only relatively few large dislocation loops.

(5) The temperature dependence of the yield stress in single crystal niobium is not appreciably changed over the range of test temperatures from 93°K to 298°K, after irradiation to 2.8×10^{17} neutrons/cm^2. The yield stress as a function of test temperature gives a reasonably good fit to the Fleischer[301] expression [equation (56), page 223], which Ohr[305] has shown to be the temperature dependence expected for the interaction of slip dislocations with dislocation loops. This agreement is consistent with the contention that radiation hardening in niobium is caused by the visible defect clusters. The lack of change in the temperature dependence upon irradiation is taken as evidence that irradiation does not change the thermally-activated mechanism of deformation in niobium. Thus, it is suggested that the radiation-produced obstacles interact strongly with slip dislocations, resulting in an athermal inhibition to dislocation motion, as would be expected for the defect clusters visible by TEM.

The experimental results outlined above permit the following tentative model of radiation and radiation-anneal hardening in niobium:

The radiation hardening is primarily governed by the interbarrier spacing, which the visible defect clusters present to slip dislocations, as indicated by the correlation of yield stress with the density and size distribution of defect clusters. The visible defect clusters are believed to be nucleated heterogeneously, presumably at individual carbon atoms in solid solution or at small-number carbon aggregates. The clusters are envisioned as forming by the migration of niobium interstitials, which should be mobile at the irradiation temperature, to the carbon, giving rise to the interstitial loops predominant in as-irradiated

material. In any case, the experimental evidence suggests that the yield stress bears a relation to the visible defect clusters through I_c and is also proportional to the square root of the carbon concentration.

Although the carbon initially in solid solution in niobium is thought to be quite low, irradiation may cause additional carbon to go into solution as suggested for iron by Seidel.[232] With increasing doses up to a critical dose of approximately 10^{18} neutrons/cm^2 the major change, as observed by TEM, is to increase the density of defect clusters. Above the critical dose, the existing defect clusters drain the volume surrounding them of newly produced interstitials, thereby growing in size and decreasing the probability of new cluster formation. As the defect clusters coarsen and the interbarrier spacing decreases, the stress increases to a critical value, relative to the cluster strength, at which slip dislocations can remove the loops in their pathways, thus causing dislocation channels.

Post-irradiation annealing between 120 and 200°C, where oxygen becomes mobile, causes oxygen to migrate to the defect cluster, slightly strengthening them as evidenced by the radiation-anneal hardening in this temperature range. Above 200°C, carbon, which appears to be more effective in strengthening the defect clusters, becomes mobile and begins to migrate to the loops causing a second, larger radiation-anneal-hardening peak. The decreased tendency for dislocation channel formation in radiation-anneal-hardened material supports the contention that the clusters are stronger and less easily removed by slip dislocations.

A number of important questions remain unanswered and should be fruitful areas for further theoretical and experimental investigations.

A key question is the mechanism whereby slip dislocations remove the defect clusters. In this regard, it is important to establish the Burgers vectors and the habit planes of the dislocation loops. Then, it appears necessary to develop a mechanism which permits {110}<111> dislocations to annihilate within a channel loops of various Burgers vectors. The problem appears to be a formidable one, requiring consideration of the contact interaction between slip dislocations and dislocation loops, which is near, if not beyond, the limits where continuum dislocation theory applies. A second closely related problem concerns the manner in which interstitial impurities strengthen the defect clusters against slip dislocations.

Questions that can be answered by a somewhat more straightforward experimental approach, include the following:

(1) The influence in niobium of interstitial impurities, such as carbon and oxygen, on the density and size distribution of defect clusters visible by TEM and on the stress and deformation behavior.

(2) The effect of higher neutron doses on the temperature dependence.

(3) More precise establishment of the nature and lattice geometry of the defect clusters in as-irradiated and post-irradiation annealed material.

(4) The characteristics of defect clusters and dislocation channels in single crystals.

LIST OF REFERENCES

LIST OF REFERENCES

1. R. P. Tucker and S. M. Ohr, "Direct Observation of Neutron Irradiation Damage in Niobium," Phil. Mag. *16*, 643 (1967).

2. R. E. Smallman and K. H. Westmacott, "Structure of Quenched and Irradiated Metals," J. Appl. Phys. *30*, 603 (1959).

3. J. Silcox and P. B. Hirsch, "Dislocation Loops in Neutron-Irradiated Copper," Phil. Mag. *4*, 1356 (1959).

4. T. S. Noggle, "Electron Microscope Observation of Radiation Damage in Gold Films," Bull. Am. Phys. Soc. *4*, 137 (1959).

5. R. M. J. Cotterill, M. Doyama, J. J. Jackson, and M. Meshii (eds.), *Lattice Defects in Quenched Metals*, Academic Press, New York, 1965.

6. J. Diehl, W. Schilling, and D. Schumacher (organizing committee), preprints of *International Conference on Vacancies and Interstitials in Metals*, 2 vols., Kernforschungsanlage Jülich, Germany, Sept. 1968.

7. K. G. McIntyre, "Interstitial Dislocation Loops in Neutron Irradiated Copper," Phil. Mag. *15*, 205 (1967).

8. M. Rühle and M. Wilkens, "Small Vacancy Dislocation Loops in Neutron Irradiated Copper," Phil. Mag *15*, 1075 (1967).

9. S. Amelinckx, "The Direct Observation of Lattice Defects by Means of Electron Microscopy," p. 682 in *The Interaction of Radiation with Solids*, edited by R. Strumane, J. Nihoul, R. Gevers, and S. Amelinckx. North-Holland Publishing Co., Amsterdam, 1964.

10. S. Amelinckx, *The Direct Observation of Dislocations*, Solid State Physics, Suppl. 6, Academic Press, New York, 1964.

11. S. Amelinckx, "The Study of Crystal Imperfections by Means of Optical Methods and by Means of Electron Microscopy and Electron Diffraction," p. 427 in *Trace Characterization Chemical and Physical*, edited by W. W. Meinke and B. F. Scribner. National Bureau of Standards, United States Department of Commerce, NBS Monograph 100. U. S. Government Printing Office, Washington, D. C., 1967.

12. M. F. Ashby and L. M. Brown, "On Diffraction Contrast from Inclusions," Phil. Mag. *8*, 1649 (1963).

13. M. F. Ashby and L. M. Brown, "Diffraction Contrast from Spherically Symmetry Coherency Strains," Phil. Mag. *8*, 1083 (1963).

14. W. L. Bell, D. M. Maher, and G. Thomas, "Vacancy Aggregates in Quenched Copper Single Crystals," p. 739 in *Lattice Defects in Quenched Metals*, edited by R. M. J. Cotterill, M. Doyama, J. J. Jackson, and M. Meshii. Academic Press, New York, 1965.

15. W. L. Bell, D. M. Maher, and G. Thomas, "Strain Contrast Images from Small Defects," p. 314 in *The Nature of Small Defect Clusters*, Vol. 2, edited by M. J. Makin. Atomic Energy Research Establishment, Harwell, Report AERE-R5269. H. M. Stationary Office, London, 1966.

16. W. L. Bell and G. Thomas, "Contrast from Large Prismatic Dislocation Loops," Phil. Mag. *13*, 395 (1966).

17. B. Edmundson and G. K. Williamson, "On the Determination of the Nature of Dislocation Loops," Phil. Mag. *9*, 277 (1964).

18. H. Hashimoto, A. Howie, and M. J. Whelan, "Anomalous Electron Absorption Effects in Metal Foils," Phil. Mag. *5*, 967 (1960).

19. H. Hashimoto, A. Howie, and M. J. Whelan, "Anomalous Electron Absorption Effects in Metal Foils: Theory and Comparison with Experiment," Proc. Roy. Soc. (London) *A269*, 80 (1962).

20. P. B. Hirsch, A. Howie, and M. J. Whelan, "A Kinematical Theory of Diffraction Contrast of Electron Transmission Microscope Images of Dislocations and Other Defects," Phil. Trans. Roy. Soc. (London) *A252*, 499 (1960).

21. P. B. Hirsch, A. Howie, R. B. Nicholson, D. W. Pashley, and M. J. Whelan, *Electron Microscopy of Thin Crystals*, Butterworths, London, 1965.

22. A. Howie, "Inelastic Scattering of Electrons by Crystals, I. The Theory of Small-Angle Inelastic Scattering," Proc. Roy. Soc. (London) *A271*, 268 (1963).

23. A. Howie and M. J. Whelan, "Diffraction Contrast of Electron Microscope Images of Crystal Lattice Defects, II. The Development of a Dynamical Theory," Proc. Roy. Soc. (London) *A263*, 217 (1961).

24. A. Howie and M. J. Whelan, "Diffraction Contrast of Electron Microscope Images of Crystal Lattice Defects, III. Results and Experimental Confirmation of the Dynamical Theory of Dislocation Image Contrast," Proc. Roy. Soc. (London) *A267*, 206 (1962).

25. D. J. Littler (ed.), *Properties of Reactor Materials and the Effects of Radiation Damage*, Butterworths, London, 1962.

26. M. J. Makin (ed.), *The Nature of Small Defect Clusters*, 2 vols., Atomic Energy Research Establishment, Harwell, Report AERE-R5269. H. M. Stationary Office, London, 1966.

27. J. B. Newkirk and J. H. Wernick (eds.), *Direct Observation of Imperfections in Crystals*, Interscience Publishers, New York, 1962.

28. M. Rühle, "Elektronenmikroskopie kleiner Fehlstellenagglomerate in bestrahlten Metallen, I. Theorie des Kontrastes und experimentelle Methoden zur Ermittlung des Defekttyps," Phys. Stat. Sol. *19*, 263 (1967).

29. M. Rühle, M. Wilkens, and U. Essmann, "Zur Deutung der elektronenmikroskopische Kontrasterscheinungen an Fehlstellenagglomeraten in neutronenbestrahltem Kupfer," Phys. Stat. Sol. *11*, 819 (1965).

30. G. Thomas, *Transmission Electron Microscopy of Metals*, John Wiley and Sons, Inc., New York, 1962.

31. G. Thomas and W. L. Bell, "Identification of Prismatic Dislocation Defects by Electron Microscopy," p. 477 in *Lattice Defects and Their Interaction*, edited by R. R. Hasiguti. Gordon and Breach Science Publishers, New York, 1967.

32. G. Thomas and J. Washburn (eds.), *Electron Microscopy and Strength of Crystals*, Interscience Publishers, New York, 1963.

33. R. von Jan, "Remarks on the Formation of Defect Clusters by Irradiation," p. 1 in *The Nature of Small Defect Clusters*, Vol. 1, edited by M. J. Makin. Atomic Energy Research Establishment, Harwell, Report AERE-R5269. H. M. Stationary Office, London, 1966.

34. M. Wilkens, "Zur Theorie des Kontrastes von elektronenmikroskopisch abgebildeten Gitterfehlen," Phys. Stat. Sol. *5*, 175 (1964).

35. M. Wilkens, "Streuung von Blochwellen schneller Elektronen in Kristallen mit Gitterbaufehlern," Phys. Stat. Sol. *6*, 939 (1964).

36. J. L. Brimhall and B. Mastel, "Deformation Structure of Neutron-Irradiated Copper-Aluminum Alloy," Appl. Phys. Letters *9*, 127 (1966).

37. J. A. Brinkman, A. Sosin, and A. Grenall, "An Interpretation of Electron Microscope Observations in Neutron-Irradiated Copper and Gold," J. Nucl. Matls. *4*, 332 (1961).

38. A Bourret and D. Dautreppe, "Type of Small Dislocation Loops in Neutron Irradiated Copper," Phys. Stat. Sol. *24*, K173 (1967).

39. R. M. J. Cotterill and T. J. Koppenaal, "Effects of Type and Density of Defects on Yield Strength of Neutron-Irradiated Cu and Cu-14 at. % Al Alloy," Appl. Phys. Letters *4*, 156 (1964).

40. J. C. Crump, "Dislocation Loops in Neutron-Irradiated Copper," Bull. Amer. Phys. Soc. *13*, 462 (1968).

41. U. Essmann and A. Seeger, "Verfestigungsverhalten neutronenbestrahlter Metalle, II. Temperaturwechselversuche und Gleitlinienbeobachtungen an Kupfereinkristallen," Phys. Stat. Sol. *4*, 177 (1964).

42. U. Essmann and M. Wilkens, "Elektronenmikroskopische Kontrastexperimente an Fehlerstellenagglomeraten in neutronenbestrahltem Kupfer," Phys. Stat. Sol. *4*, K53 (1964).

43. A. N. Goland, "Comparison of Electron Microscope Observations in Neutron-Irradiated Copper and Gold," J. Nucl. Matls. *7*, 101 (1962).

44. I. G. Greenfield and H. G. F. Wilsdorf, "Observations Concerning the Radiation Hardening in Copper and Nickel," Naturwissenschaften *47*, 395 (1960).

45. I. G. Greenfield and H. G. F. Wilsdorf, "Effect of Neutron Irradiation on the Plastic Deformation of Copper Single Crystals," J. Appl. Phys. *32*, 827 (1961).

46. T. J. Koppenaal, W. C. T. Yeh, and R. M. J. Cotterill, "Lattice Defects in Neutron Irradiated α Cu Solid Solution Alloys," Phil. Mag. *13*, 867 (1966).

47. M. J. Makin, A. D. Whapham, and F. J. Minter, "Neutron-Irradiated Copper: The Formation of Dislocation Loops," *Proceedings of the European Regional Conference on Electron Microscopy* (Delft), Vol. 1, 423 (1960).

48. M. J. Makin, A. D. Whapham, and F. J. Minter, "Dislocation Loops and Hardening in Neutron Irradiated Copper," Phil. Mag. *6*, 465 (1961).

49. M. J. Makin, A. D. Whapham, and F. J. Minter, "The Formation of Dislocation Loops in Copper During Neutron Irradiation," Phil. Mag. *7*, 285 (1962).

50. M. J. Makin and S. A. Manthorpe, "The Annealing of Dislocation Loops in Neutron Irradiated Copper," Phil. Mag. *8*, 1725 (1963).

51. K. L. Merkle, "Radiation Induced Point Defect Clusters in Copper and Gold," p. 8 in *The Nature of Small Defect Clusters*, Vol. 1, edited by M. J. Makin. Atomic Energy Research Establishment, Harwell, Report AERE-R5269. H. M. Stationary Office, London, 1966.

52. K. L. Merkle, "Radiation Induced Point Defect Clusters in Copper and Gold, I. Clusters Produced in Energetic Displacement Cascades," Phys. Stat. Sol. *18*, 173 (1966).

53. K. G. McIntyre and L. M. Brown, "Diffraction Contrast from Small Defect Clusters in Irradiated Copper," p. 351 in *The Nature of Small Defect Clusters*, Vol. 2, edited by M. J. Makin. Atomic Energy Research Establishment, Harwell, Report AERE-R5269. H. M. Stationary Office, London, 1966.

54. M. Rühle, "Elektronenmikroskopie kleiner Fehlstellenagglomerate in bestrahlten Metallen, II. Untersuchungen an neutronen-und ionen-bestrahltem Kupfer sowie neutronenbestrahltem Nickel," Phys. Stat. Sol. *19*, 279 (1967).

55. M. Rühle, F. Haussermann, P. Huber, and M. Wilkens, "On the Nature of the Defects in Neutron-Irradiated Metals," p. 377 in the *Proceedings of the IVth European Regional Conference on Electron Microscopy*, Rome, 1968.

56. M. Rühle and M. Wilkens, "Die Natur der elektronenmikroskopisch beobachtbaren Defekte in neutronenbestrahltem Kupfer," Phys. Stat. Sol. *16*, K105 (1966).

57. G. P. Scheidler, M. J. Makin, F. J. Minter, and W. F. Schilling, "The Effect of Irradiation Temperature on the Formation of Clusters in Neutron Irradiated Copper," p. 405 in *The Nature of Small Defect Clusters*, Vol. 2, edited by M. J. Makin. Atomic Energy Research Establishment, Harwell, Report AERE-R5269. H. M. Stationary Office, London, 1966.

58. C. Schwink and G. Grieshammer, "Untersuchungen des Fliessbereichs neutronenbestrahlter Kupfereinkristalle, I. Elektronenmikroskopische und mechanische Untersuchungen au Proben vor und nach dem Aulassen," Phys. Stat. Sol. *6*, 665 (1964).

59. J. V. Sharp, "Deformation of Neutron-Irradiated Copper Single Crystals," Phil. Mag. *16*, 77 (1967).

60. J. Silcox, "Radiation Damage in Face-Centered Cubic Metals," *Proceedings of the European Regional Conference on Electron Microscopy* (Delft), Vol. 1, 362 (1960).

61. A. Seeger, "Work-Hardening of Metal Single Crystals, Slip Lines, and Transmission Electron Microscopy," p. 3 in *The Relation Between the Structure and Mechanical Properties of Metals*, Vol. 1, H. M. Stationary Office, London, 1963.

62. M. Wilkens and M. Rühle, "Observations of Point Defect Agglomerations in Copper by Means of Electron Microscopy," p. 365 in *The Nature of Small Defect Clusters*, Vol. 2, edited by M. J. Makin. Atomic Energy Research Establishment, Harwell, Report AERE-R5269. H. M. Stationary Office, London, 1966.

63. T. K. Bierlein and B. Mastel, "Defect Structures Observed in Neutron-Bombarded Aluminum," J. Appl. Phys. *33*, 2873 (1962).

64. J. L. Brimhall, H. E. Kissinger, and B. Mastel, "Vacancy and Interstitial Clusters in Neutron-Irradiated Nickel," J. Appl. Phys. *37*, 3317 (1966).

65. J. L. Brimhall and B. Mastel, "Enhanced Neutron Radiation Damage at Twin Boundaries," J. Appl. Phys. *38*, 3027 (1967).

66. B. L. Eyre, "Comments on the Identification of Vacancy and Interstitial Clusters in Neutron-Irradiated Nickel," J. Appl. Phys. *38*, 1973 (1967).

67. R. V. Hesketh and D. I. R. Norris, "Further Comments on Vacancy and Interstitial Clusters in Neutron-Irradiated Nickel," J. Appl. Phys. *38*, 3033 (1967).

68. G. R. Piercy and J. L. Whitton, "Investigation of Radiation Damage in Pure Aluminum and Aluminum-1% Magnesium Alloy by Transmission Electron Microscopy," J. Inst. Metals *90*, 386 (1961-62).

69. E. Ruedl, P. Delavignette, and S. Amelinckx, "Electron Microscope Study of Irradiated Platinum," p. 363 in *Radiation Damage in Solids*, Vol. 1, International Atomic Energy Agency, Vienna, 1962.

70. E. Ruedl, P. Delavignette, and S. Amelinckx, "Electron Microscopic Study of Dislocations and Fission Damage in Platinum Foils," J. Nucl. Matls. *6*, 46 (1962).

71. E. Ruedl and S. Amelinckx, "The Direct Observation of Radiation Damage in Platinum," *Proceedings of the International Conference on Crystal Lattice Defects*, J. Phys. Soc. Japan *18*, Suppl. III, 195 (1963).

72. W. R. Thomas and J. L. Whitton, "The Behaviour of Dislocations in Neutron-Irradiated Aluminum," Acta Met. *9*, 1075 (1961).

73. H. G. F. Wilsdorf, "Nature of Radiation Damage in Nickel," Phys. Rev. Letters *3*, 172 (1959).

74. J. S. Bryner, "A Study of Neutron Irradiation Damage in Iron by Electron Transmission Microscopy," Acta Met. *14*, 323 (1966).

75. J. S. Bryner, "The Formation of Radiation Defect Clusters in Iron During Post-Irradiation Heating," p. 468 in *The Nature of Small Defect Clusters*, Vol. 2, edited by M. J. Makin. Atomic Energy Research Establishment, Harwell, Report AERE-R5269. H. M. Stationary Office, London, 1966.

76. J. S. Bryner, "An Electron Transmission Study of Defects in Neutron-Irradiated Iron," p. 213 in *Radiation Effects*, edited by W. F. Sheely. Gordon and Breach Science Publishers, Inc., New York, 1967.

77. B. L. Eyre, "Direct Observations of Neutron Irradiation Damage in α-Iron," Phil. Mag. *7*, 2107 (1962).

78. B. L. Eyre and A. F. Bartlett, "An Electron Microscope Study of Neutron Irradiation Damage in Alpha Iron," Phil. Mag. *12*, 261 (1965).

79. D. Hull and I. L. Mogford, "Precipitation and Irradiation Hardening in Iron," Phil. Mag. *6*, 535 (1961).

80. S. M. Ohr, "Electron Microscope Studies of Radiation Hardening in BCC Iron," p. 427 in *Sixth International Congress for Electron Microscopy*, Maruzen Co., Tokyo, 1966.

81. J. L. Brimhall, "Effect of Neutron Irradiation on Slip Lines in Molybdenum," Trans. Met. Soc. AIME *233*, 1737 (1965).

82. J. L. Brimhall, B. Mastel, and T. K. Bierlein, "Loop Interactions During Annealing of Neutron-Irradiated Molybdenum," J. Appl. Phys. *36*, 2585 (1965).

83. J. L. Brimhall, B. Mastel, and T. K. Bierlein, "Thermal Stability of Radiation Produced Defects in Molybdenum," Acta Met. *16*, 781 (1968).

84. J. L. Brimhall and B. Mastel, "The Effect of Prestrain and Subsequent Neutron Irradiation on Molybdenum," Acta Met. *14*, 539 (1966).

85. M. E. Downey and B. L. Eyre, "Neutron Irradiation Damage in Molybdenum," Phil. Mag. *11*, 53 (1965).

86. B. L. Eyre and M. E. Downey, "The Influence of Irradiation Temperature on the Damage Structure in Neutron Irradiated Molybdenum," p. 384 in *The Nature of Small Defect Clusters*, Vol. 2, edited by M. J. Makin. Atomic Energy Research Establishment, Harwell, Report AERE-R5269. H. M. Stationary Office, London, 1966.

87. B. L. Eyre and M. E. Downey, "The Influence of Irradiation Temperature on the Damage Structure in Neutron-Irradiated Molybdenum," Metal Science Journal *1*, 5 (1967).

88. B. L. Eyre and A. C. Roberts, "The Nature and Annealing Behavior of Irradiation Damage in Molybdenum," p. 188 in *Flow and Fracture of Metals and Alloys in Nuclear Environments*, ASTM-STP-380, American Society for Testing and Materials, Philadelphia, 1965.

89. J. F. Kerridge, S. S. Sheinen, A. A. Johnson, and H. I. Mathews, "On the Mechanism of Vacancy Annihilation in Neutron-Irradiated Molybdenum," Phil. Mag. *7*, 1073 (1962).

90. H. E. Kissinger, J. L. Brimhall, B. Mastel, and T. K. Bierlein, "Some Observations on the Annealing of Neutron-Irradiated Single-Crystal and Polycrystalline Molybdenum," p. 681 in preprints of *International Conference on Vacancies and Interstitials in Metals*, Vol. 2, Kernforschungsanlage Jülich, Germany, Sept. 1968.

91. J. J. Laidler, H. E. Kissinger, T. K. Bierlein, and B. Mastel, "Discussion to Mechanisms of Radiation-Induced Mechanical Property Changes," p. 197 in *Flow and Fracture of Metals and Alloys in Nuclear Environments*, ASTM-STP-380, American Society for Testing and Materials, Philadelphia, 1965.

92. D. M. Maher and B. L. Eyre, "The Identification of Vacancy and Interstitial Loops in Neutron Irradiated Molybdenum," Phil. Mag. *17*, 1 (1968).

93. B. Mastel, H. E. Kissinger, J. J. Laidler, and T. K. Bierlein, "Dislocation Channeling in Neutron-Irradiated Molybdenum," J. Appl. Phys. *34*, 3637 (1963).

94. B. Mastel and J. L. Brimhall, "The Combined Effect of Carbon and Neutron Radiation on Molybdenum," Acta Met. *13*, 1109 (1965).

95. J. D. Meakin and I. G. Greenfield, "Interstitial Loops in Neutron-Irradiated Molybdenum," Phil. Mag. *11*, 277 (1965).

96. P. Rao and G. Thomas, "Defects in Neutron Irradiated Molybdenum," Acta Met. *15*, 1153 (1967).

97. K. Lacefield, J. Moteff, and J. P. Smith, "Neutron Radiation Damage in Tungsten Single Crystals," Phil. Mag. *13*, 1079 (1966).

98. M. Rühle, F. Haussermann, P. Huber, and M. Wilkens, "On the Nature of Defects in Neutron-Irradiated Metals," p. 377 in the *Proceedings of the IVth European Regional Conference on Electron Microscopy*, Rome, 1968.

99. J. L. Brimhall and B. Mastel, "Effect of Neutron Radiation on Rhenium," Phil. Mag. *12*, 419 (1965).

100. J. L. Brimhall and B. Mastel, "Defect Clusters in Neutron Irradiated Rhenium," Phys. Stat. Sol. *27*, K89 (1968).

101. R. S. Barnes, "The Migration of Large Clusters of Point Defects in Irradiated Materials," J. Phys. Soc. Japan *18*, Suppl. III, 305 (1963).

102. R. S. Barnes and D. J. Mazey, "The Nature of Radiation-Induced Point Defect Clusters," Phil. Mag. *5*, 1247 (1960).

103. P. Bowden and D. G. Brandon, "The Generation of Dislocation in Metals by Low Energy Ion Bombardment," Phil. Mag. *8*, 935 (1963).

104. P. Bowden and D. G. Brandon, "The Production of Interstitial Point Defects by Low Energy Ion Bombardment," J. Nucl. Matls. *9*, 348 (1963).

105. H. Diepers and J. Diehl, "Nachweis und Entstehung von Zwischengitteratom-Agglomeraten in Ionenbestrahlten Kupferfolien," Phys. Stat. Sol. *16*, K109 (1966).

106. H. Diepers, "Elektronenmikroskopische Untersuchung von Fehlstellenagglomeraten in ionenbestrahlten Kupferfolien, I. Analyse von Agglomerattyp und -konfiguration," Phys. Stat. Sol. *24*, 235 (1967).

107. H. Diepers, "Elektronenmikroskopische Untersuchung von Fehlstellenagglomeraten in ionenbestrahlten Kupferfolien, II. Entstehung der Agglomerate," Phys. Stat. Sol. *24*, 623 (1967).

108. R. V. Hesketh and G. K. Rickards, "Vacancy Clusters and Loops in Ion Bombarded Copper," Proc. Roy. Soc. (London) *A289*, 353 (1966).

109. R. V. Hesketh and G. K. Rickards, "Heavy Ion Damage in Copper," p. 419 in *The Nature of Small Defect Clusters*, Vol. 2, edited by M. J. Makin. Atomic Energy Research Establishment, Harwell, Report AERE-R5269. H. M. Stationary Office, London, 1966.

110. R. V. Hesketh and G. K. Rickards, "The Thermal Annealing of Heavy Ion Damage in Copper," Phil. Mag. *13*, 1105 (1966).

111. L. M. Howe, R. W. Gilbert, and G. R. Piercy, "Direct Observation of Radiation Damage Produced in Copper Below 30°K During Ion Bombardment in the Electron Microscope," Appl. Phys. Letters *3*, 125 (1963).

112. L. M. Howe, J. F. McGurn, and R. W. Gilbert, "Direct Observation of Radiation Damage Produced in Copper, Gold, and Aluminum During Ion Bombardments at Low Temperatures in the Electron Microscope," Acta Met. *14*, 801 (1966).

113. L. M. Howe, J. F. McGurn, and R. W. Gilbert, "Direct Observation of Radiation Damage Produced in Copper, Gold, and Aluminum During Ion Bombardments at Low Temperatures in the Electron Microscope," p. 197 in *Radiation Effects*, edited by W. F. Sheely. Gordon and Breach Science Publishers, Inc., New York, 1967.

114. R. S. Barnes, "Mechanisms of Radiation-Induced Mechanical Property Changes," p. 40 in *Flow and Fracture of Metals and Alloys in Nuclear Environments*, ASTM-STP-380, American Society for Testing and Materials, Philadelphia, 1965.

115. C. J. Beevers and R. S. Nelson, "Evidence for a Damage Rate Dependence in the Formation of Defect Clusters in Aluminum," p. 127 in *Properties of Reactor Materials and the Effects of Radiation Damage*, edited by D. J. Littler. Butterworths, London, 1962.

116. C. J. Beevers and R. S. Nelson, "The Formation of Defect Clusters in Al by Ion Bombardment," Phil. Mag. *8*, 1189 (1963).

117. L. Henrikson, A. Johnson, J. Koch, H. H. Anderson, and R. M. J. Cotterill, "Rows of Dislocation Loops in Aluminum Irradiated by Aluminum Ions," Appl. Phys. Letters *11*, 136 (1967).

118. D. J. Mazey and R. S. Barnes, "On Interstitial Dislocation Loops in Aluminum Bombarded with Alpha Particles," Phil. Mag. *7*, 1861 (1962).

119. D. J. Mazey, R. S. Barnes, and A. Howie, "On Interstitial Dislocation Loops in Aluminum Bombarded with Alpha Particles," Phil. Mag. *7*, 1861 (1962).

120. D. I. R. Norris, "Clusters in Ion-Bombarded Aluminum and Nickel," p. 433 in *The Nature of Small Defect Clusters*, Vol. 2, edited by M. J. Makin. Atomic Energy Research Establishment, Harwell, Report AERE-R5269. H. M. Stationary Office, London, 1966.

121. K. H. Westmacott, A. C. Roberts, and R. S. Barnes, "The Growth of Dislocation Loops During the Irradiation of Aluminum," Phil. Mag. *7*, 2035 (1962).

122. D. G. Brandon and P. Bowden, "The Low Energy Ion Bombardment of Gold," Phil. Mag. *6*, 707 (1961).

123. D. G. Brandon, P. B. Bowden, and A. J. Baker, "Lattice Defects in Gold and Platinum Produced by Low-Energy Ion Bombardment," p. 120 in *Properties of Reactor Materials and the Effects of Radiation Damage*, edited by D. J. Littler. Butterworths, London, 1962.

124. R. Castaing and B. Jouffrey, "Effets d'un bombardement ionique de courte durée sur des monocristaux métalliques," Comptes Rendus Acad. Sci. Paris *252*, 2696 (1961).

125. R. M. J. Cotterill and M. W. Jones, "Irradiation-Induced Annealing of Stacking-Fault Tetrahedra in Gold," J. Phys. Soc. Japan *18*, Suppl. III, 158 (1963).

126. R. M. J. Cotterill and M. W. Jones, "Alpha-Irradiation-Induced Removal of Stacking-Fault Tetrahedra in Quenched Gold," Phil. Mag. *10*, 535 (1964).

127. L. M. Howe and J. F. McGurn, "Direct Observation of Disappearance and Collapse of Stacking-Fault Tetrahedra in Gold Foils During Ion Bombardment in the Electron Microscope," Appl. Phys. Letters *4*, 99 (1964).

128. J. W. Menter, D. W. Pashley, and A. E. B. Presland, "The Study of Radiation Damage by Ion Bombardment of Thin Films," p. 149 in *Properties of Reactor Materials and the Effects of Radiation Damage*, edited by D. J. Littler. Butterworths, London, 1962.

129. K. L. Merkle, "Energy Dependence of Fission-Fragment Damage in Gold Films," J. Appl. Phys. *38*, 301 (1967).

130. K. L. Merkle, L. R. Singer, and R. K. Hart, "Fission-Fragment Damage in Gold Films," J. Appl. Phys. *34*, 2800 (1963).

131. T. S. Noggle and O. S. Oen, "Reduction in Radiation Damage Due to Channeling of 51-Mev Iodine Ions in Gold," Phys. Rev. Letters *16*, 395 (1966).

132. G. J. Ogilvie, J. V. Sanders, and A. A. Thomson, "The Bombardment of Gold Films by Inert Gas Ions," J. Phys. Chem. Solids *24*, 247 (1963).

133. D. W. Pashley and A. E. B. Presland, "Ion Damage to Metal Films Inside an Electron Microscope," Phil. Mag. *6*, 1003 (1961).

134. L. E. Thomas and R. W. Balluffi, "Low-Energy Bombardment of Gold with Gold Ions: On Interstitial Atom Migration in Stage III," Appl. Phys. Letters *9*, 171 (1966).

135. L. E. Thomas and R. W. Balluffi, "Interstitial Defect Clusters in Gold after Bombardment with 270 eV Gold Ions," Phil. Mag. *15*, 1117 (1967).

136. L. E. Thomas and R. W. Balluffi, "Mobility of Interstitial Defects in Gold Bombarded with 270 eV Gold Ions in Stage III," Phil. Mag. *15*, 1137 (1967).

137. J. A. Venables and R. W. Balluffi, "The Migration of Interstitial Atoms in Gold, I. Experimental," Phil. Mag. *11*, 1021 (1965).

138. J. A. Venables and R. W. Balluffi, "The Migration of Interstitial Atoms in Gold, II. Analysis and Interpretation of Experiments," Phil. Mag. *11*, 1039 (1965).

139. T. S. Noggle and J. O. Stiegler, "Fission Fragment Tracks in Metal Films," J. Appl. Phys. *33*, 1726 (1962).

140. C. J. Beevers and D. J. Mazey, "Irradiation Damage in Molybdenum after Energetic H^+ and He^{++} Ion Bombardment," Phil. Mag. *7*, 1061 (1962).

141. P. R. B. Higgins and A. C. Roberts, "The Nature and Annealing Behavior of Fission Fragment Damage in Molybdenum," J. Less Common Metals *6*, 472 (1964).

142. B. C. Masters, "Dislocation Loops in Irradiated Iron," Nature *200*, 254 (1963).

143. B. C. Masters, "Dislocation Loops in Irradiated Iron," Phil. Mag. *11*, 881 (1965).

144. I. M. Bernstein and T. D. Gulden, "Clusters in Irradiated Zirconium," p. 441 in *The Nature of Small Defect Clusters*, Vol. 2, edited by M. J. Makin. Atomic Energy Research Establishment, Harwell, Report AERE-R5269. H. M. Stationary Office, London, 1966.

145. T. D. Gulden and I. M. Bernstein, "Dislocation Loops in Irradiated Zirconium," Phil. Mag. *14*, 1087 (1966).

146. M. J. Makin, "Electron Displacement Damage in Copper and Aluminum in a High Voltage Electron Microscope," Phil. Mag. *18*, 637 (1968).

147. G. P. Scheidler and G. Roth, "Electron Microscope Studies of Point Defect Clusters in Electron Irradiated Copper," p. 391 in preprints of *International Conference on Vacancies and Interstitials in Metals*, Vol. 1, Kernforschungsanlage Jülich, Germany, Sept. 1968.

148. A. Bourret, "Electron Irradiated Pure Nickel Observed by Electron Microscopy," p. 377 in preprints of *International Conference on Vacancies and Interstitials in Metals*, Vol. 1, Kernforschungsanlage Jülich, Germany, Sept. 1968.

149. M. Wilkens, "Studies of Defect Clusters by Transmission Electron Microscopy," p. 470 in preprints of *International Conference on Vacancies and Interstitials in Metals*, Vol. 2, Kernforschungsanlage Jülich, Germany, Sept. 1968.

150. E. W. Müller, "Direct Observation of Crystal Imperfections by Field Ion Microscopy," p. 77 in *Direct Observation of Imperfections in Crystals*, edited by J. B. Newkirk and J. H. Wernick, Interscience Publishers, New York, 1962.

151. E. W. Müller, "Field Ionization and Field Ion Microscopy," Adv. Electronics Electron Phys. *13*, 83 (1960).

152. E. W. Müller, "Field Ion Microscopy. Unique Magnification and Resolution Reveal Location of Atoms on the Surface of a Variety of Metals," Science *149*, 591 (1965).

153. A. H. Cottrell, "Metallography at the Atomic Level," J. Inst. Metals *90*, 449 (1961-62).

154. D. G. Brandon, M. Wald, M. J. Southon, and B. Ralph, "The Application of Field Ion Microscopy to the Study of Lattice Defects," J. Phys. Soc. Japan *18*, Suppl. II, 324 (1963).

155. B. Ralph, M. A. Fortes, and K. M. Bowkett, "Direct Observation of Small Defect Clusters in Irradiated Metals by Field-Ion Microscopy," p. 395 in *The Nature of Small Defect Clusters*, Vol. 2, edited by M. J. Makin. Atomic Energy Research Establishment, Harwell, Report AERE-R5269. H. M. Stationary Office, London, 1966.

156. M. Attardo and J. M. Galligan, "A Field Ion Microscope Study of Neutron Irradiated Tungsten," Phys. Stat. Sol. *16*, 449 (1966).

157. D. G. Brandon, M. J. Southon, and M. Wald, "The Application of Field Ion Microscopy to the Study of Radiation Damage," p. 113 in *Properties of Reactor Materials and the Effects of Radiation Damage*, edited by D. J. Littler. Butterworths, London, 1962.

158. E. W. Müller, "Field Ion Microscopy of the Defect Structure of Metal Crystals," J. Phys. Soc. Japan *18*, Suppl. II, 1 (1963).

159. D. G. Brandon and M. Wald, "The Direct Observation of Lattice Defects by Field Ion Microscopy," Phil. Mag. *6*, 1035 (1961).

160. F. P. Bowden and L. T. Chadderton, "Fission Fragment Damage to Crystal Lattices: Dislocation Formation," Proc. Roy. Soc. (London) *A269*, 143 (1962).

161. K. M. Bowkett, L. T. Chadderton, H. Norden, and B. Ralph, "A Study of Fission Fragment Damage in Tungsten with the Field Ion Microscope," Phil. Mag. *11*, 651 (1965).

162. K. M. Bowkett, L. T. Chadderton, H. Norden, and B. Ralph, "Fission Fragment Damage in Tungsten," Phil. Mag. *15*, 415 (1967).

163. M. K. Sinha and E. W. Müller, "Bombardment of Tungsten with 20-Kev-Helium Atoms in a Field Ion Microscope," J. Appl. Phys. *35*, 1256 (1964).

164. M. A. Fortes and B. Ralph, "A Field-Ion Microscope Study of Neutron-Irradiated Iridium," Phil. Mag. *14*, 189 (1966).

165. P. Petroff and J. Washburn, "A Field Ion Microscope Investigation of 10 Mev Proton Damage in Iridium," p. 485 in preprints of *International Conference on Vacancies and Interstitials in Metals*, Vol. 2, Kernforschungsanlage Jülich, Germany, Sept. 1968.

166. M. J. Attardo and J. M. Galligan, "Radiation Damage in Platinum," Phys. Rev. Letters *14*, 641 (1965).

167. M. J. Attardo and J. M. Galligan, "Annealing Studies of Irradiated Platinum," Phys. Rev. *161*, 558 (1967).

168. J. M. Galligan and M. J. Attardo, "Radiation Hardening in Platinum," Phys. Stat. Sol. *27*, 383 (1968).

169. A. H. Cottrell, "Point Defects and the Mechanical Properties of Metals and Alloys at Low Temperatures," p. 1 in *Vacancies and Other Point Defects in Metals and Alloys*, The Institute of Metals, London, 1958.

170. M. J. Makin, "The Long-Range Forces between Dislocation Loops and Dislocations," Phil. Mag. *10*, 695 (1964).

171. J. L. Strudel and J. Washburn, "Direct Observations of Interactions between Imperfect Loops and Moving Dislocations in Aluminum," Phil. Mag. *9*, 491 (1964).

172. M. J. Makin and J. V. Sharp, "A Model of 'Lattice' Hardening in Irradiated Copper Crystals with the External Characteristics of 'Source' Hardening," Phys. Stat. Sol. *9*, 109 (1965).

173. C. Schwink and H. Neuhäuser, "On the Strengthening Mechanism in Neutron Irradiated Copper Single Crystals," Phys. Stat. Sol. *17*, 35 (1966).

174. C. Schwink and H. Neuhäuser, "Untersuchungen des Fliessbereichs neutronenbestrahlter Kupfereinkristalle, II. Kinematographische Messung der Abgleitgeschwendigkeit nichtangelassener und angelassener Proben," Phys. Stat. Sol. *6*, 679 (1964).

175. H. Neuhäuser, "Untersuchungen zur aktiven Kristallänge im Fliessbereich neutronenbestrahlter Kupfereinkristalle, I. Die Ausbildung der Gleitbänder," Phys. Stat. Sol. *25*, 593 (1968).

176. H. Neuhäuser, "Untersuchungen zur aktiven Kristallänge im Fliessbereich neutronenbestrahlter Kupfereinkristalle, II. Die aktive Kristallänge," Phys. Stat. Sol. *27*, 281 (1968).

177. R. Vandervoort and J. Washburn, "On the Stability of the Dislocation Substructure in Quenched Aluminum," Phil. Mag. *5*, 24 (1960).

178. P. W. Shin and M. Meshii, "Electron Microscopic and Mechanical Study of Quenched Aluminum," J. Metals *15*, 80 (1963).

179. M. Meshii, "The Structure and Mechanical Properties of Quenched Face-Centered Cubic Metals," p. 387 in *Lattice Defects in Quenched Metals*, edited by R. M. J. Cotterill, M. Doyama, J. J. Jackson, and M. Meshii. Academic Press, New York, 1965.

180. I. Crivelli-Visconti and I. G. Greenfield, "Dependence of Yield Stress on Diameter and Density of Prismatic Dislocation Loops," J. Appl. Phys. *39*, 2845 (1968).

181. M. S. Bapna, T. Mori, and M. Meshii, "The Observation of Slip Channels in Quenched Gold," Phil. Mag. *17*, 177 (1968).

182. S. Yoshida, M. Kiritani, Y. Deguchi, and N. Kamigaki, "Hardening and Recovery of Quenched Gold," p. 83 in *Proceedings of the International Conference on the Strength of Metals and Alloys* (Tokyo, Japan, Sept. 1967), Suppl. Trans. Japan Institute of Metals, Vol. 9, 1968.

183. R. P. Tucker, M. S. Wechsler, and S. M. Ohr, "Dislocation Channeling in Neutron-Irradiated Niobium," to be published in J. Appl. Phys.

184. G. Saada and J. Washburn, "Interaction between Prismatic and Glissile Dislocations," J. Phys. Soc. Japan *18*, Suppl. I, 43 (1963).

185. F. Kroupa, "The Interaction between Prismatic Dislocation Loops and Straight Dislocations. Part I," Phil. Mag. *7*, 783 (1962).

186. F. Kroupa and P. B. Hirsch, "Elastic Interaction between Prismatic Dislocation Loops and Straight Dislocations," p. 49 in *Dislocations in Solids*, Discussions of the Faraday Society, No. 38. The Faraday Society, London, 1964.

187. F. Seitz and J. S. Koehler, "Displacement of Atoms during Irradiation," p. 307 in *Solid State Physics*, Vol. 2, edited by F. Seitz and D. Turnbull. Academic Press, New York, 1956.

188. H. Brooks, "Nuclear Radiation Effects in Solids," p. 215 in *Annual Review of Nuclear Science*, edited by J. G. Beckerley, M. D. Kamen, and L. I. Schief. Annual Reviews, Inc., Palo Alto, California, 1956.

189. G. J. Dienes and G. H. Vineyard, *Radiation Effects in Solids*, Interscience Publishers, Inc., New York, 1957.

190. D. S. Billington and J. H. Crawford, Jr., *Radiation Damage in Solids*, Princeton University Press, Princeton, New Jersey, 1961.

191. D. S. Billington (ed.), *Radiation Damage in Solids* (Proceedings of the International School of Physics Enrico Fermi Course XVIII), Academic Press, New York, 1962.

192. R. Strumane, J. Nihoul, R. Gevers, and S. Amelinckx (eds.), *The Interaction of Radiation with Solids*, North-Holland Publishing Company, Amsterdam, 1964.

193. J. A. Brinkman and H. Wiedersich, "Mechanisms of Radiation Damage in Reactor Materials," p. 3 in *Flow and Fracture of Metals and Alloys in Nuclear Environments*, ASTM-STP-380, American Society for Testing and Materials, Philadelphia, 1965.

194. L. T. Chadderton, *Radiation Damage in Crystals*, Methuen and Co. Ltd., London, 1965.

195. J. A. Brinkman, "On the Nature of Radiation Damage in Metals," J. Appl. Phys. *25*, 961 (1954).

196. A. Seeger, "On the Theory of Radiation Damage and Radiation Hardening," p. 250 in *Proceedings of the Second International Conference on Peaceful Uses of Atomic Energy*, Vol. 6, United Nations, New York, 1958.

197. A. Seeger, "The Nature of Radiation Damage in Metals," p. 101 in *Radiation Damage in Solids*, Vol. 1, International Atomic Energy Agency, Vienna, 1962.

198. A. Seeger and U. Essmann, "The Mechanism of Radiation-Hardening of F.C.C. Metals by Fast Neutrons," p. 717 in *Radiation Damage in Solids* (Proceedings of the International School of Physics Enrico Fermi Course XVIII), Academic Press, New York, 1962.

199. R. H. Silsbee, "Focusing in Collision Problems in Solids," J. Appl. Phys. *28*, 1246 (1957).

200. G. Leibfried, "Correlated Collisions in a Displacement Spike," J. Appl. Phys. *30*, 1388 (1959).

201. G. Leibfried, "Defects in Dislocations Produced by Focusing Collisions in F.C.C. Lattices," J. Appl. Phys. *31*, 117 (1960).

202. M. T. Robinson and O. S. Oen, "The Channeling of Energetic Atoms in Crystal Lattices," Appl. Phys. Letters *2*, 30 (1963).

203. O. S. Oen and M. T. Robinson, "The Effect of Channeling on Displacement Cascade Theory," Appl. Phys. Letters *2*, 83 (1963).

204. M. T. Robinson and O. S. Oen, "Computer Studies of the Slowing Down of Energetic Atoms in Crystals," Phys. Rev. *132*, 2385 (1963).

205. C. Lehmann and G. Leibfried, "Long-Range Channeling Effects in Irradiated Crystals," J. Appl. Phys. *34*, 2821 (1963).

206. S. Datz, C. Erginsoy, G. Leibfried, and H. O. Lutz, "Motion of Energetic Particles in Crystals," Ann. Rev. Nucl. Sci. *17*, 129 (1967).

207. D. K. Holmes, "Theoretical Considerations on the Temperature Dependence of the Mechanical Properties of Metals," p. 13 in *Solid State Division Annual Progress Report for Period Ending August 31, 1957*, ORNL-2413, Oak Ridge National Laboratory, Oak Ridge, Tennessee, 1957.

208. D. K. Holmes, "Radiation Damage in Non-Fissionable Metals," p. 147 in *The Interaction of Radiation with Solids*, edited by R. Strumane, J. Nihoul, R. Gevers, and S. Amelinckx, North-Holland Publishing Co., Amsterdam, 1964.

209. E. Orowan, Discussion, p. 451 in *Symposium on Internal Stresses*, The Institute of Metals, London, 1947.

210. K. H. Westmacott, C. W. Fountain, and R. J. Stirton, "On the Spacing of Dispersed Obstacles," Acta Met. *14*, 1628 (1966).

211. U. F. Kocks, "On the Spacing of Dispersed Obstacles," Acta Met. *14*, 1629 (1966).

212. U. F. Kocks, "A Statistical Theory of Flow Stress and Work-Hardening," Phil. Mag. *13*, 541 (1966).

213. A. J. E. Foreman and M. J. Makin, "Dislocations Movement Through Random Arrays of Obstacles," Phil. Mag. *14*, 911 (1966).

214. A. J. E. Foreman, "The Bowing of a Dislocation Segment," Phil. Mag. *15*, 1011 (1967).

215. A. J. E. Foreman, "Junction Reaction Hardening by Dislocation Loops," Phil. Mag. *17*, 353 (1968).

216. J. Friedel, *Dislocations*, Pergamon Press Ltd., New York, 1964.

217. J. Friedel, "On the Elastic Limit of Crystals," p. 605 in *Electron Microscopy and Strength of Crystals*, edited by G. Thomas and J. Washburn, Interscience Publishers, New York, 1963.

218. T. H. Blewitt, R. R. Coltman, R. E. Jamison, and J. K. Redman, "Radiation Hardening of Copper Single Crystals," J. Nucl. Matls. *2*, 277 (1960).

219. T. H. Blewitt, "Low Temperature Irradiation Studies," p. 630 in *Radiation Damage in Solids* (Proceedings of the International School of Physics Enrico Fermi Course XVIII), edited by D. S. Billington, Academic Press, New York, 1962.

220. J. Diehl, "The Influence of Neutron Irradiation on the Mechanical Properties of Face-Centered Cubic Metal Crystals," p. 129 in *Radiation Damage in Solids*, Vol. 1, International Atomic Energy Agency, Vienna, 1962.

221. A. Rukwied and J. Diehl, "Verfestigung neutronenbestrahlter Kupfereinkristalle, III. Interpretation und Auswertung einiger Verfestigungskenngrössen," Z. Metallkde. *55*, 266 (1964)

222. M. J. Makin and F. J. Minter, "Irradiation Hardening in Copper and Nickel," Acta Met. *8*, 691 (1960).

223. J. Diehl, C. Leitz, and W. Schilling, "Hardening of Copper Single Crystals by Neutron Irradiation at Low Temperatures," Phys. Letters *4*, 236 (1963).

224. D. O. Thompson and V. K. Paré, "Dose Dependence of the Dislocation Breakaway Stress in Neutron-Irradiated Copper as Measured by Amplitude-Dependent Internal Friction," J. Appl. Phys. *36*, 243 (1965).

225. V. J. Fischer, "Kritische Schubspannung neutronenbestrahlter Kupfer- und Gold- Einkristalle," Z. Naturf. *17a*, 603 (1962).

226. T. J. Koppenaal, "The Effect of Neutron Irradiation on the Strength of α Cu-Al Single Crystals," Acta Met. *12*, 487 (1964).

227. F. W. Young, Jr., "Etch Pit Studies of Dislocations in Copper Crystals Deformed by Bending: I. Annealed Crystals; II. Irradiated Crystals," J. Appl. Phys. *33*, 3553 (1962).

228. J. Diehl and W. Schilling, "Hardening of Face-Centered Cubic Metals Due to Reactor Irradiations," p. 72 in *Proceedings of the Third International Conference on Peaceful Uses of Atomic Energy*, Vol. 9, United Nations, New York, 1965.

229. T. H. Blewitt and C. A. Arenberg, "Irradiation Hardening at 4.2°K in Irradiated Copper," p. 226 in *Proceedings of the International Conference on the Strength of Metals and Alloys* (Tokyo, Japan, Sept. 1967), Suppl. to Trans. Japan Institute of Metals, Vol. 9, 1968.

230. J. Diehl, Discussion to paper by Blewitt and Arenberg (ref. 229), p. 231 in *Proceedings of the International Conference on the Strength of Metals and Alloys* (Tokyo, Japan, Sept. 1967), Suppl. to Trans. Japan Institute of Metals, Vol. 9, 1968.

231. T. H. Blewitt, C. A. Arenberg, A. C. Klank, and T. Scott, "Radiation Hardening in Copper," p. 547 in preprints of *International Conference on Vacancies and Interstitials in Metals*, Vol. 2, Kernforschungsanlage Jülich, Germany, Sept. 1968.

232. G. P. Seidel, "Einfluss von Neutronenbestrahlung auf die plastische Verformung von Eisen-Einkristallen mit unterschiedlichem Kohlenstoffgehalt, I. Die Fliessspannung am Verformungsbeginn," Phys. Stat. Sol. *25*, 175 (1968).

233. G. P. Seidel, "Einfluss von Neutronenbestrahlung auf die plastische Verformung von Eisen-Einkristallen mit unterschiedlichem Kohlenstoffgehalt, II. Verfestigungskurven," Z. Metallkde. *59*, 82 (1968).

234. G. P. Seidel, "Einfluss von Neutronenbestrahlung auf die plastische Verformung von Eisen-Einkristallen mit unterschiedlichem Kohlenstoffgehalt, III. Verfestigungskenngrössen," Z. Metallkde. *59*, 88 (1968).

235. J. Diehl, G. P. Seidel, and M. Weller, "Neutron Irradiation Hardening of Iron Single Crystals Containing Small Amounts of Carbon," p. 219 in *Proceedings of the International Conference on the Strength of Metals and Alloys* (Tokyo, Japan, Sept. 1967), Suppl. to Trans. Japan Institute of Metals, Vol. 9, 1968.

236. S. M. Ohr, private communication.

237. N. E. Hinkle, N. K. Smith, and M. S. Wechsler, "Tensile Test on Irradiated Iron," p. 8 in *Radiation Metallurgy Section Solid State Division Progress Report for Period Ending February 1966*, ORNL-3949, Oak Ridge National Laboratory, Oak Ridge, Tennessee, 1966.

238. A. S. Wronski, G. A. Sargent, and A. A. Johnson, "Irradiation Hardening and Embrittlement in Body-Centered Cubic Transition Metals," p. 69 in *Flow and Fracture of Metals and Alloys in Nuclear Environments*, ASTM-STP-380, American Society for Testing and Materials, Philadelphia, 1965.

239. R. P. Tucker, *The Effect of Neutron Irradiation on Plastic Deformation in Niobium Single Crystals*, ORNL-TM-1583, Oak Ridge National Laboratory, Oak Ridge, Tennessee, 1966.

240. S. M. Ohr, R. P. Tucker, and M. S. Wechsler, "Radiation Hardening in B.C.C. Niobium and Iron," p. 187 in *Proceedings of the International Conference on the Strength of Metals and Alloys* (Tokyo, Japan, Sept. 1967), Suppl. to Trans. Japan Institute of Metals, Vol. 9, 1968.

241. M. J. Makin and F. J. Minter, "The Mechanical Properties of Irradiated Niobium," Acta Met. *7*, 361 (1967).

242. C. R. Tottle, "The Physical and Mechanical Properties of Niobium," J. Inst. Metals *85*, 375 (1956-57).

243. P. R. V. Evans, A. F. Weinberg, and R. J. Van Thyne, "Irradiation Hardening in Columbium (Niobium)," Acta Met. *11*, 143 (1963).

244. M. J. Makin, F. J. Minter, and S. A. Manthorpe, "The Correlation between the Critical Shear Stress of Neutron Irradiated Copper Single Crystals and the Density of Defect Clusters," Phil. Mag. *13*, 729 (1966).

245. M. J. Makin, F. J. Minter, and S. A. Manthorpe, "The Correlation between the Critical Shear Stress of Neutron Irradiated Copper Single Crystals and the Density of Defect Clusters," p. 565 in *The Nature of Small Defect Clusters*, Vol. 2, edited by M. J. Makin. Atomic Energy Research Establishment, Harwell, Report AERE-R5269. H. M. Stationary Office, London, 1966.

246. J. H. O. Varley, "The Agglomeration into Clusters of Interstitial Atoms and Vacancies Generated by Fast Neutron Irradiation," Phil. Mag. *7*, 301 (1962).

247. M. J. Makin and S. A. Manthorpe, "The Annealing of Neutron Irradiation Hardening in Copper Crystals," Phil. Mag. *10*, 579 (1964).

248. M. Rühle, "Radiation Hardening of Neutron-Irradiated Copper Single Crystals, I. Experimental Results," Phys. Stat. Sol. *26*, 661 (1968).

249. G. P. Scheidler, M. J. Makin, F. J. Minter, and W. F. Schilling, "The Effect of Irradiation Temperature on the Formation of Clusters in Neutron Irradiated Copper," p. 405 in *The Nature of Small Defect Clusters*, Vol. 2, edited by M. J. Makin. Atomic Energy Research Establishment, Harwell, Report AERE-R5269. H. M. Stationary Office, London, 1966.

250. W. Frank, "Thermally Activated Dislocation Motion in a Solid Containing a Multiple Spectrum of Dislocation Obstacles," Phys. Stat. Sol. *26*, 197 (1968).

251. W. Frank, M. Rühle, and M. Saxlová, "Radiation Hardening of Neutron-Irradiated Copper Single Crystals," Phys. Stat. Sol. *26*, 671 (1968).

252. C. Schwink, "Untersuchungen des Fliessbereichs neutronenbestrahlter Kupfereinkristalle, III. Die charakteristischen Grössen der Gleithindernisse, insbesondere die aktivierungsenergie," Phys. Stat. Sol. *7*, 481 (1964).

253. C. Schwink, "Über den Begriff 'aktives Gleitvolumen' und dessen Bedeutung," Phys. Stat. Sol. *18*, 557 (1966).

254. C. Schwink and H. Neuhäuser, "Experiments Concerning the Critical Shear Stress of n-Irradiated Metals," p. 550 in *The Nature of Small Defect Clusters*, Vol. 2, edited by M. J. Makin. Atomic Energy Research Establishment, Harwell, Report AERE-R5269. H. M. Stationary Office, London, 1966.

255. J. Diehl, G. P. Seidel, and L. Niemann, "Thermisch aktivierte Vorgänge bei der Verformung neutronenbestrahler Kupfer-Einkristalle, I. Bestimmung der Aktivierungsenergie," Phys. Stat. Sol. *11*, 339 (1965).

256. J. Diehl, G. P. Seidel, and L. Niemann, "Thermisch aktivierte Vorgänge bei der Verformung neutronenbestrahler Kupfer-Einkristalle, II. Versetzungsbewegung bei Vorliegen eines Hindernisspektrums und Auswertung von Messungen," Phys. Stat. Sol. *12*, 405 (1965).

257. J. Diehl and G. P. Seidel, "On the Strengthening Mechanism in Neutron Irradiated Copper Single Crystals, II. Analysis of the Thermally Activated Processes," Phys. Stat. Sol. *17*, 43 (1966).

258. T. J. Koppenaal, "The Strain Rate Dependence of the Flow Stress in Neutron Irradiated Copper Single Crystals," Phil. Mag. *8*, 1313 (1963).

259. T. J. Koppenaal, "Neutron Irradiation Strengthening in Copper Single Crystals," Phil. Mag. *11*, 1257 (1965).

260. R. J. Arsenault and T. J. Koppenaal, "Thermally Activated Slip in Neutron-Irradiated Copper Single Crystals," Appl. Phys. Letters *6*, 159 (1965).

261. T. J. Koppenaal and R. J. Arsenault, "A Rate Controlling Mechanism for Slip in Neutron Irradiated Copper Single Crystals," Phil. Mag. *12*, 951 (1965).

262. T. J. Koppenaal and R. J. Arsenault, "Some Notes on the Strengthening Mechanism in Neutron Irradiated Copper Single Crystals," Phys. Stat. Sol. *17*, 27 (1966).

263. R. J. Arsenault and James C. M. Li, "Thermally Activated Dislocation Motion in a Periodic Internal Stress Field," Phil. Mag. *16*, 1307 (1967).

264. T. J. Koppenaal, "Stress Relaxation in Neutron Irradiated Copper Single Crystals," Acta Met. *15*, 681 (1967).

265. T. J. Koppenaal, "The Strengthening Mechanism in Neutron Irradiated Copper Single Crystals after Mild Annealing," Acta Met. *16*, 89 (1968).

266. A. Seeger, "Stacking Faults in Close-Packed Lattices," p. 328 in *Report on Conference of Defects in Crystalline Solids* (Bristol, 1954), The Physical Society, London, 1955.

267. J. G. Y. Chow, S. B. McRickard, and D. H. Gurinsky, "Mechanical Properties of Irradiated Iron and Iron Alloys," p. 46 in *Symposium on Radiation Effects on Metals and Neutron Dosimetry*, ASTM-STP-341, American Society for Testing and Materials, Philadelphia, 1963.

268. D. Ast and J. Diehl, "Untersuchung des Zerfalls der Leerstellen-agglomerate in neutronenbestrahltem Nickel mit Hifle der kritischen Schubspannung," Phys. Stat. Sol. *17*, 269 (1966).

269. J. Diehl and D. Ast, "Annealing of the Vacancy Agglomerates Responsible for the Enhancement of the Critical Shear Stress of Neutron Irradiated Nickel," p. 491 in *The Nature of Small Defect Clusters*, Vol. 2, edited by M. J. Makin. Atomic Energy Research Establishment, Harwell, Report AERE-R5269. H. M. Stationary Office, London, 1966.

270. M. J. Makin and T. H. Blewitt, "The Hardening of Copper Single Crystals by Electron Irradiation," Acta Met. *10*, 241 (1962).

271. M. J. Makin and E. Gillies, "The Effect of Neutron Irradiation on the Mechanical Properties of Molybdenum and Tungsten," J. Inst. Metals *86*, 108 (1957-58).

272. A. S. Wronski and A. A. Johnson, "A Hardening Effect Associated with Stage III Recovery in Neutron Irradiated Molybdenum," Phil. Mag. *8*, 1067 (1963).

273. J. Moteff, "Radiation Damage in Body-Centered Cubic Metals and Alloys," p. 727 in *Radiation Effects*, edited by W. F. Sheely, Gordon and Breach, Science Publishers, Inc., New York, 1967.

274. N. E. Hinkle, private communication.

275. D. G. Martin, "The Annealing of Point Defects in Cold-Worked Molybdenum," Acta Met. *5*, 371 (1957).

276. G. H. Kinchin and M. W. Thompson, "Irradiation Damage and Recovery in Molybdenum and Tungsten," J. Nucl. Energy *6*, 275 (1958).

277. D. E. Peacock and A. A. Johnson, "Stage III Recovery in Neutron Irradiated Mo and Nb," Phil. Mag. *8*, 563 (1963).

278. J. Nihoul, "The Recovery of Radiation Damage in Molybdenum," p. 309 in *Radiation Damage in Solids*, Vol. 1, International Atomic Energy Agency, Vienna, 1962.

279. J. Nihoul, "The Recovery of Radiation Damage in Molybdenum," Phys. Stat. Sol. *2*, 308 (1962).

280. J. Nihoul, "Note on D. Peacock and A. A. Johnson 'Stage III Recovery in Neutron Irradiated Molybdenum and Niobium'," Phil. Mag. *9*, 167 (1964).

281. L. Stals and J. Nihoul, "Stage III Recovery in Cold-Worked Niobium," Phys. Stat. Sol. *8*, 785 (1965).

282. H. Schultz, "Die Erholung Des Elektrischen Widerstandes von Kaltverformtem Wolfram," Acta Met. *12*, 649 (1964).

283. J. M. Williams, W. E. Brundage, and J. T. Stanley, "The Effect of Oxygen on 'Stage III' Annealing in Neutron-Irradiated Niobium," Met. Sci. J. *2*, 100 (1968).

284. R. Bullough, J. T. Stanley, and J. M. Williams, "The Kinetics of Migration of Impurities to Small Dislocation Loops," Met. Sci. J. *2*, 93 (1968).

285. F. Schlät and A. Köthe, "Einfluss des Sauerstoffgehalts auf die Erholung von Kaltverformtem Tantal," Acta Met. *14*, 425 (1966).

286. A. Köthe and F. Schlät, "The Influence of Interstitial Impurity Atoms on the Recovery Behaviour of Cold-Worked Vanadium," J. Matls. Sci. *2*, 201 (1967).

287. A. Köthe and F. Schlät, "Recovery of Deformed Niobium and Tantalum Degassed in Ultra-High Vacuum," Phys. Stat. Sol. *21*, K73 (1967).

288. R. J. Dinter, "Hochvakuum-Reinigung von Niob und Tantal und ihr Einfluss auf den elektrischen Widerstand," Z. Metallk. *58*, 70 (1967).

289. L. J. Cuddy, "An Electrical Resistivity Study of Deformation and Recovery of Iron at Low Temperature," Phil. Mag. *12*, 855 (1965).

290. L. J. Cuddy and J. C. Raley, "Stage III Recovery in Cold-Worked Iron," Acta Met. *14*, 440 (1966).

291. F. E. Fujita and A. C. Damask, "Kinetics of Precipitation in Irradiated Iron, II. Electrical Resistivity Measurements," Acta Met. *12*, 331 (1964).

292. A. R. Rosenfield, "Recovery of Cold-Worked Body-Centered Cubic Metals," Acta Met. *12*, 119 (1964).

293. J. Nihoul and L. Stals, "On the Reaction Order of Bimolecular Recovery Processes in Solids," Phys. Stat. Sol. *17*, 295 (1966).

294. L. Stals, J. Nihoul, and R. Gevers, "Analytical Study of Isochronal Annealing of Cold-Worked Niobium," Phys. Stat. Sol. *15*, 717 (1966).

295. J. W. Christian and B. C. Masters, "Low-Temperature Deformation of Body-Centered Cubic Metals, I. Yield and Flow Stress Measurements," Proc. Roy. Soc. (London) *281A*, 223 (1964).

296. J. W. Christian and B. C. Masters, "Low-Temperature Deformation of Body-Centered Cubic Metals, II. Mechanism of Thermally Activated Flow," Proc. Roy. Soc. (London) *281A*, 240 (1964).

297. H. Conrad, "Yielding and Flow of the B.C.C. Metals at Low Temperatures," p. 476 in *The Relation Between the Structure and Mechanical Properties of Metals*, Vol. 2, H. M. Stationary Office, London, 1963.

298. A. R. Rosenfield, G. T. Hahn, A. L. Bement, Jr., and R. I. Jaffee (eds.), *Dislocation Dynamics*, McGraw-Hill Book Co., New York, 1968.

299. G. Leibfried, "Thermal Motion of Dislocation Lines," p. 495 in *Dislocations and Mechanical Properties of Crystals*, edited by J. C. Fisher, W. G. Johnston, R. Thomson, and T. Vreeland, Jr., John Wiley and Sons, Inc., New York, 1957.

300. R. L. Fleischer, "Solution Hardening by Tetragonal Distortions: Application to Irradiation Hardening in F.C.C. Crystals," Acta Met. *10*, 835 (1962).

301. R. L. Fleischer, "Rapid Solution Hardening, Dislocation Mobility, and the Flow Stress of Crystals," J. Appl. Phys. *33*, 3504 (1962).

302. A. W. Cochardt, G. Schoek, and H. Wiedersich, "Interaction Between Dislocations and Interstitial Atoms in Body-Centered Cubic Metals," Acta Met. *3*, 533 (1955).

303. M. J. Makin, "The Thermal Activation of Slip in Neutron Irradiated Copper," Phil. Mag. *9*, 81 (1964).

304. K. Ono, "Temperature Dependence of Dispersed Barrier Hardening," J. Appl. Phys. *39*, 1803 (1968).

305. S. M. Ohr, "Temperature Dependence of Dispersed Barrier Hardening," J. Appl. Phys. *39*, 5335 (1968).

306. W. Frank, "Die kritische Schubspannung kubischer Kristalle mit Fehlstellen tetragonaler Symmetrie, I. Zur kurzreichenden Wechselwirkung von Versetzungen mit elastischen Dipolen," Z. Naturforschg. *22a*, 365 (1967).

307. W. Frank, "Die kritische Schubspannung kubischer Kristalle mit Fehlstellen tetragonaler Symmetrie, II. Der induzierte Snoek-Effekt," Z. Naturforschg. *22a*, 377 (1967).

308. W. Frank, "Die kritische Schubspannung kubischer Kristalle mit Fehlstellen tetragonaler Symmetrie, III. Elektronen- und neutronenbestrahltes Aluminum sowie elektronenbestrahltes Kupfer," Phys. Stat. Sol. *18*, 459 (1966).

309. W. Frank, "Die kritische Schubspannung kubischer Kristalle mit Fehlstellen tetragonaler Symmetrie, IV. Die unter Streckgrenze von α-Eisen," Phys. Stat. Sol. *19*, 239 (1967).

310. R. J. Arsenault, "An Investigation of the Mechanism of Thermally Activated Deformation in Tantalum and Tantalum-Base Alloys," Acta Met. *14*, 831 (1966).

311. R. J. Arsenault, "The Double-Kink Model for Low-Temperature Deformation of B.C.C. Metals and Solid Solutions," Acta Met. *15*, 501 (1967).

312. Z. S. Basinski and J. W. Christian, "The Influence of Temperature and Strain Rate on the Flow Stress of Annealed and Decarburized Iron at Subatmospheric Temperatures," Aust. J. Phys. *13*, 299 (1960).

313. D. F. Stein, "The Effect of Carbon on the Strain-Rate Sensitivity of Iron Single Crystals," Acta Met. *14*, 99 (1966).

314. D. F. Stein, "Reply to Comment on 'The Effect of Carbon on the Strain Rate Sensitivity of Iron Single Crystals'," Acta Met. *15*, 150 (1967).

315. D. F. Stein, "Some Effects of Crystal Orientation and Purity on the Dynamical Behavior of Dislocations," p. 453 in *Dislocation Dynamics*, edited by A. R. Rosenfield, G. T. Hahn, A. L. Bement, Jr., and R. I. Jaffee, McGraw-Hill Book Co., New York, 1968.

316. B. L. Mordike and P. Hassen, "The Influence of Temperature and Strain Rate on the Flow Stress of α-Iron Single Crystals," Phil. Mag. *7*, 459 (1962).

317. R. L. Fleischer, "The Flow Stress of Body-Centered Cubic Metals: Inherent Lattice Hardening or Solution Hardening?," Acta Met. *15*, 1513 (1967).

318. H. Conrad, "Comments on 'The Effect of Carbon on the Strain Rate Sensitivity of Iron Single Crystals'," Acta Met. *15*, 147 (1967).

319. W. Frank and A. Seeger, "Dispersed Barrier Hardening in Cubic Crystals," Comments on Solid State Physics *1*, 99 (1968).

320. T. E. Mitchell, R. A. Foxall, and P. B. Hirsch, "Work Hardening in Niobium Single Crystals," Phil. Mag. *8*, 1895 (1963).

321. H. C. Kim and P. L. Pratt, "Yielding and Strain Ageing of Niobium Crystals," Phys. Stat. Sol. *14*, K151 (1966).

322. P. J. Sherwood, F. Guiu, H. C. Kim, and P. L. Pratt, "Plastic Anisotropy of Tantalum, Niobium, and Molybdenum," Can. J. Phys. *45*, 1075 (1967).

323. R. J. Arsenault, "The Possibility of Irradiation Damage Affecting the Rate-Controlling Mechanism of Slip in Body-Centered Cubic Metals and Solid Solutions," Acta Met. *15*, 1853 (1967).

324. F. A. Smidt, Jr. and A. L. Bement, "Thermally Activated Dislocation Motion and Its Application to the Study of Radiation Damage," p. 409 in *Dislocation Dynamics*, edited by A. R. Rosenfield, G. T. Hahn, A. L. Bement, Jr., and R. I. Jaffee, McGraw-Hill Book Co., New York, 1968.

325. H. D. Guberman and R. E. Reed, "Deformation of Irradiated and Unirradiated Niobium Single Crystals in Compression," p. 75 in *Radiation Metallurgy Section, Solid State Division Progress Report for Period Ending January 1968*, ORNL-4246, Oak Ridge National Laboratory, Oak Ridge, Tennessee, April 1968.

326. R. E. Reed, "The Preparation and Purification of Single Crystals of Niobium," p. 35 in *Radiation Metallurgy Section Solid State Division Progress Report for Period Ending February 1966*, ORNL-3949, Oak Ridge National Laboratory, Oak Ridge, Tennessee, May 1966.

327. G. W. Mellors and S. Senderoff, "Electrodeposition of Coherent Deposits of Refractory Metals, I. Niobium," J. Electrochem. Soc. *112*, 266 (1965).

328. C. W. Dean and R. E. McDonald, *High-Purity Shape Casting with an Electron-Beam Furnace*, ORNL-TM-1935, Oak Ridge National Laboratory, Oak Ridge, Tennessee, October 1967.

329. R. E. Reed, C. W. Dean, R. E. McDonald, and J. F. Emery, *Sources of Contamination During Electron-Beam Melting*, p. 516 in *Electron and Ion Beam Science and Technology*, Third International Conference, edited by R. A. Bakish, The Electrochem. Soc., Inc., New York, 1968. (See, also, report with same title, ORNL-TM-228, Oak Ridge National Laboratory, Oak Ridge, Tennessee, July 1968.)

330. C. S. Barrett, *Structure of Metals*, second edition, McGraw-Hill Book Co., Inc., New York, 1952.

331. R. E. Reed, R. P. Tucker, and C. L. Brooks, "Evaluation of Niobium Source Materials Suitable for Electron Beam Float Zone Melting," p. 89 in *Radiation Metallurgy Section Solid State Division Progress Report for Period Ending January 1968*, ORNL-4246, Oak Ridge National Laboratory, Oak Ridge, Tennessee, April 1968.

332. R. E. Reed, H. D. Guberman, and T. O. Baldwin, "The Growth of Niobium Single Crystals with Good Crystalline Perfection," p. 829 in Proceedings of the International Conference on *Crystal Growth* (Boston, June 1966), Pergamon Press, New York, 1967.

333. R. E. Reed, "Niobium: Purification and Perfection," p. 20 in *Radiation Metallurgy Section Solid State Division Progress Report for Period Ending January 1967*, ORNL-4097, Oak Ridge National Laboratory, Oak Ridge, Tennessee, April 1967.

334. M. S. Duesbery, R. A. Foxall, and P. B. Hirsch, "The Plasticity of Pure Niobium Single Crystals," J. de Physique, Colloque C 3, Suppl. 7-8, *27*, C 3-193 (1966).

335. J. Spreadborough, M. Malone, D. L. King, D. G. Brandon, W. Bollmann, and E. Anderson, "The Effect of Radiation on the Ductile-Brittle Transition in Pressure Vessel Steels," EUR 2354E, EURAEC 1394, Euratom, 1965.

336. M. J. Whelan, "An Outline of the Theory of Diffraction Contrast Observed at Dislocations and Other Defects in Thin Crystals Examined by Transmission Electron Microscopy," J. Inst. Metals *87*, 392 (1958-59).

337. P. B. Hirsch, A. Howie, R. B. Nicholson, D. W. Pashley, and M. J. Whelan, p. 271 in *Electron Microscopy of Thin Crystals*, Butterworths, London, 1965.

338. P. B. Hirsch, A. Howie, R. B. Nicholson, D. W. Pashley, and M. J. Whelan, p. 311 and p. 415 in *Electron Microscopy of Thin Crystals*, Butterworths, London, 1965.

339. S. M. Ohr, to be published.

340. V. A. Phillips and J. D. Livingston, "Direct Observation of Coherency Strains in a Copper-Cobalt Alloy," Phil. Mag. *7*, 969 (1962).

341. P. B. Hirsch, A. Howie, R. B. Nicholson, D. W. Pashley, and M. J. Whelan, p. 497 in *Electron Microscopy of Thin Crystals*, Butterworths, London, 1965.

342. P. B. Hirsch, A. Howie, R. B. Nicholson, D. W. Pashley, and M. J. Whelan, p. 171 in *Electron Microscopy of Thin Crystals*, Butterworths, London, 1965.

343. J. W. Michell, "Equilibration of Lattice Defects in Real Crystals," J. Appl. Phys. *33*, 406 (1962).

344. M. S. Wechsler, R. P. Tucker, and R. Bode, "Radiation Hardening in Single Crystal Niobium -- The Temperature Dependence of Yielding," to be published in Acta Met.

345. D. Kuhlmann-Wilsdorf, R. Maddin, and H. G. F. Wilsdorf, "Point Defect Hardening in Face-Centered Cubic Metals," p. 137 in *Strengthening Mechanisms in Solids*, American Society for Metals, Metals Park, Ohio, 1962.

346. H. Kimura and R. Maddin, "Effect of Quenched-In Vacancies on the Mechanical Properties of Metals and Alloys," p. 319 in *Lattice Defects in Quenched Metals*, edited by R. M. J. Cotterill, M. Doyama, J. J. Jackson, M. Meshii, Academic Press, New York, 1965.

347. A. Goldsmith, T. E. Waterman, and H. J. Hirschhorn, p. I-467 in *Handbook of Thermophysical Properties of Solid Materials*, Vol. 1, Pergamon Press, New York, 1961.

348. Taylor Lyman (ed.), p. 20 in *ASM Metals Handbook*, American Society for Metals, Novelty, Ohio, 1948.

349. A. L. Titchner and M. B. Bever, "The Stored Energy of Cold Work," p. 247 in *Progress in Metal Physics*, Vol. 7, edited by B. Chalmers and R. King, Pergamon Press, New York, 1958.

350. T. P. Wang and N. Brown, "The Energy Stored in Ingot Iron Deformed by Torsion at 25, -82 and -185°C," Trans. Am. Soc. Metals *50*, 541 (1958).

351. S. M. Ohr, private communication.

352. S. B. McRickard, "Saturation and Exposure Dependence of the Yield Stress of Irradiated Iron," Phil. Mag. *18*, 915 (1968).

353. W. B. Pearson, *A Handbook of Lattice Spacings and Structures of Metals and Alloys*, Pergamon Press, New York, 1958.

354. P. E. Armstrong and H. L. Brown, "Anomalous Temperature Dependence of Elastic Moduli of Niobium Metal," Trans. Am. Soc. Metals *58*, 30 (1965).

355. K. -H. Hellwege (ed.), *Landolt-Börnstein Numerical Data and Functional Relationships in Science and Technology, Group III: Crystal and Solid State Physics*, Vol. 1, p. 6, Springer-Verlag, Berlin, 1966.

356. M. D. Goldberg, S. F. Mughabghab, S. N. Purohit, B. A. Magurno, and V. M. May, *Neutron Cross Sections*, second edition, Suppl. 2, Vols. IIA and IIB, BNL-325, Brookhaven National Laboratory Associated Universities, Inc., New York. Available from the Clearinghouse for Federal Scientific and Technical Information, National Bureau of Standards, U. S. Department of Commerce, Springfield, Virginia.

357. A. Bourret and D. Dautreppe, "Study of Agglomerated Defects in Irradiated Pure Nickel by Electron Microscopy," Phys. Stat. Sol. *29*, 283 (1968).

358. J. M. Williams, J. T. Stanley, and W. E. Brundage, "The Effect of Interstitial Impurities on Post-Irradiation Annealing Phenomena in Niobium," in *Radiation Metallurgy Section Solid State Division Progress Report for Period Ending July 1968*, ORNL-4334, Oak Ridge National Laboratory, Oak Ridge, Tennessee, February 1969.

359. R. W. Powers and M. V. Doyle, "Diffusion of Interstitial Solutes in the Group V Transition Metals," J. Appl. Phys. *30*, 514 (1959).

360. H. Schultz, "Point Defects in Body-Centered Cubic Transition Metals," Mater. Sci. Eng. *3*, 189 (1968/69).

361. M. S. Wechsler and R. Bode, private communication.

362. S. M. Ohr, R. P. Tucker, and E. D. Bolling, "The Annealing Characteristics of Neutron-Irradiated Niobium," p. 55 in *Radiation Metallurgy Section Solid State Division Progress Report for Period Ending January 1968*, ORNL-4246, Oak Ridge National Laboratory, Oak Ridge, Tennessee, April 1968.

363. R. N. Orava, A. Lawley, and H. Conrad, "Work Hardening and Dislocation Structures in Niobium Single Crystals," p. 488 in *Proceedings of the International Conference on the Strength of Metals and Alloys* (Tokyo, Japan, Sept. 1967), Suppl. to Trans. Japan Institute of Metals, Vol. 9, 1968.

364. R. E. Reed and M. S. Wechsler, "Plastic Deformation in Niobium Single Crystals," p. 36 in *Radiation Metallurgy Section Solid State Division Progress Report for Period Ending August 1965*, ORNL-3878, Oak Ridge National Laboratory, Oak Ridge, Tennessee, January 1966.

365. R. J. Arsenault, "Dislocation Dynamics Applied to the Problem of Overshoot," Acta Met. *14*, 1634 (1966).

366. G. Taylor and J. W. Christian, "The Effect of High Vacuum Purification on the Mechanical Properties of Niobium Single Crystals," Acta Met. *13*, 1216 (1965).

367. G. Taylor and J. W. Christian, "Experiments on the Deformation of Niobium Single Crystals, I. Stress versus Strain Curves and Slip Systems in Compression and Tension," Phil. Mag. *15*, 873 (1967).

368. D. K. Bowen, J. W. Christian, and G. Taylor, "Deformation Properties of Niobium Single Crystals," Can. J. Phys. *45*, 903 (1967).

369. R. A. Foxall, M. S. Duesbery, and P. B. Hirsch, "The Deformation of Niobium Single Crystals," Can. J. Phys. *45*, 607 (1967).

370. K. Farrell and P. R. V. Evans, "Some Observations on Mechanical Twinning in Polycrystalline Niobium," J. Less-Common Metals *8*, 222 (1965).

371. C. J. McHargue and H. E. McCoy, "Effect of Interstitial Elements on Twinning in Columbium (Niobium)," Trans. Met. Soc. AIME *227*, 1170 (1963).

372. S. M. Ohr, "Work Hardening Characteristics of Neutron-Irradiated Iron," Scripta Met. *2*, 213 (1968).

373. R. von Jan, "Defektverteilung in Verlagerungskaskaden, I. Kaskadentheorie," Phys. Stat. Sol. *6*, 925 (1964).

374. R. von Jan, "Defektverteilung in Verlagerungskaskaden, II. Berücksichtigung von Gittereffekten," Phys. Stat. Sol. *7*, 299 (1964).

375. R. von Jan, "Defektverteilung in Verlagerungskaskaden, III. Edelmetalle," Phys. Stat. Sol. *8*, 331 (1965).

376. A. Seeger and R. von Jan, "Radiation Damage Production," p. 339 in *Theory of Crystal Defects*, edited by B. Gruber. Prague, Academia Publishing House of the Czechoslovak Academy of Sciences, 1966.

APPENDIXES

APPENDIX A

CRYSTAL GEOMETRY OF DISLOCATION CHANNELING

In Appendix A we present three cases in addition to those in Chapter V, illustrating the crystal geometry of dislocation channeling, and show an additional case of a channel crossing a boundary. For all these cases the foils were prepared from the sample described in Chapter V, Section II, p. 109.

CASE A-1 (FIGURE A-1)

Figure A-1 shows an equilateral-triangular pattern of channels on a (111) foil surface. The sketch in Figure A-1a gives the number designations of the channels, the channel trace directions as obtained from the electron diffraction patterns, and the slip systems operating in the channels. The operating slip systems, i.e., the planes of the channels and the Burgers vectors of the slip dislocations, were deduced as described below. This determination was facilitated by the diffraction contrast analysis of electron micrographs of the same field taken with $[01\bar{1}]$, $[10\bar{1}]$, and $[1\bar{1}0]$ diffraction vectors, $\vec{g}$, as shown in Figures A-1b, A-1c, and A-1d, respectively. The vertex angles of the triangle in Figure A-1 were measured in the micrographs to be 60° to within ±2.5°.

As an aside, consider the traces which {110}, {112}, and {123} type planes, i.e., possible slip planes in bcc crystals, form in the (111). There are two sets of three {110}-type planes which give traces 60° apart in the (111). Of these two sets, only one, namely $(01\bar{1})$, $(10\bar{1})$, and $(1\bar{1}0)$, will give rise to channel traces in the observed <112> directions. The

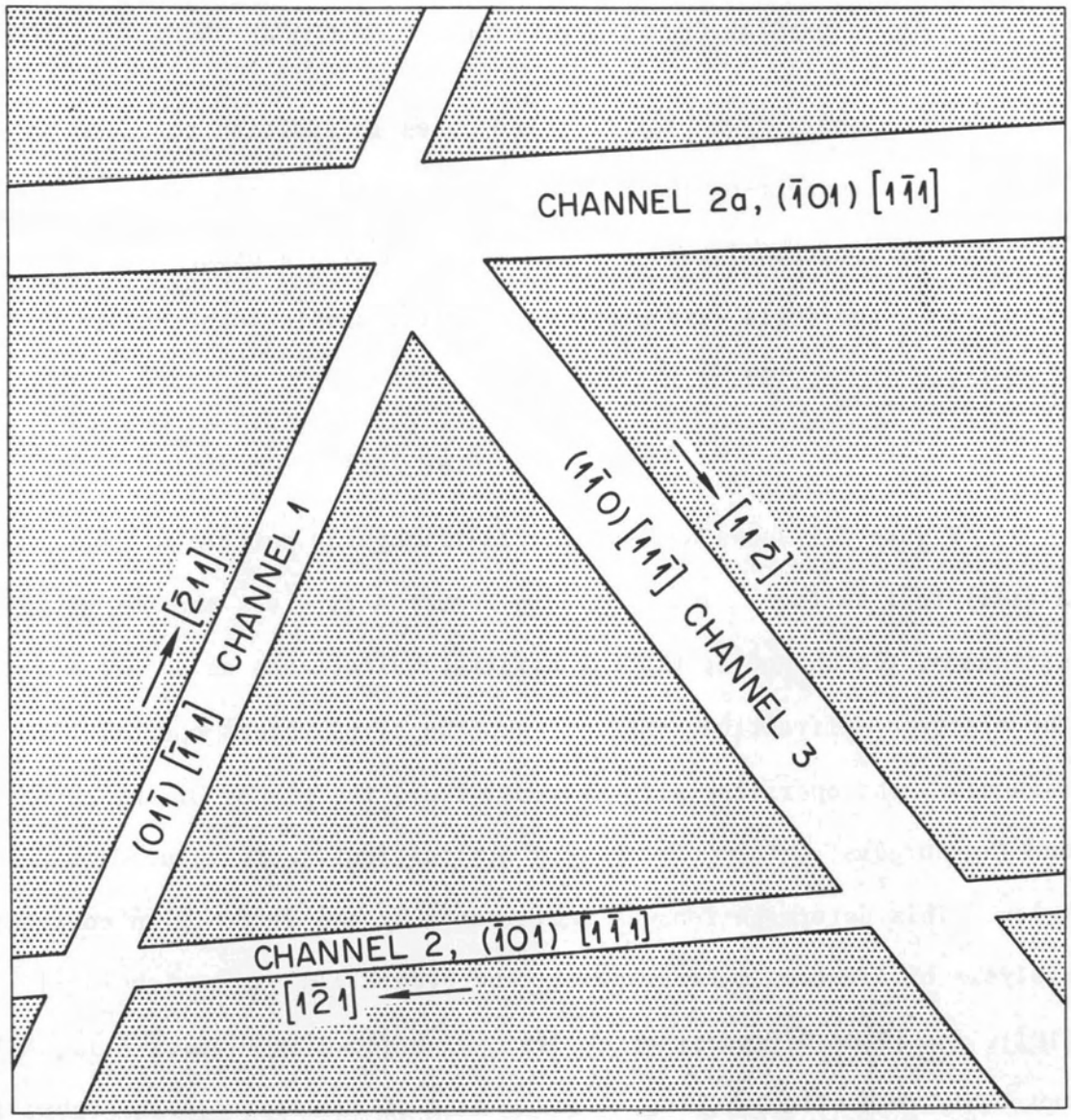

(a) Sketch of channel geometry.

Figure A-1. Equilateral-triangular pattern of dislocation channels on a (111) foil surface in CIBA-A niobium.

The same area of view is shown in each micrograph. Dose = 4.4 x 10^{18} neutrons/cm^2 (E > 1 Mev). Irradiation temperature ∿ 50°C.

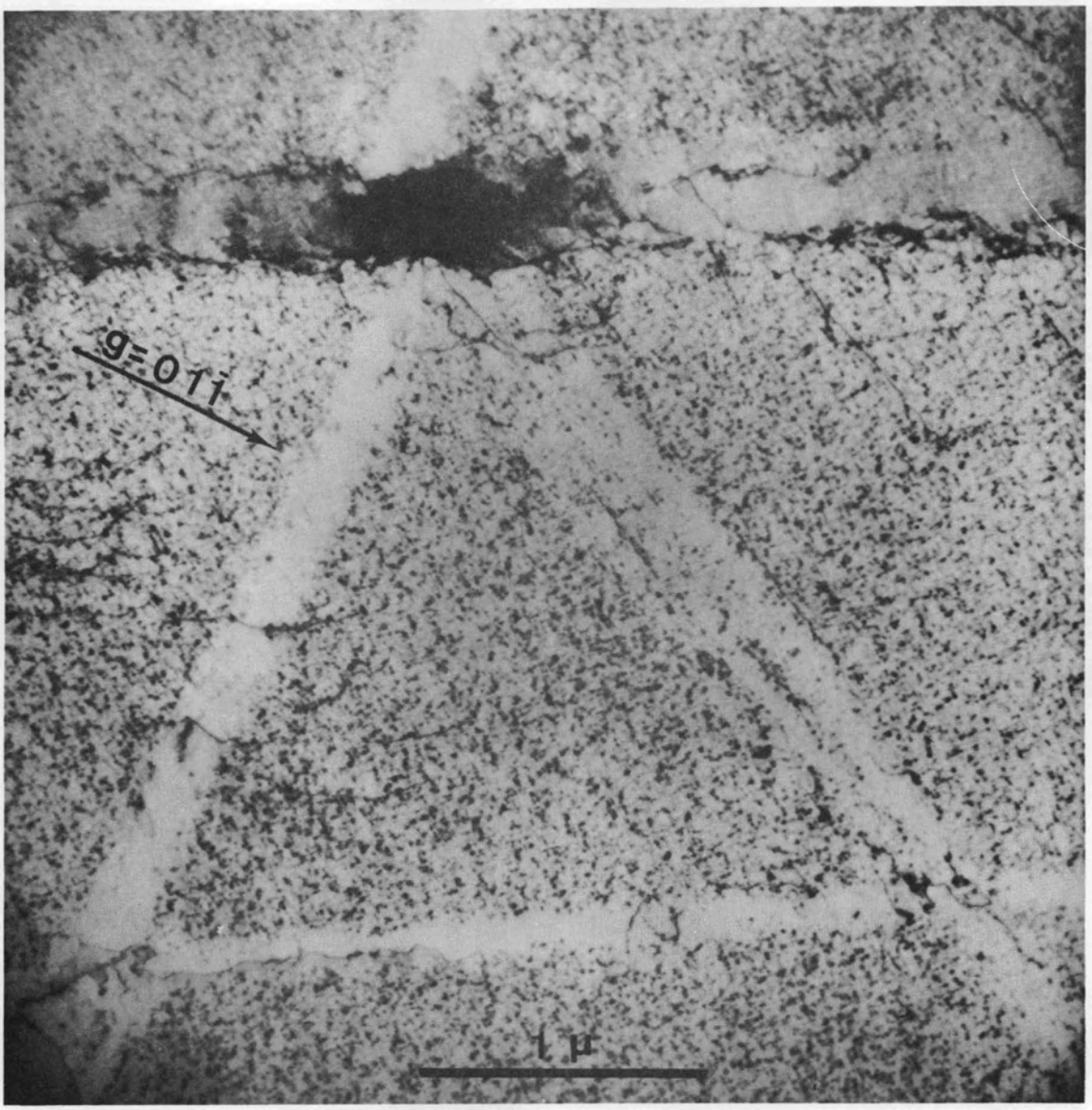

(b) $\vec{g} = [01\bar{1}]$.

Figure A-1. (continued).

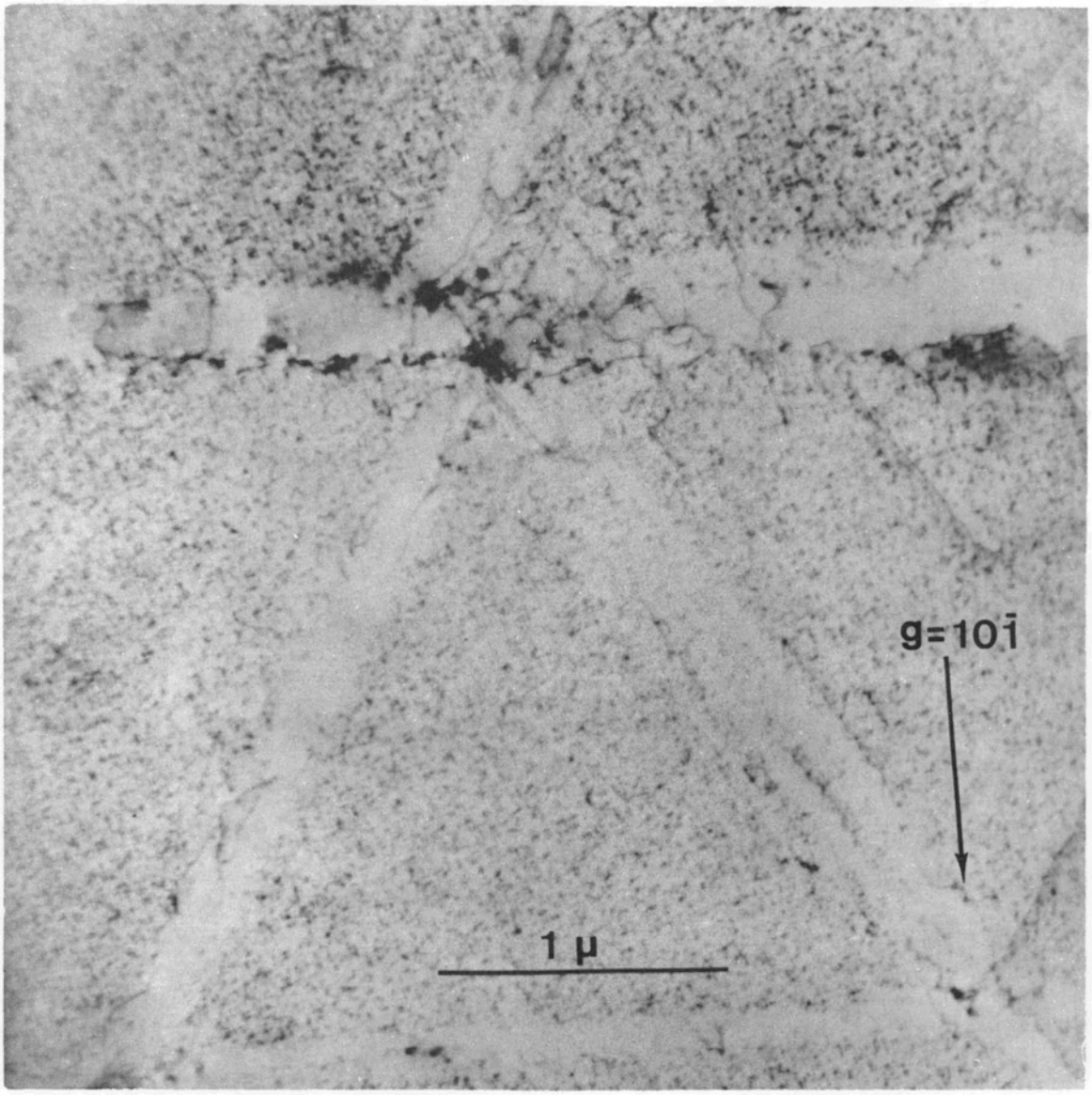

(c) g = [10$\bar{1}$].

Figure A-1. (continued).

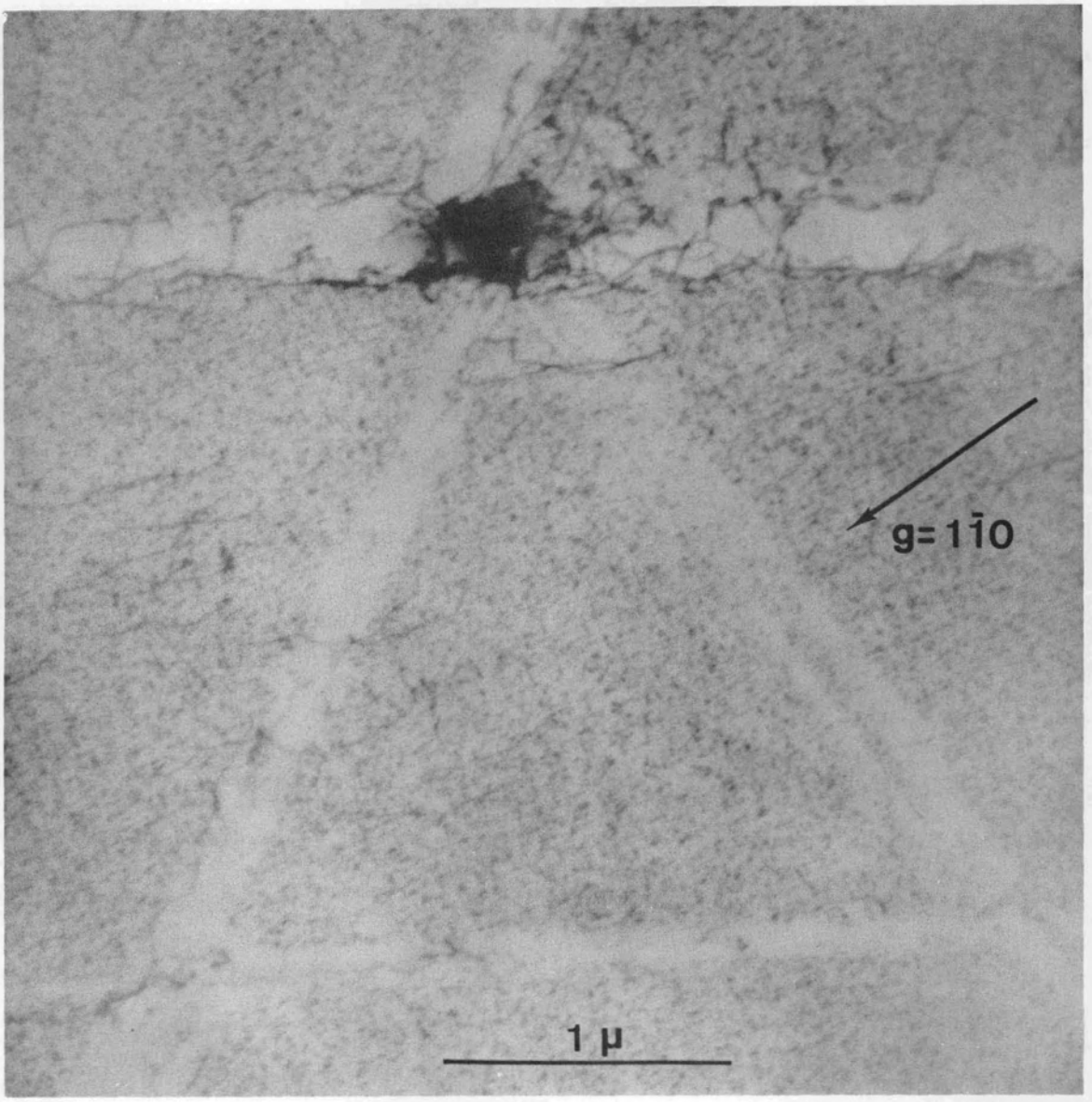

(d) $\vec{g} = [1\bar{1}0]$.

Figure A-1. (continued).

traces for the other set, (011), (101), and (110), form an equilateral triangle rotated 60° about [111] from the trace directions observed. The normals for the three {110} planes corresponding to the observed channel traces lie in (111). Thus, the channeled {110} planes would form a right equilateral-triangular prism whose axis is along [111]. Since there are no {112} planes which give <112> traces in a (111) plane, {112} channel planes may be discounted. As for {123} planes, there are two planes of this type giving traces in each of the required <112> directions. In all cases the angle between the normals to these {123} planes and [111] is 22° 12'.

We now consider the contrast of the dislocations for the various operating reflections shown in Figure A-1. Most of the dislocations are observed to lie parallel to, but not always in, the channel trace. In bcc metals, the <111> close-packed direction is the normal slip direction and hence the Burgers vector direction for slip dislocations. Diffraction contrast theory predicts that when the Burgers vector, $\vec{b}$, lies in the reflecting plane, the dislocation is invisible if pure screw and generally exhibits weak contrast or is invisible if pure edge. Thus, $\vec{g} \cdot \vec{b} = 0$ means invisibility or weak contrast for dislocations, where $\vec{g}$ is the diffraction vector. In Tables A-I and A-II the contrast for dislocations under three operating reflections (see Figure A-1) is compared to $\vec{g} \cdot \vec{b}$ for <111> Burgers vectors. From these tables we conclude that the Burgers vector for dislocations lying parallel to the traces of Channels 1, 2, and 3 are (a/2) $[\bar{1}11]$, (a/2) $[1\bar{1}1]$, and (a/2) $[11\bar{1}]$, respectively. It should be noted, as shown in Table A-II, that the [111] dislocations are always invisible for reflections from planes of the [111] zone.

TABLE A-I

CONTRAST AND VALUES OF $\vec{g} \cdot \vec{b}$ FOR DISLOCATIONS IN CASE A-1

	Contrast for Dislocations Parallel to Channel		
Channel Number	$\vec{g} = [01\bar{1}]$ Figure A-1b	$\vec{g} = [10\bar{1}]$ Figure A-1c	$\vec{g} = [1\bar{1}0]$ Figure A-1d
1	W	S	S
2,2a	S	W	S
3	S	S	W

S = Strong contrast, i.e., the dislocation is visible ($\vec{g} \cdot \vec{b} \neq 0$).

W = Weak contrast, i.e., the dislocation is invisible ($\vec{g} \cdot \vec{b} = 0$).

TABLE A-II

VALUE OF $\vec{g} \cdot \vec{b}$ FOR DISLOCATIONS IN CASE A-1

	$\vec{g} \cdot \vec{b}$		
$\vec{b}$	$\vec{g} = [01\bar{1}]$	$\vec{g} = [10\bar{1}]$	$\vec{g} = [1\bar{1}0]$
(a/2)[111]	0	0	0
(a/2)[$\bar{1}$11]	0	-1	-1
(a/2)[1$\bar{1}$1]	-1	0	1
(a/2)[11$\bar{1}$]	1	1	0

The channel planes are planes giving the observed traces in the (111) and containing the Burgers vectors of the slip dislocations. The trace directions were determined from the electron diffraction patterns and the Burgers vectors from the diffraction contrast analysis. These two directions uniquely determine the channel planes, which for Case A-1 are tabulated in Table A-III. Thus, we conclude that the channel planes are indeed the {110} set perpendicular to the (111).

We note that Channel 3 in Figure A-1 does not appear to be cleared of defect clusters to the same extent as Channels 1 and 2. This appearance is believed to be due to the formative stage of Channel 3. Perhaps the dislocations creating Channel 3 originated in the dislocation tangle at the intersection of Channels 1 and 2a and thus were generated at a later stage in the deformation than those sweeping Channels 1, 2, and 2a.

It seems clear from the offset in Channel 1 that Channel 2a formed after Channel 1 or, at the least, continued to serve as an active slip channel after Channel 1 formed. The magnitude of the offset in the direction of Channel 2a is about 1.5 centimeters in prints at a magnification of 50,500X. Thus, the actual magnitude of the offset in Channel 1 is about 3000 Å. Now, for niobium the Burgers vector for slip dislocations is 2.85 Å, and the magnitude of its component in the direction of Channel 2a is 2.70 Å. Therefore, we conclude that approximately 1100 dislocations have traveled along Channel 2a to produce the offset observed in Channel 1. It is interesting to note that the width of Channel 2a is also about 3000 Å. The spacing between {110} planes in niobium is 2.33 Å and thus approximately 1300 ($\bar{1}01$) planes are needed to account for the width of

TABLE A-III

CRYSTAL GEOMETRY OF CHANNELS IN CASE A-1

Channel Number	Channeled Plane	$\vec{b}$ for Channeling Dislocations	Channel Trace Direction	Angle Between [111] and Plane Normal
1	$(01\bar{1})$	$(a/2)[\bar{1}11]$	$[\bar{2}11]$	90°
2,2a	$(\bar{1}01)$	$(a/2)[1\bar{1}1]$	$[1\bar{2}1]$	90°
3	$(1\bar{1}0)$	$(a/2)[11\bar{1}]$	$[11\bar{2}]$	90°

Channel 2a. The ratio of the number of dislocations sweeping the channel to the number of adjacent ($\bar{1}01$) planes within the channel is 0.9.

CASE A-2 (FIGURE A-2)

The equilateral-triangular channel pattern, shown in Figure A-2 with $\vec{g} = [\bar{1}01]$, was examined using various diffraction vectors and the stereo technique. The indices of the channel planes were determined in the same way as described above for Case A-1, i.e., from the Burgers vectors of the dislocations as deduced from a $\vec{g} \cdot \vec{b}$ analysis and the channel trace directions. The results are given in Table A-IV. An examination of the stereo pairs revealed that all the channel planes in Figure A-2 were perpendicular to (111). Thus, the crystal geometry of these channels was determined uniquely to be the same as for the set of {110} planes found in Case A-1.

In contrast to Case A-1, it is interesting to note that none of the channels in Figure A-2 show a clearly defined offset where they intersect one another. If we assume that the width of a channel is related to the number of dislocations moving along it, one may suppose in the case of Channels 2, 3a, and 3b that too few dislocations have passed along these relatively narrow channels for there to be an offset perceptible at the present magnification. Following this line of reasoning, one then suggests that relatively few dislocations moved along Channel 1 after the narrower channels had formed.

The hook-shaped dislocation in the cluster-rich matrix above the tangle seen in Figure A-2 was found to have an (a/2) [$\bar{1}11$] Burgers vector. In stereo pairs this dislocation was observed to curve toward the foil

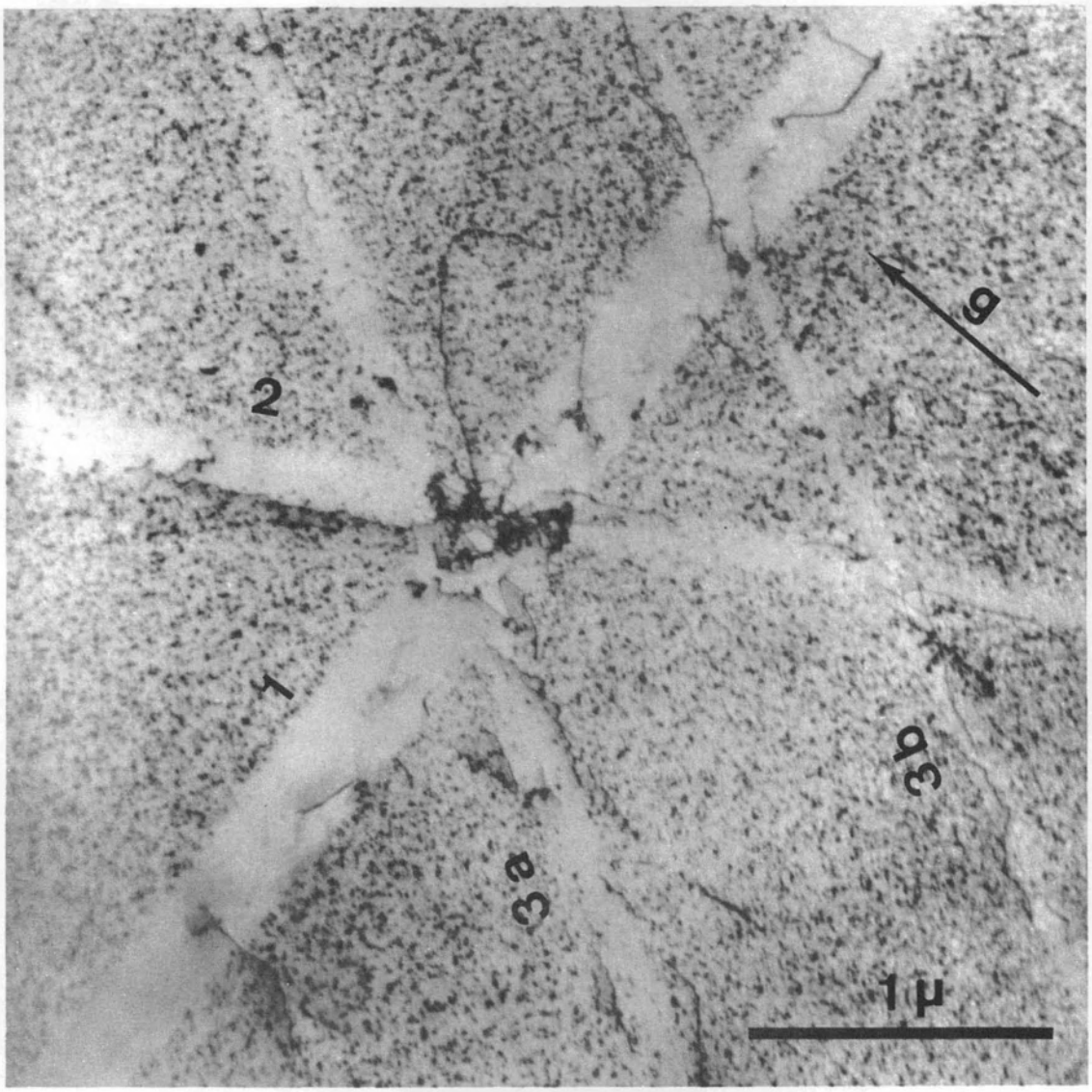

Figure A-2. Equilateral-triangular channel pattern on (111) in CIBA-A niobium for $\vec{g} = [\bar{1}01]$.

TABLE A-IV

CRYSTAL GEOMETRY OF CHANNELS IN CASE A-2

Channel Number	Channeled Plane	$\vec{b}$ for Channeling Dislocations	Channel Trace Direction	Angle Between [111] and Plane Normal
1	$(10\bar{1})$	$(a/2)[1\bar{1}1]$	$[\bar{1}2\bar{1}]$	90°
2	$(\bar{1}10)$	$(a/2)[11\bar{1}]$	$[11\bar{2}]$	90°
3a,3b	$(01\bar{1})$	$(a/2)[\bar{1}11]$	$[\bar{2}11]$	90°

surface at the bend forming the hook. Therefore, this dislocation exhibits both edge and screw character. In other micrographs the contrast is much stronger for the segment curved toward the surface as is predicted by diffraction theory for edge segments.

CASE A-3 (FIGURE A-3)

In Case A-3 attention is focused on a tangle at the intersection of four channels in a (111) foil, as shown in Figure A-3. The channel configuration is shown at low magnification in Figure A-3a under the $[1\bar{2}1]$ diffraction vector. An interesting feature observed here is the dislocation array in Channel 3 between the large tangle and Channel 1c that appears to include a helix with its axis direction across the channel. In fact, the axis direction for the helix is the same as the direction of the trace of Channel 1b. This area is shown at higher magnification with operating reflections $[1\bar{2}1]$ and $[\bar{1}10]$ in Figures A-3b and A-3c, respectively. The helix exhibits weak contrast for $\vec{g} = [\bar{1}10]$ as seen in Figure A-3c. Dislocations in Channels 1a, 1b, 1c, and 3 are also out of contrast in Figure A-3c as would be expected for $[11\bar{1}]$ dislocations. Notice also that where the helix ends at the channel wall, a step exists resulting in a narrowing of the channel. At the constriction in Channel 3 a tangle of dislocations is observed. The channel walls of this narrow region are approximately aligned with the walls of that portion of Channel 3 located to the left of the large tangle which is near the center of Figure A-3a. The channel crystallography determined by an analysis similar to that discussed in Case A-1 is given in Table A-V. The channeled planes for Channels 1b and 3 are the $(1\bar{1}0)$ and the (011) planes, whose normals

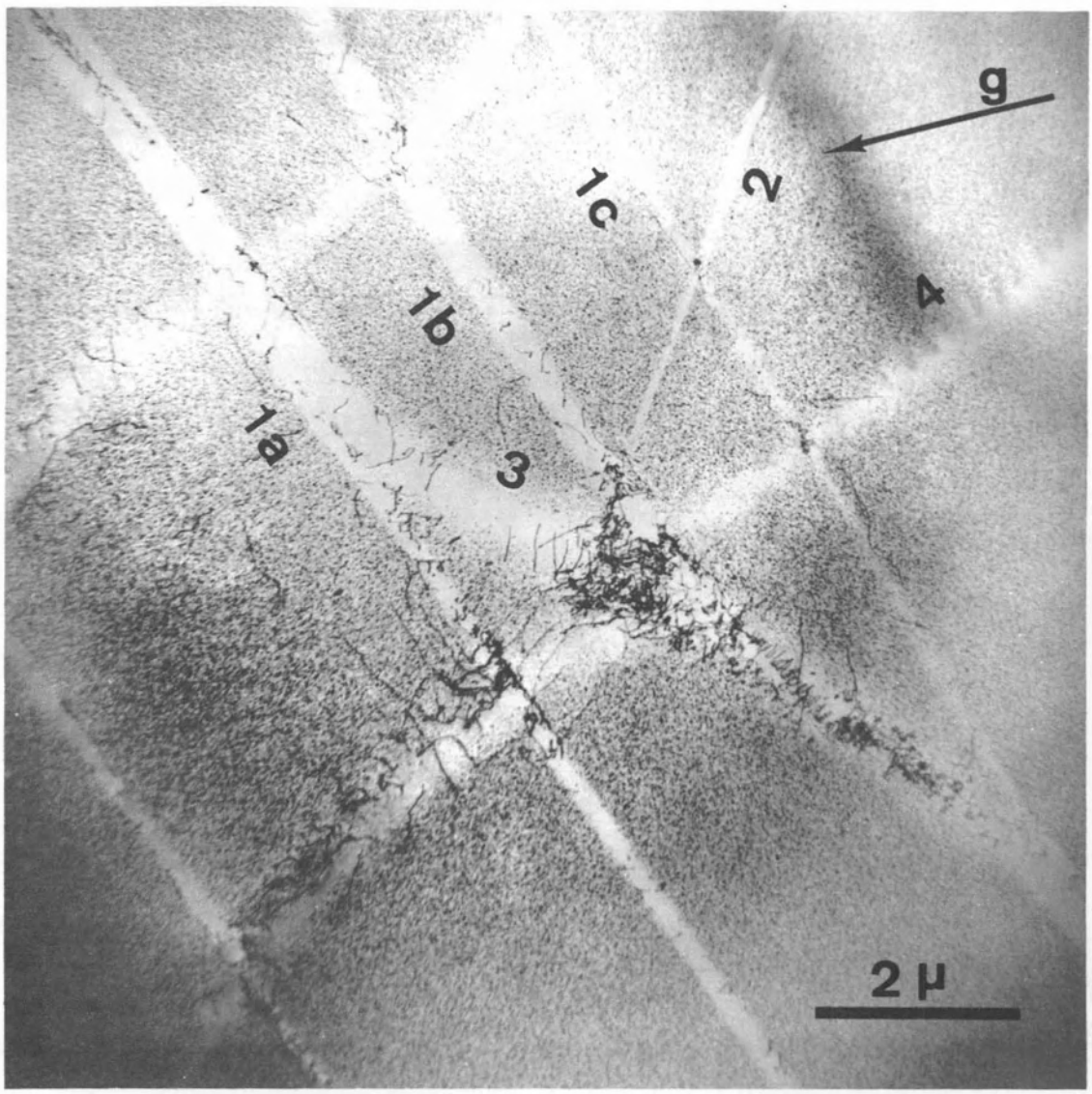

(a) $\vec{g} = [1\bar{2}1]$.

Figure A-3. Tangle at the intersection of dislocation channels on a (111) foil surface in CIBA-A niobium.

The same general area of view is shown at low magnification and at higher magnification for two diffraction conditions.

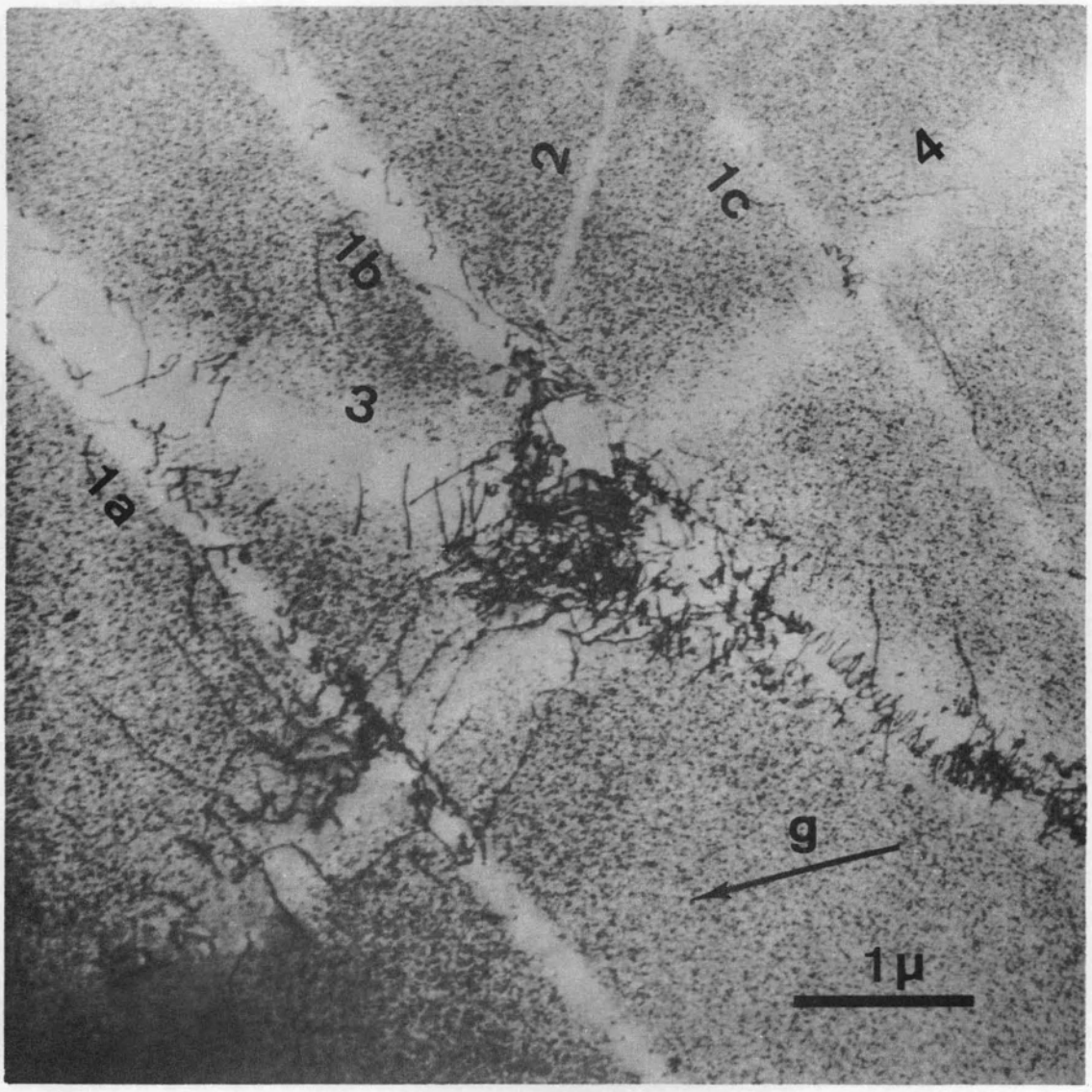

(b) $\vec{g} = [1\bar{2}1]$.

Figure A-3. (continued).

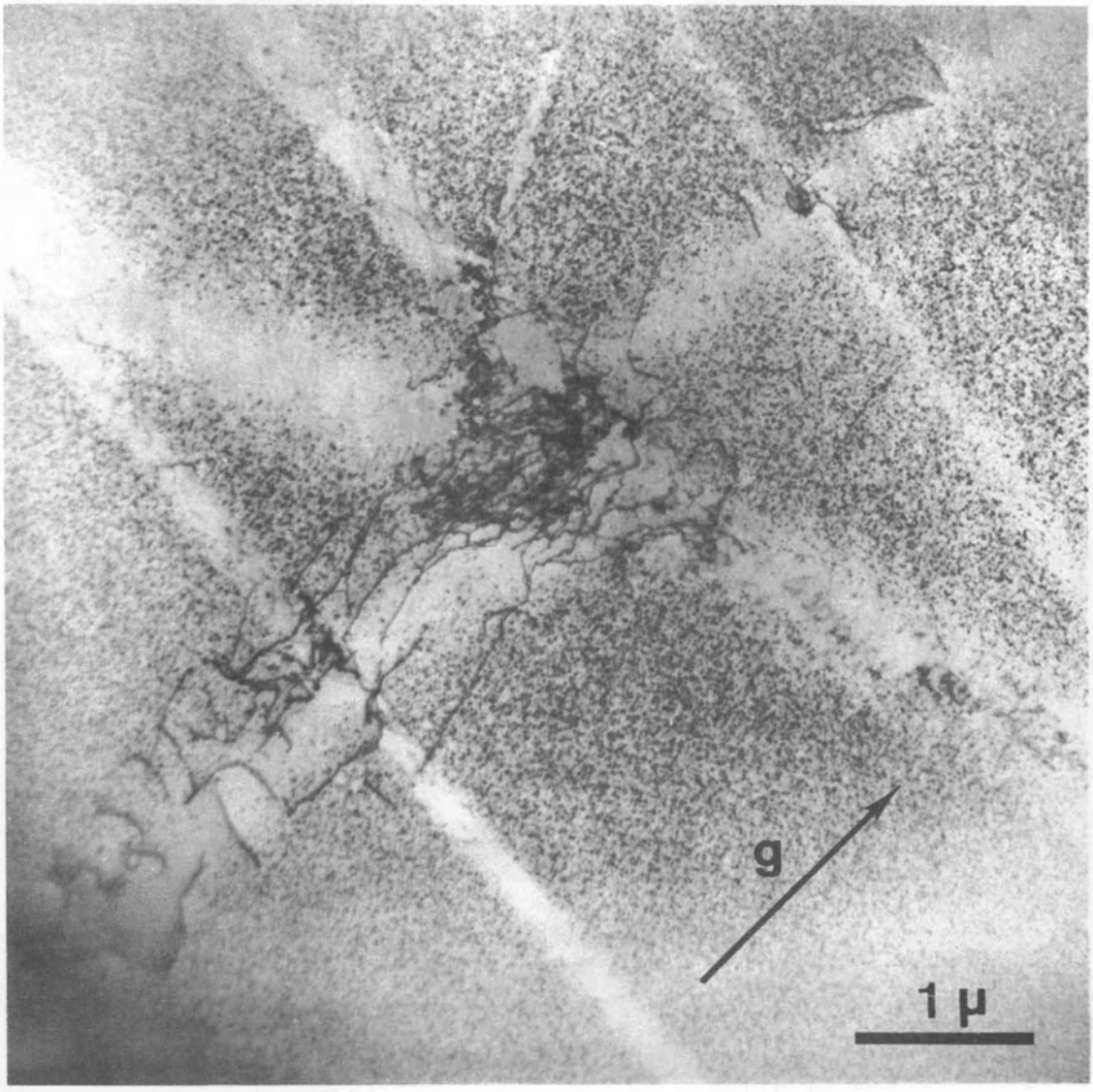

(c) $\vec{g} = [\bar{1}10]$.

Figure A-3. (continued).

TABLE A-V

CRYSTAL GEOMETRY OF CHANNELS IN CASE A-3

Channel Number	Channeled Plane	$\vec{b}$ for Channeling Dislocations	Channel Trace Direction	Angle Between [111] and Plane Normal
1a,1b,1c	$(1\bar{1}0)$	$(a/2)[11\bar{1}]$	$[11\bar{2}]$	90°
2	$(0\bar{1}1)$	$(a/2)[\bar{1}11]$	$[\bar{2}11]$	90°
3	(011)	$(a/2)[11\bar{1}]$	$[0\bar{1}1]$	35° 16'
4	(110)	$(a/2)[\bar{1}11]$	$[1\bar{1}0]$	35° 16'

make an angle with the [111] direction of 90° and 35° 16', respectively. It is suggested that the initial portion of Channel 3 to the right of the large tangle has experienced channeling on both $(1\bar{1}0)$ and (011) planes, whereas only the (011) plane is channeled in the narrower portion farther to the right in Figure A-3a. Dislocations with (a/2) $[11\bar{1}]$ Burgers vectors are the channeling dislocations for both Channels 1a and 3. It is suggested that dislocations moving on the (110) planes of Channel 1a could be shunted into Channel 3 by cross slipping onto the (011) plane. A comparison of Figures A-3b and A-3c indicates that $[11\bar{1}]$ dislocations, which are out of contrast for the $[\bar{1}10]$ operating reflection of Figure A-3c, make up a portion of the tangle at the intersection of Channels 3 and 4.

CASE A-4 (FIGURE A-4)

Figure A-4 shows a boundary crossed by a channel at W. In this case the boundary is inclined to the foil surface and is composed of a regular array of parallel dislocations about 620 Å apart. The orientations at either side of the boundary were found from diffraction patterns to be nearly the same, i.e., (111). The dislocations in the boundary project onto (111) at an angle of 10.5 to 13 degrees from $[0\bar{1}1]$. The boundary lies near the $[\bar{2}11]$ direction. The trace of the channel is in the $[\bar{1}\bar{1}2]$ direction, with $(\bar{1}10)$ the most probable channel plane and $[11\bar{1}]$ the slip dislocations. The channeling dislocations appear to have cut through the boundary removing the segments of the boundary dislocations within the channel.

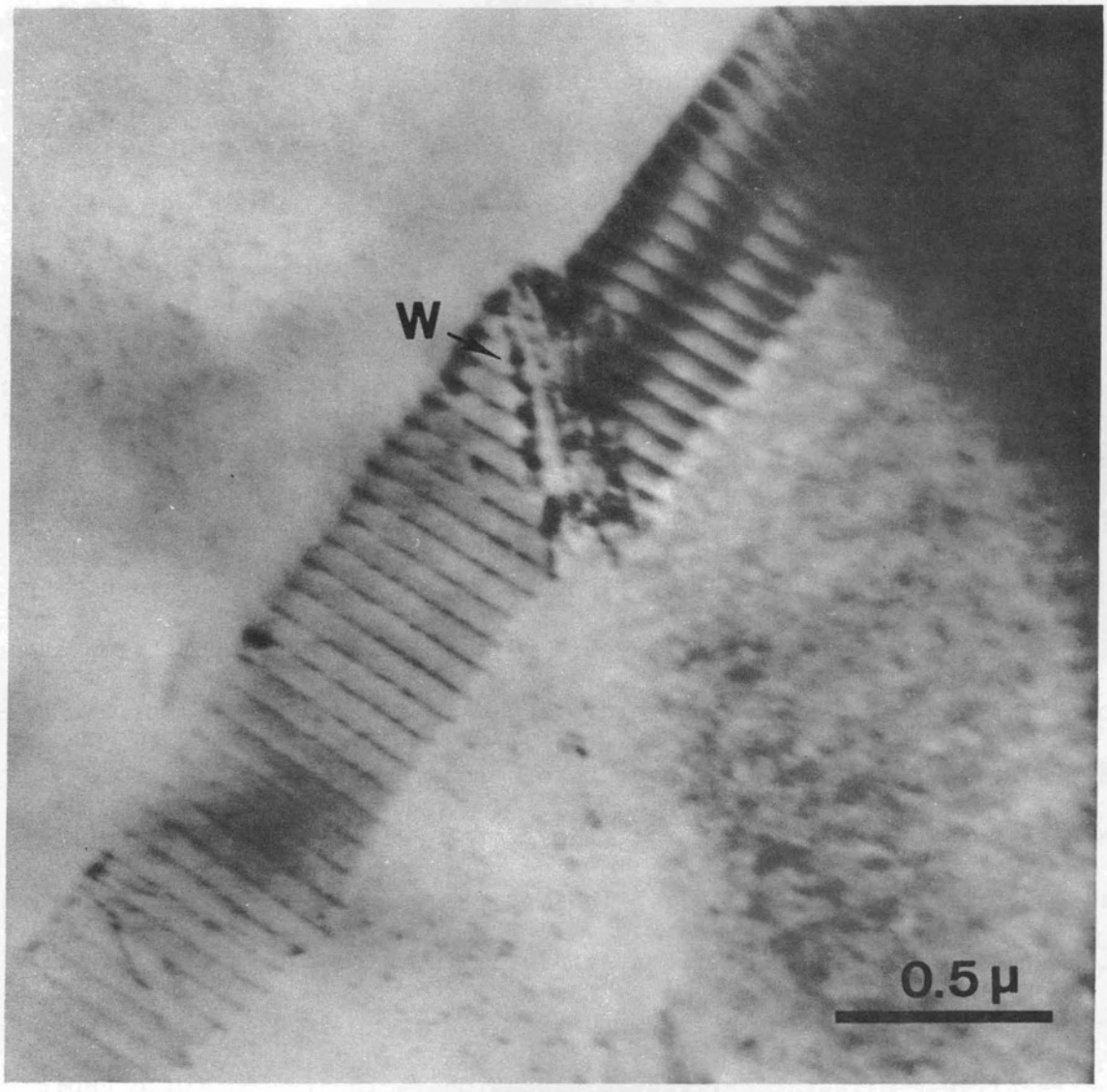

Figure A-4. Dislocation channel crossing a boundary.

APPENDIX B

CRYSTAL GEOMETRY AND BURGERS VECTORS IN CASE 5, CHAPTER V

For Case 5 (see page 130), the plane of each micrograph in Figure 20 is near (111). The operating reflection is $[0\bar{1}1]$ in Figure 20a and $[\bar{1}10]$ in Figure 20b. Thus, dislocations with Burgers vectors of (a/2) $[\bar{1}11]$ and (a/2) $[11\bar{1}]$, respectively, are expected to be out of contrast in these figures. The main channel lies in the $[\bar{1}2\bar{1}]$ direction and is nearly perpendicular to the $[\bar{1}01]$ direction. Since many dislocations are observed parallel to the channel direction, the channel plane for the main channel is believed to be $(\bar{1}01)$ which is perpendicular to the (111) foil surface. Hence, the Burgers vector for dislocations slipping in the main channel is (a/2) $[1\bar{1}1]$ and these dislocations should be visible in both micrographs of Figure 20. There is evidence, illustrated more clearly in Figure 20a and micrographs not shown, that small channels intersect the main channel where dislocation structure extends across it, for example, near M. In general, these cross-channels are aligned along $[11\bar{2}]$ (perpendicular to $[\bar{1}10]$). Thus, their slip system probably is $(\bar{1}10)$ $[11\bar{1}]$. These dislocations should be invisible in Figure 20b which indeed by comparison with Figure 20a is seen to be true for one set of the relatively straight parallel dislocations. In area N, for example, it appears that two sets of parallel dislocations are in the process of forming a network outside the channel. In addition to the $[11\bar{1}]$ dislocations out of contrast in Figure 20b, the networks appear to contain $[1\bar{1}1]$ dislocations, i.e., dislocations slipping in the main channel.

On the basis of diffraction contrast theory ($\vec{g} \cdot \vec{b}$ analysis), the dislocations of the {111} type expected to be visible in Figure 20a but absent in Figure 20b have (a/2) [11$\bar{1}$] Burgers vectors, whereas dislocations with (a/2) [$\bar{1}$11] Burgers vectors are in contrast in Figure 20b but out of contrast in Figure 20a. The [11$\bar{1}$] dislocations to the right of M in Figure 20a can be accounted for by slip dislocations from the (110) channel intersecting the main channel near M. However, the dislocations seen in Figure 20b to the right of M are *not* slip dislocations for planes giving traces in the direction of either the main or side channel. Therefore, it is difficult to account for these dislocations as [$\bar{1}$11] dislocations. If we consider the interaction of {111} type dislocations moving in the channels intersecting at M, then the following reaction is possible:

$$(a/2)\ [1\bar{1}1] + (a/2)\ [11\bar{1}] \longrightarrow (a)\ [100]\ . \qquad \text{(B-1)}$$

Dislocations with (a) [100] Burgers vectors would also be in and out of contrast as observed in Figure 20. Although the Burgers vector of the dislocations to the right of M remains uncertain, we believe the very joggy nature of these dislocations supports the contention that the two sets are interlaced into a network, forming thereby the beginning of a new cell wall.

APPENDIX C

DEFECT CLUSTER PATTERN IN POST-IRRADIATION-ANNEALED CIBA-A NIOBIUM

Figure C-1 illustrates particularly well an interesting feature observed in many micrographs. Careful examination of this micrograph reveals that the defect clusters, which at first glance may seem to be randomly distributed, are, in fact, frequently related to one another in a chain-like manner. On occasion the chain of defect clusters appear to form an arc (for example, at A), while at B the clusters exist in a rather straight chain. The sample in Figure C-1 was given a mild anneal at 300°C for one hour to make the pattern more noticeable; however, as-irradiated samples display similar patterns. At the present, the origin of these patterns is not understood. It is suggested, however, that the creation of secondary cascades along the trajectory of high-energy primary knock-ons (see, for example, Merkle,[52] von Jan,[373-375] and Seeger and von Jan[376]) possibly could account for the observations.

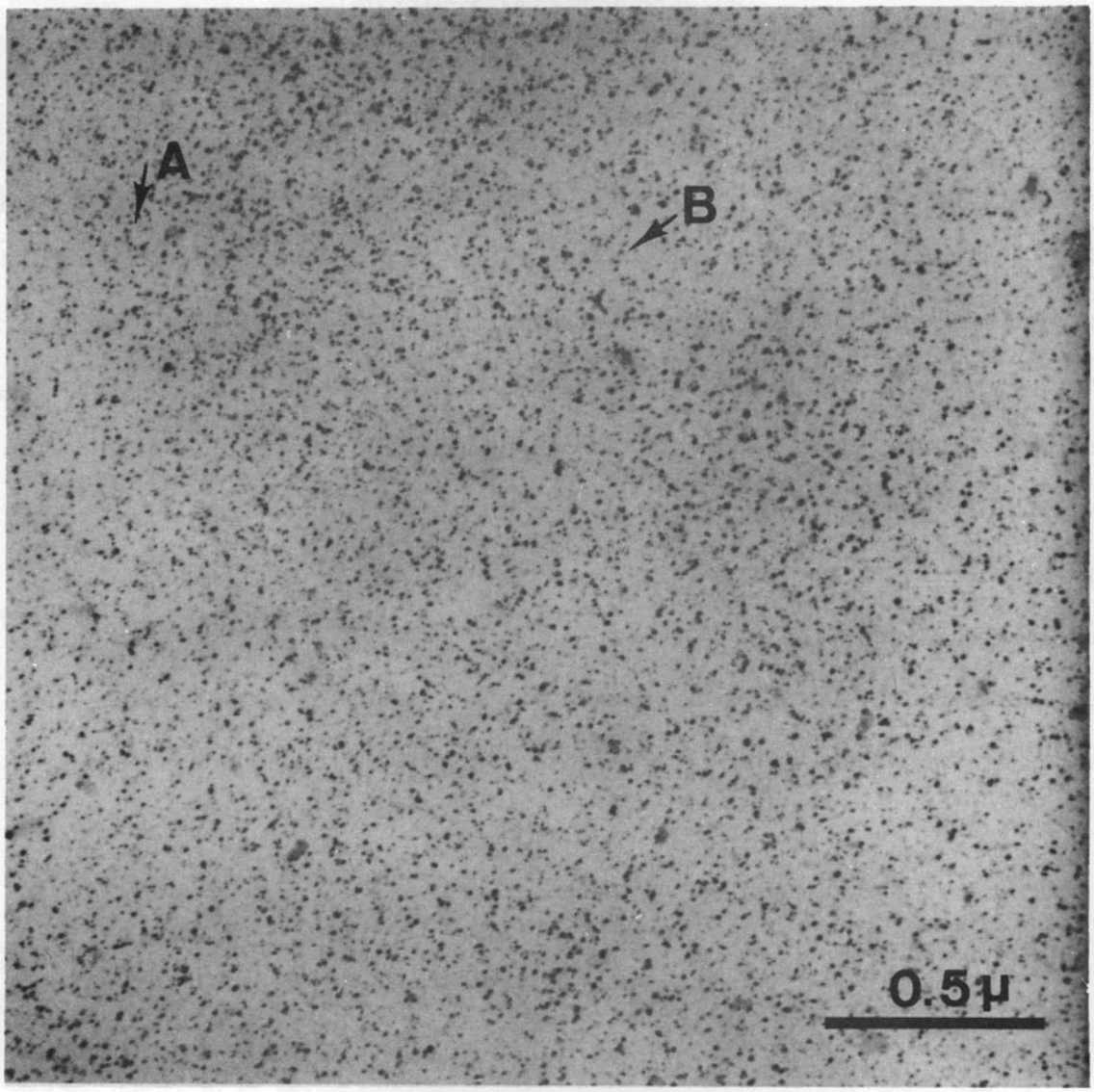

Figure C-1. Defect cluster pattern in CIBA-A niobium post-irradiation annealed for one hour at 300°C.

APPENDIX D

DISLOCATION STRUCTURES IN POST-IRRADIATION-ANNEALED-AND-DEFORMED CIBA-A NIOBIUM

DISLOCATION NETWORK

Figure D-1 shows a partially formed dislocation network in CIBA-A niobium irradiated to 2 x 10^{18} neutrons/cm^2 (E > 1 Mev) and strained 2.2 percent in tension after a post-irradiation anneal at 200°C for two hours. It is suggested that the dislocation network is composed of grown-in dislocations to which radiation-produced defect clusters have segregated. The dislocations in the network make an angle of approximately 120° with one another at their intersections and tend to be aligned along <112> directions as seen in the (111) foil plane. The significant dislocation activity near the network, especially at the junctions, appears to indicate that the grown-in network serves as an effective source of slip dislocations.

DISLOCATION LOOP ARRAY

An interesting feature illustrated in Figure D-2 is the array of dislocation loops, which appear to have been punched out by the source at S. The material is CIBA-A niobium irradiated to 2 x 10^{18} neutrons/cm^2 (E > 1 Mev) and then post-irradiation annealed at 800°C for two hours and lightly deformed. The axis of the cigar-shaped array is $[11\bar{2}]$ and the foil surface is (111). It seems reasonable to suggest that as dislocation loops are punched out and move away from the source, they expand,

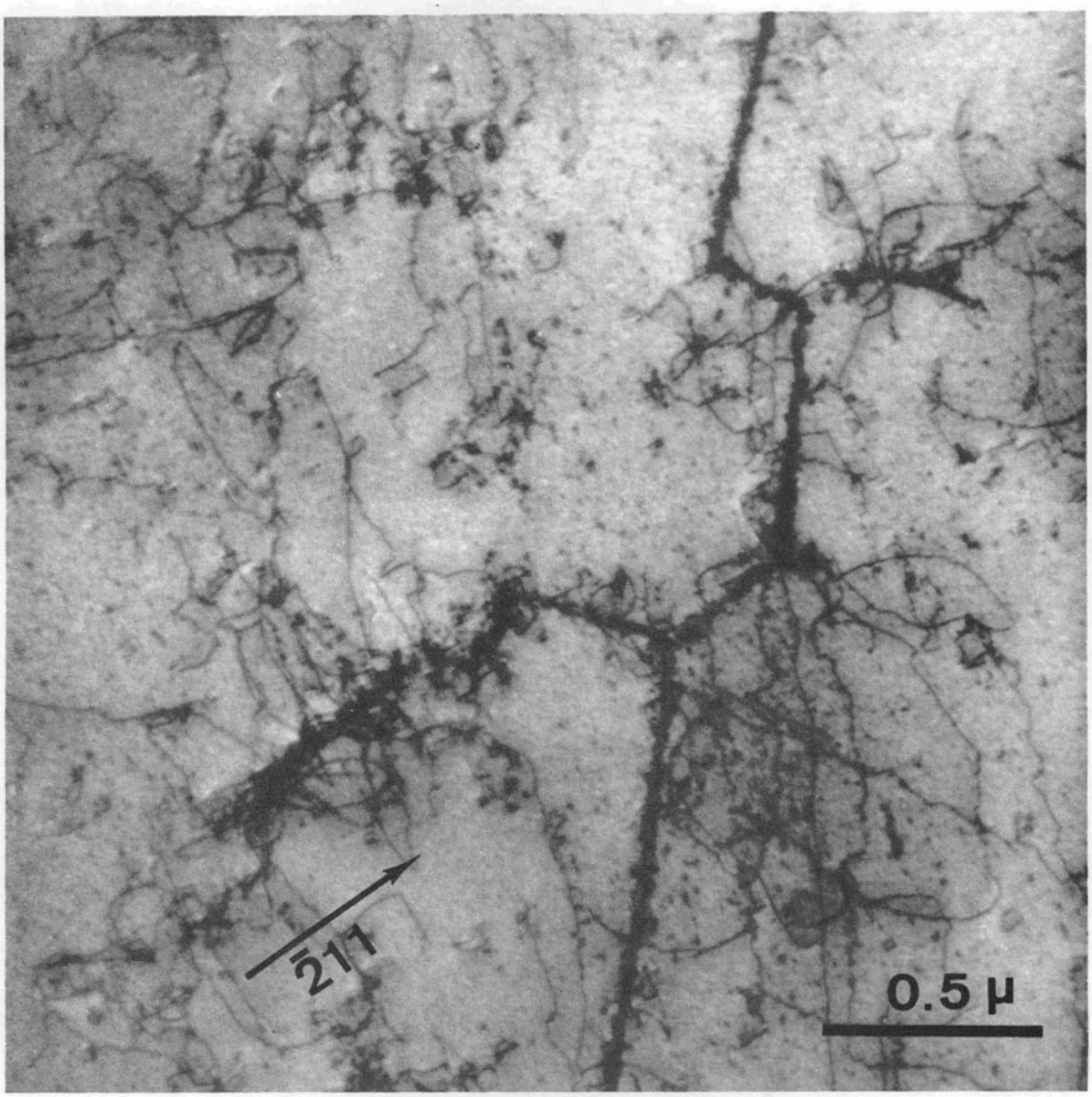

Figure D-1. Partially formed dislocation network in CIBA-A niobium post-irradiation annealed at 200°C for two hours and strained 2.2 percent in tension.

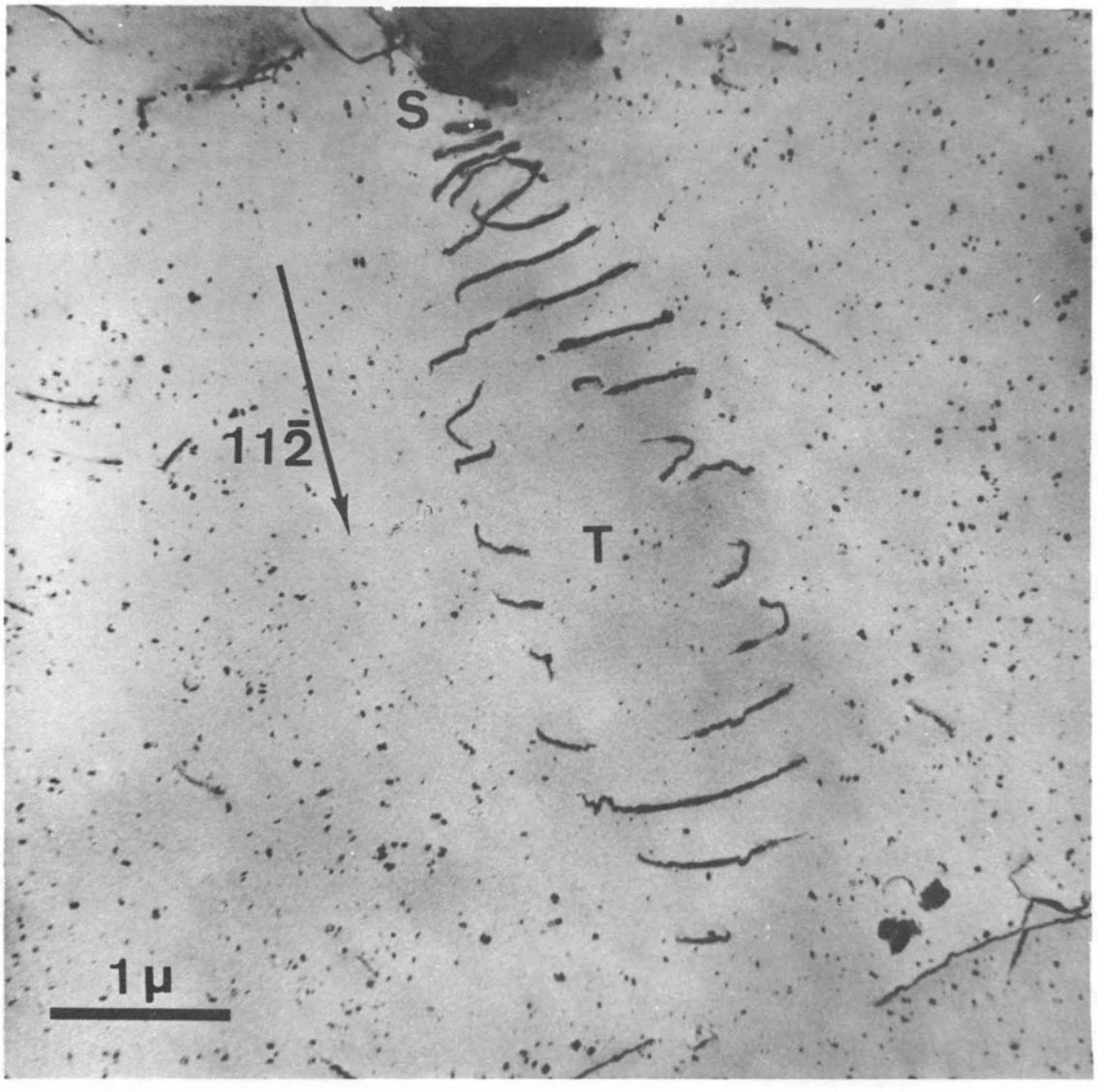

Figure D-2. Array of dislocation loops punched out by an inclusion in CIBA-A niobium post-irradiation annealed at 800°C for two hours.

perhaps by absorbing radiation-produced defects. Where the expanded loops meet the foil surface, they become separated into the segments observed at T in Figure D-2.

INTERNAL DISTRIBUTION

1-2. Central Research Library
3. Document Reference Section
4-8. Laboratory Records Department
9. Laboratory Records, ORNL, R.C.
10. ORNL Patent Office
11-25. Division of Technical Information Extension
26. Research and Development Division, ORO
27. R. W. Armstrong (Consultant)
28. D. S. Billington
29. H. Birnbaum (Consultant)
30. G. E. Boyd
31. M. A. Breazeale (Consultant)
32. W. E. Brundage
33. N. Cabrera (Consultant)
34. A. M. Clogston (Consultant)
35. R. R. Coltman
36. J. H. Crawford, Jr. (Consultant)
37. J. C. Crump, III
38. J. E. Epperson
39. J. H. Frye, Jr.
40. J. J. Gilman (Consultant)
41. H. D. Guberman
42. W. O. Harms
43. N. E. Hinkle
44. D. K. Holmes
45. L. D. Hulett
46. R. H. Kernohan
47. J. S. Koehler (Consultant)
48. G. Leibfried (Consultant)
49. H. G. MacPherson
50. C. J. McHargue
51. R. J. Maurer (Consultant)
52. J. W. Mitchell (Consultant)
53. T. S. Noggle
54. A. S. Nowick (Consultant)
55. S. M. Ohr
56. V. K. Paré
57. R. E. Reed
58. S. Siegel (Consultant)
59. J. O. Stiegler
60. A. S. Tetelman (Consultant)
61-93. R. P. Tucker
94-105. M. S. Wechsler
106. A. M. Weinberg
107. M. K. Wilkinson
108. J. M. Williams
109. F. W. Young, Jr.

EXTERNAL DISTRIBUTION

110-111. Oak Ridge Associated Universities, University Participation Office, Oak Ridge, Tennessee
112-113. Chemical and Metallurgical Engineering Department, University of Tennessee, Knoxville, Tennessee
114. S. Amelinckx, Centre d'Etude de l'Energie Nucleaire, Laboratories du C.E.N., Mol-Donk, Belgium
115. T. H. Blewitt, Metallurgy Division, Argonne National Laboratory, 9700 South Cass Avenue, Argonne, Illinois 60439
116. J. L. Brimhall, Battelle Memorial Institute, Pacific Northwest Laboratory, P. O. Box 999, Richland, Washington 99352
117. J. W. Christian, Department of Metallurgy, Oxford University, Parks Road, Oxford, England
118. J. Diehl, Max-Planck-Institut für Metallforschung, Institut für Sondermetalle, Seestrasse 92, 7000 Stuttgart 1, Germany

119. B. L. Eyre, Metallurgy Division, Atomic Energy Research Establishment, Harwell, Didcot, Berkshire, England
120. J. Friedel, Physique des Solides, Faculty des Science, Orsay 91, France
121. P. Haasen, Institut für Metallphysik der Universitat Göttingen, Hospitalstrasse 12, Göttingen, Germany
122. G. T. Hahn, Metals Science Group, Battelle Memorial Institute, 505 King Avenue, Columbus, Ohio 43201
123. A. A. Johnson, Brooklyn Polytechnic Institute, New York, New York
124. M. J. Makin, Metallurgy Division, Atomic Energy Research Establishment, Harwell, Didcot, Berkshire, England
125. T. E. Mitchell, Case Institute of Technology, University Circle, Cleveland, Ohio
126. P. L. Pratt, Department of Metallurgy, Imperial College, London, S.W. 7, England
127. R. E. Reed-Hill, Metals Research Laboratory, University of Florida, Gainesville, Florida
128. A. Seeger, Max-Planck-Institut für Metallforschung, Institut für Physik, Azenbergstrasse 12, 7000 Stuttgart 1, Germany
129. G. P. Seidel, Max-Planck-Institut für Metallforschung, Institut für Sondermetalle, Seestrasse 92, 7000 Stuttgart 1, Germany
130. J. V. Sharp, Metallurgy Division, Atomic Energy Research Establishment, Harwell, Didcot, Berkshire, England
131. J. M. Simmons, Division of Reactor Development, Atomic Energy Commission, Washington, D. C.
132. J. T. Stanley, Engineering Mechanics Department, Arizona State University, Tempe, Arizona 85281
133. E. E. Stansbury, Department of Chemical and Metallurgical Engineering, The University of Tennessee, Knoxville, Tennessee 37916
134. D. K. Stevens, Materials and Metallurgy Branch, Division of Research, U. S. Atomic Energy Commission, Washington, D. C.
135. G. Thomas, Department of Mineral Technology and Inorganic Materials Research Division, Lawrence Radiation Laboratory, University of California, Berkeley, California